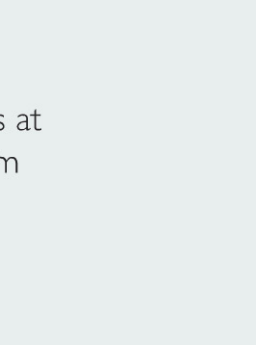
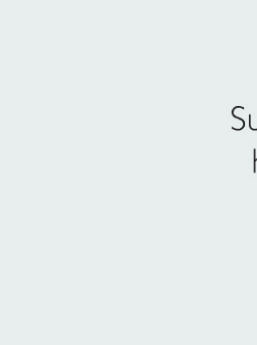
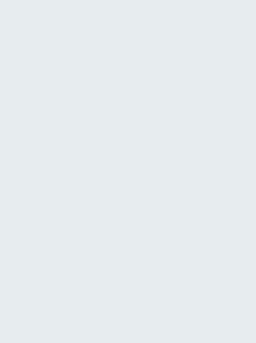
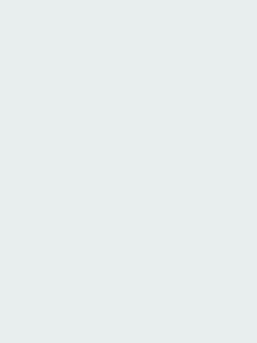
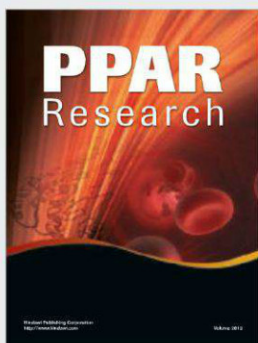
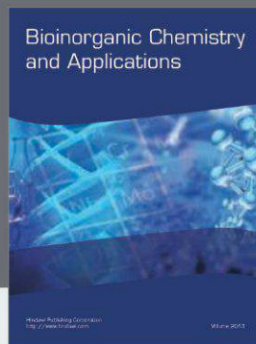
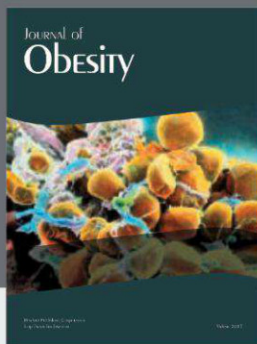
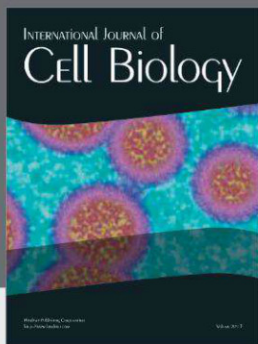


Science

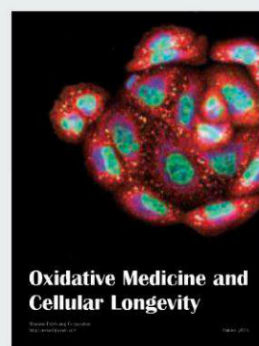
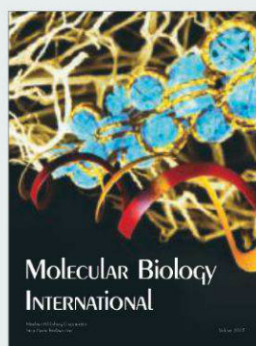
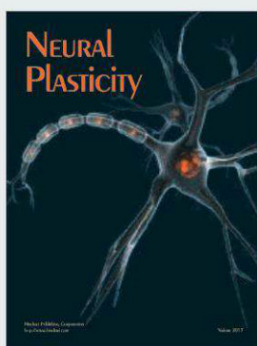
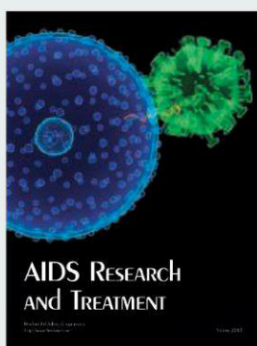
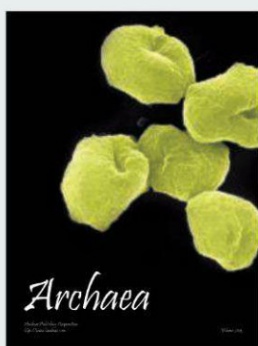
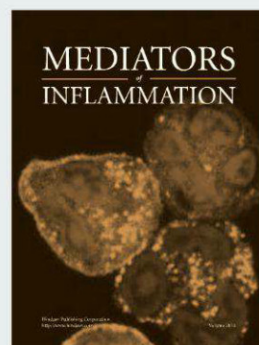
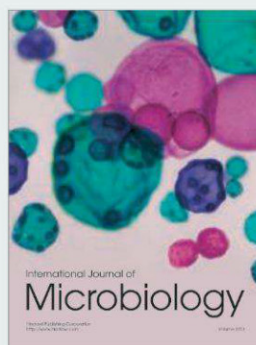
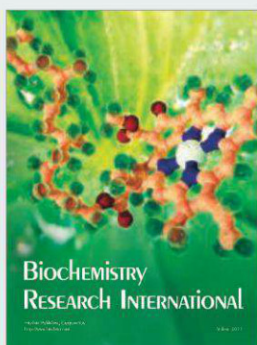
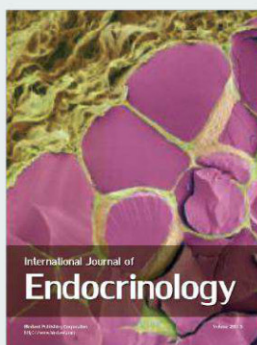
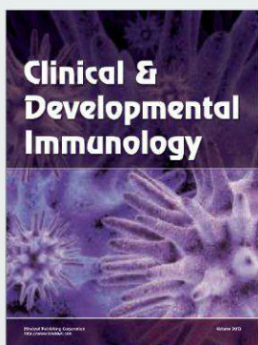
1 March 2013 | \$10





Hindawi

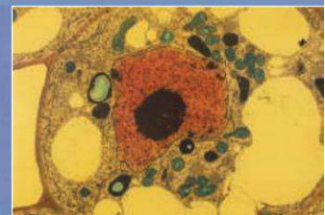
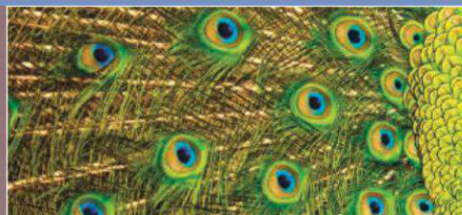
Submit your manuscripts at
<http://www.hindawi.com>



AAAS|2013 ANNUAL MEETING

14-18 FEBRUARY • BOSTON HYNES CONVENTION CENTER

THE BEAUTY AND BENEFITS OF SCIENCE



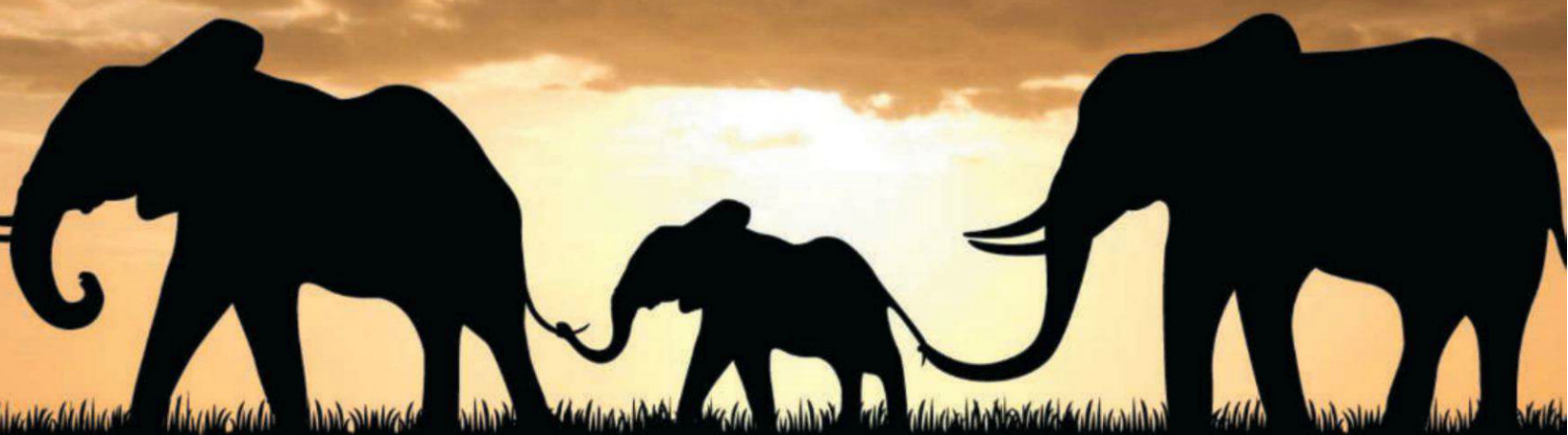
AAAS, publisher of *Science*, thanks the sponsors and supporters of the 2013 Annual Meeting



AAAS thanks
THE  KAVLI FOUNDATION
for its generous support of the Science Journalism Awards

Sponsors as of February 8, 2013

Make ends meet.



Gibson Assembly[™] Cloning Kit

New England Biolabs has revolutionized your laboratory's standard cloning methodology. The Gibson Assembly Cloning Kit combines the power of the Gibson Assembly Master Mix with NEB 5-alpha Competent *E. coli*, enabling fragment assembly and transformation in just under two hours. Save time, without sacrificing efficiency.

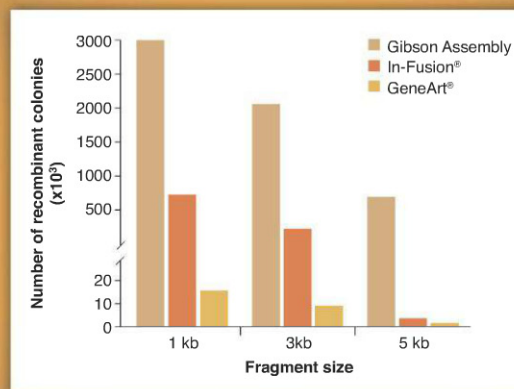
Making ends meet is now quicker and easier than ever before, with the Gibson Assembly Cloning Kit from NEB.

NEBuilder[™]
for Gibson Assembly

Visit NEBGibson.com to view the latest tutorials and to try our primer design tool.

IN-FUSION[®] is a registered trademark of Clontech Laboratories, Inc.
GENEART[®] is a registered trademark of Life Technologies, Inc.
GIBSON ASSEMBLY[™] is a trademark of Synthetic Genomics, Inc.

Gibson Assembly Cloning Kit provides robust transformation efficiencies



Assembly reactions containing 25 ng of linear pUC19 vector and 0.04 pmol of each fragment were performed following individual suppliers' recommended protocols and using the competent cells provided with the kit. The total number of recombinant colonies was calculated per 25 ng of linear pUC19 vector added to the assembly reaction.



SYNTHETIC GENOMICS[®]

Some components of this product are manufactured by New England Biolabs, Inc. under license from Synthetic Genomics, Inc.

EDITORIAL

- 1011 Why National Science Academies?
Bruce Alberts
>> *Science Podcast*

NEWS OF THE WEEK

- 1018 A roundup of the week's top stories

NEWS & ANALYSIS

- 1020 What It Means for Agencies to Be Under the Sequester
1021 U.S. Agencies Directed to Make Research Papers Available
1022 Brain Project Draws Presidential Interest, but Mixed Reactions
1024 Europe Debates Ethics Reviews, Data Release
1025 New U.S. Rules Increase Oversight of H5N1 Studies, Other Risky Science
>> *Policy Forum p. 1036*; See all H5N1 coverage online at http://scim.ag/_h5n1

NEWS FOCUS

- 1026 A Call to Cyber Arms
>> *Science Podcast*
1028 Cooling a Hot Zone
Astronomers Lend Know-How to Cleanup
1030 Pollutants Capture the High Ground in the Himalayas

LETTERS

- 1032 A Call for Integrative Thinking
D. J. Rapport and L. Maffi
Data Re-Identification: Prioritize Privacy
A. Gutmann
Data Re-Identification: Societal Safeguards
R. B. Altman et al.
Data Re-Identification: Protect the Children
D. Gurwitz
1033 CORRECTIONS AND CLARIFICATIONS
1033 TECHNICAL COMMENT ABSTRACTS

BOOKS ET AL.

- 1034 On a Farther Shore
W. Souder, reviewed by F. R. Davis
1035 The Ethics of Species
R. L. Sandler, reviewed by P. W. Hughes

POLICY FORUMS

- 1036 A Framework for Decisions About Research with HPAI H5N1 Viruses
A. P. Patterson et al.
>> *News story p. 1025*; See all H5N1 coverage online at http://scim.ag/_h5n1
1038 Legal Trade of Africa's Rhino Horns
D. Biggs et al.

PERSPECTIVES

- 1040 Machinery to Reverse Irreversible Aggregates
H. R. Saibil
>> *Report p. 1080*
1041 Two Indistinguishable Electrons Interfere in an Electronic Device
C. Schönenberger
>> *Report p. 1054*
1042 Leads and Lags at the End of the Last Ice Age
E. J. Brook
>> *Report p. 1060*
1044 Welcome to the Microgenderome
M. B. Flak et al.
>> *Report p. 1084*
1045 One Genome, Two Ontogenies
W. E. Friedman
>> *Report p. 1067*

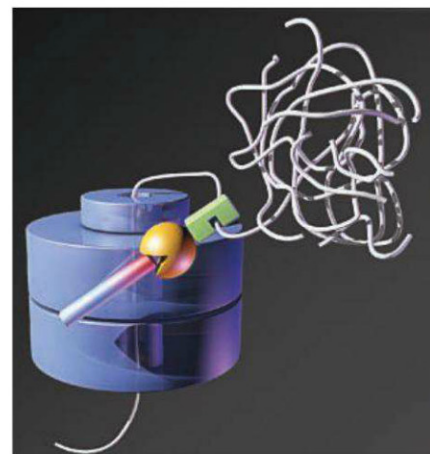
REVIEW

- 1047 The Continuing Challenge of Understanding, Preventing, and Treating Neural Tube Defects
J. B. Wallingford et al.
Review Summary; for full text: <http://dx.doi.org/10.1126/science.1222002>

CONTENTS continued >>



page 1026



pages 1040 & 1080



COVER

The rock pigeon (*Columba livia*) exhibits spectacular variation among more than 350 different domestic breeds. The adult male Old Dutch capuchine shown here is one of many breeds with a crest of reversed feathers on its head and neck. See page 1063 for a description of the genetic origins of the head crest and the relationships among breeds. For the story behind the cover, go to <http://scim.ag/cov6123>.

Photo: Sydney Stringham

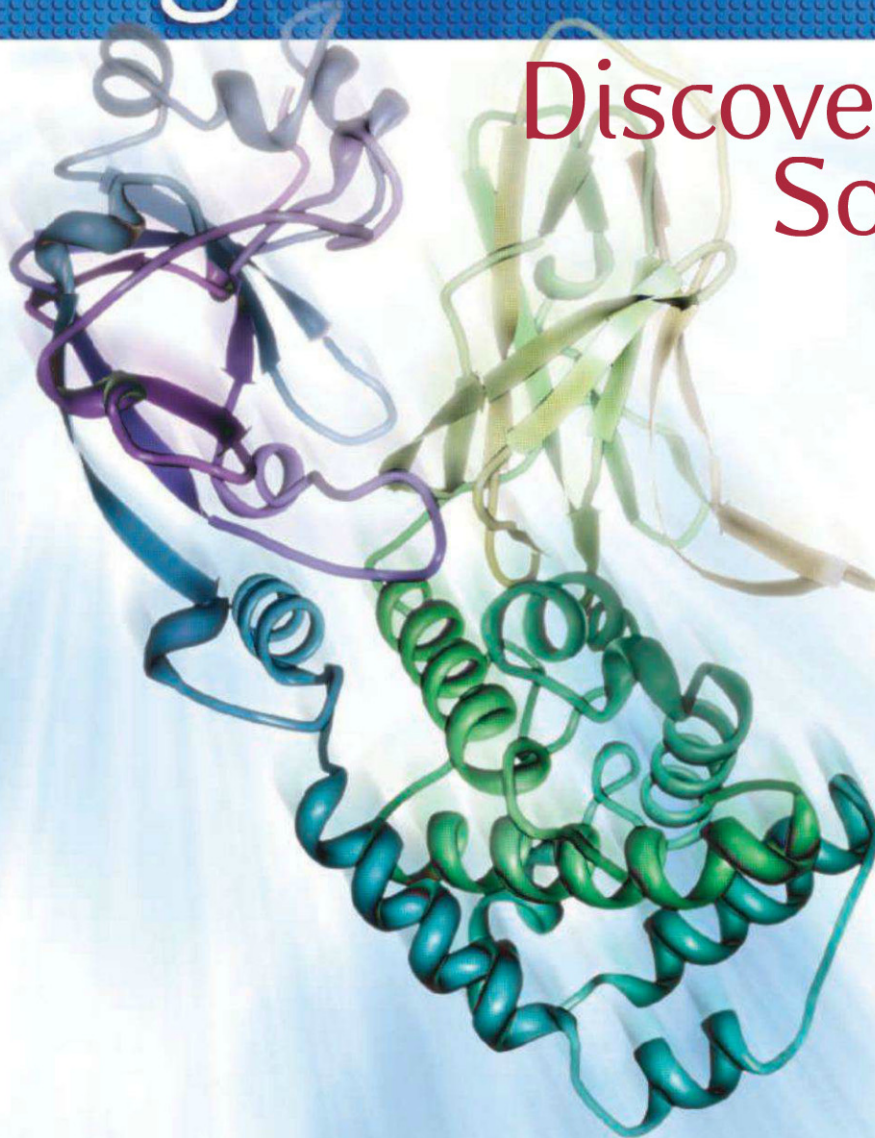
Explore our rich online offerings, including multimedia, news, *Science Careers*, and our two research journals—*Science Signaling* and *Science Translational Medicine*—at www.sciencemag.org

DEPARTMENTS

- 1009 This Week in *Science*
1012 Editors' Choice
1016 *Science Staff*
1103 New Products
1104 *Science Careers*

Reagent Proteins

Discover the
Source



Reagent Proteins is the source

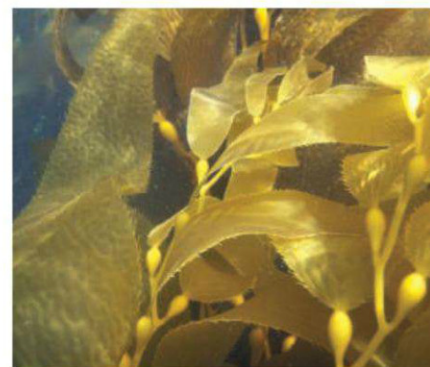
With over 5,000 recombinant proteins available, *Reagent Proteins* provides seamless access to the highest quality reagent, pre-clinical and cGMP grade proteins for research purposes.



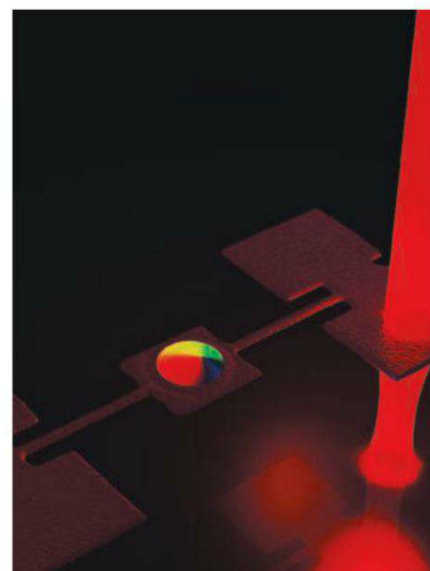
REPORTS

- 1048** A Black Hole Nova Obscured by an Inner Disk Torus
J. M. Corral-Santana et al.
Optical observations of a variable binary x-ray source reveal a black hole 3.6 times the Sun's mass in a short-period orbit.
- 1051** Quantitative Magneto-Mechanical Detection and Control of the Barkhausen Effect
J. A. J. Burgess et al.
A magnetic vortex core is used to probe nanoscale changes in magnetization.
- 1054** Coherence and Indistinguishability of Single Electrons Emitted by Independent Sources
E. Bocquillon et al.
The interference of single electrons emitted from independent sources is demonstrated.
>> *Perspective p. 1041*
- 1057** InP Nanowire Array Solar Cells Achieving 13.8% Efficiency by Exceeding the Ray Optics Limit
J. Wallentin et al.
Nanowire solar cells were fabricated that exhibit high photocurrents and low surface recombination.
- 1060** Synchronous Change of Atmospheric CO₂ and Antarctic Temperature During the Last Deglacial Warming
F. Parrenin et al.
Rising air temperature did not lead the increase of atmospheric carbon dioxide concentration during the last deglaciation.
>> *Perspective p. 1042*
- 1063** Genomic Diversity and Evolution of the Head Crest in the Rock Pigeon
M. D. Shapiro et al.
From Piazza San Marco to Trafalgar Square, pigeons have captured the attention of tourists from around the world.
- 1067** KNOX2 Genes Regulate the Haploid-to-Diploid Morphological Transition in Land Plants
K. Sakakibara et al.
A transcription factor enables land plants to alternate between haploid and diploid status in successive generations.
>> *Perspective p. 1045*
- 1071** Mps1 and Ipl1/Aurora B Act Sequentially to Correctly Orient Chromosomes on the Meiotic Spindle of Budding Yeast
R. E. Meyer et al.
Two kinases mediate a partner-changing interlude that prevents chromosome segregation errors in yeast meiosis.

- 1074** Genome-Wide Quantitative Enhancer Activity Maps Identified by STARR-seq
C. D. Arnold et al.
A map of thousands of *Drosophila* cell type-specific enhancers is revealed using a new method.
- 1077** Genomic Analysis of Non-NF2 Meningiomas Reveals Mutations in *TRAF7*, *KLF4*, *AKT1*, and *SMO*
V. E. Clark et al.
The mutational profiles of meningiomas, a common type of brain tumor, correlate with their anatomical location and clinical status.
- 1080** Unraveling the Mechanism of Protein Disaggregation Through a ClpB-DnaK Interaction
R. Rosenzweig et al.
Bacterial protein disaggregation elucidated via a combined biochemical methyl-transferase relaxation-optimized spectroscopy nuclear magnetic resonance approach.
>> *Perspective p. 1040*
- 1084** Sex Differences in the Gut Microbiome Drive Hormone-Dependent Regulation of Autoimmunity
J. G. M. Markle et al.
In mice, the gut microbiota influences levels of sex hormones and the development of autoimmune disease.
>> *Perspective p. 1044*
- 1088** Interferon- ϵ Protects the Female Reproductive Tract from Viral and Bacterial Infection
K. Y. Fung et al.
The cytokine interferon- ϵ is expressed in the female reproductive tract and protects against sexually transmitted diseases.
- 1092** Spreading Depression Triggers Headache by Activating Neuronal Panx1 Channels
H. Karatas et al.
Migraine results from a sequence of events starting from stressed cortical neurons and leading to the trigeminal nucleus.
- 1095** Stress in Puberty Unmasks Latent Neuropathological Consequences of Prenatal Immune Activation in Mice
S. Giovanoli et al.
Unfortunate synergies between stressors at vulnerable stages may underlie psychopathologies in mice.



pages 1045 & 1067



page 1051

SCIENCE (ISSN 0036-8075) is published weekly on Friday, except the last week in December, by the American Association for the Advancement of Science, 1200 New York Avenue, NW, Washington, DC 20005. Periodicals Mail postage (publication No. 484460) paid at Washington, DC, and additional mailing offices. Copyright © 2013 by the American Association for the Advancement of Science. The title SCIENCE is a registered trademark of the AAAS. Domestic individual membership and subscription (51 issues): \$149 (\$74 allocated to subscription). Domestic institutional subscription (51 issues): \$990; Foreign postage extra: Mexico, Caribbean (surface mail) \$55; other countries (air assist delivery) \$85. First class, airmail, student, and emeritus rates on request. Canadian rates with GST available upon request, GST #1254 88122. Publications Mail Agreement Number 1069624. Printed in the U.S.A.

Change of address: Allow 4 weeks, giving old and new addresses and 8-digit account number. Postmaster: Send change of address to AAAS, P.O. Box 96178, Washington, DC 20090-6178. Single-copy sales: \$10.00 current issue, \$15.00 back issue prepaid includes surface postage; bulk rates on request. Authorization to photocopy material for internal or personal use under circumstances not falling within the fair use provisions of the Copyright Act is granted by AAAS to libraries and other users registered with the Copyright Clearance Center (CCC) Transactional Reporting Service, provided that \$30.00 per article is paid directly to CCC, 222 Rosewood Drive, Danvers, MA 01923. The identification code for Science is 0036-8075. Science is indexed in the Reader's Guide to Periodical Literature and in several specialized indexes.



Research is still your favorite?

MAKE GREAT THINGS HAPPEN

Opportunities for natural scientists: Do you want to explore, research, change things? Welcome to EMD. With leading research in pharmaceuticals, through analysis of microorganisms, all the way to liquid crystals for LCDs, Merck continues developing innovative products. We offer excellent development perspectives in challenging research

projects aimed at improving people's lives. Join us and take part in shaping our diversified global business by making your passion a true calling. Ready to tread new paths?

come2emd.com





Interfering Single Electrons

Quantum information processing requires the generation of indistinguishable and coherent particles. While these have been demonstrated for photons, carrying it over for electrons and the possibility of quantum electronic implementations has been challenging. Using two independent single-electron sources patterned into a two-dimensional electron gas, **Bocquillon *et al.*** (p. 1054, published online 24 January; see the Perspective by **Schönenberger**) performed single-electron interference experiments. The results demonstrate that the generated electrons can possess the desired properties for potential quantum applications.

Prevention or Repair

Neural tube defects, such as spina bifida, remain remarkably common, despite widespread efforts to prevent them through supplementing maternal diets with folic acid. Surgery early in development has seen some success, but problems often remain. **Wallingford *et al.*** (p. 1047) review normal and abnormal neural tube development and suggest that discovering the genetic risk factors for these serious birth defects could provide ways to prevent and treat neural tube defects.

A Hidden Black Hole?

Black holes with masses comparable to that of the Sun are often associated with variable x-ray sources. **Corral-Santana *et al.*** (p. 1048) report optical observations of a faint and variable x-ray source detected in our galaxy with the Swift Burst Alert Telescope. The optical data reveal a black hole with a mass greater than three times that of the Sun in a 2.8-hour period around a low-mass donor star. Unusual for this type of system, the black hole binary is seen at a very high inclination.

Controlling Magnetic Noise

Ferromagnetic materials contain a number of magnetic domains, with individual domains switching stochastically as the field strength is increased. As magnetic memory elements shrink in size, it is important to understand, and ultimately control, this magnetic noise. Using a magnetic

vortex core integrated with a nanomechanical torsion balance, **Burgess *et al.*** (p. 1051, published online 17 January) created a two-dimensional map of the magnetic potential within the sample with nanoscale resolution. Moreover, introducing geometric defects (dimples) in the sample allowed the magnetization to be stabilized.

How Migraine Develops

Migraine is a common medical disorder. Unfortunately, how and why migraine headache is initiated is unclear. **Karatas *et al.*** (p. 1092) now describe a signaling pathway between stressed neurons and meningeal trigeminal afferents, which may explain how migraine headaches can be generated.

No Leader to Follow

Changes in the concentration of atmospheric CO₂ and surface air temperature are closely related. However, temperature can influence atmospheric CO₂ as well as be influenced by it. Studies of polar ice cores have concluded that temperature increases during periods of rapid warming have preceded increases in CO₂ by hundreds of years. **Parrenin *et al.*** (p. 1060; see the Perspective by **Brook**) present a revised age scale for the atmospheric component of Antarctic ice cores, based on the isotopic composition of the N₂ that they contain, and suggest that temperature and CO₂ changed synchronously over four intervals of rapid warming during the last deglaciation.

Mastering Meiosis

Two conserved kinases (Ipl1/Aurora B and Mps1) are known to be critical for correct chromosome orientation on the spindle during meiosis, but their roles and relationships in controlling chromosome segregation are unclear. Working in yeast, **Meyer *et al.*** (p. 1071, published online 31 January) monitored chromosomes as they go through the steps of properly attaching to the spindle microtubules and dissected the roles of the two kinases in chromosome pairing, orientation, and segregation.

Genetic Clues to Meningioma

Meningiomas are the most common primary brain tumors in adults. Located within the layer of tissue covering the brain, these tumors are usually slow-growing and benign but can cause serious neurological complications. About half of these tumors have mutations in the *neurofibromin 2* gene (*NF2*). To identify other genes that contribute to meningioma pathogenesis, **Clark *et al.*** (p. 1077, published online 24 January) performed genome sequence analysis on 300 tumors. Meningiomas fell into two general classes: benign tumors located at the skull base—which tend to harbor mutations in the *TRAF7*, *KLF4*, *AKT1*, and *SMO* genes—and higher-grade tumors located in the cerebral and cerebellar hemispheres harbor mutations in *NF2*.



A Role for IFN-ε

Type I interferons (IFNs) are critical cytokines involved in host defense against pathogens, particularly viruses. IFN-ε is an IFN-like gene encoded within the type I IFN locus in mice and humans whose function has not been characterized. **Fung *et al.*** (p. 1088) created mice with a genetic deletion in *Ifn-ε* and found that, like other type I IFNs, IFN-ε signals through the IFN-α receptors 1 and 2. However, unlike these other cytokines, which are primarily expressed by immune cells and are induced upon immune cell triggering, IFN-ε was expressed exclusively by epithelial cells of the female reproductive tract in both mice and humans and its expression was hormonally regulated. IFN-ε-deficient mice were more susceptible to infection with herpes simplex virus 2 and *Chlamydia muridarum*, two common sexually transmitted pathogens.

CHANEL

RECHERCHE ET TECHNOLOGIE
RESEARCH AND TECHNOLOGY

CHANEL - CE.R.I.E.S. RESEARCH AWARD



The CHANEL - CE.R.I.E.S. Research Award of 40,000 € is intended to honor a scientific researcher with a proven track record in fundamental or clinical research work, for a one-year period, on the subject of:

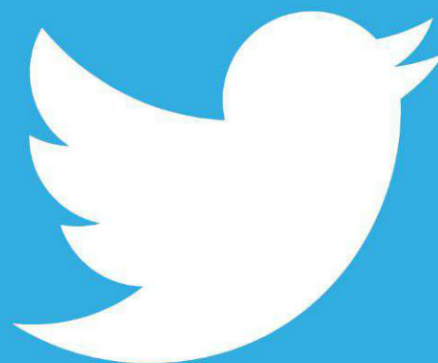
PHYSIOLOGY OR BIOLOGY OF HEALTHY SKIN AND/OR ITS REACTIONS TO ENVIRONMENTAL FACTORS

Previous CHANEL - CE.R.I.E.S.
Research Award Winners:

2012	Martin Röcken, M.D., Ph.D., Tübingen, Germany
2011	Joke A. Bouwstra, Ph.D., Leiden, Netherlands
2010	Howard Y. Chang, M.D., Ph.D., Stanford, USA
2009	Sabine Werner, Ph.D., Zurich, Switzerland
2008	Paul A. Khavari, M.D., Ph.D., Stanford, USA
2007	Richard L. Gallo, M.D., Ph.D., San Diego, USA
2006	Irwin McLean, Ph.D., DSc, FRSE, Dundee, Scotland, UK
2005	Masayuki Amagai, M.D., Ph.D., Tokyo, Japan
2004	Thomas Schwarz, M.D., Kiel, Germany
2003	Angela M. Christiano, Ph.D., New York, USA
2002	Dennis R. Roop, Ph.D., Houston, USA
2001	Fiona M. Watt, D.Phil., London, UK
2000	Michael Karin, Ph.D., San Diego, USA
1999	Jonathan Rees, M.D., Edinburgh, UK
1998	Jean Krutmann, M.D., Düsseldorf, Germany
1997	Jens-Michael Schröder, Ph.D., Kiel, Germany
1996	Akira Takashima, M.D., Ph.D., Dallas, USA

Deadline for applications: May 31, 2013

Requests for application forms must be addressed to:
www.research-technology.chanel.com



Join the Conversation!

Twitter is a great way to connect with AAAS members and staff about the issues that matter to you most. Be a part of the discussion while staying up-to-date on the latest news and information about your personal member benefits.

**Follow us @AAASmember
and join the conversation
with #AAAS**



MemberCentral.aaas.org



Bruce Alberts is Editor-in-Chief of *Science*.

Why National Science Academies?

NEXT WEEK MARKS THE 150TH ANNIVERSARY OF THE NATIONAL ACADEMY OF SCIENCES OF THE UNITED STATES. In the midst of the Civil War, a bill introduced by Congressman Henry Wilson of Massachusetts was passed on 3 March 1863 and signed into law by President Abraham Lincoln the same day. The Academy's charter thus created stipulated that a new Academy, formed by a group of not more than 50 of the nation's best scientists, "... shall, whenever called upon by any department of the Government, investigate, examine, experiment, and report upon any subject of science or art ... but the Academy shall receive no compensation whatever for any services to the Government of the United States." Lacking funds, the new Academy got off to a very shaky start.* But today it thrives as part of the influential National Academies, the name given to the expanded institution that now includes the National Research Council, the National Academy of Engineering, and the Institute of Medicine. Why has this organization prospered and grown over the course of the past 150 years? Critical to success is its unique mission to provide independent, evidence-based scientific advice to the nation's policy-makers.

I was the full-time president of the National Academy of Sciences from 1993 to 2005, and I am a strong believer in its value. Whom it elects to membership and honors with its prestigious awards sets a standard for scientific excellence that has important implications for the future, as those selected often become empowered as leaders in their own institutions. Moreover, the membership of the Academy, now numbering 2200, plus the nearly 4000 members of the National Academy of Engineering and the Institute of Medicine, serves as the foundation for the many committees of experts convened to advise the government. The subjects range from improving medical care or educating students in science, to prioritizing investments in the large instruments required to better understand the universe. Thousands of such reports—many highly relevant and beneficial to all nations of the world—are freely available and readily searchable on the Web site of The National Academies Press (www.nap.edu).

An academy's advisory roles are crucial because science's remarkable understandings about how the world works have profound implications for policy-makers. Science enables humanity to benefit from knowing the future consequences of today's activities. Thus, for example, through detailed analyses of what science can confidently predict about the impact of greenhouse gas emissions on climate change, the National Academies are increasingly issuing wake-up calls that demand coherent action (see nas-sites.org/americasclimatechoices). Science needs to achieve a louder voice in this, and many other areas, if we are to counteract the short-term political expediency that too often prevents nations from doing the right thing for our grandchildren.

There are now academies of science in more than a hundred nations of the world. Some, like the Royal Society in the United Kingdom, are much older than the U.S. Academy. Many of these academies were founded to improve the communication and science of their members, with no responsibility to provide advice to their nations. But this has been changing in the past two decades, due to the formation of the InterAcademy Panel (IAP)—the Global Network of Science Academies, which explicitly focuses on helping its member academies become more proactive in their nation's policy-making. An even newer organization, the InterAcademy Council, provides worldwide scientific advice to international organizations such as the United Nations.† This is good news for the world's future. And it is not too far-fetched to claim that the mission of these two new international organizations derives from the "whenever called upon" responsibility that was thrust upon the U.S. National Academy of Sciences in its unique charter, exactly 150 years ago.

— Bruce Alberts

10.1126/science.1236831

*D. J. Kevles, *Issues Sci. Technol.* **29**, 37 (2013). †Y. Quéré, *Nature* **465**, 1009 (2010).



EVOLUTION

Darwinian Genomics

The finches of the Galapagos archipelago helped Darwin articulate the theory of evolution by natural selection as he identified differences in bird phenotypes, especially size and beak shape, across the island chain. Rands *et al.* provide a draft sequence of the genome of the large ground finch and compared it to other previously sequenced genomes, including its closest sequenced relative—the zebra finch. Comparative genomics was used to establish a gene set from the sequences and identified selective constraint in both of the genomes. Analyses of positive selection identified genes, including those that likely have a role in reproduction, that are under selection in both zebra finches and large ground finches. In addition, genes specific to the ground finch were identified, including those that have demonstrated effects on beak phenotypes. This study lays the groundwork for further analysis of the genomic changes that accompany speciation and adaptation. — LMZ

BMC Genomics **14**, 95 (2013).

CELL BIOLOGY

HIF Puts on the Brakes

The ability of most cells to respond appropriately to availability or absence of oxygen is a fundamental requirement for survival. Much of the physiological response of a cell or organism to hypoxia, from angiogenesis and metabolic changes to control of cell division, is coordinated by the transcription factor hypoxia-inducible factor-1 (HIF-1). Hubbi *et al.* report that the HIF-1 α subunit also has a nontranscriptional role in promoting arrest of the cell division cycle when cells sense hypoxia. In cells deprived of oxygen, HIF-1 α accumulated and bound to the prereplication complex, a set of proteins that mark origins of DNA replication, thus rapidly blocking DNA replication and cell division. The transcriptional transactivation domain of HIF-1 α was not required for this effect. HIF-1 α appears to be a balancing point for the cell's response to oxygen: Growth-promoting signals oppose

the actions of HIF-1 α and promote its binding to another protein at replication origins, the helicase MCM (minichromosome maintenance), which enhances degradation of HIF-1 α . — LBR

Sci. Signal. **6**, ra10 (2013).

CELL BIOLOGY

It Takes Teamwork

Cells contain molecular motors, including dynein and kinesin, that move a variety of cargoes along microtubules. Dyneins are often used by cells to generate large forces during, for example, nuclear migration, mitotic spindle orientation, and reorientation of the cytoskeleton during wound healing. Individual motors, however, are limited in the amount of force they can generate on their own. How are large forces generated and sustained inside cells? Rai *et al.* developed methods to use optical tweezers for precise, quantitative force measurement inside cells. The results show, paradoxically, that dyneins, which are weak and

erratic at the single-motor level, show excellent teamwork to generate large and persistent forces inside cells. Kinesins, on the other hand, which are strong and persistent at a single-motor level, fail to generate force collectively. The forces upon moving phagosomes loaded with latex beads increased linearly with dynein number. Hendricks *et al.* also found that transport of phagosomes was driven by multiple dynein motors. Thus a force of certain magnitude can be generated simply by changing the number of dynein motors depending on the specific requirement in the cell. — SMH

Cell **152**, 172 (2013); *Proc. Natl. Acad. Sci.*

U.S.A. **109**, 18447 (2012).

BEHAVIOR

Too Busy to Pick Up the Phone

One version of an adage attributed by some to Yogi Berra is that the difference between theory and practice is greater in practice than in theory. One arena where the existence of such a difference is intuitively plausible is when researchers ask questions of a sample of humans in the general population. Despite extensive prior work in many disciplines, not only on survey design but also on adjusting for the relatively high contemporary rates of nonresponse, Heffetz and Rabin have succeeded in identifying a new and intriguing source of potential bias that affects whether inferences drawn from the sample can be applied more widely. They look at the relation between the number of phone calls required to reach a respondent and the answer to a yes/no question about happiness across a handful of demographic dimensions. Splitting the respondents into above versus below median income, they find that almost 9 out of 10 of the richer people are happy versus about 4 out of 5 of the poorer folk—and that there is no difference between busier (i.e., harder to reach) and not-so-busy respondents. On the other hand, women who are easy to reach are happier than similar men, whereas the opposite is true when comparing men and women who are harder to reach. One final point is that inferences about the population would be very much affected by whether people who could not be reached at all would be assumed to be similar to the average respondent or to the busier ones. — GJC

Am. Econ. Rev., in press (2013); <http://ssrn.com/abstract=2101097>.

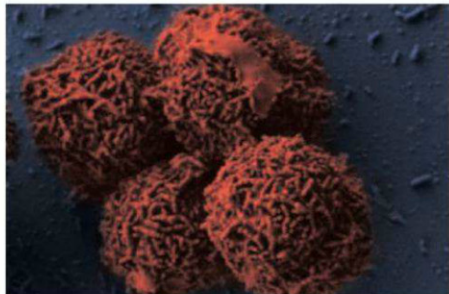
MICROBIOLOGY

Bacterial Growth at -15°C

Life as a bacterium in the permafrost is not easy. Not only are subzero temperatures the norm, but the liquid water that is available is quite salty. Therefore, for bacteria to survive in these condi-

CREDIT: PUTNEYMARK/FICKR

tions, they need to be well adapted to cold and high-salinity environments. Isolated from Arctic permafrost, the aerobic heterotroph *Planococcus halocryophilus* is an example of one such species that is up to the task. Through a series of batch and microcosm growth experiments, Mykytczuk *et al.* show that *P. halocryophilus* grew—albeit at the slow generation time of 50 days—and had an active carbon metabolism at -15°C . Genomic analyses suggest that this organism has a diverse



set of traits to help it survive in addition to those related to cold and osmotic adaptation, including several modifications to the cell envelope and increased tolerance to oxidative stress. Indeed, transcriptomic profiles from cells grown at a range of temperatures and salinities down to -15°C and 18% NaCl show specific parallel responses to mitigate cold and salty conditions. Because a large portion of the world's soil is in permafrost regions, increased activity of these microbial communities may result from warmer temperatures or greater temperature fluctuations. — NW

ISME J. 10.1038/ismej.2013.8 (2013).

BIOCHEMISTRY

Mimicking a Membrane

A challenge in membrane structure determination is selecting membrane-mimicking media that facilitate proper protein folding and function. Detergent micelles are commonly used for structural studies; however, these are often not optimal for protein stability and function. Phospholipid nanodiscs are a promising membrane mimetic; however, the large molecular weight of nanodiscs has hampered their use in structural determination by multidimensional nuclear magnetic

resonance (NMR) spectroscopy. Nanodiscs are formed by two copies of a membrane scaffold protein wrapping around a patch of phospholipid bilayer. Hagn *et al.* engineered a set of shorter variants of the scaffold protein ApoA-I that formed a range of smaller nanodiscs. Using membrane proteins embedded in these smaller nanodiscs together with high deuteration levels of proteins and lipids and advanced NMR methods allowed NMR resonance assignment and high-resolution structure determination of membrane proteins. The set of scaffold proteins could be screened for optimal NMR spectra of small to medium-sized membrane proteins. This method allowed the authors to obtain good-quality spectra for bacteriorhodopsin and to determine the structure of OmpX, a bacterial outer-membrane protein. — VV

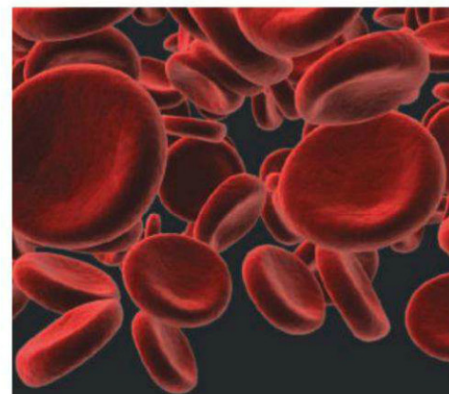
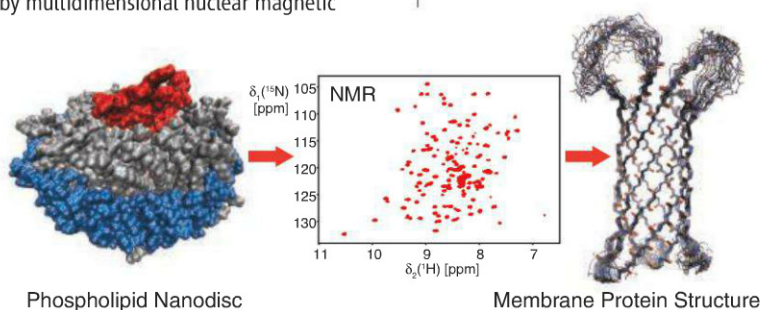
JACS **135**, 1919 (2013).

PLANETARY SCIENCE

The Moon's Indigenous Water

Until 5 years ago, the Moon was thought to be essentially bone dry. Analysis of the samples brought back by the Apollo and Luna missions had not revealed any hydrous components. Recent studies, however, using improved analytical techniques, reported the detection of water in some lunar rocks, and observations from orbiting spacecraft showed that water is present in the lunar surface. Some of this water is thought to have been delivered by meteorites and through solar-wind implantation of hydrogen; another part is thought to be indigenous. Using Fourier transform infrared spectroscopy, Hui *et al.* have detected water in two Apollo samples representative of the Moon's primary crust, crystallized from the lunar magma ocean that is thought to have once covered the Moon. Water in these samples is indigenous—with solar-wind implantation ruled out by the use of grains that came from the interior of the individual Apollo rocks—and it was present at very early times, before the crust solidified. The authors estimate that the initial water content of the lunar magma ocean was around 320 parts per million. This water could have prolonged the crystallization of the magma ocean. — MJC

Nat. Geosci. 10.1038/ngeo1735 (2013).



Looking for Biomarkers in Biofluids?

Discover the potential of microRNA with Exiqon

microRNA in cell-free biofluids and have great potential as highly informative biomarkers.

Exiqon offers RNA isolation and LNATM-enhanced microRNA analysis tools specifically optimized for biofluids.

For details see:
www.exiqon.com/biofluids

Get expert advice from Exiqon

EXIQON



Support the sciences. **Get rewarded.**

Show your AAAS pride and reward yourself with the new AAAS Platinum Advantage Rewards Card from NASA Federal Credit Union.

Apply now and get
10,000 bonus points!

Go to nasafcu.com/AAASpromo



Get **10,000 bonus points** if you sign up for a card and spend \$3,000 within 90 days of account opening.

Learn more at
nasafcu.com/AAASpromo.

Subject to credit approval.
Membership in AAAS and NASA FCU is required.
NASA FCU is federally insured by NCUA.



Intensive research
Nabriva
Therapeutics
relies on the
biotech
know-how of
Austria as a
business
location.



Photo: iStockphoto

A healthy future

International companies in the biomedical sector highly value the Austrian business location. A dynamic research environment and attractive financial incentives win over investors.

Research for life, innovations for a healthy future: in Austria international biomedical companies are striving to developing new

products and services for the health care sector. In Vienna alone some 9,000 scientists and trained specialists are involved. Every second biotech company in Austria is located in the capital. "Innovation-friendly conditions such as the ten percent research premium make Austria a sought-after location," says René Siegl, Managing Director of the national investment promotion agency ABA – Invest in Austria, which provides cost-free consulting and support on all issues related to starting up a company. This is confirmed by Ralf Schmid, CEO of the Vienna-based firm Nabriva Therapeutics. He

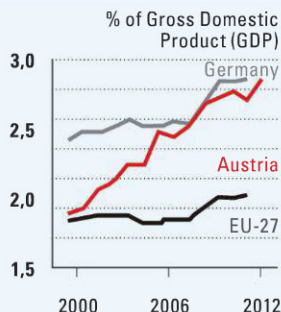
considers reliable funding conditions to be an important location factor, especially because biopharmaceutical firms face high development risks. "The research premium in Austria provides a positive impetus for us."

RESEARCH WITH SUCCESS

In cooperation with its American research and development partner Forest Laboratories, which will invest about USD 25 million in joint activities, Nabriva is developing an antibiotic to treat serious infectious diseases. Numerous universities, universities of applied sciences and industry clus-

ters create an extremely dynamic research environment which firms like Nabriva value. Chief Medical Officer William T. Prince says: "Our professional team consisting of highly qualified and dedicated scientists at the Vienna site ensures our long-term success."

Research investment



Sources: Eurostat, Statistik Austria

Development of R&D expenditure in Austria, Germany and the EU-27

Do you have questions?

Please contact us:
office@aba.gv.at

www.investinaustria.at/research

**RESEARCH LOCATION
AUSTRIA**

**1200 New York Avenue, NW
 Washington, DC 20005**
 Editorial: 202-326-6550, FAX 202-289-7562
 News: 202-326-6591, FAX 202-371-9227
**Bateman House, 82-88 Hills Road
 Cambridge, UK CB2 1LQ**
 +44 (0) 1223 326500, FAX +44 (0) 1223 326501

SUBSCRIPTION SERVICES For change of address, missing issues, new orders and renewals, and payment questions: 866-434-AAAS (2227) or 202-326-6417, FAX 202-842-1065. Mailing addresses: AAAS, P.O. Box 96178, Washington, DC 20090-6178 or AAAS Member Services, 1200 New York Avenue, NW, Washington, DC 20005

INSTITUTIONAL SITE LICENSES please call 202-326-6755 for any questions or information

REPRINTS: Author Inquiries 800-635-7181

Commercial Inquiries 803-359-4578

PERMISSIONS 202-326-7074, FAX 202-682-0816

MEMBER BENEFITS AAAS Travels: Betchart Expeditions 800-252-4910; Apple Store www.store.apple.com/us/go/epstore/aaas; NASA Federal, 1-888-NSA-FCU (1-888-627-2328) or www.nasafcu.com; Cold Spring Harbor Laboratory Press Publications www.cshlpress.com/affiliates/aaas.htm; GEICO Auto Insurance www.geico.com/landingpage/go51.htm?logo=17624; Hertz 800-654-2200 CDP#343457; Office Depot https://bsd.officedepot.com/portal/login.do; Seabury & Smith Life Insurance 800-424-9883; Subaru VIP Program 202-326-6417; VIP Moving Services www.vipmayflower.com/domestic/index.html; Other Benefits: AAAS Member Services 202-326-6417 or www.aaasmember.org.

science_editors@aaas.org (for general editorial queries)
 science_letters@aaas.org (for queries about letters)
 science_reviews@aaas.org (for returning manuscript reviews)
 science_bookrevs@aaas.org (for book review queries)

Published by the American Association for the Advancement of Science (AAAS), *Science* serves its readers as a forum for the presentation and discussion of important issues related to the advancement of science, including the presentation of minority or conflicting points of view, rather than by publishing only material on which a consensus has been reached. Accordingly, all articles published in *Science*—including editorials, news and comment, and book reviews—are signed and reflect the individual views of the authors and not official points of view adopted by AAAS or the institutions with which the authors are affiliated.

AAAS was founded in 1848 and incorporated in 1874. Its mission is to advance science, engineering, and innovation throughout the world for the benefit of all people. The goals of the association are to: enhance communication among scientists, engineers, and the public; promote and defend the integrity of science and its use; strengthen support for the science and technology enterprise; provide a voice for science on societal issues; promote the responsible use of science in public policy; strengthen and diversify the science and technology workforce; foster education in science and technology for everyone; increase public engagement with science and technology; and advance international cooperation in science.

INFORMATION FOR AUTHORS

See pages 716 and 717 of the 8 February 2013 issue or access www.sciencemag.org/about/authors

SENIOR EDITORIAL BOARD

A. Paul Alivisatos, Lawrence Berkeley Nat'l. Laboratory
Carl Bergmann, The Rockefeller Univ.
Ernst Fehr, Univ. of Zurich
Erin O'Shea, Harvard Univ.
Michael S. Turner, University of Chicago

BOARD OF REVIEWING EDITORS

Adriano Aguzzi, Univ. Hospital Zürich
Takuzo Aida, Univ. of Tokyo
Leslie Aiello, Wenner-Gren Foundation
Sonia Altizer, Univ. of Georgia
Stefan Amigorena, Institut Curie
Angelika Amon, MIT
Kathryn Anderson, Memorial Sloan-Kettering Cancer Center
Stig G. E. Andersson, Uppsala Univ.
Peter Andolfatto, Princeton Univ.
Meinrat O. Andreae, Max Planck Inst., Mainz
Paola Ariotti, Harvard Univ.
Johan Auwerx, EPFL
David Auschloss, Univ. of California Santa Barbara
Ben Barres, Stanford Medical School
Jordi Bascompte, Estación Biológica de Doñana, CSIC
Raymond Batista, London Research Inst.
Fay H. Baughman, Univ. of Texas, Dallas
David Baum, Univ. of Wisconsin
Mark Bear, Massachusetts Inst. of Technology
Yasmine Belkaid, NIAID, NIH
Philip Benfey, Duke Univ.
Stephen J. Benkovic, Penn State Univ.
Christophe Bernard, Aix-Marseille Univ.
Gregory C. Berzosa, Georgia Inst. of Technology
Gabriele Bergers, Univ. of California, San Francisco
Peer Bork, EMBL
Bernard Bourdon, Ecole Normale Supérieure de Lyon
Chris Bowler, Ecole Normale Supérieure
Ian Boyd, Univ. of St. Andrews
Christian Büchel, Universitätsklinikum Hamburg-Eppendorf
Joseph A. Burns, Cornell Univ.
William P. Butz, Population Reference Bureau
György Buzsáki, New York Univ., School of Medicine
Mats Carlsson, Univ. of Oslo
Mildred Cho, Stanford Univ.
David Clapham, Children's Hospital, Boston
David Clary, Univ. of Oxford
Jonathan D. Cohen, Princeton Univ.
Robert Cook-Deegan, Duke Univ.
James Collins, Boston Univ.
Alan Cowman, Walter & Eliza Hall Inst.
Robert H. Crabtree, Yale Univ.
Wolfgang Cramer, Mediterranean Inst. of Biodiversity and Ecology
Jeff L. Dangl, Univ. of North Carolina
Tom Daniel, Univ. of Washington

Frans de Waal, Emory Univ.
Stanislav Dehaene, Collège de France
Robert Desimone, MIT
Claude Desplan, New York Univ.
Ap Dijksterhuis, Radboud Univ. of Nijmegen
Dennis Discher, Univ. of Pennsylvania
Gerald W. Dorn II, Washington Univ., School of Medicine
Jennifer A. Doudna, Univ. of California, Berkeley
Julian Downward, Cancer Research UK
Bruce Dunn, Univ. of California, Los Angeles
Christopher Dye, WHO
David Ehrhardt, Carnegie Inst. of Washington
Tim Elston, Univ. of North Carolina at Chapel Hill
Gerhard Ertl, Fritz-Haber-Institut, Berlin
Barry Everitt, Univ. of Cambridge
Paul G. Falkowski, Rutgers Univ.
Ernst Fehr, Univ. of Zurich
Tom Fenchel, Univ. of Copenhagen
Michael Feuer, The George Washington Univ.
Alain Fischer, INSERM
Susan Fiske, Princeton Univ.
Anne C. Ferguson-Smith, Univ. of Cambridge
Peter Fratzl, Max Planck Inst.
Elaine Fuchs, Rockefeller Univ.
Wulfraam Gerstner, EPFL Lausanne
Andrew Gewirth, Univ. of Illinois
Karl-Heinz Glassmeier, IZ Braunschweig
Elizabeth Grove, Univ. of Chicago
Kip Guy, St. Jude's Children's Research Hospital
Taekijp Ha, Univ. of Illinois at Urbana-Champaign
Christian Haass, Ludwig Maximilians Univ.
Steven Hahn, Fred Hutchinson Cancer Research Center
Gregory J. Hannun, Cold Spring Harbor Lab.
Martin Heimann, Max Planck Inst., Jena
Yka Helariutta, Univ. of Finland
Isaac Held, NOAA
James A. Hendler, Rensselaer Polytechnic Inst.
Janet G. Hegsgaard, Swiss Fed. Inst. of Aquatic Science & Technology
Ray Hilborn, Univ. of Washington
Michael E. Himmel, National Renewable Energy Lab.
Kai-Uwe Hinrichs, Univ. of Bremen
Kei Hirose, Tokyo Inst. of Technology
David Hodell, Univ. of Cambridge
David Holden, Imperial College
Lora Hooper, UT Southwestern Medical Ctr at Dallas
Jeffrey A. Hubbell, EPFL Lausanne
Thomas Hudson, Ontario Inst. for Cancer Research
Ray Huey, Univ. of Washington
Steven Jacobsen, Univ. of California, Los Angeles
Kai Johnson, EPFL Lausanne
Peter Jonas, Universität Freiburg
Matt Kaeblerlein, Univ. of Washington
William Kaelin Jr., Dana-Farber Cancer Inst.

Daniel Kahne, Harvard Univ.
Daniel Kammen, Univ. of California, Berkeley
Joel Kingsolver, Univ. of North Carolina at Chapel Hill
Robert Kingston, Harvard Medical School
Roberto Kolter, Harvard Medical School
Alberto R. Kornblith, Univ. of Buenos Aires
Leonid Kruglyak, Princeton Univ.
Thomas Lager, Univ. of Cologne
Mitchell A. Lazar, Univ. of Pennsylvania
David Lazer, Harvard Univ.
Virginia Lee, Univ. of Pennsylvania
Ottoline Leyser, Cambridge Univ.
Marcia C. Linn, Univ. of California, Berkeley
Jianglu Li, Michigan State Univ.
Luis Liz-Marzan, CIC biomaGUNE
Jonathan Losos, Harvard Univ.
Ke Lu, Chinese Acad. of Sciences
Christian Lüscher, Univ. of Geneva
Laura Machesky, CRUK Beatson Inst. for Cancer Research
Aime Magurran, Univ. of St. Andrews
Oscar Marin, CSIC & Miguel Hernández
Charles Marshall, Univ. of California, Berkeley
Chris Marshall, Inst. of Cancer Research
Martin M. Matzuk, Baylor College of Medicine
C. Robertson McClung, Dartmouth College
Graham Medley, Univ. of Warwick
Yasushi Miyashita, Univ. of Tokyo
Richard Morris, Univ. of Edinburgh
Edward Most, Norwegian Univ. of Science and Technology
Sean Munro, MRC Lab. of Molecular Biology
Thomas Murray, The Hastings Center
Naoto Nagao, Univ. of Tokyo
James N. Newlin, Cold Spring Harbor Lab.
Daniel Newmark, Univ. of California, Berkeley
Stuart Newman, New York Medical College
Timothy W. Nilsen, Case Western Reserve Univ.
Pär Nordlund, Karolinska Inst.
Helga Nowotny, European Research Advisory Board
Luke O'Neill, Trinity College, Dublin
Stuart Newman, New York Medical College
N. Phuan Orr, Princeton Univ.
Joe Orenstein, Univ. of California, Berkeley & Lawrence
Berkeley National Lab.
Harry Orr, Univ. of Minnesota
Andrew Oswald, Univ. of Warwick
Steve Palumbi, Stanford Univ.
Jane Parker, Max-Planck Inst. of Plant Breeding Research
Donald R. Paul, Univ. of Texas at Austin
David Pearson, Univ. of California, Berkeley
John H. J. Petri, Memorial Sloan-Kettering Cancer Center
Simon Phillips, Univ. of Florida
Joshua Plotkin, Univ. of Pennsylvania
Philippe Poulin, CNRS
Colin Renfrew, Univ. of Cambridge

FULFILLMENT SYSTEMS AND OPERATIONS (membership@aaas.org); **CUSTOMER SERVICE SUPERVISOR** Pat Butler; **SPECIALISTS** LaToya Casteel, Michelle Ofordire, April Marshall; **MANAGER, DATA ENTRY** Mickie Napoleoni; **DATA ENTRY SPECIALISTS** JJ Regan, Jaimee Wise, Fiona Gildin

BUSINESS OPERATIONS AND ADMINISTRATION Director Deborah Rivera-Wienhold; **BUSINESS SYSTEMS AND FINANCIAL ANALYSIS** Director Randy Yi; **MANAGER, FULFILLMENT SYSTEMS** Frits Buningh; **SYSTEMS ANALYST** Nicole Mehmedovich; **MANAGER, BUSINESS ANALYSIS** Eric Knott; **MANAGER, BUSINESS OPERATIONS** Jessica Tierney; **BUSINESS ANALYSTS** Cory Lipman, Celeste Troxler; **Christine Wehrli**; **FINANCIAL ANALYST** Jeremy Clay; **RIGHTS AND PERMISSIONS** ADMINISTRATOR Emilie David; **ASSOCIATE** Elizabeth Sandler; **MARKETING DIRECTOR** Ian King; **MARKETING MANAGERS** Alison Chandler, Julianne Wielga, Justin Sawyers; **MARKETING ASSOCIATES** Mary Ellen Crowley, Elizabeth Sattler, Rebecca Riffkin; **SENIOR MARKETING EXECUTIVE** Jennifer Reeves; **DIRECTOR, SITE LICENSING** Tom Ryan; **DIRECTOR, CORPORATE RELATIONS** Eileen Bernadette Moran; **SENIOR PUBLISHER RELATIONS SPECIALIST** Kiki Forsythe; **PUBLISHER RELATIONS MANAGER** Catherine Holland; **PUBLISHER RELATIONS, EASTERN REGION** Keith Layson; **PUBLISHER RELATIONS, WESTERN REGION** Ryan Rexroth; **CUSTOMER RELATIONS MANAGER** Iquo Edim; **MARKETING MANAGER** Christina Schlecht; **MARKETING ASSOCIATES** Paulina Curto, Mitchell Edmund; **CUSTOMER RELATIONS ANALYSTS** Simon Chong, Lana Gu; **ELECTRONIC MEDIA** DIRECTOR Elizabeth Harman; **ASSISTANT MANAGER** Lisa Stanford; **PRODUCTION SPECIALISTS** Antoinette Hodal, Michele Johnston, Lori Murphy, Kimberly Oster; **WEB AND NEW MEDIA** SENIOR PROJECT MANAGER Trista Smith, PROJECT LEADER Luke Johnson COMPUTER SPECIALISTS Walter Jones, Kai Zhang, WEB DEVELOPER Chris Coleman; PROGRAM DIRECTOR, AAAS MEMBER CENTRAL Peggy Mihelich

DIRECTOR, GLOBAL COLLABORATION, CUSTOM PUBLICATIONS, ADVERTISING Bill Moran

EDITOR, CUSTOM PUBLISHING Sean Sanders: 202-326-6430

ASSISTANT EDITOR, CUSTOM PUBLISHING Tianna Hicklin 202-326-6463

ASSOCIATE DIRECTOR, COLLABORATION, CUSTOM PUBLICATIONS/CHINA/TAIWAN/KOREA/ SINGAPORE Ruolei Wu +86-1367-101-5294

PRODUCT (science_advertising@aaas.org); **MIDWEST** Rick Bongiovanni: 330-405-7080, FAX 330-405-7081; **EAST COAST/E. CANADA** Laurie Faraday: 508-747-9395, FAX 617-507-8189; **WEST COAST/W. CANADA** Lynne Sticker: 415-931-9782, FAX 415-520-6940; **UK EUROPE/ ASIA** Roger Gonçalves: TEL/FAX +41 43 243 1358; **JAPAN**, Makiko Hara: +81 (0) 3 6802 4616, FAX +81 (0) 3 6802 4615; **ads@sciencemag.jp**; **CHINA/TAIWAN** Ruolei Wu: +86 1367 1015 294 ruwu@aaas.org

WORLDWIDE ASSOCIATE DIRECTOR OF SCIENCE CAREERS Tracy Holmes: +44 (0) 1223 326525, FAX +44 (0) 1223 326532

CLASSIFIED (advertise@sciencecareers.org); **U.S.: EAST COAST/WEST COAST/SOUTH CENTRAL/SOUTH AMERICA** Tina Burks: 202-326-6577; **MIDWEST/CANADA/INDUSTRY** Allyson Rosen: 202-326-6578; **SALES ADMINISTRATOR** Marci Gallun; **EUROPE/ROW** Sales Kelly Nelson; **SALES ASSISTANT** Kelly Garg; **JAPAN** Yuri Kobayashi +81 (0)90-9110-1719; **careerads@sciencemag.jp**; **CHINA/TAIWAN** Ruolei Wu: +86 1367 1015 294 ruwu@aaas.org; **ADVERTISING SUPPORT MANAGER** Karen Foote: 202-326-6740; **ADVERTISING PRODUCTION OPERATIONS MANAGER** Deborah Tompkins; **SENIOR PRODUCTION SPECIALIST/GRAPHIC DESIGNER** Amy Hardcastle; **PRODUCTION SPECIALIST** Yuse Lajiminmuhup; **SENIOR TRAFFIC ASSOCIATE** Christine Hall; **SALES COORDINATOR** Shirley Young; **MARKETING MANAGER** Allison Pritchard; **MARKETING ASSOCIATE** Aimee Aponte

AAAS BOARD OF DIRECTORS RETIRING PRESIDENT, chair Nina V. Fedoroff; PRESIDENT William H. Press; PRESIDENT-ELECT Phillip A. Sharp; TREASURER David E. Shaw; CHIEF EXECUTIVE OFFICER Alan I. Leshner; BOARD MAY R. Berenbaum, Bonnie L. Bassler, Stephen L. Mayo, Raymond Orbach, Julia M. Phillips, Sue V. Rosser, David D. Sabatini, Inder M. Verma



Trevor Robbins, Univ. of Cambridge
Jim Roberts, Fred Hutchinson Cancer Research Ctr.
Barbara A. Romanowicz, Univ. of California, Berkeley
Jens Rostrup-Nielsen, Haldor Topsøe
Mike Ryan, Univ. of Texas, Austin
Shimon Sakaguchi, Kyoto Univ.
Miguel Salmeron, Lawrence Berkeley National Lab
Jürgen Sandkühler, Medical Univ. of Vienna
Alexander Schier, Harvard Univ.
Randy Seeley, Univ. of Cincinnati
Vladimir Shalae, Purdue Univ.
Joseph Silk, Institut d'Astrophysique de Paris
Denise Simon, Arizona State Univ.
Alison Smith, Johns Hopkins Univ.
Davor Solter, Inst. of Medical Biology, Singapore
Peter Sorger, Harvard Medical School
John Speakman, Univ. of Aberdeen
Allan C. Spradling, Carnegie Institution of Washington
Jonathan Sprent, Garvan Inst. of Medical Research
Paula Stephan, Georgia State Univ. and National Bureau of Economic Research
Elisbeth Stern, ETH Zürich
V. S. Subrahmanian, Univ. of Maryland
Ira Tabas, Columbia Univ.
Yoshiko Takahashi, Kyoto University
Sarah Teichmann, Cambridge Univ.
John Thomas, Duke Univ.
Herbert Vogel, Washington Univ.
Bert Vogelstein, Johns Hopkins Univ.
Cynthia Volkert, Univ. of Göttingen
Bruce D. Walker, Harvard Medical School
Douglas Wallace, Dalhousie Univ.
Jan Walmsley, Univ. of Oxford
David A. Wardle, Swedish Inst. of Agric Sciences
David Waxman, Fudan Univ.
Jonathan Weissman, Univ. of California, San Francisco
Kathy Willis, Oxford Univ.
Ian A. Wilson, The Scripps Res. Inst.
Timothy D. Wilson, Univ. of Virginia
Rosemary Wyse, Johns Hopkins Univ.
Jan Zaenen, Leiden Univ.
Kenneth Zaret, Univ. of Penn. School of Medicine
Jonathan Zehr, Univ. of California, Santa Cruz
Maria Zuber, MIT

BOOK REVIEW BOARD

John Aldrich, Duke Univ.
David Bloom, Harvard Univ.
Angela Creager, Princeton Univ.
Richard Shweder, Univ. of Chicago
Ed Wasserman, DuPont
Lewis Wolpert, Univ. College London

What's green
and has its own
gravitational pull?

Huge savings from GEICO.

1-800-368-2734
geico.com/sci/aaas

GEICO® Tell us you're a member.

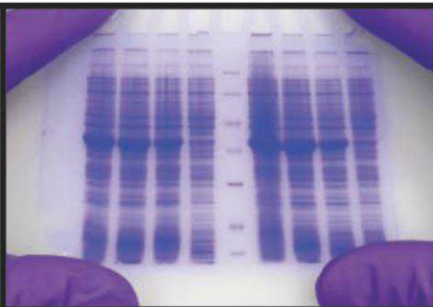


Discount amount varies in some states. Discount is not available in all states or in all GEICO companies. One group discount applicable per policy. Coverage is individual. In New York a premium reduction may be available. GEICO is a registered service mark of Government Employees Insurance Company, Washington, D.C. 20076; a Berkshire Hathaway Inc. subsidiary. GEICO Gecko image © 1999-2013. © 2013 GEICO

Produced by the *Science*/AAAS Custom Publishing Office

Life Science Technologies
Proteomics

Not Your PI's Western Blot



In This Issue

More than three decades after its invention, the Western blot remains a crucial tool for investigators who need to reliably identify specific proteins. A host of recently released products use a variety of approaches to improve the reproducibility, sensitivity, quantifiability, and speed of Western blot experiments.

See the full story on page 1100.

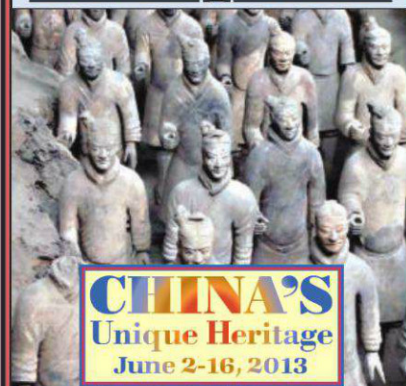
Upcoming Features

Fluorescence Multiplexing—April 12

The Microbiome—May 10

Proteomics: MALDI Imaging—May 31

AAAS Travels



Discover fascinating cultural sites and the natural history of China... from Beijing to the terra cotta warriors in Xi'an, feathered dinosaurs to the Silk Road, the edge of the Gobi Desert to the renowned Buddhist grottoes of Dunhuang. Optional extension on a Yangtze River Cruise, June 16-21. \$3,995 + air + extension.

**For a detailed brochure,
please call (800) 252-4910**

All prices are per person twin share + air



BETCHART EXPEDITIONS Inc.
17050 Montebello Rd, Cupertino, CA 95014
Email: AAASInfo@betchartexpeditions.com
www.betchartexpeditions.com

AROUND THE WORLD



Beijing 1

China's Environmental Ministry Acknowledges 'Cancer Villages'

For the first time, China's government has acknowledged the existence of "cancer villages": locations where exposure to environmental hazards, often water pollution, is believed to have contributed to elevated cancer rates.

"Toxic chemicals have caused many environmental emergencies," reads a planning document released by China's environ-

ment ministry on 20 February. "There are even some serious cases of health and social problems, like the emergence of cancer villages in individual regions." The document outlines the ministry's plan to more strictly

regulate the use of chemicals in, for example, petrochemical factories, steel and iron refineries, and power plants. Cancer is the leading cause of death in urban China, accounting for one in every four deaths (*Science*, 29 August 2008, p. 1155). The little-studied "cancer villages" have been rumored to exist for years; journalist Deng Fei, formerly of the *Phoenix Weekly* newsmagazine, raised the villages' profile in 2009 when he posted a map online showing the locations of more than 100 impacted communities.

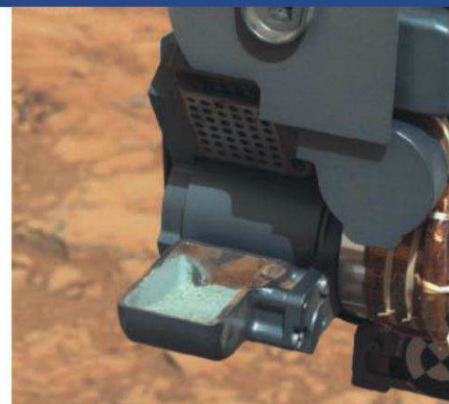
Washington, D.C. 2

AIDS Relief Program Gets High Marks

A 680-page report released on 20 February by the Institute of Medicine (IOM) found that the President's Emergency Plan for AIDS Relief (PEPFAR), a 10-year-old effort to help 31 "partner countries" treat their HIV-infected people, has been "a tremendously successful effort." The program disbursed \$21.8 billion in aid between 2004 and 2010.

The report noted that PEPFAR has "played a transformative role" with its contribution to the global response to HIV, providing more than 3 million people with antiretroviral drugs in fiscal year 2010 and an estimated 600,000 HIV-infected pregnant women with antiretrovirals.

PEPFAR has funding through 2013, and some HIV/AIDS advocates worry that Congress might cut its support. But IOM committee members hope the report will help educate the new generation elected to Congress and their staff members. "[PEPFAR is] a really great example of how you can deliver development assistance," says committee member Jennifer Kates, director of Global Health &



Touch of Gray On the Red Planet

NASA's Curiosity rover holds out a fistful of gray powder—the first sample extracted from the interior of Mars by the rover's drill. Earlier this month, the rover gave its drill gear a test run, burrowing about 6 centimeters into an outcrop on Mars known as "John Klein": a site with rocks that were once saturated with water. The drilling revealed gray sediment beneath the planet's surface layer of rust-colored rock, tinted by oxidized iron. "We're ... seeing a new coloration for Mars here, and it's an exciting one to us," said Joel Hurowitz, sampling system scientist for Curiosity at NASA's Jet Propulsion Laboratory in Pasadena, California, at a press conference on 20 February. The sediment "may preserve some indication of what iron was doing in these samples without the effect of some later oxidative process."

HIV Policy at The Henry J. Kaiser Family Foundation in Washington, D.C.
<http://scim.ag/PEPFARrep>

Canberra 3

Cutting R&D Tax Breaks To Fund Innovation Networks

A jobs and innovation package announced by the Australian government on 17 February proposes to cut AUD \$1 billion from research and development tax breaks to help pay for a new network of up to 10 "Industry Innovation Precincts." The government wants to spend AUD \$500 million over 4 years to establish and support the precincts, but funding for the new networks will take a bite out of R&D tax breaks for up to 20 of the nation's biggest firms, including large mining companies such as Rio Tinto, Caltex, and Shell Australia.



ment ministry on 20 February. "There are even some serious cases of health and social problems, like the emergence of cancer villages in individual regions." The document outlines the ministry's plan to more strictly

NOTED

>Psychologists will soon have a major prize of their own. Cognitive scientist Richard Atkinson, president emeritus of the University of California, last week gave \$3.5 million to the National Academy of Sciences to establish a new **\$200,000 biennial prize in the psychological and cognitive sciences**, beginning in 2014.

The move is intended to foster collaborations between academic, government, and industry researchers to improve Australia's track record on commercializing its research discoveries, which analysts say is relatively poor. But opponents say the cuts could make Australia less attractive to international investors.

Two precincts, a Melbourne- and Adelaide-based center on defense manufacturing and a Melbourne-based center on food manufacturing, have already been selected. If Parliament approves the plan, the remaining precincts will be selected by a competitive process this year and established in 2014. An independent National Precincts Board will advise the government on the selection. <http://scim.ag/ausinno>

NEWSMAKERS

Breakthrough Prize Awards Millions to Life Scientists

Eleven biomedical researchers were awarded the new Breakthrough Prize in Life Sciences last week. Each winner receives \$3 million, courtesy of several Silicon Valley entrepreneurs including venture capitalist Yuri Milner, who also founded the Fundamental Physics Prize.

Recipients included **Cornelia I. Bargmann** of Rockefeller University in New York City; **David Botstein** of Princeton University; **Lewis C. Cantley** of Weill Cornell Medical College in New York City; **Hans Clevers** of the Hubrecht Institute in the Netherlands; **Napoleone Ferrara** of the University of California, San Diego; **Titia de Lange** of Rockefeller University; **Eric S. Lander** of Harvard University and the Massachusetts Institute of Technology (MIT) in Cambridge; **Charles L. Sawyers** of Memorial Sloan-Kettering Cancer Center in New York City; **Bert Vogelstein** of Johns Hopkins University in Baltimore, Maryland; **Robert A.**



Bargmann



de Lange

Science LIVE

Join us on Thursday, 7 March, at 3 p.m. EST for a live chat on **open access publishing**. What does the United States's new policy mean for the scientific community? <http://scim.ag/science-live>

Random Sample

Thanks to Christianity, Horsemeat Went Out of Style

Horsemeat in hamburgers might scandalize modern Britons, but their ancestors weren't always so squeamish. A study of horse bones at early, middle, and late Anglo-Saxon sites suggests that slaughtering and eating equines went out of fashion only with the rise of Christianity.

Horses were central to Anglo-Saxon life, a period extending from the end of Roman control around 410 C.E. to the Norman conquest of 1066. Associated with warrior gods in several pagan religions, the animals were frequently buried with humans in early Saxon graves—although they were eaten only some of the time, perhaps at ritual feasts or when food was scarce. Horse bones showing signs of butchery consistent with human consumption were found at 27% of the early Saxon sites surveyed in the new study.

In the 8th century, the Catholic Church started harshly condemning what it saw as the pagan practice of horsemeat consumption, says archaeologist Kristopher Poole, who recently received a Ph.D. from the University of Nottingham in the United Kingdom. Indeed, as Christianity spread, horsemeat consumption declined, Poole notes in an upcoming issue of the *Oxford Journal of Archaeology*. Butchered horse bones show up at only about 13% of middle and late Saxon sites, usually at poor or remote settlements, where Christianity's influence was relatively weak.

It's the first time an animal bones expert "has really compared the record from excavations ... with the few written sources we have" to investigate the outcome of the church's crackdown on horse meat, says archaeologist Helena Hamerow of the University of Oxford in the United Kingdom. One lingering mystery, she says, is why this particular food taboo persists in England but has faded in other European countries such as France.



On horseback. The Bayeux Tapestry depicts the Norman conquest of England.

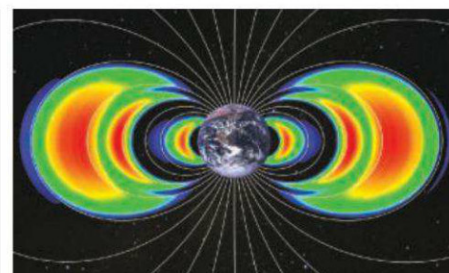
Weinberg of MIT; and 2012 Nobel laureate **Shinya Yamanaka** of Kyoto University and the Gladstone Institutes in San Francisco.

"It's nice as a scientist to feel that these very successful businesspeople appreciate the importance of work in biology and medicine," says Bargmann, who studies how genetics and the environment influence the nervous system. The foundation plans to annually award five Breakthrough Prizes. <http://scim.ag/Breakprize>

FINDINGS

Another Radiation Belt For Van Allen

More than 50 years after the United States's first satellite, Explorer 1, discovered two donuts of radiation stacked over Earth's equator, a pair of NASA satellites has stunned space physicists with the discovery of a third Van Allen radiation belt (albeit a temporary one). Theorists did not see it coming, and none of the instrumented satellites flying since the 1958 discovery could reveal the new belt's highly energetic charged subatomic particles zipping about at near the speed of light.



Addressing that shortcoming, NASA launched the twin Van Allen Probes on 30 August last year. Anxious to compare their readings with those from NASA's SAMPEX satellite, due to fall out of orbit soon, team members turned on their high-energy electron detector just 4 days after launch. Good thing or they would have missed a third belt of exceptionally energetic electrons (middle red crescent in cross section of belts) that appeared 2 days after turn-on and abruptly disappeared on 1 October. These observations, published online this week in *Science*, should help scientists track how disturbances blasting out from the sun rattle Earth's magnetic field (gray lines), accelerating particles until they reach the energies of a Van Allen belt.



U.S. SCIENCE POLICY

What It Means for Agencies To Be Under the Sequester

U.S. science agencies have been warning for months about the dire consequences of looming mandatory spending cuts. But if the cuts, known as sequestration, go into effect as expected on 1 March (after *Science* went to press), there are likely to be few immediate signs that the world has changed dramatically. In fact, it could be weeks or months before most scientists feel the impacts.

The lower spending required under the 2011 Budget Control Act—an \$85 billion cut for the current fiscal year that ends on 30 September—would eventually have serious consequences for the research community as well as for the general public. The federal government is now operating under a temporary extension of 2012 spending levels called a continuing resolution (CR). The sequestration imposes a further cut of roughly 5% to domestic programs and 7.3% for defense programs, although the cuts will seem steeper because they must be carried out in the remaining 7 months of the 2013 fiscal year.

Although an imminent deal between Congress and the White House seems unlikely, some relief could arrive later this month if Congress passes a regular spending bill for the rest of the fiscal year. That would allow agencies to protect activities seen as most central to their mission and delay or terminate those regarded as less important. The sequester gives them much less opportunity to move money around.

A bigger factor would be the size of the new spending package. A bill that incorpo-

rates the sequester would fall nearly \$70 billion below the current \$1.043 trillion tagged for discretionary spending, from which almost all research is funded. On the other hand, legislators could cancel the sequester or replace it with something less austere.

More pain may be on the horizon. This week's cuts are only the first installment of a \$1.2 trillion spending reduction to be spread over 10 years. The nightmare for federal science officials is that Congress will apply the lower spending ceilings stipulated by the 2011 law to future annual budgets. Those repeated cuts would hollow out federal support for science, they argue.

The differences in how agencies manage research make it hard to generalize the impact of sequestration. The National Institutes of Health (NIH) expects to squeeze existing grantees, for example, while researchers applying to National Science Foundation (NSF) will face stiffer competition.

Those decisions reflect each agency's traditional approach to grantmaking. NIH tells investigators that continued funding for most multiyear awards is contingent on NIH's future budget. And last week, NIH said investigators are likely to see their out-year budgets trimmed by several percentage points. With annual grants averaging \$431,000, that's real money.

In contrast, NSF typically makes what it calls standard awards in which all of the money for a 3-year grant is committed up front. That policy should allow current NSF

Unhealthy cuts. Senator Barbara Mikulski joined NIH Director Francis Collins in warning of dire effects from sequestration.

investigators, whose awards are, on average, less than one-third the size as those given out by NIH, to escape the fiscal knife.

NSF's approach also means that the only way for the agency to absorb a sudden large funding cut is to slash the number of new awards. And that's exactly what NSF officials have warned will happen this year. They predict a drop of 1000 new awards, or nearly 10%, from 2012 levels. NIH, with a budget four times larger than NSF's, anticipates making "hundreds fewer" awards.

Furloughs are not expected to be an issue at either agency because most of their money goes out the door. (The fate of NIH's intramural program, about 11% of NIH's overall budget, rests with the directors of each parent institute and center.) But the situation could be grimmer for scientists at agencies with a larger proportion of staff scientists.

The National Institute of Standards and Technology (NIST), for example, has warned that it plans "the elimination of at least 100 research associates" because of the reduced funding for its core labs. NIST says those cuts will also prevent it from staffing its network of Manufacturing Extension Partnership centers.

The directors of the Department of Energy's 10 science-oriented national labs have a different problem: Funding cuts could prevent them from running at full capacity the x-ray sources and large other facilities that draw scientists from around the world. For example, Oak Ridge National Laboratory in Tennessee, home of the \$1.4 billion Spallation Neutron Source (SNS), has already trimmed its staff by 9% in the past 2 years, says lab director Thom Mason. If the lower funding in the sequester becomes a new baseline for the lab, Mason says, Oak Ridge won't be able to afford the utilities, supplies, and staff members needed to run all of SNS's 18 beam lines. "Our bias would be to do a smaller number of things and do them well instead of doing everything poorly," he says.

Last month, Senator Barbara Mikulski (D-MD), chair of the Senate Appropriations Committee, asked agencies to describe the impact of sequestration in advance of a hearing on the topic. In letters released by her office, they wrote that less money would mean less research, which in turn will lead to delays in understanding the natural world, treating and curing diseases, and tackling

CREDIT: NIH

pressing societal problems such as world hunger and clean energy.

Agency heads were reluctant to go into more detail, however, because their implementation plans must first be approved by the White House Office of Management and Budget before going to Congress. The 2011 law gives agencies until 30 March to inform legislators. But a few were prepared to cite specific impacts:

- The U.S. Geological Survey plans to take offline more than 10% of its network of about 3100 stream gages. Data from the gages help in forecasting floods, studying changes in land use, and monitoring climate change as well as informing water managers in the public and private sectors.

- NSF says cuts to the agency's big facilities account "will result in the termination" of \$35 million in construction contracts for two large national networks of observatories being built to monitor ecological systems and the oceans (NEON and OOI). Managers for

both projects say they are on schedule, but NSF will likely ask them to generate a new timetable and scope of operations.

- Cuts to the Census Bureau will mean that proposed cost-saving measures won't be ready for the 2020 census. Robert Groves, who stepped down as director last summer to become provost at Georgetown University, says that now is the time to test planned alternatives to the hiring of 600,000 people to follow-up on gaps in replies to the initial census form, including the use of existing government records and the Internet. That can't happen if the bureau's budget is cut, he says.

- Budget cuts could also produce a 2- to 3-year delay in launching two satellites key to U.S. weather forecasting. The Geostationary Operational Environmental Satellite-R craft would replace current orbiters in 2015 and 2017. But meeting that schedule will require a major funding increase this year for the \$10.9 billion program, says the National Oceanic and Atmospheric Administration.

- NASA plans a 5% cut in the number of awards to scientists who want to analyze the massive stream of data from a slew of current missions. "People are already getting out of the business" because of the diminishing chances in recent years of obtaining NASA funding, says Mark Sykes, director of the Planetary Science Institute in Tucson, Arizona. The latest cuts, he says, mean that NASA is "thinking of now, not the future."

Whatever happens this week, policy-makers are already talking about the next showdown. The federal government could shut down if Congress doesn't act before the CR runs out on 27 March. And in May, the government's authority to borrow money to pay the national debt expires. So 1 March may well turn out to have been merely the latest installment in a never-ending spending crisis.

—JEFFREY MERVIS

With reporting by Adrian Cho, Jocelyn Kaiser, Richard Kerr, and David Malakoff.

SCIENTIFIC PUBLISHING

U.S. Agencies Directed to Make Research Papers Available

After deliberating for more than 3 years on ways to expand public access to taxpayer-funded research papers, the White House is finally taking action. In a memo last week, the Office of Science and Technology Policy (OSTP) asked agencies to make papers on research that they fund freely available online within 12 months after the results appear in a journal.

That policy is similar to a 2008 National Institutes of Health rule that requires investigators to deposit their peer-reviewed manuscripts in NIH's PubMed Central archive for posting within 12 months after publication. "The Obama Administration agrees that citizens deserve easy access to the results of research their tax dollars have paid for," OSTP Director John Holdren wrote last week in a response to a petition signed by 65,000 people that called for expanding the NIH policy. Agencies that spend more than \$100 million a year on research must submit a draft plan within 6 months, but OSTP is leaving it to agencies to figure out where the papers will be posted.

Traditionally, scientists have published their work in scholarly journals that charge readers a subscription fee. In recent years,



Opening up. OSTP Director John Holdren says U.S.-funded research papers should be free.

however, libraries and others concerned about high journal prices have pushed to make papers free—in some cases, immediately after publication; instead of billing readers, journals charge authors a fee to cover peer review and other costs. Many journals and scientific societies have resisted this model, however, arguing that it will destroy the revenue streams they need to survive.

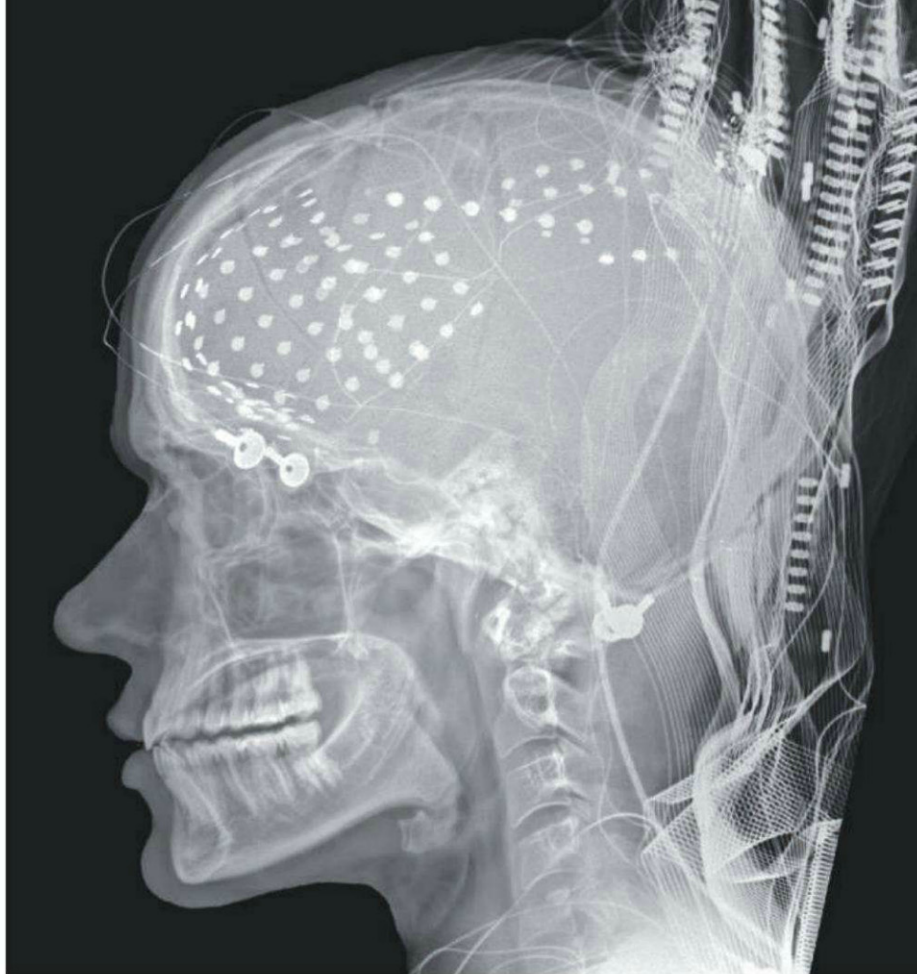
The Association of American Publishers called the OSTP policy "reasonable" and praised the fact that the 12-month embargo is only a guideline that agencies can tailor

for particular scientific fields.

Some agencies have pilot projects under way to comply, says Fred Dylla, executive director for the American Institute of Physics in College Park, Maryland. Several publishers and agencies, including the National Science Foundation (NSF) and the Department of Energy (DOE), will soon launch FundRef, a system for including grant numbers in papers so they can be tracked. DOE is also working with Wiley and Elsevier to link journal abstracts to agency research reports, a potential link to full text after an embargo. "Neither DOE nor NSF needs to invest in a PubMed Central-like repository," Dylla says.

The U.S. plan contrasts with the United Kingdom's, which urges investigators to publish in open access journals. It also falls short of a bill in the U.S. Congress called the Fair Access to Science and Technology Research Act (FASTR) that would make U.S.-funded research papers available after just 6 months. "FASTR is better," says Heather Joseph, executive director of the Scholarly Publishing and Academic Resources Coalition, an open access lobbying group in Washington, D.C. But the OSTP directive "is an enormous step forward."

—JOCELYN KAISER



Brain gain. A proposed research effort to map brain activity could help make electrode arrays, such as the one shown, finer and more flexible.

NEUROSCIENCE

Brain Project Draws Presidential Interest, but Mixed Reactions

Shortly after President Barack Obama made a seemingly innocuous pitch for more brain research in his State of the Union address last month, National Institutes of Health (NIH) Director Francis Collins sent out a note to his Twitter followers: “Obama mentions the #NIH Brain Activity Map in #SOTU.”

Few paid heed, however, until a week later when a front-page story in *The New York Times* indicated that the mysterious tweet referred to a soon-to-be announced NIH-led effort rivaling the Human Genome Project in cost and ambition, one that Obama planned to call for in his upcoming annual budget proposal. The initiative aimed to do no less than “build a comprehensive map of [the human brain’s] activity” within a decade, the newspaper reported.

The story stunned and excited many in the scientific community but angered and worried others. Lacking any official declaration of the project’s cost or how it would be funded, some researchers bristled at the prospect of a large new federal initiative that could take money from traditional grants

for individual scientists, especially at a time when NIH faces a massive budget cut (see p. 1020). *The Atlantic*, for example, published online a series of negative tweets, mainly from non-neuroscientists, decrying the Brain Activity Map (BAM) proposal, including this one from biologist Michael Eisen: “someone has to go to congress and explain why basic research is so important, not pander to them with big science crap.”

Even some in the neuroscience community expressed concern. “If this takes away from any of the R01s [individual investigator grants] that would normally be funded by the NIH, it would be bad,” says Eve Marder of Brandeis University in Waltham, Massachusetts, a former president of the Society for Neuroscience, who had attended one of the early planning workshops for BAM. “Right now the community is already so strapped we’re at a breaking point.”

Whatever one’s initial reaction to the new initiative, there is little doubt that researchers, and potentially physicians, would benefit from better ways of observing the brain

in action. “The biggest need in neuroscience is to develop technologies that would allow us to record the activity of many, many neurons in a circuit to understand how the circuit functions through that aggregated activity,” says Story Landis, director of the National Institute of Neurological Disorders and Stroke. “And we just don’t have the tools to do that.”

Neuroscientists arguably can only crudely measure the activity of a brain now. They can turn to PET and MRI imaging that each detect “activation” of broad regions through proxies such as oxygen use, or they can measure the electrical activity of individual or small groups of neurons. However, the brain’s most interesting functions, such as thought and perception, probably incorporate thousands to millions of neurons, says neuroscientist John Donoghue of Brown University, who has participated in planning the new project. To understand “thought disorders” such as schizophrenia, he says, we need to know what level of cellular activity produces thought. “Does it take 1000 cells? 10 million? 100 million?”

In 2011, at a meeting of neuroscientists and nanoscientists in England sponsored by the Kavli, Gatsby, and Allen foundations, a handful of scientists proposed that the two disciplines combine forces to develop tools to answer that question, by recording “every action potential from every neuron within a circuit.” Some naysayers called the idea “ridiculous,” says Rafael Yuste, a Columbia University neuroscientist who has helped plan the BAM project. But George Church, the Harvard University molecular geneticist in charge of the Personal Genome Project, pointed out that nearly every objection had also been raised against the Human Genome Project. “The more questions people asked,” Yuste says, “the stronger the argument became that this could be done.”

After the meeting, Yuste, Church, and three other scientists hashed out a white paper on their idea. Miyoung Chun, the vice president of science programs at the Kavli Foundation, soon became its most vocal and organized advocate, Yuste says. After the group coined the name “Brain Activity Map” for the project, Chun sent the document to the Office of Science and Technology Policy (OSTP) at the White House. Within a few months, Yuste says, they “made the rounds” in Washington, visiting OSTP, NIH, the National Science Founda-

CREDIT: COURTESY OF NED T. SAHIN, PH.D./WWW.NEDSAHIN.COM

tion, and the Defense Advanced Research Projects Agency.

In June 2012, the group published a paper in *Neuron* outlining how three areas of technological development could lead to a better understanding of brain function. First, they envisioned finer, more pliant micro-electrode arrays that mold seamlessly to brain tissue and record from larger groups of neurons. Second, they proposed an effort to advance the field of optogenetics—which has lately revolutionized neuroscience by allowing researchers to manipulate neurons using light (*Science*, 15 December 2006, p. 1674)—by incorporating voltage-sensitive, light-emitting particles such as quantum dots and nanodiamonds into neurons, allowing scientists to track and manipulate neuronal activity on a much larger scale.

Finally, drawing on the growing field known as synthetic biology, they expressed interest in one day inserting artificial DNA-synthesizing enzymes into neurons so that every time the neuron fired, the enzyme would make an error in its DNA assembly, thus recording the cell's activity through a series of mistakes. Whether such molecules could ever be used in humans, or how the data they generate could be recovered is still unknown, the authors said.

Such tools are far from being ready for human use, the scientists caution. Nonetheless, they suggest that over 15 years the field could ramp up from monitoring the equivalent of the whole brain activity of the roundworm *Caenorhabditis elegans*, which has 302 nerve cells, to up to a million nerve cells—equivalent to the entire brain function of a zebrafish or the Etruscan shrew, one of the world's smallest mammals.

"There are people who may say this is not possible, that we are smoking something. But if you look back at the genome project, a lot of people said it was crazy and would never work. There are very few people saying that today," says nanoscientist Paul Alivisatos, director of the Lawrence Berkeley National Laboratory in California and one of the project's planners.

A big unknown is how much pursuing such an initiative would cost. *The New York Times* reported that Yuste and others involved have suggested the cost would be \$300 million annually for a decade, comparable to the \$3.8 billion spent on the Human Genome Project, yet the researchers offered no explanation for that cost estimate when asked by *Science*. And OSTP and NIH have so far declined to address the cost of the project and whether it would draw on existing budgets or new money. Private money

OTHER BIG BETS ON THE BRAIN



- **The Human Connectome Project:** A 5-year, \$38.5 million project funded by the National Institute of Mental Health to map structural connections (above) in the brains of hundreds of healthy adults.
- **The Human Brain Project:** A €1 billion European-led project to build a computer model of the human brain over at least the next 10 years (*Science*, 11 November 2011, p. 748).
- **The Allen Brain Atlases:** Maps of gene expression in the brain. A mouse brain atlas, completed in 2006, cost \$41 million; a human atlas is under way.

might aid the effort, but only the Kavli Foundation has so far made any public commitment, stating it expects to contribute up \$4 million to \$5 million per year of the total. Gerald Rubin, executive director of Howard Hughes Medical Institute's Janelia Farm Research Campus in Ashburn, Virginia, says his facility has already spent more than \$150 million on research relevant to the Brain Activity Map over the past 6 years and will continue to use its yearly budget of \$100 million along those lines.

Beyond the budgetary issue, some researchers have questioned the realism of BAM's stated goals. Partha Mitra, a neuroscientist at Cold Spring Harbor Laboratory in New York, called several of its technological proposals "science fiction." And although he supports the project as a whole, "I flinched when I read the phrase 'every spike from every neuron,'" says David Kleinfeld, a neurophysicist at the University of California (UC), San Diego. Capturing pulses of scattered light from nanodiamonds embedded deep in the brain's intricately folded tissue would require inventing cameras and microscopes that can record photons from all planes in three dimensions at

the millisecond speed that neurons fire—all the while making sure that the method doesn't itself alter brain activity, he notes. Kleinfeld says he has concluded from some rough calculations that such a feat isn't physically achievable in more than a small region of cortex.

Further confusion about the project stems from a discrepancy between its description in the *Neuron* paper, which focused on animal models, and the current iteration, which reflects a "socially responsible," more human-oriented version, Yuste says. During meetings with NIH, he explains, officials said, "This is good that you're going to map the activity of every neuron in the brain, but how about solving schizophrenia? What is this going to do for mankind?" At that point, Yuste says the group invited researchers with more practical links to patient care to join the planning. In the updated version of the project, research with humans will be conducted in parallel with more basic science, says Donoghue. He hopes that BAM will reveal how the brain encodes movement, which would help him build better brain-machine interfaces that allow paralyzed people to mentally operate robotic arms more naturally.

Still, don't expect a complete human brain activity map by 2025. For ethical and safety reasons, most of the techniques described in the group's new proposal are decades away from being applicable to humans, Rubin says. Research proposed in the *Neuron* paper will largely focus on flies, worms, zebrafish, and mice, he says.

The most recent description of the project suggests establishing national "brain observatories" that would "provide access to new technology to all potential users, and serve as a collaborative node for the BAM community." But it is impossible to tell how the project will be administered at this point, says Ralph Greenspan, a systems neuroscientist at UC San Diego and one of the core scientists planning the initiative.

Based on his experience with large research efforts such as the Human Genome Project, Greenspan says new dedicated funding is needed to go ahead with BAM. "In no sense is this something that should replace other basic research" like the connectome project (see box), he says. But that decision is largely out of his hands, Greenspan adds. "Our role was to bring it to the attention of people in Washington, who to our delight seemed to embrace it enthusiastically." Now, he says, "they'll do it the way they see fit."

—EMILY UNDERWOOD

With reporting by Jocelyn Kaiser and Robert F. Service.

CLINICAL TRIALS

Europe Debates Ethics Reviews, Data Release

European countries are embroiled in a debate over how to redo rules for clinical trials, an effort to replace a controversial 12-year-old directive that critics say bound human research studies in red tape. But preserving stringent patient protections without tipping into excessive bureaucracy—and getting 27 countries to agree—is no easy task.

Among the sticking points are changes in the requirements for ethics reviews and a proposal that the results of all clinical trials in the European Union be made publicly accessible. The new rules face a vote in Parliament in April.

The regulation would replace unpopular rules that the European Union adopted in 2001. These rules, clinical trialists say, added layers of unnecessary bureaucracy that slowed clinical research and made it more expensive, especially for academic researchers (*Science*, 30 May 2003, p. 1353).

The European Commission's new plan, several years in the making, garnered praise when it was publicly unveiled in July 2012. Particularly welcome is a streamlined process

for persons who collectively have the necessary qualifications and experience." That prompted criticism that the new regulation would allow studies to go forward without independent ethical review and that researchers might "shop around" for loose oversight.

The reaction was particularly strong in Germany, where ethics committees play a powerful role in reviewing trial applications. The German Medical Association said the proposal undermines "protection of study subjects, scientific quality, and public trust in clinical research." In February, four of the five parties in the German Bundestag also released a statement of concern. The worries weren't limited to Germany; the European Group on Ethics in Science and New Technologies, which advises the European Commission, said it was "deeply concerned" by the failure to explicitly require ethics committee review. Some U.S. experts echo that worry: "I definitely don't think they should move to something where there's a reduced role for ethics boards," says Kay Dickersin, director of the Center for Clinical Trials at the

that satisfy individual countries, such as Germany, while minimizing red tape thanks to cross-border differences. The commission should set up a platform that encourages ethics committees to cooperate across national boundaries, Willmott says. Those amendments received wide support at parliamentary committee hearings on 19 and 20 February and look likely to be accepted.

Also sparking controversy is how much data from completed trials should be released. (Detailed results are already shared with drug approval agencies, but not always with the general public.) Now, many trials—especially those with negative results—are never published. The commission's proposal calls for the sponsor to share a summary from each completed study, but Willmott and Rivasi want to go further. They suggest that upon a trial's completion, the sponsor publish the full "clinical study report," which includes efficacy and safety data. Sponsors who fail to comply could be fined—up to €7000 per day in Rivasi's proposal.

That effort could push the bounds of trial registration, which has already changed substantially on both sides of the Atlantic. In 2004, an alliance of 12 leading medical journals announced that they would not publish any clinical trial that had not been registered from the start in a public database, such as the one established by the World Health Organization or on clinicaltrials.gov, part of the National Institutes of Health (NIH). Then in 2007, the U.S. Congress mandated that NIH create a "results database," which includes summary data from some trials. "That was a big, huge game-changer," says Deborah Zarin, the director of clinicaltrials.gov. "We now have about 8000 sets of results." They are less complete than what Willmott and Rivasi propose, however. And listings of results so far are a drop in the bucket compared with the more than 140,000 trials that appear on clinicaltrials.gov.

Whether the E.U. proposal will survive the parliamentary vote scheduled for 25 April and negotiations with the European Council, which represents member states, is far from clear, says Peter Gøtzsche, director of the Nordic Cochrane Centre in Copenhagen. "It is running into a lot of opposition" from the pharmaceutical industry and other lobbyists, he says. Negotiations are expected to last through autumn. The commission has said it hopes the regulation could take effect by 2016.

—GRETCHEN VOGEL

AND JENNIFER COUZIN-FRANKEL



Safe and effective? The European Union is drawing up new rules for clinical trials.

for approval of trials that take place in more than one E.U. country. The new rules will also have the force of law in member states. Previous rules gave countries some flexibility, leading to more than a dozen interpretations of key passages and complicating cross-border trials, says Joerg Hasford, chair of the Association of German Research Ethics Committees.

But some have reservations. The commission's proposal left out any reference to ethics committees, saying only that applications should be evaluated "by a reasonable num-

ber of persons who collectively have the necessary qualifications and experience." Johns Hopkins Bloomberg School of Public Health in Baltimore, Maryland.

In amendments proposed in early February, the European Parliament's lead legislators on the issue, Glenis Willmott from the United Kingdom and Michèle Rivasi from France, sought to assuage the critics. They proposed explicitly requiring the approval of an ethics committee that includes both health professionals and patient representatives, similar to the current 2001 rule. The challenge will be to preserve ethics reviews

DUAL USE RESEARCH

New U.S. Rules Increase Oversight Of H5N1 Studies, Other Risky Science

Scientists interested in doing experiments involving the H5N1 avian influenza virus and 14 other potentially dangerous biological agents face new requirements in getting funding from the U.S. government.

Researchers and universities are offering mixed reactions to two sets of rules announced last week. They are a direct response to a global controversy that erupted in late 2011 after scientists created H5N1 viruses that some feared could spark a deadly human pandemic. Meanwhile, some researchers are resuming their H5N1 work now that a voluntary moratorium is over (*Science*, 4 January, p. 16), including a laboratory in China with year-old results apparently similar to those that caused the initial furor.

One set of rules, from the U.S. Department of Health and Human Services (HHS), applies only to scientists seeking to create potentially dangerous new H5N1 strains (see p. 1036).

These final guidelines set out seven criteria that experiments must meet to be eligible for HHS funding, including a requirement that scientists address issues “with high significance to public health.” Engineered viruses also must be capable of being “produced through a natural evolutionary process.”

A draft released late last year was criticized as being too broad and vaguely worded (*Science*, 7 December 2012, p. 1271). The final version addresses those concerns, federal officials say. They narrowed the scope to mammal-transmissible viruses, for instance, and removed language that required “evidence” that engineered viruses could naturally evolve in the “foreseeable future.”

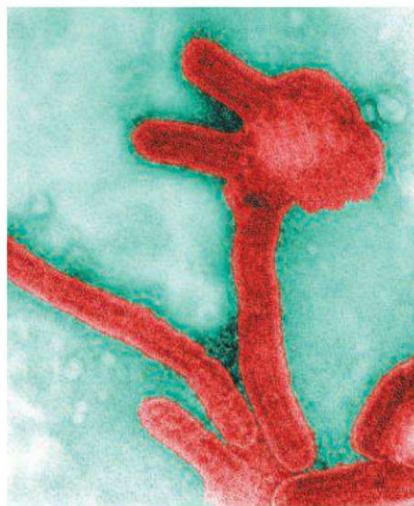
Such changes please many in the small H5N1 research community. But some advocates for tougher biosecurity oversight aren't happy. “It's been watered down to the point where it is essentially wholly empty,” says molecular biologist Richard Ebright of Rut-

gers University in Piscataway, New Jersey.

Ebright is happier with the other document, released on 21 February by the White House's Office of Science and Technology Policy (OSTP). It asks the public to comment by 23 April on a draft of broader rules designed to identify biology studies that could be used for good or evil—or “dual use research of concern” (DURC) in official parlance. Existing U.S. rules, released in March 2012, already require funding agencies to consider whether studies involving 15 especially dangerous agents, including mammal-transmissible H5N1 and anthrax, could be “directly misapplied” to do harm (*Science*, 6 April 2012, p. 21).

The new policy aims to start DURC reviews earlier. It creates institutional committees that would determine whether a proposed study falls into any of seven categories of experiments, including those that could make a toxin more deadly or confer resistance to treatment. Potentially problematic studies would trigger a second review, officials say. A DURC designation “does not mean that the research should not be conducted or communicated,” the draft notes, but it would require researchers to devise a plan to mitigate risks.

The new rules are expected initially to affect not more than a few hundred laboratories, officials say. And, “at first blush,” they don't appear to be too onerous, says Carrie Wolinetz of the Association of American Universities in Washington, D.C. But she worries that the second review “may be of marginal benefit” because federal “select agent” regulations already cover much of the listed research. University officials also want the government to clarify how disputes will be resolved and how DURC reviews will be both transparent and able to withhold certain information. Government officials, meanwhile, say the rules ultimately could be extended to other types of biological studies.



Stricter scrutiny. Proposed rules would require universities working with 15 dangerous agents, including the Ebola virus (above), to consider whether the results could cause harm.

Officials say the two H5N1 studies that sparked the recent controversy likely would have been approved under both new policies. But those laboratories—led by Yoshihiro Kawaoka at the University of Wisconsin, Madison, and Ron Fouchier of Erasmus MC in Rotterdam, the Netherlands—will now have to go through the new reviews to resume similar work with U.S. funding. That could take a month.

Fouchier, however, says he's not waiting. In mid-February he resumed his studies using an existing E.U. grant. “I won't be silenced by the Americans anymore,” Fouchier says.

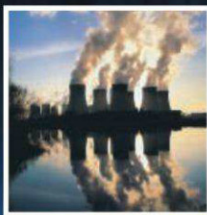
A lab in China that has stayed under the radar has likely also resumed its work on H5N1 transmissibility, Fouchier says. Chen Hualan and her colleagues at the Harbin Veterinary Research Institute published a paper in 2009, co-authored by Kawaoka, that homed in on mutations that made the H5N1 virus more transmissible in guinea pigs. Fouchier says a new paper by the same group was held up by the moratorium, which Chen signed. She confirmed that her group has submitted a paper to a journal but declined to answer other questions.

Fouchier says one short-term project is to discover the minimum number of mutations needed to make H5N1 airborne—or able to spread through coughing and sneezing—between ferrets. His paper, which *Science* published last June after a long delay, describes several airborne H5N1 strains, each of which had at least nine mutations. All strains had five mutations in common; but it was unclear if this core set suffices to make a strain airborne or what the remaining mutations might contribute. “We're already pretty far along” in finding out, Fouchier says. “We could be writing a new paper a month from now.”

The work was done using an H5N1 strain from Indonesia, but a next step is to test whether the same mutations do the trick in H5N1 viruses found in other countries, and whether other avian influenza subtypes, such as H7N7, could become airborne as well. He has also applied for an E.U. grant to do similar studies in the coronavirus family, including the SARS virus, which caused a fast-moving global outbreak in 2003.

Fouchier may encounter more roadblocks, however. A spokesperson for the Dutch Ministry of Foreign Affairs says that papers similar to the *Science* paper would need an export license before being submitted for publication, as Fouchier obtained under protest for the paper that *Science* published last year. His institution has gone to court to fight the government's decision.

—DAVID MALAKOFF AND MARTIN ENSERINK



Twenty-first century battleground. The U.S. government is ramping up efforts to shore up power grids, air traffic control systems, and other critical infrastructure against cyber incursions.

A Call to Cyber Arms

China's extensive cyber research activities and allegations over cyber espionage have put the United States on high alert



XI'AN, CHINA—The leaflet posted in the school of information engineering here at Xi'an Jiaotong University was brief but enticing, offering computer-savvy graduates a hefty stipend and the chance to serve their motherland. "I was curious," says Liu, who asked that only his surname be used in this article. It was the spring of 2007, and Liu, then 24 years old, was wrapping up a master's degree in computer algorithms. Encouraged by his supervisor, Liu called the number on the leaflet; that summer, he joined an elite corps of the People's Liberation Army (PLA) that writes code designed to cripple command-and-control systems of enemy naval vessels.

PLA writings call the electromagnetic spectrum "the fifth domain of battle space," putting cyberspace on an equal footing with ground, air, sea, and space. Cyber conflicts "threaten national security and the very existence of the state," two scholars with the Academy of Military Sciences wrote in *China Youth Daily* in 2011. State media regularly tout PLA activities in cyber defense, a catchall term encompassing everything from surveillance and espionage to weapons such as electromagnetic pulse generators that disable computer networks and malware designed to take down power grids or contaminate water supplies. Augmenting PLA efforts is a legion of civilian researchers and hackers whose efforts ostensibly are directed at repelling electronic intruders. In 2011, more than 8.5 million computers in China "were attacked by rogue programs every day," a 48% increase over the previous year, says Li Yuxiao, a cyber law expert at Beijing Univer-

sity of Posts and Telecommunications.

But evidence is accumulating that China can dish it out, too. In a report issued last week, the U.S. computer security firm Mandiant tracked one especially adept group of hackers, sometimes called the Comment Crew or Comment Group, to a neighborhood in Shanghai housing Unit 61398, a bureau of the PLA General Staff Department's Third Department. According to Mandiant, other computer security analysts, and U.S. State Department sources, hackers in China have gathered gigabytes of data on industrial secrets, military hardware, and government strategy for political negotiations.

This is not a unilateral arms buildup. Another heavyweight in the cyber arena is Russia; hackers took down Georgian government servers in advance of Russia's invasion of that former Soviet republic in August 2008. The United States, too, has gone all-in on cyber warfare. In 2009, it established the U.S. Cyber Command in Fort Meade, Maryland, to conduct "full-spectrum military cyberspace operations." The Defense Department's operational needs "will require the integration of cyber and electronic warfare at unprecedented levels," said Regina Dugan, then-director of the U.S. Defense Advanced Research Projects Agency, in a statement released by DARPA before the Senate took up the 2013 defense authorization. According to U.S. Defense Secretary Leon Panetta, the Pentagon spends about \$3 billion a year on cyber security.

An early fruit of this massive enterprise may be the most successful cyber weapon deployed to date: Stuxnet. The computer worm came to light in 2010 after instructing centrifuges in Iran that enrich uranium to spin at damaging speeds. Computer security experts have credited the United States and Israel for Stuxnet's sophisticated code and for orchestrating its insertion into the Iranian machines. Whoever's handiwork it was, Stuxnet has "shown the world how to stage a damaging cyber attack," says James A. Lewis, an analyst with the Center for Strategic and International Studies in Washington, D.C.

Now that Pandora's box is open, the United States fears that it, too, may someday be on the receiving end of an effective attack. In his State of the Union speech on 12 February, U.S. President Barack Obama declared that unidentified enemies are "seeking the ability to sabotage our power grid, our financial institutions, [and] our air traffic control systems." That day, he signed an executive order to strengthen cyber defenses and called on Congress to pass legislation that would "give our government a greater capacity to secure our networks and deter attacks." Last week, the U.S. Department of Energy announced \$20 million in funding for the development of technologies to strengthen the cyber security of delivery systems for electricity, oil, and gas.

A one-two punch featuring a cyber attack on critical infrastructure and a physical strike against U.S. targets could leave the country reeling from a "cyber Pearl Harbor," Panetta

Online

sciencemag.org



Podcast interview
with author
Richard Stone ([http://
scim.ag/pod_6123](http://scim.ag/pod_6123)).

warned in a speech last October. “It would paralyze and shock the nation and create a new, profound sense of vulnerability,” he said. Panetta did not call out China. But with territorial disputes between China and U.S. allies raising tensions in East Asia, Panetta, in a meeting with Chinese defense officials in Beijing last September, said that he “underscored the need to increase communication and transparency with each other so that we could avoid a misunderstanding or a miscalculation in cyberspace.”

Raising an army

In a quiet corner of a hotel lobby here in the capital of western China's Shaanxi Province last November, Liu sips puer tea and shifts nervously in his chair as he describes how his high marks in mathematics propelled him from rural Shaanxi to Xi'an Jiaotong University. Like many other computer science students there, he says, he learned to hack in his spare time. “We felt it was a patriotic duty,” he says.

In the PLA unit, which he declined to identify, Liu says he spends about half of his time working on programming teams to develop algorithms ordered by superiors. The rest of the time he reads up on computer literature or political ideology and takes part in simulations with other units in which he and his colleagues stage or repel attacks. “Our work is purely defensive,” says Liu, who claims he was given permission to speak with *Science* in order to emphasize the defensive nature of the research. PLA and foreign ministry spokespersons last week insisted that China has not carried out cyber espionage or attacks on other nations.

The kaleidoscopic patterns of activity in cyberspace may be hard to interpret, but the wellspring of China's strength is hundreds of computer and information departments across the country. Civilian research sits at one end, and it is largely out in the open. For example, over the past 5 years China's National Administration for the Protection of State Secrets has tapped 10 universities to host academies for training students in computer science and other disciplines for sensitive jobs in government agencies. Research in information engineering and cyber defense is also funded through standard science grant programs as well as initiatives supporting sensitive dual-use projects, including the information ministry's 242 program and the security ministry's 115 program.

In the academic world, a leader in cyber defense research is Shanghai Jiao Tong University's School of Information Security Engineering. In the past several years, its scientists have published openly on the injection of Trojan horses into the Windows platform, for instance, and on the pros and cons of Rootkit, a program for hijacking a computer system. In Changsha, the National University of Defense Technology has a research program in electronic and information warfare. And at Dalian University of Technology in northeast China, a pair of researchers funded by the science ministry and the National Natural Science Foundation of China published a report in *Safety Science* in July 2011 on vulnerabilities in the western U.S. power grid.

The real action in the cyber sphere is in the PLA's General Staff Department. As one of several bureaus in the Third Department, Unit 61398 “appears to function as

by Northrop Grumman Corp. analysts for the U.S.-China Economic and Security Review Commission.

In a speech last May, the head of the United Kingdom's MI5 counterintelligence agency, Jonathan Evans, decried an “astonishing” level of cyber espionage in the world, with “industrial-scale processes involving many thousands of people lying behind both state-sponsored cyber espionage and organized cyber crime.” Evans did not name China, but security experts were quick to point out that no country rivals China's dedication, and prowess, in cyber espionage.

China so far has shown only some of its cards. Chinese hackers have allegedly used computer network exploitation techniques such as spearphishing, in which malware is embedded in target computers, to harvest data from a long list of Fortune 500 companies, think tanks, and government agencies. Since 2006, the Mandiant report documents,

the Shanghai-based hacking group it tracked has pilfered hundreds of terabytes of data from 141 organizations, including 115 in the United States. Information technology and aerospace firms were targeted most frequently. Mandiant said it believes the activity it observed “represents only a small fraction of the cyber espionage” committed by the Shanghai outfit. Delays and cost overruns in the U.S. F-35 fighter jet program “may be the result of cyber espionage, as could the rapid development of China's J-20 stealth fighter,”

Lewis testified before the U.S.

Congress last April. “Cyber espionage is the most pressing threat we face,” he asserted.

On the diplomatic front, the State Department in 2011 established an Office of the Coordinator for Cyber Issues. “We're writing foreign policy from scratch,” says a U.S. State Department official who requested anonymity. Chinese and U.S. defense officials have begun swapping views on cyber security under a Strategic Security Dialogue launched last year. The two sides have struggled to identify confidence-building measures that would reduce distrust, says the State official.

In the meantime, the official says, “there is a debate going on” in the U.S. government about whether China's cyber espionage activities “have reached a level where they constitute a national security threat.” It's only a matter of time, he says, before China crosses that Rubicon.

—RICHARD STONE



Digital hands on deck! In a conflict in the Pacific, the *USS Blue Ridge*, the U.S. Navy's command ship in the region, would be a ripe target for a cyber strike.

the Third Department's premier entity targeting the United States and Canada, most likely focusing on political, economic, and military-related intelligence,” according to a 2011 report from the Project 2049 Institute, a think tank in Arlington, Virginia. (At least one Unit 61398 researcher has published in the open literature, as co-author with three colleagues at Shanghai Jiao Tong University of a 2009 abstract on network security alerts and attack scenarios. Mandiant's report flagged job recruitment fairs for Unit 61398 in 2004 at the Harbin Institute of Technology and Zhejiang University in Hangzhou that were advertised openly on the universities' Web sites.) The General Staff's Fourth Department, meanwhile, “has primary responsibility for the offensive electronic-based information warfare missions in the PLA,” states a report last March on China's cyber espionage capabilities, prepared



Filling up. Radioactive waste collected from across Fukushima is overwhelming temporary storage sites.

JAPAN DISASTER

Cooling a Hot Zone

Two years after the Fukushima Daiichi Nuclear Power Plant disaster, Japan is trying new approaches to decontamination while evacuees wait to go home

NAMEGAWA, JAPAN—On the outskirts of this town 60 kilometers northwest of Tokyo, on the grounds of a sprawling precast concrete factory, stands a bare-bones, four-story steel structure bristling with piping and full of shiny tanks of various shapes and sizes. The tower may seem an unlikely symbol of hope. But the engineers who built this pilot plant think it may hold a key to Japan's recovery from the March 2011 nuclear disaster.

On a late winter day, the machinery is idled for tweaks to the plant's process. When running, it consumes batches of soil and other materials seeded with non-radioactive cesium, a proxy for the cesium isotopes contaminating the land around the Fukushima Daiichi Nuclear Power Plant. In each batch, 50 kilograms of material is fed into a hopper and mixed with water. This slurry is pumped to vessels below, where the temperature and pressure are raised to the point (260°C) at which cesium breaks away from sand particles. In the next tank, the pressure is suddenly released, shattering clay crystals and allowing more cesium to escape into the water. After solids are removed, ferric ferrocyanide (Prussian blue) is added to absorb the cesium and then settled out. The cleansed water is recycled back to the initial mixing tank while the decontaminated solids are squeezed dry and ready for disposal. Less than 2.5 kilograms of cesium-bearing Prussian blue are the only waste at the end of each batch requiring burial in specialized landfills.

This approach will be able to strip 80% to 95% of the radioactive cesium from contaminated soil and other materials, says

Kenji Takeshita, a chemical engineer at the Tokyo Institute of Technology, who developed the technique in cooperation with CDM Consulting, an engineering firm, and Maeda Corp., a general contractor. He also notes that it avoids the use of chemicals that would become secondary waste and need further processing.

Hydrothermal blasting, as the technique is called, is one of several technologies now vying to be included in Japan's efforts to clean up the radioactive material scattered over some 13,000 square kilometers of land by the Fukushima accident triggered by the 11 March 2011 earthquake and tsunami. Japan's government is under intense pres-

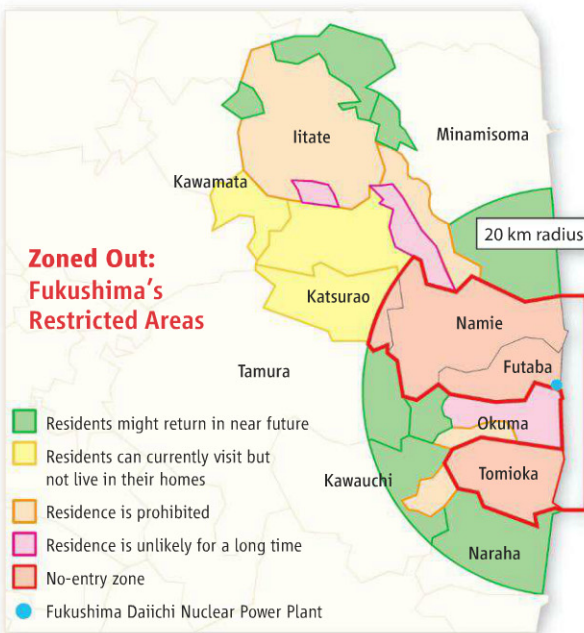
sure to clean up as much land as possible so that the 110,000 people still displaced by the nuclear disaster can return to their homes, farms, and businesses.

Japan hasn't implemented a scheme—or even chosen sites—for disposal of the spent fuel routinely removed from the nation's nuclear reactors. Now, suddenly, it faces the disposal of 16 million to 41 million cubic meters of contaminated waste, according to the Ministry of the Environment. The government is trying to find a balance between cost, the volume of waste, the capabilities of decontamination technologies, and the size of disposal sites, says Yoshitake Shiratori, an official with the Japan Atomic Energy Agency (JAEA), which is evaluating the experimental decontamination techniques. “Gaining the acceptance of the local people” is a key challenge, he says. Judging from local press reports, it may be the biggest one.

The big scrape

The meltdowns and explosions at the Fukushima reactors, though devastating, left a smaller toxic legacy than the 1986 Chernobyl accident. Fukushima spewed somewhere between 6 and 37 petabecquerels of cesium-137, according to a summary of estimates by a JAEA scientist. This compares to the 85 petabecquerels of the isotope released at Chernobyl, according to the 2005 U.N. Chernobyl Forum expert group report. And Chernobyl, unlike Fukushima, released significant amounts of other radionuclides, including plutonium isotopes with half-lives of thousands of years. Cesium-137, the major health concern in Fukushima, has a half-life of 30 years.

By several estimates, about 80% of the Fukushima atmospheric radioactivity drifted out to sea, where it combined with water leaking from the stricken reactors. “It was very severe contamination,” says Jyota Kanda, a biogeochemical oceanographer at Tokyo University of Marine Science and Technology. Fisheries in the vicinity are closed; marine products from the northeast coast are being checked. However, Kanda expects the long-term effect on marine life to be negligible because the contaminants dispersed rapidly.



But on land, leaving nature to take its course while people wait to return is not a political option. So the government is now trying to scrape clean large swaths of Fukushima Prefecture, aiming to get exposure from the contaminated environment down to 1 millisievert (mSv) per year above the background level. This is the maximum exposure recommended by the International Commission on Radiological Protection for the general public. Much of the evacuated area is still at levels well above that.

The governmental reconstruction agency has split the evacuated areas into five zones based on the radiation doses residents would face (see map). The most contaminated areas, mostly within 20 kilometers of the plant where the annual radiation doses would top 50 mSv, will be off-limits for the foreseeable future. At the other end of the spectrum are areas where residents would get less than 5 mSv per year. Cleaning these would allow 22,000 residents to return home. The government hopes to allow that within an unspecified near term.

The first cleanup step relies on the labor-intensive removal of contaminated topsoil, pavement, and leaves, and washing building surfaces. JAEA evaluated decontamination procedures and produced guidelines on such things as the depth of topsoil, typically 5 centimeters, and the amount of pavement to remove.

This work is generating mountains of low-level radioactive waste, now piling up in more than 5000 temporary storage sites, according to the Fukushima Prefecture government. In addition, NHK, the national broadcaster, last fall reported that an estimated 260,000 45-liter garbage bags containing radioactive waste collected by citizens and municipal workers are sitting in corners of gardens, school yards, and fields. The government wants to move all this waste into interim storage sites—landfills lined with double walls and floors of concrete surrounded by bentonite, a claylike sealant, and covered by topsoil. To reduce the volume of waste needing this expensive storage, atomic energy agency officials have been evaluating a number of technology demonstration projects funded by the government.

Construction and chemical companies, university groups, and national labs stepped forward with proposals. The Japan Aerospace Exploration Agency, for example, tried digesting contaminated plant matter with thermophilic bacteria it had been studying for possible use in space agriculture. A Kyoto University group tried using nanobubbles to wash contamination out of concrete paving.

Astronomers Lend Know-How to Cleanup

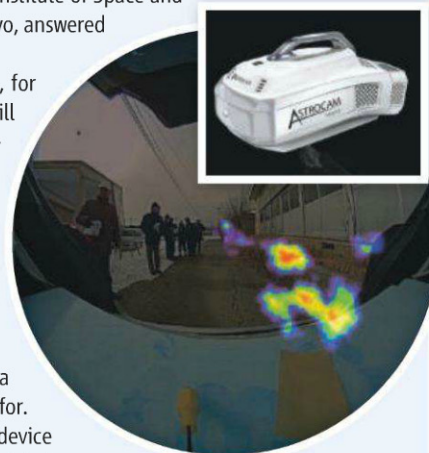
The Fukushima radioactivity cleanup is getting an assist from an unexpected source: Japanese astronomers. They have repurposed cutting edge gamma ray detection technology intended to observe distant stars in a device to help uncover hotspots of radiation.

Shortly after the March 2011 accident at the Fukushima Daiichi Nuclear Power Plant, engineers from plant owner Tokyo Electric Power contacted the Japan Aerospace Exploration Agency (JAXA) asking if its x-ray observation technology, developed for a series of satellites, could help track terrestrial radiation. The x-ray astronomy group at JAXA's Institute of Space and Astronautical Science (ISAS), in Sagami-hara near Tokyo, answered the challenge.

The group is readying its next mission, ASTRO-H, for a 2014 launch. One of ASTRO-H's six instruments will be a Soft Gamma-ray Detector (SGD). The device analyzes the trajectories of gamma rays and the electrons they hit within the detector to determine the energy and direction of the incoming rays. ISAS physicist Tadayuki Takahashi likens this to reconstructing the force and direction of a cue ball by analyzing the scatter of the billiard balls that it hits. Cesium-137 and cesium-134, the major radioactive contaminants in Fukushima Prefecture, emit gamma rays—but of a higher energy than SGD was designed for.

The ISAS team tweaked the SGD design to make a device sensitive to those higher energies. Their prototype detector, which they mounted in the back of a car, superimposes color-coded radiation data on digital images so hot spots can be located in real time. Unlike existing portable devices, it does not have to be close to the source. The team successfully demonstrated its capabilities in Fukushima's heavily contaminated Iitate Village in spring 2012. Mitsubishi Heavy Industries is commercializing the device and plans to have it on the market by the end of March.

"I believed this kind of next-generation detector could be used in various fields, such as medicine," Takahashi says. But he never imagined using it to trace the effects of a nuclear accident. —D. N.



Down to Earth. A gamma ray detector intended for space can see radiation hot-spots and is being commercialized (inset).

Construction companies experimented with soil scrubbing techniques. Some removed 70% of the radioactivity and reduced the volume of waste requiring special storage. These techniques are low-cost and realizable, JAEA's Shiratori says. "But the question is whether local residents would accept that level of remaining contamination."

At least three groups are working on technologies that break the cesium free from contaminated materials. One is the hydrothermal blasting technique developed by Takeshita and his partners. Shiratori says the technology has potential, but the agency would like to see it tested on contaminated material from Fukushima. That step is now being planned.

A second prospect came from Taiheiyo Cement Corp. of Tokyo, which has developed a process to heat contaminated materials plus a catalyst to temperatures above 1300°C. This technique removed 99% of the cesium from contaminated waste and collected it in filters. Shiratori says the pro-

cess could be scaled up. But it is expensive, and the ceramic kilns required would also become contaminated, adding to the volume of waste.

A third idea, from Toshiba Corp. of Tokyo, relies on oxalic acid to break open the soil structure and release the cesium, which can then be captured by an absorbent. The test runs indicated that 93% of the cesium could be removed, and the volume of waste for special disposal would be reduced by 95%. Although the process is efficient, Shiratori says it could be costly to scale up. One issue with all these approaches is that the resulting bulk product may be clean, but "it's not soil anymore," Takeshita says. Stripped of organic material, it can't be used as topsoil.

Shiratori says the government is continuing evaluations of these and other techniques. Before putting them to use, national and local governments and affected residents have to come to terms on locating storage sites and hosting decontamination plants.

—DENNIS NORMILE

ENVIRONMENTAL SCIENCE

Pollutants Capture the High Ground in the Himalayas

In high alpine areas once thought pristine, dust and soot appear to be accelerating glacier melting and may alter monsoon patterns

PYRAMID OBSERVATORY, NEPAL—On the south slope of Mount Everest, mountaineers tricked out in the latest high-tech gear and Nepalese porters trundle up the Khumbu Valley. Fragments of conversation are lost in the low rumble of the Dudh Kosi River and the tinkling of yak bells from nearby slopes. For Angela Marinoni, this is a familiar route—but she is not a typical trekker. Pausing for a drink, Marinoni, a climate scientist at the Institute of Atmospheric Sciences and Climate in Bologna, Italy, watches wisps of smoke from cookstoves and forest fires drift into the highlands. Pollution from combustion, not the summit of Everest, is her main quarry.

Since 2006, Marinoni and colleagues have been gathering climatological data at what they imagined would be a pristine site in the Himalayas. The idea was to establish a baseline against which they could measure regional pollution. What they have discovered instead, Marinoni says, was “a total surprise”: dust and soot wafting high into the mountains.

The implications are troubling. The Himalayas were long presumed to form a bulwark against airborne pollutants from the Indian subcontinent. But “the barrier is leaky,” Marinoni says. Heavier pollutant loads reaching Himalayan peaks and the Tibetan Plateau beyond “could increase glacier melt, pollute streams, and change monsoon patterns,” threatening the livelihoods of millions of people, warns Arnico Panday, an atmospheric scientist at the International Centre for Integrated Mountain Development (ICIMOD) in Kathmandu.

Such a potent risk may have remained overlooked had scientists from the Ev-K2-CNR Committee, a nonprofit scientific association in Bergamo, Italy, and the Nepal Academy of Science and Technology not established nine outposts, including a major facility called the Nepal Climate

Observatory at Pyramid, in the Khumbu Valley. The stations provide “a unique data set” of atmospheric circulation in high mountains, says Roy Rasmussen, a climate scientist at the National Center for Atmospheric Research in Boulder, Colorado. The challenge, he says, is to piece together where the pollutants come from, how they are transported to the Himalayas, and how they are influencing regional climate.

Pristine no more

After 6 arduous days trekking up the Khumbu Valley, lush forests have given way to a treeless, rock-strewn highland dusted with fresh snow. At last, 5079 meters above sea level, a two-story stone building topped with a glass pyramid comes into sight. Khumbu Glacier extrudes from a cleft in the hills, its gravel-covered tongue reaching toward Pyramid Station. Atop an adjacent rise is a cluster of instruments, including an

ozone analyzer, particle counters, and photometers for measuring light absorption and scattering by aerosols.

Fatigued by the altitude, Marinoni clambers up the station's roof to check an air sampler; the team journeys here twice a year to calibrate instruments and install sensors. One villain they are tracking is soot, called black carbon in the scientific literature. With its atmospheric persistence measured in days to weeks, black carbon, spawned by incomplete combustion of biomass, coal, and diesel fuel, is known as a short-lived climate forcer. (Carbon dioxide molecules, by comparison, can persist in the atmosphere for hundreds of years.) South Asia is a black-carbon hotspot; more than half of the estimated 8 million tons of black carbon released into the air each year across the globe originates in the Indo-Gangetic Plain mostly from the burning of wood, dung, and crop residues.

Six years of measurements at Pyramid have generated a wealth of data on black carbon and other pollutants. Marinoni and her colleagues have found that the southern slope of the Himalayas is particularly vulnerable to the pollutant-laden haze that gathers in the foothills below. “Khumbu Valley is like a big chimney,” Marinoni says. “The valley breezes can effectively channel the pollutants to high altitudes.”

More than 30 days a year, on average, the instruments here have recorded what Marinoni calls “acute” pollution, in which black carbon concentrations shoot up fourfold and ozone increases by one-third compared with average days. “It is particularly bad during dry spells” between January and May, before the onset of the monsoon and its cleansing rains, says Paolo Bonasoni, who heads the Bologna research team. In one out of every 5 days, a thick brown cloud settles over Khumbu Valley and black carbon may exceed 5 micrograms per cubic meter—a concentration rivaling that of an average-sized Indian city.

A looming threat

How big a punch black carbon and other pollutants may pack in the Himalayas is open to debate. At higher altitudes, greenhouse gases and particulates play an outsized role in climate, Bonasoni says. “The air is very thin and clean,” he says, “so the pollutants have a much longer lifetime and can accumulate.” That, in turn, could influence climate by decreasing solar radiation reaching the surface and by interfering with cloud formation and precipitation, Marinoni says. On a few occasions, elevated pollutant levels coincided with sudden breaks in the monsoon on the Indian



Reaching new heights. Angela Marinoni adjusts a sun photometer for measuring aerosol properties at Pyramid.

CREDIT: JANE GIU

subcontinent that lasted up to 2 weeks. “It’s difficult to say for sure whether pollution stopped the rain,” she says, “but it’s certainly one possibility.”

Another concern is faster glacier melting. After accounting for wind speeds and topography, Marinoni’s group estimated that the amount of black carbon deposited on Himalayan slopes during the dry season reduces glacier reflectivity by as much as 5%, which increases the melting rate of a typical glacier by up to one-third. “The effects are cumulative,” says Xu Baiqing, a glaciologist at the Institute of Tibetan Plateau Research of the Chinese Academy of Sciences in Beijing. His studies show that soot concentrations are magnified at least 10-fold a year in a glacier’s accumulation area, where snow becomes denser after repeated partial melting and refreezing. “As snow melts, water slowly percolates through ice and leaves pollutants behind,” which are then trapped in the accumulation zone during refreezing, Xu says. As temperatures rise and snow lines retreat to higher altitudes, he says, the melting of decades-old accumulation zones should liberate more and more black carbon and accelerate glacial melting. “The maximal effect of black carbon may not be now, but in the coming decades,” Xu says. He and colleagues have found that black carbon and organic carbon—the unburned remains of biomass burning—in glaciers in southeastern Tibet increased 30% between 1990 and 2003, coinciding with rapid industrialization on the Indian subcontinent.

Scientists are loath to rely solely on Pyramid Station’s data to gauge the regional threat. “But there are big gaps in the Himalayas where there is little observation,” Panday says. As a step toward filling that lacuna, Ev-K2-CNR scientists last summer installed instruments to measure pollution at Askole in the Karakoram Mountains of Pakistan. Unlike the monsoon-dominated eastern Himalayas, the Karakoram is subjected to the westerlies, which can bring dust and pollutants all the way from Africa and the Middle East.

In the meantime, Bonasoni’s team is developing computer models to simulate climate and pollutant transport in the region at resolutions of less than 10 kilometers. The



Lab with a view. Data collected at Pyramid Observatory, on Mount Everest’s south slope, have woken scientists to the threat that pollutants pose to the Himalayas and the Tibetan plateau.

models will account for more than 200 pollutants and will be driven by real-time meteorological data, says Ev-K2-CNR’s Bhupesh Adhikary, an expert on air pollution and climate simulation in Kathmandu. Studies to date have been mainly descriptive and based on limited observations, he says. “They tell us what happened, but cannot tell us why or what will happen in the future.” Adhikary hopes that modeling studies will help answer those questions and inform mitigation and adaptation measures.

Another challenge is coaxing Himalayan countries to work together to curb emissions of black carbon and other short-lived climate forcers. Last year, with \$3.9 million in seed funding from the Swedish International Development Cooperation Agency, ICIMOD launched an initiative to boost research capacity, assess mitigation options in mountain regions, and promote collaboration of Himalayan countries in emission reductions, says Panday, who leads the effort. “Long-term observation is the key,” he says. “There is an urgent need to set up stations across the entire region.”

Reining in black carbon would pay big dividends, and fast. “Cutting short-lived climate forcers would have immediate climate effects because they are quickly removed from the atmosphere,” says Veerabhadran Ramanathan, a climate scientist at the Scripps Institution of Oceanography in San Diego, California. Turning back the pollution tide won’t be easy though. Simple strategies like replacing cookstoves with cleaner burning models can be tricky in the Himalayas, as many cookstove models work poorly at high altitudes.

At Pyramid, the winds are howling as Italian and Nepalese researchers sit down for spaghetti Bolognese and a glass of red wine. They talk over plans for an expedition to repair an automated station on the South Col, the highest camp for mountaineers attempting to summit Everest. Pema Sherpa, a Nepalese technician who helped set up South Col station in 2008, is ready to give it another shot. “Mountain people are very vulnerable to climate change,” he says. “This will help us better prepare for the future.”

—JANE QIU

Jane Qiu is a writer in Beijing. Her trip to Pyramid Observatory was supported by a journalism fellowship from the European Geosciences Union.



LETTERS

edited by Jennifer Sills

A Call for Integrative Thinking

IN THE 30 NOVEMBER 2012 ISSUE OF *SCIENCE*, WE WERE STRUCK by the juxtaposition of two News & Analysis stories by R. A. Kerr. One article ("Experts agree global warming is melting the world rapidly," p. 1138) summarizes the discussions among glaciologists



about the rate at which global warming is accelerating the melting of the Greenland ice sheet, as well as the net losses of ice in Antarctica. The other ("An oil gusher in the offing, but will it be enough?," p. 1139) analyzes the International Energy Agency's most recent report, which shows that it is possible to meet the world's energy demands through 2035 by drawing upon increasingly difficult-to-process oil reserves. Neither article refers to the information contained in the other. Yet, the two topics present a glaring contradiction between scientists' concern about increasingly rapid climate change (amid World Bank warnings of the dire consequences for human well-being) and the oil industry's preoccupation with how it can meet an undiminished world market demand for fossil fuel. If there was ever a call for the kind of problem-solving and integrative thinking that K. V. Hodges advocates in the same issue ("Solving complex problems," Essay, p. 1164), undoubtedly this is it.

DAVID J. RAPPORT* AND LUISA MAFFI

EcoHealth Consulting, Salt Spring Island, BC, V8K 2N6, Canada.

*To whom correspondence should be addressed. E-mail: drapport@ecohealthconsulting.com

Data Re-Identification:
Prioritize Privacy

IN OUR OCTOBER 2012 REPORT, "PRIVACY and progress in whole genome sequencing" (1), the Presidential Commission for the Study of Bioethical Issues ("Bioethics Commission") called for a consistent floor of privacy protections across state lines covering genomic data, regardless of how the data were obtained.

The need for this consistent approach to privacy protections is now more urgent than ever in light of recent advances that demonstrate the limits of genomic deidentification ("Identifying personal genomes by surname inference," M. Gymrek *et al.*, Reports, 18 January, p. 321), which challenge obtaining the benefits of genomic data sharing ("The complexities of genomic identifiability," L. L. Rodriguez *et al.*, Policy Forum, 18 January, p. 275).

The promise of genomic technologies will not be realized if individuals are unwilling to share their sensitive data with

the research community because of privacy concerns, or if those who share their data later discover that their privacy was invaded without their informed consent. The decline in scientists' abilities to keep personal data "deidentified" threatens to further erode public confidence around the privacy of unique genomic data.

A "deidentified" genome has become a spectrum of possibilities for re-identification, rather than an absolute protection against privacy invasion. It therefore is incumbent on clinicians and researchers to obtain informed consent before any whole-genome sequencing and to develop and enforce appropriate limits on access to and use of all genomic data. In addition to strengthening consent and security standards, we need to streamline and strengthen laws governing the collection and use of whole-genome sequence data.

The identification of purportedly "deidentified" genomic data is no longer merely conceivable, it is already occurring. The Bioethics Commission anticipated these advances in its report and urges the adoption of the strong baseline protections

that are critical to protecting individual privacy and data security—while also encouraging the information sharing that propels scientific and medical progress.

AMY GUTMANN

Chair, Presidential Commission for the Study of Bioethical Issues and President, University of Pennsylvania, Philadelphia, PA 19104, USA. E-mail: info@bioethics.gov

Reference

1. Presidential Commission for the Study of Bioethical Issues, "Privacy and progress in whole genome sequencing" (2012); http://bioethics.gov/cms/sites/default/files/PrivacyProgress508_1.pdf.

Data Re-Identification:
Societal Safeguards

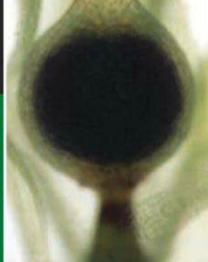
THE REPORT BY M. GYMREK *ET AL.* ("IDENTIFYING personal genomes by surname inference," 18 January, p. 321) demonstrates that DNA samples can be combined with surname and other data to re-identify seemingly anonymous records. The study adds to the literature showing that large, publicly available data sets can be leveraged to infer personal information (1) and identify unique individuals (2). In 2005,

CREDIT: ISTOCKPHOTO



Gender, microbes,
and disease

1044



Jekyll-and-Hyde
plants

1045

a 15-year-old tracked down his sperm donor father using a similar approach (3). This demonstration may undermine individual research subjects' confidence that their DNA can be shared in a way that is not re-identifiable. To counteract this effect, we must augment imperfect technical safeguards with measures that make such re-identification socially, legally, and economically unacceptable.

Society can work in many ways to mitigate risks and maintain a climate of confidence that will continue to encourage research subject participation. Subjects must be informed of the risk that their DNA sequence will be identified and connected to them. Data stewards must make a good-faith effort to protect DNA-based records, including continuing to deidentify the data (e.g., remove explicit identifiers). Systems for audit of access and use of the data should be routine, and data should be protected from anonymous access. Data use agreements should provide institutional and legal remedies when societal boundaries and robust research norms of respect for the privacy of individuals are violated.

The diversity of human genomes guarantees that each person will harbor markers for higher-than-average risk for some adverse outcomes. Thus, further risk mitigation should include regulatory approaches such as expansion of protections currently provided under the Genetic Information Nondiscrimination Act and other anti-discrimination laws, which currently protect against some forms of discrimination, but not others, such as long-term care or life insurance.

RUSS B. ALTMAN,¹ ELLEN WRIGHT CLAYTON,² ISAAC S. KOHANE,³ BRADLEY A. MALIN,^{4*} DAN M. RODEN⁵

¹Department of Bioengineering, Stanford University, Stanford, CA 94305, USA. ²Center for Biomedical Ethics and Society, Vanderbilt University, Nashville, TN 37232, USA.

³Department of Pediatrics, Children's Hospital Boston, Boston, MA 02115, USA. ⁴Department of Biomedical Informatics, Vanderbilt University, Nashville, TN 37232, USA. ⁵Department of Medicine, Vanderbilt University, Nashville, TN 37232, USA.

*To whom correspondence should be addressed. E-mail: b.malin@vanderbilt.edu

References

1. K. El Emam, E. Jonker, L. Arbuckle, B. Malin, *PLoS ONE*, **6**, e28071 (2011).
2. M. A. Jobling, *Trends Genet.* **17**, 353 (2001).
3. I. Sample, "Teenager finds sperm donor dad on Internet," 2 November 2005; www.guardian.co.uk/science/2005/nov/03/genetics.news.

Data Re-Identification: Protect the Children

IN THEIR POLICY FORUM "THE COMPLEXITIES of genomic identifiability" (18 January, p. 275), L. L. Rodriguez *et al.* correctly point out that in view of the intriguing recent demonstration of the identifiability of donors participating in genomic studies ("Identifying personal genomes by surname inference," M. Gymrek *et al.*, Reports, 18 January, p. 321), the research community needs to optimize the balance between the need for data sharing and respect for the privacy of research participants.

In our 2009 *Science* Policy Forum (1), we proposed specific measures to improve the current policies and provide greater protection for children. Children are among the most vulnerable populations whose DNA samples are being collected in large numbers for epidemiologic studies. Sadly, it seems that our suggestions have not led to distinct biobanking policies for children.

We reiterate our 2009 call for the scientific research community to agree on extra safeguards, particularly restrictions on sharing

the individual genome sequences of children, unless they are contacted again as adults and provide their own consent at that time. In the case of fatal pediatric disease research (when obtaining adult and consented donor samples is implausible), conditions for sharing the personal genome sequences of children could be eased. In spite of the current genetic non-discrimination legislation widely enacted, our duty remains to ensure extra privacy protections for children, balanced with the need to continue research on pediatric diseases.

DAVID GURWITZ

Human Molecular Genetics and Biochemistry, Sackler Faculty of Medicine, Tel Aviv University, Tel Aviv, 69978, Israel. E-mail: gurwitz@post.tau.ac.il

Reference

1. D. Gurwitz, I. Fortier, J. E. Lunshof, B. M. Knoppers, *Science*, **325**, 818 (2009).

TECHNICAL COMMENT ABSTRACTS

Comment on "Lethally Hot Temperatures During the Early Triassic Greenhouse"

N. Goudemand, C. Romano, A. Brayard, P. A. Hochuli, H. Bucher

Sun *et al.* (Reports, 19 October 2012, p. 366) reconstructed Permian to Middle Triassic equatorial seawater temperatures. After correct temporal positioning of their data points, their presumed trends of temperature changes, and hence their assumption of a one-to-one relationship between putative "lethally hot" seawater temperatures and a disputable equatorial "eclipse" of some organisms, are no longer supported by their data. Full text at <http://dx.doi.org/10.1126/science.1232924>

Response to Comment on "Lethally Hot Temperatures During the Early Triassic Greenhouse"

Yadong Sun, Michael M. Joachimski, Paul B. Wignall, Chunbo Yan, Yanlong Chen, Haishui Jiang, Lina Wang, Xulong Lai

Goudemand *et al.* replotted a subset of our well-constrained data using a new Early Triassic biostratigraphic scheme based on a lower-resolution ammonoid zonation scheme and hypothetical ammonoid-conodont correlation to produce a less distinct seawater temperature history. We dispute their unsubstantiated correlation and, consequently, their allegations.

Full text at <http://dx.doi.org/10.1126/science.1233090>

CORRECTIONS AND CLARIFICATIONS

Perspectives: "Toward molecular-scale MRI" by P. Hemmer (1 February, p. 529). The caption should say "a single NV inside a diamond nanocrystal is used to image a ribosome in the act of translation inside a live cell." A ribosome translates genetic information; it does not transcribe it. The HTML and PDF versions online have been corrected.

News & Analysis: "Final report on Stapel also blames field as a whole" by M. Enserink (7 December 2012, p. 1270). The story incorrectly stated that the committee that investigated another social psychologist, Dirk Smeesters of Erasmus University in Rotterdam, looked at only three of Smeesters' papers. The panel applied a statistical test based on work by Uri Simonsohn to experiments in every paper for which Smeesters had control over the data and to which the test was applicable—a total of 22 experiments in 10 papers. Simonsohn's test suggested data manipulation in three papers, which were investigated in more detail. The committee also investigated data files for two studies and found both to be suspicious. The HTML version online has been corrected.

Letters to the Editor

Letters (~300 words) discuss material published in *Science* in the past 3 months or matters of general interest. Letters are not acknowledged upon receipt. Whether published in full or in part, Letters are subject to editing for clarity and space. Letters submitted, published, or posted elsewhere, in print or online, will be disqualified. To submit a Letter, go to www.submit2science.org.

BIOGRAPHY

From the Sea to *Silent Spring*

Frederick R. Davis

The 50th anniversary of the publication of Rachel Carson's *Silent Spring* (1) has come and gone like the tide, and some of us are left wondering how this momentous event could have passed with so little fanfare. By contrast, the bicentennial of Darwin's birth saw considerably more than a year of celebrations all over the world, popular and scholarly alike. But, befitting the temperament of its author (who generally avoided the glare of celebrity), *Silent Spring*'s anniversary caused barely a ripple.

Fortunately, writer William Souder marked the occasion with a new biography: *On a Farther Shore: The Life and Legacy of Rachel Carson*. Readers familiar with Carson's story from earlier accounts will want to know what is novel about Souder's treatment of this iconic figure in the history of the American environmental movement. Souder skillfully situates Carson's life and particularly her writing career into the context of important events in the United States and around the world. More to the point, Souder's Carson is a portrait of the writer and, significantly, her writerly influences. Finally, Souder carefully analyzes Carson's personality and relationships.

For example, Carson found inspiration in the works of English nature writers Henry Williamson and Richard Jefferies and of the Dutch-born children's author Hendrik van Loon. Souder reveals that Carson could be selective in her appreciation, praising Williamson's books on nature while ignoring his well-documented Nazi sympathies. In van Loon, Carson found an enthusiastic correspondent and supporter, and she called on the prominent author to introduce her to the renowned deep-sea explorer William Beebe. Carson also solicited van Loon's advice on the mundane details of book publishing, such

as royalties and advances.

Souder plumbs the depths of Carson's personality and explains apparent tensions. Widely portrayed as quiet and shy, Carson revealed herself to be a keen judge of character and a sharp wit to her close friends. Her letters to editors and publishers display her complete confidence in her considerable skills as a writer and naturalist along with her willingness to defend and promote herself and her abilities (particularly when her

finances were at stake). Carson's agent Marie Rodell became her champion and advocate in all things literary and financial. Rodell negotiated with the *New Yorker* on Carson's behalf, opening a long and prosperous relationship with that leading literary weekly and its editor William Shawn. To Carson's delight, Shawn published much of *The Sea Around Us* (2) across three issues before its release in book form. *Silent Spring* also made its debut in the pages of the *New Yorker*.

While Carson enjoyed the support of her literary colleagues, she also cultivated a small circle of devoted friends. In analyzing a series

breadwinner shortly after leaving graduate school at Johns Hopkins. After his mother's unexpected death, Carson assumed parental responsibilities for her niece's son, Roger. The tasks of supporting her relatives defined her choices in life. After the publication of *Silent Spring*, misogynistic attacks on its author as a "spinster" mischaracterized someone utterly dedicated to family, albeit nontraditional.

Focused on Carson qua writer, Souder shrewdly divides his account into two roughly equal parts: the sea and *Silent Spring*. Such a division circumvents chronological and temporal imbalances. Carson's legacy seems to be evenly divided between her writings on the sea and pesticides. Nevertheless, Souder captures the full extent of Carson's long-term interest in the unintended consequences of synthetic insecticides. He also demonstrates how knowledge of marine ecology served her larger effort to reveal the parallels between the environmental effects of radioactive fallout and indiscriminate use of pesticides. Thus, in one of many dramatic reconstructions, Souder recounts the tragic story of the crew of the *Lucky Dragon* in the aftermath of exposure to the fallout of nuclear testing on Bikini Atoll in the South Pacific. By tracing the development of nuclear arms during and after World War II and the parallel development of chemical insecticides across the same period, Souder foreshadows the process whereby Carson drew the most powerful analogy of *Silent Spring*. Her compelling comparison of pesticides to nuclear fallout captivated the minds of Americans in the early years of the nuclear age. As memories of the arms race fade, a new generation of readers should find such context clues help to explain Carson's inspiration and the profound impact of *Silent Spring*.

There is another sense in which *On a Farther Shore* constitutes a writer's biography. Souder has crafted a beautifully written account of Carson's life. Even when the stories ring familiar, his deft turn of phrase imbues them with new vitality. Thus, he offers readers a wonderful opportunity to celebrate a naturalist, author, and inspiration to the modern environmental movement.

offers readers a wonderful opportunity to celebrate a naturalist, author, and inspiration to the modern environmental movement.

References

1. R. Carson, *Silent Spring* (Houghton Mifflin, Boston, 1962); reviewed in (3).
2. R. Carson, *The Sea Around Us* (Oxford Univ. Press, New York, 1951).
3. I. L. Baldwin, *Science* **137**, 1042 (1962).

On a Farther Shore
The Life and Legacy of
Rachel Carson
by William Souder
Crown, New York, 2012.
515 pp. \$30, C\$35.
ISBN 9780307462206.



of impassioned letters, Souder delineates the extent of Carson's most intense relationship, with Dorothy and Stan Freeman. Souder argues that Carson shared with Dorothy a love of nature, the sea, music, and literature, which is to say the beautiful aspects of life associated with the highest category of Platonic love. Carson also remained devoted to her family (especially her mother, two nieces, and a great nephew) throughout her life. She became its

The reviewer is at the Department of History, Florida State University, Tallahassee, FL 32306-2200, USA. E-mail: fdavis@fsu.edu

BIOLOGY AND PHILOSOPHY

Are Species Special?

P. William Hughes

With the 12 June 2012 death of Lonesome George, the last known full-blooded Pinta Island tortoise (*Chelonoidis nigra abingdonii*), his subspecies apparently became extinct. [However, there is DNA evidence from intraspecific hybrids suggesting that some undiscovered individuals survive in the wild (1).] George's situation caught the public eye; condemned to solitude, he became a symbol of the grim fate that may await many threatened species. Intuitively, we feel that species (and subspecies) are valuable, that it is good that they persist naturally, and that wantonly destroying them is not ethically permissible. But unlike Lonesome George, *C. n. abingdonii* cannot suffer or feel harm—so what ethical status can we attribute to it? In *The Ethics of Species: An Introduction*, philosopher Ronald Sandler (Northeastern University) draws on virtue ethics to construct and apply a systematic account of the value of species.

Sandler begins by working through what species are. (He operationally defines them as “groups of biologically related individuals that are distinguished by their form of life.”) He next considers what kind of value species are thought to have (distinct from the value of the individuals among them) and the applicability of these values for biology. Sandler follows these examinations with two longer sections, in which he applies his account to real-world scenarios: to species conservation and to a discussion of species boundaries. Overall, the author makes a worthy addition to a burgeoning subfield of bioethics, although in applying his conception of species value he reaches several unusual conclusions. Here, I'll introduce Sandler's argu-

ments in favor of the value of species and note briefly how he uses them in his considerations of conservation biology and species boundaries.

The book's principal contribution lies in Sandler's justification of why and how species have value. From the start, the fact that he writes as a virtue ethicist is crucial. Virtue ethics (historically associated with Aristotle) is oriented toward understanding (and imbuing) capacity-based virtues that enable flourishing relative to some fixed teleological



Conservation icon. Lonesome George, long considered the last member of the Pinta Island subspecies of Galápagos tortoise.

“good.” It contrasts with the other principal bioethical approaches: utilitarianism (maximizing happiness and reducing suffering; associated with Jeremy Bentham, John Stuart Mill, and, more recently, Peter Singer) and deontology (obligation-based ethics; associated with Immanuel Kant).

Sandler argues that living individuals (human and nonhuman alike) have an etiological “good of their own,” which is such that “we ought to care about their good for their own sake.” He considers these two qualities as providing sufficient grounds to confer objective value. His account differs importantly from other definitions of inherent worth found in bioethics, which often measure nonhuman species in terms of qualities specific to humans (e.g., sentience). Sandler holds that “there is no non-question-begging reason why the capacities that are crucial to our [human] form of life (or the form of life of any other species, for that matter) should be the standard for whether members of other species have inherent worth.”

In contrast with the ethical status of individuals, Sandler explains, species do not have a good of their own and thus lack inherent worth. He argues instead that species pos-

sess value because either they have subjective value (i.e., they are perceived by us as beautiful, impressive, or otherwise worthy of consideration) or they have instrumental value (i.e., they are valued for what they do, usually in terms of their ecological role within a functional ecosystem). Sandler also maintains that these two types of value are not equal for all species. For instance, those species vital to the well-being of an ecosystem have a good deal of instrumental value, whereas others may have little or none at all. Sorting out the normative value of any particular species is therefore complicated, requiring case-by-case evaluation.

Interestingly, Sandler's application of his account of species' value leads him to some conclusions that fall well outside mainstream opinion. With respect to conservation biology, Sandler argues against most forms of ecological restoration and assisted colonization (claiming that the justifications for both are undermined by climate change) and also against the reintroduction of (cloned) extinct species such

as the woolly mammoth. Sandler's account supports in situ preservation of threatened species (about which he remains optimistic), but he does contend that species preservation is often overemphasized as an ethical imperative. In discussing species boundaries, Sandler reaches even more controversial conclusions. He maintains that species boundaries are not inviolable and that nearly any form of transgenic organism (part-human or not) is morally permissible. Sandler argues transparently and fairly, and his case is often very persuasive. (E.g., Sandler capably dismisses the “argument from nature” as an objection to the existence of transgenic species.) Given how novel his conclusions are, his success is impressive.

Sandler addresses problems intuitively familiar to us—what species are and why we value them—in an intellectually rigorous and engaging manner. Although at times plodding and dense, his account is developed well. For the philosophically inclined, *The Ethics of Species* provides a readable and comprehensive perspective on current ethical analysis of species, transgenics, and conservation biology.

References

1. M. Russello et al., *Curr. Biol.* **17**, R317 (2007).

The Ethics of Species

An Introduction

by Ronald L. Sandler

Cambridge University Press,
Cambridge, 2012. 245 pp.

\$85, £50.

ISBN 9781107023468.

Paper, \$29.99, £18.99.

ISBN 9781107658707.

The reviewer is at the Department of Biology, 227 Nesbitt Building, Carleton University, 1125 Colonel By Drive, Ottawa, ON K1S 5B6, Canada. E-mail: william_hughes@carleton.ca

RESEARCH FUNDING

A Framework for Decisions About Research with HPAI H5N1 Viruses

Amy P. Patterson,¹ Lawrence A. Tabak,¹ Anthony S. Fauci,¹ Francis S. Collins,¹ Sally Howard²

Since it appeared in Hong Kong in 1997, the highly pathogenic avian influenza (HPAI) H5N1 virus has presented a persistent threat to public health and agriculture. Worldwide, hundreds of millions of birds have died as a result of infections or culling to prevent further spread of outbreaks among domestic flocks (1). HPAI H5N1 has caused severe respiratory illness and death in a relatively small number of humans—primarily those who have worked in direct contact with infected poultry (2). Of the ~600 laboratory-confirmed human cases from 2003 to the present, nearly 60% were fatal. At present, the virus does not appear well-adapted for sustained transmission among mammals by respiratory droplets. However, if the viruses occurring in nature were to become readily transmissible among mammals, they could pose the risk of a pandemic.

Research aimed at understanding the host adaptability and transmission of HPAI H5N1 virus is a public health imperative. Internationally, scientists are seeking insights that will enable more effective surveillance capabilities, vaccines, and therapies, as well as a foundation for innovative public health solutions in the future.

In 2011, two studies funded by the National Institutes of Health (NIH), which examined mammalian transmissibility of HPAI H5N1, generated controversy (3, 4). Using a “gain-of-function” approach, researchers engineered HPAI H5N1 viruses to render them transmissible by respiratory droplets among ferrets, an animal commonly used to model human influenza infection. These studies provided critical information to scientists and public health officials by demonstrating that HPAI H5N1 viruses can mutate to enable them to spread efficiently

among certain mammals and, therefore, perhaps among humans. However, the generation of these strains raised safety and security concerns centered on whether the engineered strains could be released accidentally or used nefariously to threaten public health or national security. They triggered a global discussion regarding the benefits and risks of funding, conducting, and publishing these types of gain-of-function studies.

As a result, members of the influenza research community initiated a voluntary moratorium on gain-of-function studies involving HPAI H5N1 mammalian transmissibility (5, 6). This pause allowed for intense discussions of the risks and benefits

The U.S. Department of Health and Human Services unveils a Framework for funding decisions about highly pathogenic avian influenza H5N1 research.

guiding funding decisions on individual proposals involving HPAI H5N1 research with specific attributes. The Framework aims to ensure a robust review of research proposals—before making a funding decision—that considers the scientific and public health benefits of the proposal, the biosafety and biosecurity risks associated with the proposal, and the appropriate risk mitigation measures required for such research. In November 2012, a draft version of this Framework was presented to the National Science Advisory Board for Biosecurity (NSABB) for its consideration and subsequently posted for public comment.

HHS also sought international and multidisciplinary perspectives at a workshop held in Maryland on 17 and 18 December 2012 (9). Participants discussed the risks and benefits of HPAI H5N1 gain-of-function research, the biosafety conditions that should be in place for conducting such research, and the importance of international cooperation in preventing future pandemics. Some expressed concerns that the information generated by this research could enable others to replicate the studies under less-than-ideal biosafety conditions

or for malevolent purposes. Although it was generally noted that gain-of-function studies will provide important scientific insights, there was debate over how readily and directly this information can be applied to vaccine development or surveillance efforts, at least in the near term.

Commenters noted that while gain-of-function experiments that enhance virulence or alter host range of HPAI H5N1 are concerning, it is conferring the ability to efficiently spread among mammals by respiratory droplets that raises the most concern and warrants special consideration prior to funding. This and other input was instrumental in finalizing the HHS Framework. In developing the Framework, HHS has considered several key questions: Is this subset of gain-of-function experiments necessary to address the public health threat

CRITERIA FOR GUIDING HHS FUNDING DECISIONS FOR CERTAIN H5N1 GAIN-OF-FUNCTION RESEARCH PROPOSALS

- Such a virus could be produced through a natural evolutionary process.
- The research addresses a scientific question with high significance to public health.
- There are no feasible alternative methods to address the same scientific question in a manner that poses less risk than does the proposed approach.
- Biosafety risks to laboratory workers and the public can be sufficiently mitigated and managed.
- Biosecurity risks can be sufficiently mitigated and managed.
- The research information is anticipated to be broadly shared in order to realize its potential benefits to global health.
- The research will be supported through funding mechanisms that facilitate appropriate oversight of the conduct and communication of the research.

associated with the research and provided governments and other funding organizations an opportunity to develop appropriate oversight policies. The moratorium was initially intended to last 60 days but was extended for 1 year. Recently, the signatories have announced an end to the moratorium for scientists with appropriate facilities and national oversight (7). They urged scientists to continue the research pause if they are working in countries that had not yet finalized the appropriate conditions for conducting HPAI H5N1 transmission research.

The U.S. Department of Health and Human Services (HHS) has grappled with the challenge of how best and, indeed, whether to support certain types of HPAI H5N1 gain-of-function research (8). Toward this end, HHS has developed a Framework (www.phe.gov/S3/dualuse) for

¹National Institutes of Health, Bethesda, MD 20892, USA.

²Department of Health and Human Services, Washington, DC 20201, USA.

*Author for correspondence. E-mail: pattersa@od.nih.gov

posed by HPAI H5N1 viruses? Would discontinuing this type of research introduce new risks by compromising our ability to prepare for and respond to influenza outbreaks? Should such research be supported by HHS and its funding agencies? If so, under what biosafety conditions should this research be conducted? In considering these questions, a number of important principles have emerged.

First, open communication of research methodologies and results is a hallmark of the life sciences and of the research that HHS and its agencies support. Widespread dissemination of research results allows rapid and sustained scientific progress and facilitates full realization of the associated public health benefits. As hypotheses and conclusions are validated or repudiated, our knowledge base is expanded, laying the foundation for new therapeutics and other applications. Therefore, HHS will only fund research that is reasonably anticipated, at the proposal stage, to generate information that can be broadly shared and openly communicated.

Second, HPAI H5N1 research involving transmission among mammals by respiratory droplets must address a scientific question with high significance to public health. HHS is a strong supporter of fundamental research, which may add to our understanding of basic biological processes and often contributes to new innovations and technologies. However, because HPAI H5N1 gain-of-function research of this type may involve a higher level of risk than other areas of study, it is important that the fundamental questions to be addressed by the research not only have high scientific merit but can be reasonably anticipated to generate information that will ultimately advance public health. Before committing to a gain-of-function approach that brings with it certain risks, researchers should explore alternative methods for addressing the same scientific question in a manner with the fewest attendant risks.

Third, the biosafety and biosecurity risks associated with a research project must be manageable. With its principal mission to protect and promote public health, HHS must, out of necessity, support some scientific research that involves a certain level of inherent risk but that is nevertheless essential for our health and well-being. Furthermore, HHS should only support proposals through funding mechanisms that allow implementation of additional risk mitigation measures as appropriate.

Like all proposals submitted to HHS

funding agencies, HPAI H5N1 gain-of-function proposals are subjected to peer review to assess scientific merit. In addition, this research falls within the scope of the *U.S. Government Policy for the Oversight of Life Sciences Dual Use Research of Concern* and thus undergoes an initial and periodic review for dual use potential (10). The new HHS Framework requires additional funding agency and department-level review for research proposals that are anticipated to generate HPAI H5N1 viruses transmissible among mammals by respiratory droplets.

The Framework lists seven criteria (see the table), all of which must be met for such research proposals to be acceptable for HHS funding. The funding agency will assess whether proposed research meets these criteria and, if so, will submit the proposal for additional HHS-level review. The department-level review will bring to bear multidisciplinary expertise—including public health, scientific, security, intelligence, and countermeasures—in assessing the risks and benefits of the proposal and will also consider the proposal within the context of the broader HHS influenza research portfolio. Other federal departments and agencies; external advisory bodies—such as the NSABB, the NIH Recombinant DNA Advisory Committee (RAC), and the National Biodefense Science Board; and nongovernmental experts—may be consulted. The department-level review will determine the appropriate risk mitigation measures and whether a given proposal is acceptable for HHS funding. Research proposals that do not meet the seven criteria or involve risks that cannot be adequately mitigated will not receive HHS funding. Characterization studies of naturally occurring H5N1 viruses are not subject to this review Framework.

HPAI H5N1 research, in common with other life-sciences research, is subject to guidelines, policies, laws, and international agreements that govern biosafety, physical security, personnel reliability, informational risks, and nonproliferation (11). Such oversight is aimed at managing risks throughout the course of the research. Risks associated with infectious disease research cannot be eliminated entirely. However, they can be managed, and as the risk-benefit landscape changes, our policy response must also change as necessary. In this regard, the Centers for Disease Control and Prevention has sought public comment regarding whether certain HPAI H5N1 viruses should be regulated as an HHS Select Agent, as well as whether any special precautionary measures (i.e., biosafety containment and practices)

are necessary (12).

The NIH RAC has also recently recommended additional enhancements to biosafety level 3 containment and practices for work with HPAI H5N1 viruses that are transmissible among mammals by respiratory droplets (13). The *NIH Guidelines for Research Involving Recombinant DNA Molecules* (14) have been amended to include these measures.

Science is unpredictable, and not all research results can be anticipated. The HHS Framework aims to ensure consideration, at the outset, of gain-of-function research proposals that may generate HPAI H5N1 viruses that are transmissible among mammals by respiratory droplets and to make the most-informed decisions possible about whether and how to support and conduct this research. The HHS Framework will be evaluated over time and adapted to ensure that critical research needs are being met and that risks are managed appropriately. HHS will continue to engage in the collective global effort to identify the best path forward so that important research addressing this critical public health concern can continue in the most responsible manner possible.

References

1. Food and Agriculture Organization, H5N1 Highly Pathogenic Avian Influenza—Global Overview (FAO, Rome, 2012); www.fao.org/docrep/015/an388e/an388e.pdf.
2. Centers for Disease Control and Prevention, Highly Pathogenic Avian Influenza A (H5N1) in People; www.cdc.gov/flu/avianflu/h5n1-people.htm.
3. S. Herfst *et al.*, *Science* **336**, 1534 (2012).
4. M. Imai *et al.*, *Nature* **486**, 420 (2012).
5. R. A. M. Fouchier, A. García-Sastre, Y. Kawaoka, *Nature* **481**, 443 (2012).
6. R. A. M. Fouchier *et al.*, *Science* **335**, 400 (2012).
7. R. A. M. Fouchier, A. García-Sastre, Y. Kawaoka, *Nature* **493**, 609 (2013).
8. HHS, www.hhs.gov.
9. Gain-of-Function Research on Highly Pathogenic Avian Influenza H5N1 Viruses: An International Consultative Workshop, Bethesda, Maryland, 17 to 18 December 2012; <http://oba.od.nih.gov/biosecurity/internationalwebcast.html#Dec2012>.
10. Office of Biotechnology Activities, NIH, *U.S. Government Policy for Oversight of Life Sciences Dual Use Research of Concern*, 29 March 2012; www.phe.gov/s3/dualuse/Documents/us-policy-durc-032812.pdf.
11. Report of the Trans-Federal Task Force on Optimizing Biosafety and Biocontainment Oversight (HHS, Washington, DC, 2009), pp. 40–67; www.phe.gov/Preparedness/legal/boards/biosafetytaskforce/Documents/transfedbiocontainmentrpt092009.pdf.
12. Centers for Disease Control and Prevention (CDC) HHS, *Fed. Regist.* **77**(201), 63783 (2012).
13. RAC meetings, http://oba.od.nih.gov/rdna_rac/rac_past_meetings_2010.html.
14. *NIH Guidelines for Research Involving Recombinant DNA Molecules* (NIH, HHS, Washington, DC, 2013), http://oba.od.nih.gov/rdna/nih_guidelines_oba.html.

10.1126/science.1236194

CONSERVATION

Legal Trade of Africa's Rhino Horns

Duan Biggs,^{1*} Franck Courchamp,² Rowan Martin,³ Hugh P. Possingham¹

Africa's western black rhino *Diceros bicornis longipes* was declared extinct by the International Union for the Conservation of Nature (IUCN) in 2011. Africa's other rhino populations are also under siege. South Africa is home to more than 90% of the world's 20,000 white rhino *Ceratotherium simum*, and 40% (more than 80% together with its neighbor Namibia), of the 5000 remaining black rhino (1–3). Yet, poaching in South Africa has, on average, more than doubled each year over the past 5 years (see the chart). If poaching continues to accelerate, Africa's remaining rhino populations may become extinct in the wild within 20 years (4, 5).

Because of the CITES (Convention on the Trade of Endangered Species) ban on the trade of rhino horn, in place since 1977, demand can only be met through the illegal market, which primarily relies on the killing of rhinos by poachers for their horns (6). The ban is failing because it artificially restricts supply in the face of persistent and growing demand (4, 7). The only remaining option is a carefully regulated legal trade based on the humane and renewable harvesting of horn from live white rhinos. Provincial conservation agencies in South Africa and southern African rhino management groups have asked the South African government to put forward a proposal for regulated international trade in rhino horn at the 16th CITES Conference of the Parties (COP-16), held 3 to 14 March 2013.

Why the Trade Ban Has Failed

Skyrocketing poaching levels are driven by tremendous growth in the retail price of rhino horn, from around \$4,700 per kilogram in 1993 (8) to around \$65,000 per kilogram in 2012 (9). Rhino horn is now worth more, per unit weight, than gold, dia-

monds, or cocaine. Robberies of horns from museum specimens across Europe have taken place (10). Even dehorning rhinos to reduce the incentive to poach has proven ineffective without the provision of additional security, because of the value of the remaining horn stubs (11).

Rhino horn is used for dagger handles in Yemen and has been used in Chinese traditional medicine for millennia as a presumed cure for a wide range of ailments (10). Rapid economic growth in east and southeast Asia is assumed to be the primary factor driving the increased demand for horn (12). The tremendous financial rewards have led poachers to use increasingly sophisticated technologies, including helicopters and immobilization darts. The protection of rhinos has therefore become increasingly expensive not only in financial terms but in human lives (13). The increased militarization of rhino protection

A trade ban limits supply, therefore raising prices and driving black market poaching.

Stronger enforcement efforts will be further hampered by the cooption of corruptible government officials by crime syndicates in a very lucrative illegal trade (17, 19). Furthermore, as wildlife products, such as rhino horn, become rarer, their prices soar, which pushes them ever further into an economic supply-and-demand extinction vortex (10, 17, 20).

Humane, Renewable Harvest and Legal Trade

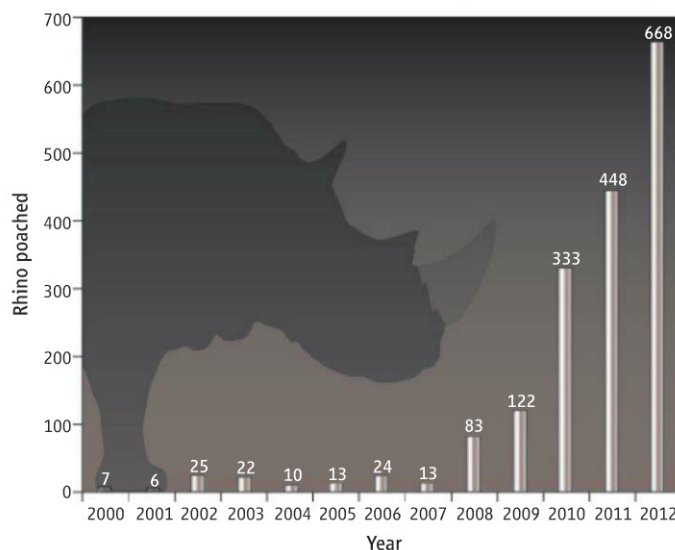
Rhino horn is composed entirely of keratin and regrows when cut. Sedating a rhino to shave its horn can be done for as little as \$20. The annual horn production of one white rhino averages 0.9 kg per year (11). The current speculative estimates of the demand for horn based on the illegal supply (21) could therefore be met by the 5000 white rhinos on private conservation land in South Africa alone. The natural death rate of rhinos of 2.6% would also provide hundreds of horns annually. The

income generated for conservation through a legal trade in rhino horn, accounting for the costs of dehorning and management, is substantial (4). In addition, with current technology, the risks to rhinos from dehorning are minimal, and there is limited evidence of significant behavioral change following dehorning (11). A legal trade could simultaneously supply horns, fund rhino protection, and provide an incentive for their sustainable use and long-term survival. The trade in crocodile skin is an example of how a legal market has reduced poaching pressure on wild populations (22).

Evidence from studies of other wildlife products [e.g., (23–28)] suggests that a legal trade can

reduce the incentive for poaching if: (i) regulators can prevent the laundering of a threatening level of illegal supply under the cover of a legal trade; (ii) the legal supply can deliver the product (horn) more easily, reliably, and cost-effectively than the illegal trade; (iii) the demand does not escalate to dangerous levels as the stigma associated with the illegality of the product is removed; and (iv) legally harvested horns from live animals can substitute for horns obtained from wild, poached animals.

A highly regulated legal trade based on the renewable cropping of horns from rhinos is



Annual rhino poaching in South Africa since 2000. Data from (2, 3).

has resulted in a reallocation of conservation resources and is adversely affecting other conservation actions (14, 15).

Moreover, higher levels of militarized enforcement of a trade ban with harsher penalties may only serve to drive up prices further because supply is restricted in the face of inelastic and growing demand (4). This will create more profitable opportunities for crime syndicates and increase the incentives for poachers, as has been demonstrated in attempts to ban or control alcohol, illicit drugs, and other wildlife products (16–18).

¹Australian Research Council Centre of Excellence for Environmental Decisions, Centre for Biodiversity and Conservation Science, University of Queensland, Brisbane, Queensland 4072, Australia. ²Ecologie, Systematique et Evolution, Universite Paris-Sud, UMR CNRS 8079, Orsay, France. ³Independent Consultant, Harare, 00263, Zimbabwe.

*Author for correspondence. E-mail: ancientantwren@gmail.com

likely to succeed if these conditions are met (7, 21, 23, 29). First, the technology exists to track the legality of individual horns through the selling chain to the end consumer to minimize laundering and the illegal trade (4). Each legal rhino horn traded can carry a small traceable transponder and have a recorded DNA signature (for less than \$200 per horn), which remains identifiable through the market chain to the buyer (4). Second, accounting for land, management, and horn-harvesting costs, the cost-effectiveness, reduced risk, and lower transaction costs associated with a legal trade are likely to attract buyers away from the illegal market (4, 30). Third, an increase in demand for horn once it is legalized (23) would imply a success of the market. This demand could be met by an increase of the supply through a growing rhino population. White rhino populations increase at 8% per annum if provided with appropriate savannah habitat (31). Therefore, as a financially valuable umbrella species, an increase in land managed for white rhino will enable the conservation of accompanying biodiversity and will generate revenue for rural communities (4, 7).

Central Selling Organization

One option for the implementation of a highly regulated trading system is through a Central Selling Organization (CSO). A CSO would negotiate and manage the selling of horns so that it is more attractive, reliable, and cost-effective for buyers to obtain the product legally than through illegal means (28). A CSO would be supported by and accountable to the white rhino range states, and the CITES COP (which includes governments of demand countries) for its performance. CITES is already in the process of evaluating a CSO for the management of ivory sales (28). It could be funded by a percentage from each horn sold and could ensure that the proceeds from rhino horn are channeled toward enforcement of the legal trade, that horn harvesting is humane and renewable, and that financial benefits are returned to landholders and communities where rhino occur.

A CSO can be structured to manage the uncertainties and risks that may emerge from a legal trade in four ways (4, 28). First, the CSO should be the only authority that can legally sell horns to registered buyers. Buyer's stockpiles should be subject to regular audits, and they should commit to processing all horn themselves. As proposed for the ivory CSO, a short and closely monitored market chain can be more effectively controlled, so as to limit the incentives for speculation and hoarding and to reduce the risk of corruption, because it will

be difficult to circumvent the controls (28). Second, at the onset of a legal market, sales of the 15 to 20 tons of stockpiled horns held in South Africa (13) could be used to attract buyers to the legal trade and away from the black market. Later sales can be used to dampen the price of horn should it escalate dangerously.

Third, the CSO should work in partnership with the governments of demand countries to ensure that strong penalties are enforced for any buyers who operate outside of the legal market. Fourth, a monitoring system, funded by the CSO, is required to develop an understanding of the market for horn. This will enable the adaptive management of the CSO and the trade. There is currently limited data on the market for horn because of the trade ban, and through monitoring and studying a legal trade, an understanding of the market characteristics will emerge (4). If a legal trade in horn leads to an unexpected and dangerous upsurge in poaching, the legal trade can be restructured or closed down. With these safeguards, a carefully regulated, adaptively managed legal trade is more likely to lead to the successful conservation of Africa's rhino than the current trade ban.

Opponents of a legal trade in rhino horn argue that the bulk sales of ivory by countries in southern Africa lead to increased poaching elsewhere on the continent (32). Yet, there is no conclusive empirical evidence that supports this (28, 33). Moreover, the ivory sales take place too infrequently and unpredictably to attract buyers away from the illegal market and to reduce poaching pressure (28).

Attempts to suppress the supply of horns through the CITES trade ban are failing in Africa (7). A legal trade in rhino horn was first proposed two decades ago but rejected at COP-8 as premature on the grounds that the problem lay with insatiable demand from importing countries (33–35). Yet, education, enforcement, protection, and awareness efforts aimed at reducing the use of horn have all demonstrably failed to turn the tide of this rising demand (4, 10). Legitimizing the market for horn may be morally repugnant to some, but it is probably the only way to prevent extinction of Africa's remaining rhino, as demonstrated by the successful legal trade in crocodile skin (21). As primary custodian of Africa's rhino, the South African and Namibian governments should take leadership to enable serious consideration of a highly regulated legal trade as soon as possible.

References and Notes

1. IUCN, IUCN Red List of Threatened Species (IUCN, Gland, Switzerland, 2011).
2. F. Mketeni, South Africa Department of Environmental Affairs: Rhino Poaching—Government interventions presentation, public hearing on 26 January 2012; www.pmg.org.za/report/20120126-public-hearings-solutions-rhino-poaching-culling-old-bull-elephants-k.

3. Department of Environmental Affairs, South Africa; www.environment.gov.za/?q=content/rhino_poaching_statistics.
4. R. Martin, *A Legal Trade in Rhino Horn: Hobson's Choice* (Rhino Survival Trust, Johannesburg, South Africa, 2012).
5. S. M. Ferreira et al., *PLoS ONE* 7, e45989 (2012).
6. N. Leader-Williams, *World Trade in Rhino Horn: A Review* (TRAFFIC International, Cambridge, 1992).
7. B. Child, *S. Afr. J. Sci.* 108, 21 (2012).
8. J. Loh, K. Loh, *TRAFFIC Bull.* 14, 55 (1994).
9. L. Marshall, *Newsweek*, 11 December 2012; <http://newsweek.nationalgeographic.com/2012/12/11/record-618-south-african-rhinos-poached-for-horns-in-2012-so-far/> (2012).
10. K. Nowell, *Species Trade and Conservation: Rhinoceroses: Assessment of Rhino Horn as a Traditional Medicine* (CITES Secretariat, on behalf of TRAFFIC, Geneva, 2012).
11. P. A. Lindsay, A. Taylor, A study on the dehorning of African Rhinoceroses as a tool to reduce the risk of poaching (Endangered Wildlife Trust and the South African Department of Environmental Affairs, Johannesburg, South Africa, 2011).
12. CITES, Conservation of and trade in African and Asian Rhinoceroses—61st meeting of the standing committee, Geneva, 15 to 19 August 2011.
13. T. Milliken, J. Shaw, The South Africa–Viet Nam rhino horn trade nexus: A deadly combination of institutional lapses, corrupt wildlife industry professionals and Asian crime syndicates (TRAFFIC, Johannesburg, 2012).
14. S. Ferreira, B. Okita-Ouma, *Pachyderm* 51, 52 (2012).
15. South African National Parks Annual Report 2011–12, www.sanparks.org/assets/docs/general/annual-report-2012.pdf.
16. P. Rivalan et al., *Nature* 447, 529 (2007).
17. M. Cussen, W. Block, *Am. J. Econ. Sociol.* 59, 525 (2000).
18. B. G. Daly et al., Perspectives on dehorning and legalised trade in rhino horn as tools to combat rhino poaching (Endangered Wildlife Trust, Johannesburg, South Africa, 2011).
19. R. J. Smith et al., *Nature* 426, 67 (2003).
20. F. Courchamp et al., *PLoS Biol.* 4, e415 (2006).
21. T. Milliken, R. H. Emslie, B. Talukdar, African and Asian rhinoceroses—Status, conservation and trade (CoP15 Doc. 45.1 Annex, IUCN Species Survival Commission, Gland, Switzerland, 2009).
22. J. Hutton, G. Webb, in *Crocodiles: Proceedings of the 16th Working Meeting of the Crocodile Specialist Group*, IUCN—The World Conservation Union, Gland, Switzerland, and Cambridge, UK (IUCN, Gland, Switzerland, 2002), pp. 1–10.
23. C. Fischer, *J. Environ. Econ. Manage.* 48, 926 (2004).
24. E. H. Bulte, R. Damania, *Conserv. Biol.* 19, 1222 (2005).
25. C. Fischer, *Rev. Environ. Econ. Policy* 4, 103 (2010).
26. R. Damania, E. H. Bulte, *Ecol. Econ.* 62, 461 (2007).
27. C. Costello et al., *Nature* 481, 139 (2012).
28. R. B. Martin, D. H. M. Cumming, G. C. Craig, S. C. Gibson, D. A. Peake, Decision-making mechanisms and necessary conditions for a future trade in African elephant ivory (SC62 Doc. 46.4, Annex, CITES, Geneva, 2012).
29. G. Brown, D. Layton, in *Protecting Endangered Species in the United States: Biological Needs, Political Realities, and Economic Choices*, J. F. Shogren, J. Tschirardt, Eds. (Cambridge Univ. Press, Cambridge, 2001), pp. 32–50.
30. V. Ruggiero, N. South, I. Taylor, Eds., *The New European Criminology: Crime and Social Order in Europe* (Routledge, London, 1998).
31. R. B. Martin, White Rhino Conservation Strategy for Namibia: Background Study (Ministry of Environment and Tourism, Windhoek, Namibia, 2010).
32. S. Wasser et al., *Science* 327, 1331 (2010).
33. R. W. Burn et al., *PLoS ONE* 6, e24165 (2011).
34. E. J. Milner-Gulland et al., *Proc. Biol. Sci.* 249, 83 (1992).
35. CITES, Eighth meeting of the COP, Kyoto, Japan, 2 to 13 March 1992, Prop. 16–18.

Acknowledgments: M. 't Sas-Rolfes and E. J. Milner-Gulland reviewed an earlier draft. S. Ferreira and D. Pienaar, from South African National Parks, and C. Harper and R. Loon provided valuable insights.

10.1126/science.1229998

Machinery to Reverse Irreversible Aggregates

Helen R. Saibil

Protein misfolding and aggregation would drastically shorten the life of cells were it not for the molecular chaperones that prevent these damaging processes (1). In vitro, aggregation is irreversible under physiological conditions. Remarkably, the cells of bacteria, plants, and fungi have evolved machinery to neatly extract polypeptide chains from large aggregates and refold them to the native state, with little specificity for protein sequence or fold (2–4). Although the components of this machinery are well known, an understanding of how they accomplish disaggregation has been elusive. Several recent studies (5–8), including one by Rosenzweig *et al.* (9) on page 1080 of this issue, identify interaction sites within a chaperone system consisting of an Hsp70 chaperone (bacterial DnaK) and a protein-remodeling adenosine triphosphatase (ATPase) of the AAA⁺ family (bacterial ClpB or yeast Hsp104). Nuclear magnetic resonance (NMR), crystallographic, and biochemical studies reveal a series of molecular toggles that control polypeptide aggregate binding, extraction, threading, and refolding by this bichaperone system.

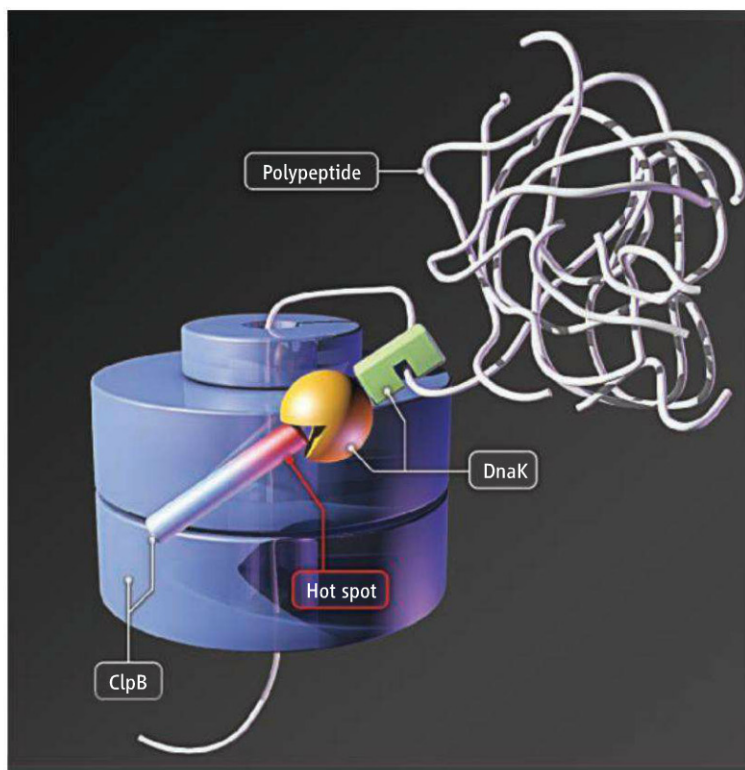
The heat shock protein Hsp70 plays a major role in protein homeostasis, quality control, and the regulation of folding and unfolding. Its nucleotide-binding domain is a highly flexible structure, with two domains that enclose a nucleotide-binding cleft. A linker connects it to the substrate-binding domain, which captures extended polypeptides in a shallow channel that is covered by a mobile lid. In the adenosine 5'-diphosphate (ADP)-bound (or apo) state, the two

domains are not in contact and the lid is closed, but adenosine 5'-triphosphate (ATP) binding favors a docked state in which the substrate-binding domain is wide open and wrapped around different parts of the nucle-

Cells can untangle protein aggregates through an extraction process that unfolds polypeptide.

misfolding, such as Alzheimer's and Parkinson's diseases. ClpB is a three-tiered hexamer with an amino-terminal ring stacked upon two ATPase rings. The three rings surround a central channel, and a long coiled-coil domain that may be docked on the surface of the hexamer (7). Threading of substrates through the channel proceeds from the amino- to carboxyl-terminal rings (11), and ClpB disaggregation activity is sensitive to a mutational "hot spot" (12) at the tip of the coiled-coil domain that is oriented toward the amino terminus.

A chemical cross-link scan has identified ClpB residue glutamine 488, adjacent to the hot spot, as a site in close proximity to DnaK (8). However, a specific complex containing both ClpB and DnaK has not been isolated. Their actions are difficult to disentangle, for two reasons. This system has three different ATPases working together (DnaK and the two ATPase domains of ClpB), and DnaK is required both for targeting substrates to ClpB and for subsequent refolding. A hybrid system engineered to separate these two actions has isolated the step in which



Neat extraction. A model illustrates DnaK association with the ClpB hexamer (stacked ring structure), the extraction of a polypeptide from an aggregate, and its translocation through the ClpB channel. After translocation through ClpB, the polypeptide is refolded by DnaK or by other chaperones.

otide-binding domain. A docked state of DnaK has recently been captured, furnishing details of the allosteric interactions (5, 6) and resembling its yeast relative Hsp110 (10). Like other chaperone ATPases, DnaK is highly dynamic, with transient excursions to and from the docked state.

DnaK by itself cannot extract or unfold proteins from aggregates, but it can work with the ClpB/Hsp104 subfamily of Hsp100 ATPases to accomplish those tasks. The unique ability of these proteins to mediate disaggregation has focused attention on the potential of harnessing such an activity to combat diseases that are linked to protein

DnaK stimulates ClpB. This interaction operates a toggle mechanism in which disaggregation activity is stimulated by release of the hot spot but repressed by its stable binding on the surface of the first ATPase domain of ClpB (7). Thus, the coiled-coil domain of ClpB is a regulator that couples ClpB to DnaK, with its release presumably enabling movements of the ATPase domain that are needed for translocating the polypeptide substrate.

Rosenzweig *et al.* characterized the transient interaction between DnaK and ClpB by methyl-transverse relaxation-optimized spectroscopy NMR using selective label-

ing of methyl groups, and confirmed interatomic distances by paramagnetic resonance enhancement. The coiled-coil hot spot of ClpB lodges in the jaws of the DnaK ATPase domain, inhibiting DnaK nucleotide exchange and activating the ClpB toggle. As part of its chaperone function, activation of DnaK by the nucleotide exchange factor GrpE triggers release of bound substrate into solution. By contrast, during disaggregation, ClpB binding to DnaK reprograms DnaK to hand over its polypeptide substrate for translocation through the ClpB channel (see the figure). Indeed, ClpB and GrpE compete for the same binding site on the DnaK ATPase domain. After translocation through ClpB, the polypeptide is refolded by the DnaK system or by other chaperones such as GroEL. A critical step in the pathway is that the polypeptide must find its way from DnaK to the entrance of the

ClpB channel. A model for the DnaK-ClpB complex with DnaK in the domain-docked state suggests that the substrate-binding site faces away from the ClpB ring. Moreover, ClpB binding to DnaK is not compatible with the docked position of the DnaK helical lid, suggesting that the ClpB interaction may involve a different, as yet undescribed, DnaK domain assembly.

Although the mechanism of polypeptide handover from DnaK to ClpB is still unclear, the mapping of DnaK-ClpB binding interactions and the competition between different binding partners for the DnaK ATPase domain reveal key steps of protein disaggregation in bacteria, plants, and fungi. Mammalian cells appear to have a similar disaggregation activity, but so far no direct homologs of ClpB have been found in animals. Although there is no immediate prospect of combating conditions such as Alzheimer's

disease with a “disaggregase,” these recent studies provide an important advance in understanding the remarkable ability of cells to reverse protein aggregation.

References

1. F. U. Hartl, A. Bracher, M. Hayer-Hartl, *Nature* **475**, 324 (2011).
2. D. A. Parsell, A. S. Kowal, M. A. Singer, S. Lindquist, *Nature* **372**, 475 (1994).
3. J. R. Glover, S. Lindquist, *Cell* **94**, 73 (1998).
4. P. Goloubinoff, A. Mogk, A. P. Zvi, T. Tomoyasu, B. Bukau, *Proc. Natl. Acad. Sci. U.S.A.* **96**, 13732 (1999).
5. R. Kityk, J. Kopp, I. Sinning, M. P. Mayer, *Mol. Cell* **48**, 863 (2012).
6. A. Zhuravleva, E. M. Clerico, L. M. Gierasch, *Cell* **151**, 1296 (2012).
7. Y. Oguchi *et al.*, *Nat. Struct. Mol. Biol.* **19**, 1338 (2012).
8. F. Seyffert *et al.*, *Nat. Struct. Mol. Biol.* **19**, 1347 (2012).
9. R. Rosenzweig, S. Moradi, A. Zarrine-Afsar, J. R. Glover, L. E. Kay, *Science* **339**, 1080 (2013); 10.1126/science.1233066.
10. Q. Liu, W. A. Hendrickson, *Cell* **131**, 106 (2007).
11. J. Weibezahn *et al.*, *Cell* **119**, 653 (2004).
12. U. Lee *et al.*, *Plant Cell* **17**, 559 (2005).

10.1126/science.1236012

PHYSICS

Two Indistinguishable Electrons Interfere in an Electronic Device

Christian Schönenberger

In quantum mechanics, particles can be prepared in entangled states, so that measurement of a property on one particle determines the outcome for the other, no matter how far apart the particles may be. This “spooky action at distance” was demonstrated first with photons (1). One goal of condensed-matter physics has been to replicate quantum optics experiments with electrons (2). For example, the Hong-Ou-Mandel (HOM) experiment (3) can determine if two photons are indistinguishable—meaning that they have the same wavelength and polarization, and that they can become entangled if they overlap during propagation, as can happen at a beam splitter (a semitransparent mirror; see the figure, panels A and B). An electronic device that could demonstrate indistinguishability of electrons would be useful for quantum computing applications. On page 1054 of this issue, Bocquillon *et al.* (4) demonstrate such an analog of the HOM experiment with two electrons, generated from two different single-electron sources, colliding in

the equivalent of a beam splitter in a single device.

The authors assembled all of the electronics analogs of the necessary optical components in a gate-tunable electronic device. First, an electron beam source requires that electrons move as nearly free particles. The edges of two-dimensional electron gas systems formed in layered heterostructures of semiconductors are ideal channels for electrons; like light beams, they can be made directional with an applied magnetic field (5). Tunable electron beam splitters are realized with so-called quantum point contacts that can adjust the fraction of electrons transmitted and reflected (6).

The statistical properties of this process can be analyzed by measuring electronic noise (7). The partitioning of incoming electrons at the beam splitter results in a random occupation of the outgoing channels with a fixed average occupation defined by the predetermined transmission and reflection probabilities. The noise is maximized at 50% transmission probability and otherwise suppressed.

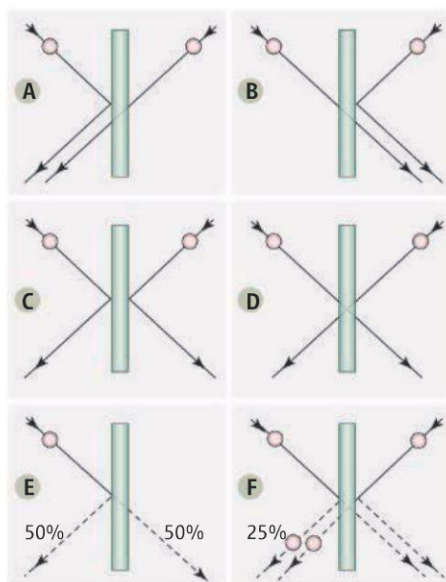
Instead of measuring the noise, which is the autocorrelation of the time-dependent electrical current, cross-correlations

An electronic device that entangles indistinguishable electrons from two independent sources has applications in quantum information processing.

between two different channels are a useful alternative. In the HOM experiment, the coincidence rate of photons in two partial beams was measured. The coherence of a source is now commonly characterized by measuring intensity correlations, a method that goes back to Hanbury-Brown and Twiss (HBT), who realized that both temporal and spatial coherence can be obtained from intensities alone [see, for example, (8)].

The HBT experiment was later realized with electron beams (9, 10), but the devices used only a single electron source. If there are two sources with two beams incident on a beam splitter, two quantum particles may collide at the same time and entangle. The entangled state must obey a symmetry rule for interchange of two particles, changing sign for fermions (e.g., electrons) or not for bosons (e.g., photons). This rule leads to distinct differences in observables in the HOM experiment (see the figure). After the interaction at the beam splitter, the two particles may exit in one of four ways: (A) Both particles exit at the left or (B) at the right; (C) the left particle remains on the left side, while the right particle remains on the right side; or (D) the two particles exchange. If the particles do not interact, each possibil-

Department of Physics, University of Basel, Klingelbergstrasse 82, CH-4052 Basel, Switzerland. E-mail: christian.schoenenberger@unibas.ch



To bunch or not to bunch. Indistinguishable quantum particles incident from left and right sides of a 50% beam splitter can scatter in four ways. The symmetry of the wave function determines the outcome. For bosons, only (A) and (B) are possible (causing “bunching”), while for fermions only (C) and (D) are possible (causing “antibunching”). For comparison, (E) shows the random partitioning of particles incident on one input alone, and (F) illustrates the partitioning of two input beams of distinguishable particles. For example, for distinguishable bosons, two bosons exit with a probability of 25%, whereas indistinguishable bosons would show a twice-as-high probability of 50% for the same process.

ity should occur equally if the transmission and reflection probabilities were adjusted to 50%. However, fermions and bosons are not independent because they must obey symmetry rules. Bosons exclusively choose (A) and (B), causing them to bunch together to the same side, whereas fermions can only choose (C) and (D) and avoid each other—they antibunch.

In the optical HOM experiment, if the photons are distinguishable, they partition independently at the beam splitter (outcome F in the figure). In the electronic HOM experiment, Bocquillon *et al.* measured the noise in one of the output channels. If two indistinguishable electrons collided at the same time at the beam splitter, the noise was suppressed because both states were fully occupied without any randomness. If the two incident electrons appeared at different times at the beam splitter, they would be independent and randomly partitioned, resulting in noise. The noise suppression at zero time delay between the two electron wave packets confirmed the formation of a two-particle coherent fermionic state.

Two-particle interference in electronic devices have been studied before, exploiting two sources with a single beam splitter (11) and an impressive double Mach-Zehnder interferometer (12). The experiment by Bocquillon *et al.* comes much closer to a state-of-the-art quantum-optics experiment as it is realized in an electronic device that uses single-electron sources (13). In these sources, electrons can be launched on demand and with a predetermined time delay for tuning the wave-function overlap.

Unlike photons, electrons are charged particles that strongly interact. Hence, two-particle interference experiments may shed new light on the dephasing problem of electronic quantum states in quantum computing. Edge states also exist in the fractional quantum Hall state, which hosts quasiparticles with statistics distinct from those for both fermions and bosons. Recently, evidence for Majorana-like particles have been found in nanoelectronic devices (14), so it may be possible to probe their scattering and test their non-Abelian statistics. Less demanding, but still very exciting, is the interaction of the quasiparticle launched by the single-electron source with the “vacuum state,” which for an electron system is

not “empty” but a filled Fermi sea. Finally, because the electron source used by Bocquillon *et al.* provides an alternating current, it launches an electron at one instance and then a hole half a period later, which should allow the study of the interactions of electrons and holes that originate from different sources.

References

1. A. Aspect, P. Grangier, G. Roger, *Phys. Rev. Lett.* **49**, 91 (1982).
2. H. van Houten, C. Beenakker, *Phys. Today* **49**, 22 (1996).
3. C. K. Hong, Z. Y. Ou, L. Mandel, *Phys. Rev. Lett.* **59**, 2044 (1987).
4. E. Bocquillon *et al.*, *Science* **339**, 1054 (2013); 10.1126/science.1232572.
5. M. Büttiker, *Phys. Rev. B* **38**, 9375 (1988).
6. B. J. van Wees *et al.*, *Phys. Rev. Lett.* **60**, 848 (1988).
7. C. Beenakker, C. Schönenberger, *Phys. Today* **56**, 37 (2003).
8. R. Q. Twiss, A. G. Little, R. Hanbury Brown, *Nature* **180**, 324 (1957).
9. M. Henny *et al.*, *Science* **284**, 296 (1999).
10. W. D. Oliver, J. Kim, R. C. Liu, Y. Yamamoto, *Science* **284**, 299 (1999).
11. R. C. Liu, B. Odom, Y. Yamamoto, S. Tarucha, *Nature* **391**, 263 (1998).
12. I. Neder *et al.*, *Nature* **448**, 333 (2007).
13. G. Fève *et al.*, *Science* **316**, 1169 (2007).
14. V. Mourik *et al.*, *Science* **336**, 1003 (2012).
15. J. Alicea, Y. Oreg, G. Refael, F. von Oppen, M. P. A. Fisher, *Nat. Phys.* **7**, 412 (2011).

10.1126/science.1234199

ATMOSPHERE

Leads and Lags at the End of the Last Ice Age

Edward J. Brook

Carbon dioxide concentrations and Antarctic temperatures were tightly coupled during the last deglaciation.

Over the course of Earth history it is generally believed that atmospheric carbon dioxide (CO_2) and climate are closely coupled (1). The most direct evidence comes from polar ice cores. Snow falling in Antarctica and Greenland gradually compacts to form solid ice and trap air. Polar ice also records past temperatures in the ratio of heavy to light isotopes in the water molecule. Ice core analyses have shown that Antarctic temperature and atmospheric CO_2 concentrations are highly correlated over the large-scale climate cycles of the past 800,000 years (2). But which

came first? Does CO_2 drive climate cycles or is it a feedback in the system that contributes to warming? On page 1060 of this issue, Parrenin *et al.* (3) address this question in a study of CO_2 concentrations and Antarctic temperatures during the last deglaciation.

One reason that the answer to the above question is more complicated than it may seem is a peculiarity of air preservation in ice. Over the top 50 or 100 m of an ice sheet, the snowpack (firn) gradually becomes denser before it becomes solid ice containing air bubbles. Air diffuses rapidly through the firn, and the trapped air is therefore younger than the surrounding ice. In places with little snowfall, the age difference can be several thousand years. The age difference cannot be reconstructed perfectly, leading

College of Earth, Ocean, and Atmospheric Sciences, Oregon State University, Corvallis, OR 97331, USA. E-mail: brooke@geo.oregonstate.edu

to uncertainty in the age of the air (containing the CO₂ record) relative to that of the ice (containing the climate record).

A second problem is related to the question itself. The global carbon cycle is an interlinked set of processes that both impact, and are impacted by, climate. For example, warming of the sea surface releases CO₂, and that increase contributes to further warming. Ocean circulation changes driven by changes in climate affect the amount of CO₂ sequestered in the deep ocean, in turn influencing surface temperature. It seems unlikely that a change in global climate would not influence CO₂ concentrations and vice versa. Seeking simple cause and effect is thus difficult.

A third issue is that different methods have been used to analyze the relationship between CO₂ concentrations and temperature over different time periods (4), making it difficult to compare results. And finally, ice core temperature records are mixtures of local and large-scale regional climate trends, and the large-scale importance of any one record, particularly over short time periods, is not clear. In contrast, CO₂ is well mixed in the atmosphere, and any ice core record should provide a global signal.

The best data capturing a major change in climate are for the last deglaciation, which took place between ~20,000 and ~10,000 years ago. The clearest CO₂ data set from that time period comes from the EPICA Dome C ice core. The original publication (5) reported that at the start of deglacial warming ~18,000 years ago, CO₂ lagged temperature change at Dome C by 800 ± 600 years, a figure that is widely cited. However, although the CO₂ data are excellent, the gas age–ice age difference at this site is very large, making the result—which depends on a model of firn compaction—uncertain.

Parrenin *et al.* address these concerns by using a different method to establish the gas age–ice age difference and by creating a composite record of Antarctic temperature from several ice cores from the Antarctic interior. They use the ratio of ¹⁵N/¹⁴N in nitrogen (N₂), which is enriched in firn due to gravitational settling (6). The enrichment depends on the depth of the firn column. Once this depth is determined from the

nitrogen data, a simple model can predict the offset in depth between gas and coeval ice and the amount of time this represents. Parrenin *et al.* verify the approach with two independent estimates of the relationship

because they improve our understanding of when CO₂ changed with respect to temperature in the ice core record. Of course, questions remain. One is how to very precisely relate to the timing of CO₂ changes to climate changes recorded in other

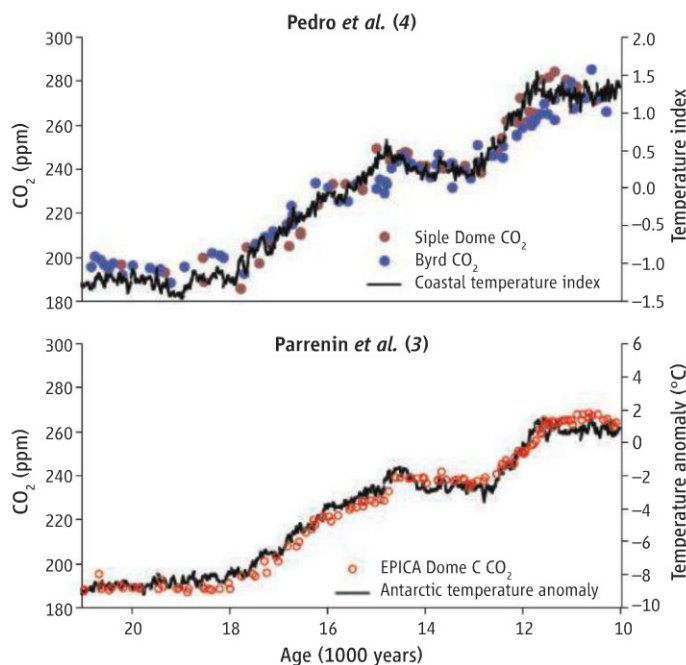
paleoclimate archives (8), given differences in dating methods. The time period around 18,000 years in the ice core record has been difficult to place firmly in an absolute chronology. New annually resolved ice cores and better correlations of ice cores from both hemispheres may alleviate this problem.

We also do not know whether the results can be generalized to other time periods. Previous work on older climate intervals supported a lead of temperature relative to CO₂ concentrations, but most, though not all (9), suffer from the same deficiencies that Parrenin *et al.* try to overcome. Analyzing older climate transitions will require high-resolution CO₂ records for those time periods, a laborious but probably worthwhile task, and development of better understanding of the transformation of snow to ice.

The ultimate question is what mechanisms influence both Antarctic climate and CO₂ concentrations on such intimate time scales. Many have been discussed, and many are plausible, including changes in CO₂ outgassing from the ocean due to changes in sea ice, changes in iron input to the ocean that influence CO₂ uptake by phytoplankton, and large-scale ocean circulation changes that cause release of CO₂ to the atmosphere. Deciding which are viable has proven difficult, but the new results of Parrenin *et al.* are a prerequisite for further understanding of the carbon cycle and climate.

References

1. D. L. Royer, *Geochim. Cosmochim. Acta* **70**, 5665 (2006).
2. D. Lüthi *et al.*, *Nature* **453**, 379 (2008).
3. F. Parrenin *et al.*, *Science* **339**, 1060 (2013).
4. J. B. Pedro, S. O. Rasmussen, T. D. van Ommen, *Clim. Past* **8**, 1213 (2012).
5. E. Monnin *et al.*, *Science* **291**, 112 (2001).
6. H. Craig, Y. Horibe, T. Sowers, *Science* **242**, 1675 (1988).
7. R. F. Anderson *et al.*, *Science* **323**, 1443 (2009).
8. J. D. Shakun *et al.*, *Nature* **484**, 49 (2012).
9. N. Caillon *et al.*, *Science* **299**, 1728 (2003).



Lead and lag. Carbon dioxide concentrations and averages of temperature proxy records for last deglaciation, as compiled by Parrenin *et al.* (3) and Pedro *et al.* (4). Pedro *et al.* used existing CO₂ and temperature proxy data from coastal Antarctic cores and the temperature anomaly is presented in standard deviation units (the number of standard deviations from the mean of the record) to illustrate the average timing of temperature change. Parrenin *et al.*'s record is the average temperature anomaly for all the records they combine (in °C), relative to modern conditions. Using largely independent methods and data, both studies indicate a very tight coupling between regional Antarctic temperatures and CO₂.

between depth and age for EPICA Dome C. Their analysis indicates that CO₂ concentrations and Antarctic temperature were tightly coupled throughout the deglaciation, within a quoted uncertainty of less than 200 years (see the figure).

Support for this conclusion comes from recent independent work of Pedro *et al.* (4). They used existing CO₂ and temperature proxies from coastal Antarctic cores with smaller gas age–ice age differences, but somewhat noisier CO₂ data and complex climate histories. They concluded that CO₂ lagged temperature by less than 400 years on average over the entire deglaciation and could not exclude the possibility of a slight lead.

In many ways, these results are not surprising, given the coupled nature of the carbon cycle and climate and the fact that oceanic processes around Antarctica probably play a key role in glacial-interglacial CO₂ dynamics (7). They are important, however,

IMMUNOLOGY

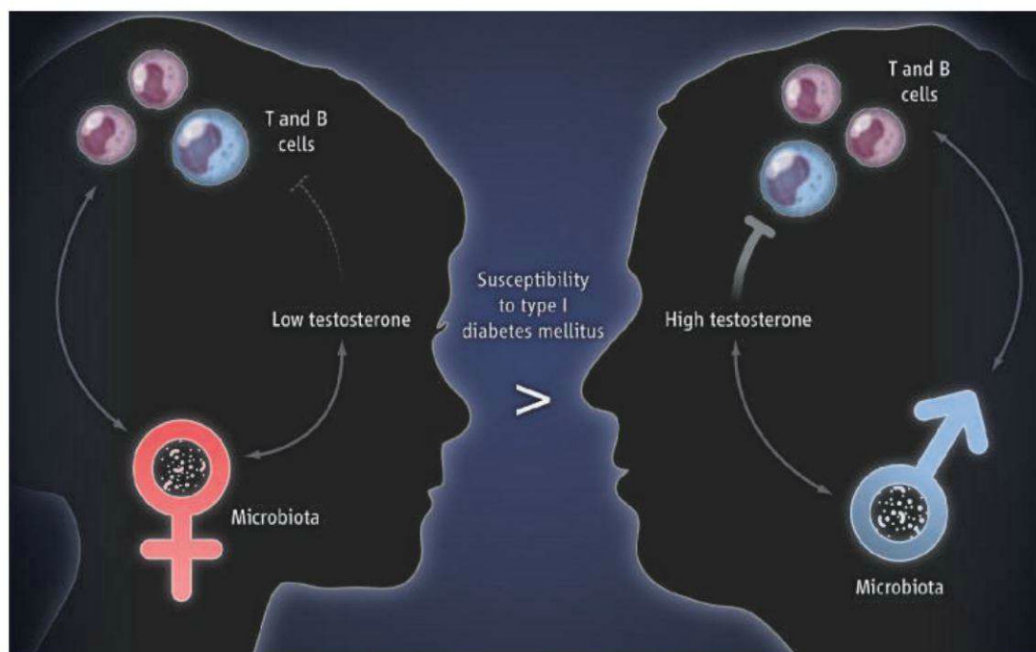
Welcome to the Microgenderome

Magdalena B. Flak, Joana F. Neves, Richard S. Blumberg

The gender bias observed in numerous diseases has long been understood as an entirely host-intrinsic factor. It is one of the many puzzling features of some autoimmune conditions (inappropriate immune responses that attack self antigens and destroy host tissue) including type 1 diabetes mellitus, in which sex hormones affect disease susceptibility and severity (1, 2). On

of autoimmune diseases such as type 1 diabetes mellitus, inflammatory bowel disease, multiple sclerosis, and rheumatoid arthritis has been rising, pointing to a role of the environment in these disorders. The so-called “hygiene hypothesis” (4) has cast early-life environmental exposures as a determinant of later-life susceptibility to diseases with an immune-mediated etiology (such

Commensal gut bacteria reinforce the gender bias observed in an autoimmune form of diabetes.



Gender, microbes, and disease. Male puberty (in mice; not shown) leads to changes in the gut microbiota that reinforce testosterone production, which is protective against the development of T and B cell functions linked to autoimmune disease. In mice, the protective properties of the male-associated microbiota can be transferred to younger females and confer testosterone-mediated protection from autoimmune disease upon the recipients.

page 1084 of this issue, Markle *et al.* (3) introduce an astonishing twist to this view, suggesting that gender bias may be exercised and/or reinforced by the commensal microbiota of the host. This extrinsic, albeit commensal, factor appears to regulate sex hormone levels and arguably the gender bias observed in type 1 diabetes mellitus. The finding contributes to an expanding field of translational research aiming to convert our growing knowledge of the host-microbiota relationship into therapeutic approaches.

In recent years, the worldwide prevalence

as asthma). Such early-life environmental events may confer susceptibility to autoimmune disease through functional alterations of commensal microbiota in the gut (5). Indeed, in several autoimmune disease models, the development of tissue injury can be prevented under axenic (germ-free) conditions wherein microbiota are absent or in other cases where they are altered (2, 3, 6). This raises the hope that beneficial properties of the microbiota may be transferable, and forms the basis for microbial transplantation and similar types of manipulation as therapies for autoimmune diseases.

Markle *et al.* show that the pronounced sensitivity of female mice versus resistance of male mice to type 1 diabetes mellitus [in

the non-obese diabetic (NOD) mouse model, which confers genetic susceptibility to this disorder] could be directly attributed to the commensal microbiota. Specifically, the authors observed that the composition of the commensal microbiota of male and female animals diverged at the time of puberty, which implies that maleness and femaleness exerted specific influences on the composition of the microbiota. Removal of the microbiota increased the circulating testosterone concentration in female mice but decreased the concentration in male mice. This suggests a bidirectional interaction between the amount of male sex hormone and the microbiota. Thus, puberty in males (and, although not directly demonstrated, testosterone) may orchestrate alterations in the commensal microbiota, and the microbiota may “record” the state of maleness, which is then “played back” to the host in a self-reinforcing program of masculinization (see the figure).

Markle *et al.* further demonstrate that the effect of bidirectional interaction between the host and microbes on disease susceptibility can be transferred between animals. Protection from type 1 diabetes mellitus was lost when male mice were made germ-free (there was also a decrease in testosterone concentration in this context); this observation is consistent with the protective effects of testosterone on the development of the disorder (1). The protective effects of the commensal microbiota on the full development of T and B cell responses associated with type 1 diabetes mellitus could be transferred during early life from male mice to female mice. Such transfer of masculinized microbiota to young female mice was associated with conferring a metastable state of maleness to the commensal microbiota of the female recipients, as shown by increases and decreases of specific microbes that were characteristic of male mice. These changes in the microbiota induced by fecal transfer were further associated with increased amounts of testosterone

Division of Gastroenterology, Department of Medicine, Brigham and Women's Hospital, Harvard Medical School and Harvard Digestive Diseases Center, Boston, MA 02115, USA. E-mail: rblumberg@partners.org

CREDIT: C. BICKEL/SCIENCE

one and a testosterone-dependent metabolic profile in the female recipients.

The ability of the microbiota as a whole to transfer and induce characteristics associated with both detrimental and beneficial phenotypes, as shown by Markle *et al.*, has been demonstrated in a number of instances. Transfer of the microbiota from obese mice induced obesity in previously lean recipient mice (7). Transplanting microbiota from children suffering from kwashiorkor into mice, when combined with a suboptimal diet, resulted in weight loss in these mice, but not in mice with conventional microbiota fed the same diet (8). Furthermore, a clinical trial on the efficacy of fecal transplants from healthy individuals into patients suffering from recurrent *Clostridium difficile* infections in the gut, who are unresponsive to the conventional treatment based on antibiotics, has yielded encouraging results (9).

Characterizing the interactions between individual species within the commensal microbial community and the host has revealed potential mechanisms that may underlie such biologic outcomes. For example, *Bacteroides fragilis* and segmented filamentous bacteria regulate the deviation of T cells into specific fates (10, 11). And a protective effect of segmented filamentous bacteria in female, but not male, mice against the development of type 1 diabetes melli-

tus has been demonstrated (2). It would thus be interesting to determine whether colonization by segmented filamentous bacteria in female mice augments testosterone production. Along similar lines, antibiotic-induced reduction in commensal microbiota in early, but not adult, life distorts the quantity and function of invariant natural killer T cells in mucosal tissues and poises the host for heightened sensitivity to environmental agents that incite asthma and inflammatory bowel disease (5). Thus, age-specific interactions of the host with specific microbes may exert beneficial and/or detrimental influences on the biology of the host, including either protection from or susceptibility to autoimmune disease.

These observations raise the possibility that identifying the responsible host or microbial factors will allow for their therapeutic addition or removal. However, our current knowledge of such manipulation is very limited, with the potential for unforeseen adverse consequences. Although the effect may be durable to displace pathogenic species, it is not clear that it will be stable enough to afford long-lasting changes. Furthermore, microbiota transfer studies in human, mouse, and rat reveal a high degree of host specificity of the gut microbiota (12). Efficient colonization and associated effects also seem to be most successful in

young animals, likely because their microbiota is not yet stabilized (6, 13). But the study by Markle *et al.* invites the intriguing question of the possible transfer of protective microbiota from pubertal human males to younger females during early life, when the commensal microbiota are amenable to the introduction of microbial successors (13). If so, family units with fathers and older brothers may offer a unique, unanticipated benefit for the health of their young daughters and sisters.

References and Notes

1. H. S. Fox, *J. Exp. Med.* **175**, 1409 (1992).
2. M. A. Kriegel *et al.*, *Proc. Natl. Acad. Sci. U.S.A.* **108**, 11548 (2011).
3. J. G. M. Markle *et al.*, *Science* **339**, 1084 (2013); 10.1126/science.1233521.
4. R. Blumberg, F. Powrie, *Sci. Transl. Med.* **4**, 137rv7 (2012).
5. T. Olszak *et al.*, *Science* **336**, 489 (2012).
6. L. Wen *et al.*, *Nature* **455**, 1109 (2008).
7. P. J. Turnbaugh *et al.*, *Nature* **444**, 1027 (2006).
8. M. I. Smith *et al.*, *Science* **339**, 548 (2013).
9. E. van Nood *et al.*, *N. Engl. J. Med.* **368**, 407 (2013).
10. K. Atarashi *et al.*, *Science* **331**, 337 (2011).
11. I. I. Ivanov *et al.*, *Cell* **139**, 485 (2009).
12. H. Chung *et al.*, *Cell* **149**, 1578 (2012).
13. I. Cho *et al.*, *Nature* **488**, 621 (2012).

Acknowledgments: Supported by NIH grants DK044319, DK051362, DK053056, and DK088199 and Harvard Digestive Diseases Center grant DK0034854 (R.S.B.) and by a Crohn's and Colitis Foundation of America research fellowship (M.B.F.).

10.1126/science.1236226

PLANT SCIENCE

One Genome, Two Ontogenies

William E. Friedman^{1,2}

The fascination of humans with the notion of multiple personalities (and morphologies) is perhaps best captured in Robert Louis Stevenson's 1886 tale of the *Strange Case of Dr Jekyll and Mr Hyde*. Land plants have been pulling off this trick for 475 million years, although perhaps to less acclaim. All of the roughly 300,000 extant species of land plants (1) engage in a complex life cycle that alternates between sporophytes (spore-producing organisms) and gametophytes (gamete-producing organisms). Biologists have long pondered how each species of land plant can maintain separate developmental programs that produce fundamentally dis-

similar ontogenies and morphologies. On page 1067 of this issue, Sakakibara *et al.* (2) provide insights into the developmental and evolutionary origins of this alternation of generations.

Today, the sporophyte generation dominates in most extant lineages of land plants (lycophods, ferns, horsetails, and seed plants), but this was not always the case (3). Among the earliest groups of land plants (liverworts, mosses, and hornworts), the gametophyte generation was and is the dominant component of the life cycle; the minute and nutritionally dependent sporophyte with its single spore-producing capsule grows upon the body of the larger and morphologically more complex gametophyte (see the figure).

But, which came first, the gametophyte or the sporophyte? The closest living rela-

Identification of genes that regulate the complex life cycles of land plants helps to explain their evolutionary origins.

tives of land plants (4) are groups of green algae that lack an alternation of generations. Their only organismic generation is a haploid gametophyte; after fertilization and the formation of a diploid zygote, meiosis creates haploid propagules that reestablish new gametophytes. Thus, the only diploid phase in the life cycles of the ancestors of land plants was the single-celled zygote. The multicellular sporophyte as we know it (such as a leafy fern, pine tree, water lily, and buttercup) is a developmental innovation of land plants.

Sakakibara *et al.* now provide critical insight into the evolutionary developmental underpinnings of the diploid sporophyte generation in the first land plants. Working with the model moss species *Physcomitrella patens*, they show that the creation of the sporophyte and its ontogeny in the

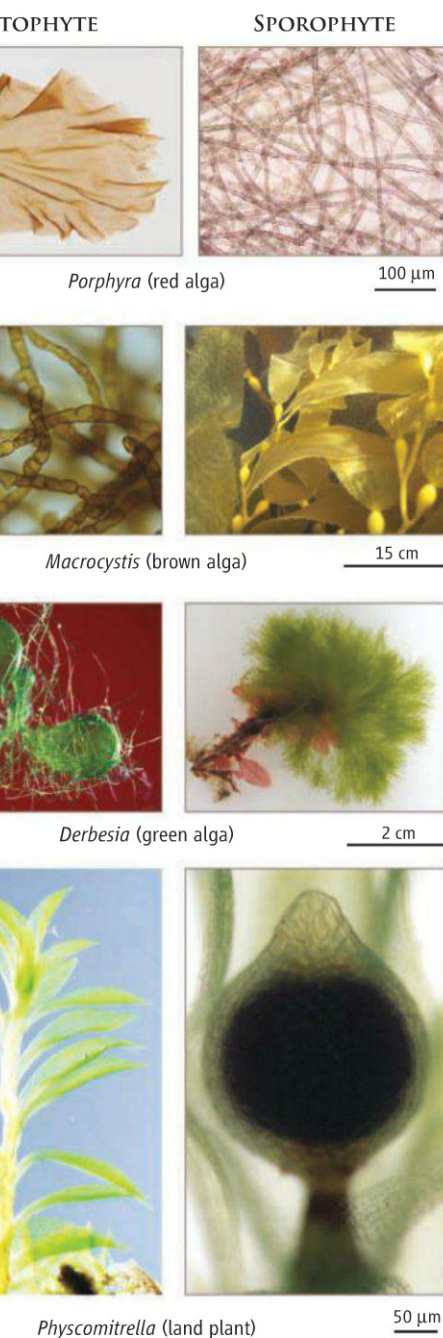
¹Department of Organismic and Evolutionary Biology, Harvard University, Cambridge, MA 02138, USA. ²Arnold Arboretum of Harvard University, Boston, MA 02131, USA. E-mail: ned@oeb.harvard.edu

life cycle of early land plants may have been facilitated by a mechanism that suppresses the expression of the ancestral gametophyte ontogeny brought onto land by green algal pioneers.

The authors show that *KNOX2* genes, whose functions in land plants were previously poorly understood (5), are necessary for maintaining the sporophyte developmental program in *P. patens*. Mutant knockouts for the *KNOX2* gene *MKN6* unleash the expression of gametophyte ontogeny in diploid sporophytes. The data are compelling: The absence of *MKN6* leads to a transition from the embryo/sporophyte ontogeny to the initiation of filamentous structures (protonema), whose morphology is characteristic of early gametophyte development in *P. patens* and many other mosses. Subsequent initiation of leafy shoot systems from protonema seals the case for the clear expression of the complete gametophyte ontogeny when sporophytes lack the proper expression of *KNOX2* genes.

The discoveries of Sakakibara *et al.* complement the work of Okano *et al.* (6) and Mosquna *et al.* (7), who have shown that in *P. patens*, genes that encode subunits of the polycomb repressive complex 2 (PRC2) are essential for the maintenance of gametophyte ontogeny. Gametophytes with deletions or mutations for these key components of the polycomb complex have a Jekyll-and-Hyde-like habit of initiating sporophyte ontogeny. Thus, two central regulators of the contrasting gametophyte and sporophyte ontogenies of members of an ancient lineage of land plants are now known.

Genes encoding homeobox-containing transcription factors (homeoproteins), which include members of the *KNOX* family, are found in almost all major eukaryotic clades (8) and were probably present in the common ancestor of all eukaryotes (9). Evidence from the green alga *Chlamydomo-*



nas indicates that two homeoproteins, *Gsp1* and *Gsm1*, are essential for the transition from gametic fusion to proper zygote development (8). How far back and how often might homeoproteins have been involved in the evolution and regulation of complex life cycles? After all, land plants are not the only clade of eukaryotes to have made the transition from an ancestral simple life history with a single multicellular generation to a complex alternation of generations (see the figure).

Brown algae have isomorphic (sporophytes and gametophytes are morphologi-

Alternations of generations. The red alga *Porphyra* has a large multicellular gametophyte (used to make nori, the wrappers for sushi) and a small microscopic filamentous sporophyte. In contrast, the brown alga *Macrocystis* has a large multicellular sporophyte (kelp) and a small microscopic filamentous gametophyte. The green alga *Derbesia* has a filamentous sporophyte and a gametophyte that is so radically different in form that until recently, the two organisms were separately classified in different genera (*Derbesia* and *Hali-cystis*). The leafy gametophyte of the moss (land plant) *Physcomitrella* is the dominant phase of the life cycle; the sporophyte grows on the body of the leafy gametophyte. Sakakibara *et al.* show that homeoproteins in an ancient lineage of land plants are central to the regulation of the proper expression of the ontogeny of the sporophyte generation and maintenance of a heteromorphic alternation of generations. Scale bars are approximate.

cally similar) and heteromorphic (sporophytes and gametophytes are morphologically distinct) alternations of generations (10). Red algae have heteromorphic alternations of generations that cycle between morphologically distinct gametophytes and sporophytes. Among the many lineages of green algae, most of which have gametophyte-only life cycles (with the zygote as the only diploid phase), clades with isomorphic or heteromorphic alternations of generations have evolved several times.

Have photosynthetic eukaryotic lineages been rooting around in the same ancestral toolkit during the several separate evolutionary origins of heteromorphic alternations of generations? Only time, a solid knowledge of algal diversity, and the proper phylogenetic choices for genome sequencing will tell. Long-sought answers to age-old questions of homoplasy and evolutionary pattern await the study of future model systems that reflect the amazing diversity of photosynthetic life.

References

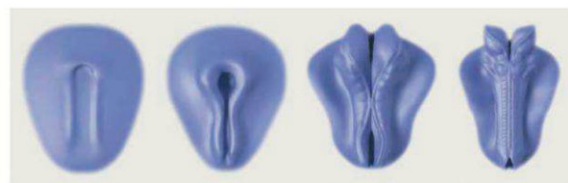
1. C. Mora, D. P. Tittensor, S. Adl, A. G. B. Simpson, B. Worm, *PLoS Biol.* **9**, e1001127 (2011).
2. K. Sakakibara *et al.*, *Science* **339**, 1067 (2013).
3. W. E. Friedman, R. C. Moore, M. D. Purugganan, *Am. J. Bot.* **91**, 1726 (2004).
4. R. E. Timme, T. R. Bachvaroff, C. F. Delwiche, *PLoS ONE* **7**, e29696 (2012).
5. A. Hay, M. Tsiantis, *Development* **137**, 3153 (2010).
6. Y. Okano *et al.*, *Proc. Natl. Acad. Sci. U.S.A.* **106**, 16321 (2009).
7. A. Mosquna *et al.*, *Development* **136**, 2433 (2009).
8. J.-H. Lee, H. Lin, S. Joo, U. Goodenough, *Cell* **133**, 829 (2008).
9. K. Mukherjee, L. Brocchieri, T. R. Bürglin, *Mol. Biol. Evol.* **26**, 2775 (2009).
10. L. E. Graham, J. M. Graham, L. W. Wilcox, *Algae* (Benjamin Cummings, San Francisco, 2009).

10.1126/science.1234992

The Continuing Challenge of Understanding, Preventing, and Treating Neural Tube Defects

John B. Wallingford,^{1*} Lee A. Niswander,² Gary M. Shaw,³ Richard H. Finnell⁴

Background: Neural tube defects (NTDs) are debilitating birth defects involving the central nervous system (CNS). Despite recent advances, NTDs represent the second most common group of human birth defects. These defects arise when the complex process of early CNS development goes awry. Normally, the brain and the spinal cord begin to form as a flat sheet of cells that rolls up and closes to form a hollow neural tube. Failure in this rolling and sealing process results in an NTD,



Successive images showing the progression of neural tube closure in a stylized vertebrate embryo. Initially, the CNS is a flat sheet; paired neural folds elevate along the rostrocaudal axis (rostral = up) and move medially, eventually fusing to enclose the neural tube. Disruption of this process during human embryogenesis results in neural defects, such as spina bifida.

such as spina bifida. From animal models, we know of over 200 genes that regulate this process, with many more still likely to be discovered. Environmental factors also can have a profound influence on neural tube closure, as evidenced by the impact of folic acid on NTD prevalence. However, the mechanisms by which environmental factors affect the process of neural tube closure and their critical interaction with genetic factors remain largely a mystery.

Advances: Three major advances from three different directions—genetics, epidemiology, and surgery—have advanced understanding, prevention, and treatment of NTDs. The rapidly expanding knowledge of the genetic causes of NTDs in animal models is poised to inform high-throughput whole-genome studies of human patients. Epidemiological studies have led to the identification of folic acid as a primary prevention strategy for NTDs. Recent advances in in utero surgical repair of spinal NTDs have improved the clinical outcome by comparison with postnatal surgery.

Outlook: Despite the advances, NTDs remain a very common birth defect and, even with surgical intervention, result in enormous clinical, emotional, financial, and societal costs. The implementation of large-scale genomic studies of human NTD patients is expected to move the field beyond its current focus on individual genetic pathways. Experimental animal systems can complement and extend the information that flows from genomic studies, and animal models can also be exploited to understand the mechanisms by which environmental factors alter the risk for NTDs. The technology exists to create patient-derived stem cells, which may hold a key for understanding this very early developmental process in humans and could provide a platform for screening therapeutic agents. Overall, the key challenge will be to understand the developing neural tube, a complex three-dimensional structure that changes rapidly over time and is dependent on the surrounding tissues for developmental signals and biomechanical forces to drive the dynamic and important process of neural tube closure.

READ THE FULL ARTICLE ONLINE
<http://dx.doi.org/10.1126/science.1222002>

Cite this article as Wallingford *et al.*, *Science* **339**, 1222002 (2013). DOI: 10.1126/science.1222002

ARTICLE OUTLINE

NTDs Are a Problem of Embryology

NTDs: Not One Disease, But Many

Epidemiology of Human NTDs

Diagnosis, Treatment, and Outcome

Primary Prevention of NTDs by Folic Acid

The Cell Biology of NTDs

The Genetics of NTDs in Animal Models

Future Directions

BACKGROUND READING

Research with animal models is expanding our understanding of normal and defective neural tube development. These insights can be relayed to intervention strategies to prevent and treat human defects.

H. J. Blom, G. M. Shaw, M. den Heijer, R. H. Finnell, Neural tube defects and folate: Case far from closed. *Nat. Rev. Neurosci.* **7**, 724–731 (2006). doi:10.1038/nrn1986

N. S. Adzick *et al.*, A randomized trial of prenatal versus postnatal repair of myelomeningocele. *N. Engl. J. Med.* **364**, 993–1004 (2011). doi:10.1056/NEJMoa1014379

M. J. Harris, D. M. Juriloff, Mouse mutants with neural tube closure defects and their role in understanding human neural tube defects. *Birth Defects Res. A Clin. Mol. Teratol.* **79**, 187–210 (2007). doi:10.1002/bdra.20333

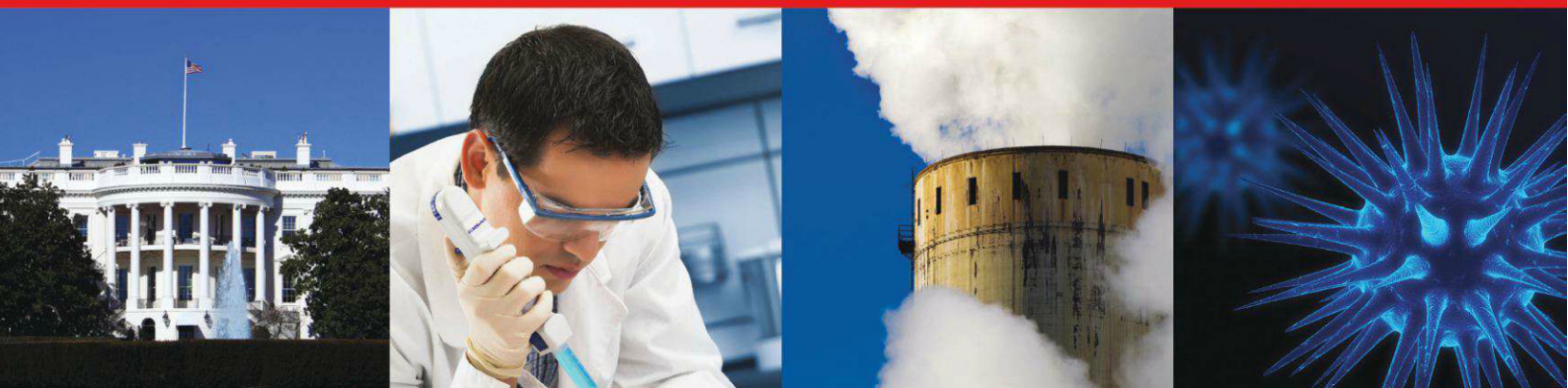
M. J. Harris, D. M. Juriloff, An update to the list of mouse mutants with neural tube closure defects and advances toward a complete genetic perspective of neural tube closure. *Birth Defects Res. Part A Clin. Mol. Teratol.* **88**, 653–669 (2010). doi:10.1002/bdra.20676

Neurodevelopment
Part of an occasional series
www.sciencemag.org/extra/neurodev

¹Howard Hughes Medical Institute, Section of Molecular Cell and Developmental Biology, The University of Texas at Austin, Austin, TX 78712, USA. ²Howard Hughes Medical Institute, Department of Pediatrics, University of Colorado School of Medicine, Aurora, CO 80045, USA. ³Department of Pediatrics, Stanford University School of Medicine, Stanford, CA 94305, USA. ⁴Dell Pediatric Research Institute, Department of Nutritional Sciences and Department of Chemistry and Biochemistry, The University of Texas at Austin, Austin, TX 78723, USA.

*Corresponding author. E-mail: wallingford@austin.utexas.edu

Stem Cell Lawsuit Finally Over. Russian Team Retrieves First Sample from Lake Vostok. Surprise Choices Mark New Leadership on U.S. House Science Panel. India Unveils Ambitious Science Policy.



Now, more than ever, developments in the lab are directly connected to decisions made in the halls of government.

ScienceInsider, the policy blog from the journal *Science*, is your source for news from the intersection of science and policy. From budget debates in the United States Congress, to climate change agreements at the United Nations, *ScienceInsider* covers the issues that have an impact on your work, your field, and your world.

Keep up to date and keep informed. Go inside the issues at www.ScienceInsider.org



*Science***Insider**

Breaking news and analysis from the world of science policy



The Continuing Challenge of Understanding, Preventing, and Treating Neural Tube Defects

John B. Wallingford,^{1*} Lee A. Niswander,² Gary M. Shaw,³ Richard H. Finnell⁴

Human birth defects are a major public health burden: The Center for Disease Control estimates that 1 of every 33 United States newborns presents with a birth defect, and worldwide the estimate approaches 6% of all births. Among the most common and debilitating of human birth defects are those affecting the formation of the neural tube, the precursor to the central nervous system. Neural tube defects (NTDs) arise from a complex combination of genetic and environmental interactions. Although substantial advances have been made in the prevention and treatment of these malformations, NTDs remain a substantial public health problem, and we are only now beginning to understand their etiology. Here, we review the process of neural tube development and how defects in this process lead to NTDs, both in humans and in the animal models that serve to inform our understanding of these processes. The insights we are gaining will help generate new intervention strategies to tackle the clinical challenges and to alleviate the personal and societal burdens that accompany these defects.

The vertebrate neural tube serves as the precursor to the central nervous system (CNS): the brain and spinal cord. Structural birth defects of the CNS, called neural tube defects (NTDs), are a multifactorial disorder that arise from a complex interaction of genetic and environmental factors. Although we are only now beginning to understand the etiologies of NTDs, two major advances have been made in their prevention and treatment. First, it is widely known that taking folic acid (FA; vitamin B9) during child-bearing years can greatly reduce a woman's risk of having a baby with a NTD (*1*). Second, studies have demonstrated that in utero repair of spina bifida improves patient outcomes relative to surgery performed in the post-parturition period (*2*). In spite of these advances, we have only just begun to tackle the problem of NTDs. For example, 16 years after mandated folate fortification in the United States, NTD rates remain unacceptably high: 1 in 2000 births in the United States and considerably higher still in developing areas such as China (27.8 per 2000 births) (*3*) and Latin America (4.4 per 2000 births in Argentina; 6.2 per 2000 births in Brazil) (*4*). Furthermore, we understand relatively little about the mechanism by which folate acts on NTDs. Similarly, many NTD patients that have undergone surgery

suffer wide-ranging neurological, urological, and orthopedic problems. Thus, NTDs continue to present a major public health burden.

Here, we review the process of neural tube development and how defects in this process lead to NTDs. We discuss both human NTDs and the ways in which animal studies are providing new insights. We focus on recent important findings and highlight unanswered questions about the molecular basis of FA action and genetic susceptibility to NTDs. Lastly, we discuss strategies that could build on our current understanding to lessen the personal and societal burdens that accompany these serious malformations.

NTDs Are a Problem of Embryology

NTDs arise as a defect in embryonic development. During embryogenesis, the central nervous system normally develops as a flat sheet of cells that subsequently rolls up and fuses shut to form the hollow neural tube (Figs. 1 and 2A). NTDs arise when this process of neural tube closure (NTC) is disrupted (Fig. 2B). As discussed below, cellular changes that drive NTC and the molecular mechanisms that control them are largely conserved from humans and mice to birds and amphibians. Indeed, decades of work in animal models have established a comprehensive framework for the developmental processes that underlie NTC (*5–8*).

NTDs: Not One Disease, But Many

Although often lumped into a single category, NTDs encompass a wide array of morphologically distinct malformations. In general, failure of NTC is associated with defects in the overlying bony structures (i.e., cranial vault and neural arches) such that neural tissue is exposed. Consequently, most defects of primary NTC are referred to as open NTDs.

There are also a number of closed or skin-covered conditions; however, relatively little is known about their etiology. The open NTDs fall into three general categories, but further refinement of these classifications—such as vertebral location and extent of the defect—will help parse some of the differing underlying etiologies.

NTDs restricted to the cranial regions are referred to as anencephaly (Fig. 1C). This invariably lethal condition is characterized by absence of the cranial vault and severe defects in the cerebral hemispheres. The cerebellum is usually absent, and the brain stem may be hypoplastic. NTDs restricted to the caudal portion of the neural tube are referred to generally as spina bifida (meningomyelocele) (Fig. 1C). More prevalent than anencephaly, this condition is associated with defects in the neural arches, through which meninges and spinal cord tissue protrude. The majority of fetuses with meningomyeloceles are live born and, with proper treatment, survive to adulthood. Failure of NTC over the entire body axis, called craniorachischisis (Fig. 1C), is also lethal but relatively rare. Not only do the natural histories of these disorders vary, but even within a single classification, such as meningomyelocele, the degree of handicap is variable. Refinement in the classification of these malformations (e.g., by precise vertebral position of spina bifida) and the assignment of contributing gene pathways should translate into more effective preventative measures and management of affected infants.

Epidemiology of Human NTDs

Prevalence of NTDs has varied over time and geography. Prevalence in the United States is about one in 2000 births and was about 2 in 1000 births in the late 1960s. In neighboring Mexico, the prevalence is significantly higher (3.2 per 2000) (*9*). NTDs are etiologically complex, and both genetic and environmental risk factors have been proposed. In terms of genetic underpinnings, monozygotic twinning and single-gene disorders have long been associated with NTDs (*10*), with concordance rates of monozygotic twins (7.7%) exceeding that of dizygotic twins (4.0%), attesting to some genetic contribution to their etiology (*11*). Numerous studies have explored a variety of candidate gene pathways [reviewed in (*12*)], such as the folate/1-methyl carbon metabolic pathway (*13, 14*), glucose metabolism and/or transport (*12*), DNA repair (*15*), oxidative stress pathway (*12*), retinoic acid receptors (*16*), and the WNT/planar cell polarity (PCP) signaling network (*17*). In a following section, we discuss animal studies that are shedding new light on genetic factors that govern NTC. However, it is crucial to note that the population burden of

¹Howard Hughes Medical Institute, Section of Molecular Cell and Developmental Biology, The University of Texas at Austin, Austin, TX 78712, USA. ²Howard Hughes Medical Institute, Department of Pediatrics, University of Colorado School of Medicine, Aurora, CO 80045, USA. ³Department of Pediatrics, Stanford University School of Medicine, Stanford, CA 94305, USA. ⁴Dell Pediatric Research Institute, Department of Nutritional Sciences and Department of Chemistry and Biochemistry, The University of Texas at Austin, Austin, TX 78723, USA

*To whom correspondence should be addressed. E-mail: Wallingford@austin.utexas.edu

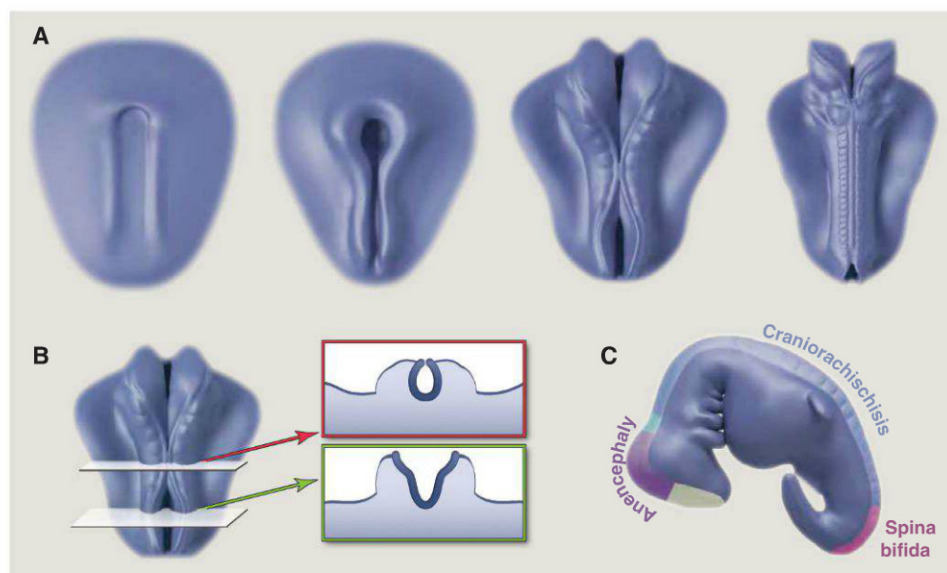


Fig. 1. (A) Successive images showing the progression of neural tube closure in a stylized vertebrate embryo (rostral = up). Initially, the CNS is a flat sheet; paired neural folds elevate along the rostrocaudal axis and move medially, eventually fusing to enclose the neural tube. (B) Cross sections illustrate closed (red) and open (green) regions of the neural tube. (C) Region-specific NTDs.

human NTDs thus far explained by known genetic polymorphisms remains quite small, a fact that almost certainly reflects the relatively modest amount of research effort in this area rather than a relative lack of importance of genetic factors in NTDs. Indeed, no large-scale NTD-focused genomic discovery project (genome-wide association study, exome sequencing, etc.) has yet been published.

The key role that environment plays in NTD etiology is highlighted by the impact of maternal nutrition, specifically folate intake. Both observational studies and randomized trials have provided evidence that FA reduces the risk of NTD-affected pregnancies (1, 18). However, 30 to 50% of NTDs are not folate preventable, and other environmental factors must be considered (1). Among the most notable environmental risk factors for NTDs are maternal pregestational insulin-dependent diabetes (19) and maternal prepregnant obesity (20), as well as maternal use of specific anticonvulsant drugs, including valproic acid (VPA) (21).

The teratogenic potential of maternal pregestational diabetes is well established and includes a 2- to 10-fold increase in the risk of CNS malformations (including NTDs) among the offspring of affected women relative to the general population (22). Moreover, lack of periconceptional glycemic control and intake of foods of higher glycemic index values have been associated with the risk of NTDs in the offspring of diabetic women (23, 24). Because human embryos lack pancreatic function until after the seventh week of gestation and NTC occurs between weeks 3 and 4, the teratogenic effect of maternal diabetes may be due to embryonic exposure to elevated glucose concentrations. Pre-pregnancy obesity is another consistently observed risk factor for NTDs. The risk increases with increasing

maternal body mass index (BMI). Women in the highest BMI categories have a 1.5- to 3.5-fold higher risk of having an NTD-affected child than women with lower BMI (20, 25, 26). The increased risk of NTDs in the offspring of obese women may be attributable to hyperinsulinemia (27). This could provide a common explanation for the associations between NTD risk and maternal obesity and maternal pregestational diabetes, because hyperinsulinemia may coexist with both conditions.

With respect to pharmaceutical NTD teratogens, the anticonvulsant drug VPA (Depakene, Abbott Laboratories) has been associated with a 1 to 2% risk of having a pregnancy affected with spina bifida, whereas the risk of anencephaly does not appear to be increased (28). VPA may influence neural tube development via its action as a potent inhibitor of histone deacetylases (HDACs) (29, 30), and studies in model animals are consistent with this idea [see below and (31–33)]. Class I and II HDACs are involved with histone modification and therefore play a role in the regulation of gene expression. It is also possible that posttranslational gene modification is compromised by VPA exposure, which inhibits HDACs and limits the availability of folate molecules (34), thereby increasing the risk of NTDs.

Diagnosis, Treatment, and Outcome

Screening to identify pregnant women at risk for carrying NTD-affected fetuses is achieved by evaluation of maternal serum alpha-fetoprotein levels, amniocentesis, and ultrasound imaging (35). Individuals with spina bifida can generally survive if they undergo surgical repair in utero or soon after birth (36, 37). A recent randomized trial showed that in utero repair of spina bifida

improved patient outcomes in terms of improved motor function and ambulation and mental development compared with those receiving surgery postpartum (2). Moreover, 40% of infants receiving in utero surgery required a ventriculoperitoneal shunt at 12 months of age, compared with 82% of infants undergoing postnatal surgery (2).

However, even after surgery (in utero or postnatally), individuals with spina bifida remain at elevated risk for nervous system malformations, including hydrocephalus and skull malformations that press the brain downward into the spinal canal. Lower extremity weakness and paralysis, sensory loss, and bowel and bladder dysfunction are also common. Individuals with spina bifida are also at risk for a range of orthopedic abnormalities including clubfoot, contractures, hip dislocation, scoliosis, and kyphosis. Moreover, although most individuals with spina bifida have normal intelligence, specific cognitive and language difficulties are common (38).

Even successful surgical repairs represent only a partial solution. Because NTC occurs early in development (~3 weeks postconception), a NTD will leave the delicate neural tissue, normally encased within bone, exposed and subjected to trauma in utero until the much later time point for surgical intervention. As such, substantial effort should be focused on understanding the mechanisms of NTC and the biological basis of NTDs, with an eye toward developing preventive strategies.

Primary Prevention of NTDs by Folic Acid

NTDs stand out as one of few birth defects for which primary prevention strategies are available. Research spanning decades, including randomized and community-based trials, demonstrate that maternal, periconceptional supplementation with FA alone or multivitamins containing FA can reduce the risk of NTDs in offspring (1, 39, 40). Fortification of FA in the U.S. food supply has been associated with upward of a 20% decline of anencephaly and a 34% decline in spina bifida (41–43). Reported prevalence declines have been higher in Canada and Chile (44, 45). How FA acts to prevent NTDs is a major outstanding question, and the answer will be complex because folate is central to numerous cellular reactions. These include production of purines and thymidylate, the building blocks for DNA and RNA biosynthesis, and production of the universal methyl donor S-adenosyl-methionine (SAM), used in methylation of DNA, histones, proteins, and lipids. Therefore, deficits in FA metabolism could affect cell proliferation, cell survival, transcriptional regulation, or a host of other cellular reactions; defects in any of these processes could disrupt NTC. To bring insight into the mechanisms by which FA acts during NTC, studies have turned to animal models, in particular mouse NTD models, which are thought to be representative

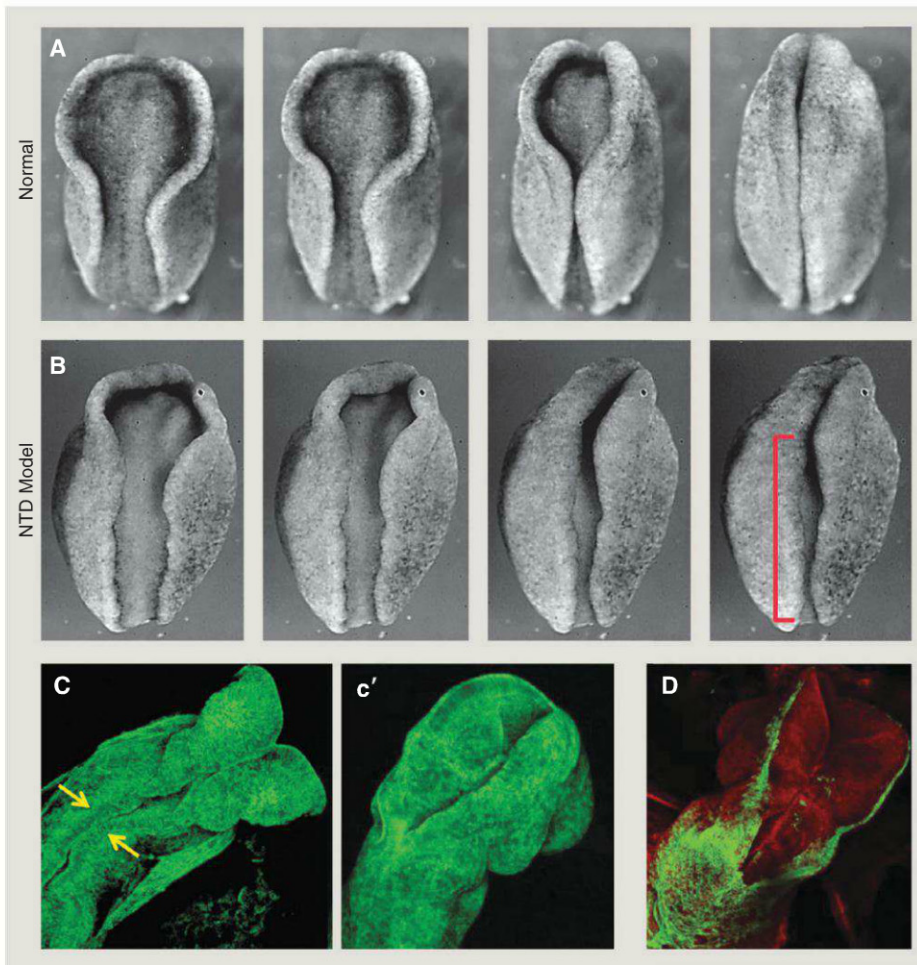


Fig. 2. (A) Still frames from a time-lapse movie showing the progress of NTC in an amphibian embryo (rostral = up). (B) Disruption of PCP signaling results in disrupted NTC (red bracket). (C) Still frame from a movie of mouse neural tube closure; arrows indicate initial meeting of neural folds (66). (c') NTC has progressed in a later time point. (D) Genetically inducible fluorescent reporters allow visualization of specific tissues, in this case the ectoderm (green) that borders the neural tissue (red).

of human neurulation anatomically and molecularly and in which folate levels can be altered before or during pregnancy.

Mutations have been made in numerous mouse genes required for FA metabolism or use; however, only three mutated genes [*Folr1*, *Slc19a1* (previously *Rfc*), and *Mthfd11*] have overt NTD phenotypes (46–48). Even under conditions of folate deficiency, there is relatively little evidence of altered NTD incidence for mouse FA pathway mutations (49). Moreover, there is as yet no compelling association between *Folr1* or *Slc19a1* and human NTDs, although a few *Mthfr* polymorphisms have been identified as possible risk factors for human NTDs (14). Currently, in the folate-replete population in the United States, the majority of human pregnancies are within the normal range of FA levels, and recent studies found little association between NTD risk and maternal FA intake, perhaps suggesting that FA-sensitive NTDs have largely been prevented (50). Therefore, data to date suggest that deficits in the FA

pathway likely represent only a modest fraction of NTD risk.

Looking beyond the folate pathway to elucidate gene-environment interactions. The large number of mouse NTD models with no apparent link to the FA pathway provides enormous potential to explore how genetics impact responsiveness to FA and to define mechanisms by which FA influences NTC. This potential has been only minimally realized, because only 23 of the >200 mouse NTD mutants have been tested for FA responsiveness (49, 51, 52). FA treatment has a preventive effect in 11 mouse NTD models; some show a correlation with compromised FA use, but others do not, indicating that disrupted FA metabolism is unlikely to be the full explanation for FA-mediated effects. Currently there is little that ties together NTD models that are FA-responsive or FA-resistant at a mechanistic level. Testing a far greater number of mouse mutants will expand this data set, may reveal common pathways or targets, and should lead

to better predictions as to whether FA or perhaps another treatment would be most effective in preventing NTDs.

Contrary to expectations, FA treatment in a few mouse NTD models resulted in detrimental effects, including an increased risk for NTDs and embryo loss before the time of NTC (51, 52). These findings of early embryo loss are consistent with the possibility raised in 1997 based on miscarriage risk that embryo loss may explain some of the decrease in human NTD occurrence upon FA supplementation (53). If these findings are relevant to human NTDs, it could suggest that, for certain mutations, FA may not be protective or even neutral in its action. Additional studies in animal models will be required to determine the basis for the observed detrimental effect and whether there are particular gene or pathway mutations that are more susceptible, either positively or negatively, to FA effects.

Possible epigenetic changes induced by FA. FA is known to cause epigenetic changes. Alterations in SAM levels could affect DNA methylation and histone modification, both of which can influence gene transcription. Indeed, there is evidence that methyl donor-enriched diets can induce alterations in gene expression, and long-term generational exposure can result in increasing variation in DNA methylation even in wild-type mice (54). Moreover, questions have been raised as to whether the increase in FA intake acting through the methylation cycle may predispose to allergic airway disease, although the current evidence is conflicting (55–57). With respect to NTD risk, some mutant mice showed a beneficial response to increased FA over a single gestation period but a detrimental response over multiple generations (52). This contradictory response depending on the length of FA exposure highlights the difficulties in considering how best to model human exposure to FA as currently implemented. Moreover, it raises the question of whether there may be unexpected effects of long-term FA fortification and supplementation in humans or potential effects because of increased levels of metabolized and unmetabolized FA.

The variation in NTD risk depending on the length of FA exposure (52) points toward the possibility of epigenetic changes. Consistent with this idea, mutations in genes that affect DNA methylation, histone modification (in particular acetylation), or chromatin remodeling result in NTDs in mice (6, 31, 58). As previously described, the antiepileptic drug VPA is a HDAC inhibitor, and it is a well-known risk factor for NTDs in humans (21). Interestingly, NTDs in mice bearing mutations in the HDACs GCN5 or CITED2 can be prevented with FA supplementation (32, 33). Epigenetic influence has also been suggested to help explain the predominance of cranial NTDs in females versus males. X chromosome inactivation is maintained by DNA methylation, and hence there is more demand on the methylation cycle in female cells after every

division relative to male cells (59). Epigenomic studies should bring new insights into how FA may affect transcriptional programs during NTC.

The Cell Biology of NTDs

One complication that has hindered our understanding of NTDs generally, and of FA action specifically, is the generally underappreciated complexity of NTC. Although it can be described simply and succinctly as a sheet rolling up to form a tube, NTC is actually the sum of several autonomous and region-specific changes in cell behavior (5–8). For example, NTC begins not with rolling but instead with a thickening of the neural ectoderm, only after which do the neural folds elevate and begin moving toward the midline. This medial movement of the folds is facilitated by bending of the epithelial sheet and by narrowing and lengthening of the neural tissue. In addition, some studies suggest that the epidermis generates a pushing force that aids the movement of neural folds toward the midline (8). Lastly, a poorly defined process of epithelial fusion links the two neural folds into a sheet of epidermal cells covering the hollow neural tube [e.g., (60)].

Adding to this complexity is the discontinuity of the NTC process along the rostrocaudal axis. Rather than progressing continuously from one end or the other, NTC initiates at multiple sites along the axis and progresses rostrally and/or caudally from those sites. The cellular machines that drive the rolling up of the neural tube differ regionally along the length of the neural tube. This point is important in light of the heterogeneity observed in human NTDs (e.g., spina bifida versus anencephaly; Fig. 1C), because studies in animals now make clear that these spatially restricted subtypes of NTD stem from regional differences in the underlying cell behaviors.

One example is the process of convergent extension, whereby cells interdigitate mediolaterally in order to elongate the tissue perpendicularly along the rostrocaudal axis (Fig. 3, pink/green cells). This process acts specifically in the hindbrain and spinal cord, with disruption of genes governing convergent extension resulting in craniorachischisis (7, 17). In contrast, another cellular process called apical constriction converts columnar cells into wedge-shaped cells, leading to localized bending of the neural epithelium and facilitating NTC (Fig. 3, blue cells). Apical constriction is most important in the future brain and the caudal-most spinal cord, because disruption of genes controlling apical constriction is associated most strongly with anencephaly and caudally restricted spina bifida (7).

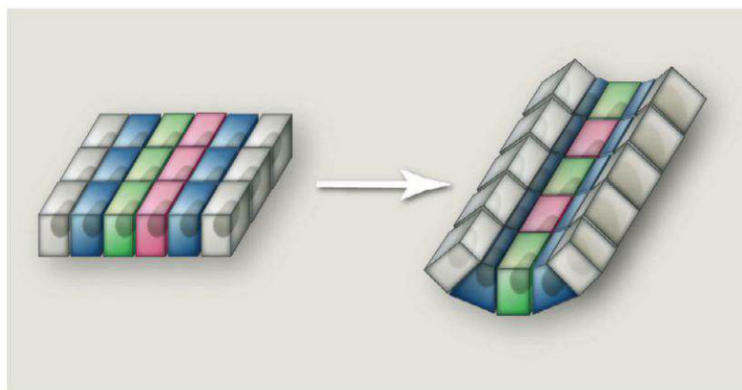


Fig. 3. Multiple cell behaviors contribute to neural tube morphogenesis. In this schematic, pink and green cells illustrate convergent extension. By exchanging neighbors specifically in the mediolateral (horizontal) axis, the sheet of cells is elongated in the anteroposterior (vertical) axis. Blue cells illustrate apical constriction. These cells do not move but rather change their shape, leading to a bend in the tissue sheet. [Schematic adapted from (7)]

Lastly, much of what is known about the dynamic events of vertebrate NTC comes from live imaging studies of amphibian and chick embryos (Fig. 2A and Movie 1) (61–64), but important advances have recently been made such that dynamic imaging of NTC is now possible in the living mouse embryo (Fig. 2, C and D, and Movie 2) (60, 65, 66). The emerging ability to combine prolonged live imaging with the wealth of mouse genetic mutants will drive a deeper understanding of how gene function regulates the cell and tissue behaviors necessary for this critical and sensitive stage of embryonic development.

The Genetics of NTDs in Animal Models

Animal studies have identified hundreds of genes as candidates for human genetic studies. In the mouse, over 200 genes are causative for NTDs (58, 67), and many others have been provided by studies in amphibians (7). These genes fall into diverse functional classes and include regulators of actin dynamics, cell adhesion, electron transport, DNA damage repair, and other processes (58, 67). Because most studies reporting NTDs in mutant animals were focused primarily on other biological questions, the majority of these models are only cursorily characterized. Nonetheless, some themes are emerging.

1) *Genetic modules govern closure in discrete regions of the CNS.* NTDs in mutant mice fall into heterogeneous subtypes similar to those seen in humans, and genes with common cell-biological functions tend to associate with the same subtype. For example, disruption of genes encoding Shroom3, Abl, or Mena results in highly penetrant exencephaly and caudally restricted spina bifida (68–70), and each of these genes has been implicated in the control of apical constriction (71–73). As described below, exencephaly also consistently results from disruption of any of a large number of genes associated with the assembly or function of cilia, whereas mutations in

genes associated with the PCP signaling network associate with craniorachischisis (17, 74, 75). These linkages of genetic modules to particular NTD subtypes is important, because they suggest that more accurate and more specific diagnosis of human NTD subtypes will facilitate studies of how specific genetic polymorphisms confer NTD risk in humans.

2) *Cilia and NTDs.* One genetic module that is well defined and has emerged as a critical regulator of NTC is that governing ciliogenesis (75). Cilia are small microtubule-based cellular protrusions that are essential for cell-cell signaling (76), a discovery first made in the course of mouse genetic screens focused on neural tube morphogenesis (77, 78). Roughly two dozen genes associated with ciliogenesis have now been implicated in NTC in mice (75). The cell biological mechanism linking cilia to NTDs remains unclear, but there is evidence to suggest defects in apical constriction. First, like mutation of genes associated with apical constriction, mutation of cilia-related genes elicits exencephaly specifically (75). Second, cilia are crucial organelles for Hedgehog signal transduction (76), and Hedgehog signals have been linked directly to neural patterning and to neural epithelium bending, a process facilitated by apical constriction (79).

This work in animals has paralleled work in humans revealing a link between cilia and an array of human diseases, and this “ciliopathy” disease spectrum includes both severe and milder forms of NTDs (80–82). For example, the *fuz* gene is crucial for ciliogenesis and NTC in animal models (83, 84), and mutations in *fuz* have also been associated with human NTDs (85). Moreover, a number of genes associated with Meckel-Gruber syndrome, in which occipital encephaloceles are frequently observed, are also known to compromise cilia formation (81, 82).

3) *PCP and NTDs.* Another genetic module for which a link to NTDs is emerging is the PCP network, which was discovered in *Drosophila* and has now been shown to govern a wide array of polarized cell behaviors (74). Beginning with studies of the mouse mutant *loop-tail*, researchers have found that mutations in many PCP genes (*Fz*, *Dvl*, *Vangl*, and *Celsr*) lead to NTDs (17, 74, 86). In mice, most manipulations of PCP function result in craniorachischisis, and studies in frogs revealed that craniorachischisis was in fact a secondary phenotype stemming from an essential role for PCP genes in neural convergent extension (61, 87). In the absence of PCP function, cells fail to interdigitate mediolaterally, and the resulting overly wide neural tissue cannot fuse (61, 87). Subsequent studies demonstrated the same mechanism in mice with

craniorachischisis (88, 89). Importantly, human fetuses with craniorachischisis frequently display shortened and widened axes, consistent with a failure of convergent extension (90, 91). Taking cues from these animal studies, concerted efforts have now identified mutations in several PCP genes in patients with NTDs (17, 86).

Although the association of PCP gene variants with human NTDs is exciting, these data also highlight the difficulty in predicting genotype-phenotype relationships in human or in animal models: The NTDs in patients with PCP gene mutations range from the expected craniorachischisis to open spina bifida and even to closed NTDs (17). This outcome likely reflects the hypomorphic nature of the particular PCP gene mutations in these patients, because strong homozygous mutation of PCP genes in mice generally leads to craniorachischisis, whereas trans-heterozygosity for many of these mouse mutations results in other types of NTDs (17).

The growing abundance of genotype-phenotype data for genes with a shared biological function demonstrates the importance of cilia-related and PCP genes in determining susceptibility to NTDs, and studies are now needed to determine the proportion of human NTDs accounted for by variation in these genetic modules and how these variants place embryos at risk of failed NTC. As the first of what is likely to be many such genetic modules to be discerned, these data provide a conceptual framework for future NTD gene identification.

Future Directions

Identification of NTD-associated mutations in humans. A major advance in the past 10 years has been the discovery in animal models of over 200 genes whose function is required for NTC, and many new genes continue to be discovered [e.g., (58)]. These insights should now be translated into medical sequencing efforts in human NTD patients and the existing large cohorts of NTD patient DNA. Going forward, it will be important to move beyond the analysis of single candidate genes to genome-wide sequencing efforts of large sets of patient samples in order to have the power to reveal significant associations and to begin to understand the multifactorial nature of NTDs in humans. Polymorphisms and possible genetic interactions identified in human NTD cases can then be validated in animal models, where both specific mutations as well as multiple genetic changes can be tested.

Epigenomic studies. Epigenetic mechanisms can underlie human disease, as is becoming evident for neurological diseases and cancer (92–94). On the basis of findings that epigenetic regulators play key roles in mouse NTC and that such factors may be affected by FA (31–33), it is likely that genome-wide analyses will reveal epigenomic changes associated with NTDs. In animal models, advanced technologies can evaluate the transcriptional profile of specific cell types and correlate this with changes in DNA

methylation, histone marks, and higher-order chromatin states. These technologies can also be used in human tissues, with the caveat that transcriptional and epigenetic signatures may be vastly different between the available tissue (generally collected at the time of delivery or in infancy) and the early embryonic tissues that mediate NTC. Nonetheless, substantial efforts have begun to define the DNA methylation and histone states in numerous control and diseased tissues from human patients, including some preliminary studies of DNA methylation from human NTD tissue (95). Future studies incorporating information on FA status should help to define potential FA-mediated changes, with a particular focus on the genes known to be necessary for NTC.

Developing new therapies for FA-resistant NTD based on knowledge of molecular pathways. Not all NTDs are preventable with FA treatment in human or in animal models (49, 50, 58), underscoring the need to consider alternative therapies. Mouse NTD models provide a substantial resource to develop alternative strategies based on biochemical and mechanistic information. For example, there is evidence for some preventive effect of inositol in *curly tail* (*Grhl3*) mutants; inositol deficiency increases NTD incidence in mice and rats, and mutations in genes associated with inositol metabolism and use can lead to NTDs in mice (6, 96). This evidence has led to a small PONTI Study (Prevention of NTDs by Inositol, www.ucl.ac.uk/ich/research-ich/neural-development/ponti_study), in conjunction with FA for women with a previous NTD-affected pregnancy. Expansion of studies to additional micronutrients—for instance, vitamin B12 or zinc, low levels of which appear to be associated with NTD risk in humans (97, 98)—carry the possibility of defining which genetic risk factors may be best targeted by therapies beyond FA.

Stem cell alternatives to animal models. Although animal models clearly serve as important tools, work with induced pluripotent stem cells now allows direct study of basic biological processes in cells derived from human patients. With the recent demonstration that complex three-dimensional morphogenetic events can be recapitulated in vitro using stem cells (99, 100), it is now conceivable that NTC could also be modeled in this way. The promise of such an approach would be threefold. First, it would allow for direct, dynamic studies of neural morphogenesis in human cells. Second, by using cells derived from human NTD patients, this approach would allow direct comparison of normal and affected tissues as they engage in NTC; this should increase the efficacy of transcriptomic and epigenomic studies proposed above. Lastly, a stem cell approach could provide more abundant material and a relatively fast time frame to analysis; such increased efficiency could provide a tractable platform with which to screen small molecules for therapeutic or preventive potential.

In conclusion, although the risk of NTD remains high and the occurrence of NTDs translates

to a great cost in terms of physical, emotional, and financial burden on the affected child and family, much remains undefined for NTD etiology. New approaches should overcome the technical barriers to ascertaining the causes, whether genetic or environmental. Important and rich human data sources have now become available such as the National Birth Defects Prevention Study (101), which has collected environmental and lifestyle data and DNA samples on thousands of women and their infants. Such data will be excellent resources to which new technologies for risk factor discovery can be applied. Furthermore, the rapid advances being made in animal models are contributing substantially to understanding the genetic basis of human NTD and the intersection with environmental factors. Increased attention to this problem is essential for the development of alternative therapies to help to prevent NTDs.

Movie 1. Live imaging of NTC in a frog (*Xenopus*) embryo. These large embryos have large cells, and by labeling cell membranes with a fluorescent marker every cell in the early CNS can be monitored during NTC. A few still frames in this movie were published previously (102). [Credit: C. Lee]

Movie 2. Live imaging of NTC in the hindbrain and midbrain of a mouse embryo visualized by mosaic fluorescent labeling (membrane tomato in red, membrane GFP in green). Zipping proceeds rostrally from closure point I, and caudally from closure point II/III, to continue to close the cranial neural tube. [Credit: C. Fees and L.A.N.]

References and Notes

- H. J. Blom, G. M. Shaw, M. den Heijer, R. H. Finnell, Neural tube defects and folate: Case far from closed. *Nat. Rev. Neurosci.* **7**, 724 (2006). doi: [10.1038/nrn1986](https://doi.org/10.1038/nrn1986); pmid: [16924261](https://pubmed.ncbi.nlm.nih.gov/16924261/)
- N. S. Adzick *et al.*, A randomized trial of prenatal versus postnatal repair of myelomeningocele. *N. Engl. J. Med.* **364**, 993 (2011). doi: [10.1056/NEJMoa1014379](https://doi.org/10.1056/NEJMoa1014379); pmid: [21306277](https://pubmed.ncbi.nlm.nih.gov/21306277/)
- Z. Li *et al.*, Extremely high prevalence of neural tube defects in a 4-county area in Shanxi Province, China. *Birth Defects Res. A Clin. Mol. Teratol.* **76**, 237 (2006). doi: [10.1002/bdra.20248](https://doi.org/10.1002/bdra.20248); pmid: [16575897](https://pubmed.ncbi.nlm.nih.gov/16575897/)
- E. E. Castilla, I. M. Orioli, J. S. Lopez-Camelo, M. G. Dutra, J. Nazer-Herrera, Preliminary data on changes in neural tube defect prevalence rates after folic acid fortification in South America. *Am. J. Med. Genet. A* **123A**, 123 (2003). doi: [10.1002/ajmg.a.20230](https://doi.org/10.1002/ajmg.a.20230); pmid: [14598335](https://pubmed.ncbi.nlm.nih.gov/14598335/)
- Y. Yamaguchi, M. Miura, How to form and close the brain: Insight into the mechanism of cranial neural tube closure in mammals. *Cell. Mol. Life Sci.* (2012). doi: [10.1007/s00018-012-1227-7](https://doi.org/10.1007/s00018-012-1227-7); pmid: [23242429](https://pubmed.ncbi.nlm.nih.gov/23242429/)
- A. J. Copp, N. D. E. Greene, Genetics and development of neural tube defects. *J. Pathol.* **220**, 217 (2010). pmid: [19918803](https://pubmed.ncbi.nlm.nih.gov/19918803/)
- J. B. Wallingford, Neural tube closure and neural tube defects: Studies in animal models reveal known knowns and known unknowns. *Am. J. Med. Genet.* **135C**, 59 (2005). doi: [10.1002/ajmg.c.30054](https://doi.org/10.1002/ajmg.c.30054); pmid: [15806594](https://pubmed.ncbi.nlm.nih.gov/15806594/)
- J. F. Colas, G. C. Schoenwolf, Towards a cellular and molecular understanding of neurulation. *Dev. Dyn.* **221**, 117 (2001). doi: [10.1002/dvdy.1144](https://doi.org/10.1002/dvdy.1144); pmid: [11376482](https://pubmed.ncbi.nlm.nih.gov/11376482/)

9. Centers for Disease Control and Prevention (CDC), Neural tube defect surveillance and folic acid intervention—Texas-Mexico border, 1993-1998. *MMWR Morb. Mortal. Wkly. Rep.* **49**, 1 (2000). PMID: 10993565
10. K. L. Deak *et al.*, Further evidence for a maternal genetic effect and a sex-influenced effect contributing to risk for human neural tube defects. *Birth Defects Res. A Clin. Mol. Teratol.* **82**, 662 (2008). doi: [10.1002/bdra.20511](#); PMID: 18937341
11. J. L. Hall, M. J. Harris, D. M. Juriloff, Effect of multifactorial genetic liability to exencephaly on the teratogenic effect of valproic acid in mice. *Teratology* **55**, 306 (1997). doi: [10.1002/\(SICI\)1096-9926\(199705\)55:5<306::AID-TERA2>3.0.CO;2-X](#); PMID: 9261924
12. K. S. Au, A. Ashley-Koch, H. Northrup, Epidemiologic and genetic aspects of spina bifida and other neural tube defects. *Dev. Disabil. Res. Rev.* **16**, 6 (2010). doi: [10.1002/ddrr.93](#); PMID: 20419766
13. G. M. Shaw *et al.*, 118 SNPs of folate-related genes and risks of spina bifida and conotruncal heart defects. *BMC Med. Genet.* **10**, 49 (2009). doi: [10.1186/1471-2350-10-49](#); PMID: 19493349
14. A. M. Molloy, L. C. Brody, J. L. Mills, J. M. Scott, P. N. Kirke, The search for genetic polymorphisms in the homocysteine/folate pathway that contribute to the etiology of human neural tube defects. *Birth Defects Res. A Clin. Mol. Teratol.* **85**, 285 (2009). doi: [10.1002/bdra.20566](#); PMID: 19235830
15. A. F. Oshlan, G. M. Shaw, R. C. Millikan, C. Laurent, R. H. Finnell, Polymorphisms in DNA repair genes as risk factors for spina bifida and orofacial clefts. *Am. J. Med. Genet. A* **135A**, 268 (2005). doi: [10.1002/ajmg.a.30713](#); PMID: 15887293
16. P. X. Tran *et al.*, Association of retinoic acid receptor genes with meningomyelocele. *Birth Defects Res. A Clin. Mol. Teratol.* **91**, 39 (2011). doi: [10.1002/bdra.20744](#); PMID: 21254357
17. D. M. Juriloff, M. J. Harris, A consideration of the evidence that genetic defects in planar cell polarity contribute to the etiology of human neural tube defects. *Birth Defects Res. A Clin. Mol. Teratol.* **94**, 824 (2012). doi: [10.1002/bdra.23079](#); PMID: 23024041
18. S. G. Obican, R. H. Finnell, J. L. Mills, G. M. Shaw, A. R. Scialli, Folic acid in early pregnancy: A public health success story. *FASEB J.* **24**, 4167 (2010). doi: [10.1096/fj.10-165084](#); PMID: 20631328
19. J. S. Sheffield, E. L. Butler-Koster, B. M. Casey, D. McIntire, K. J. Leveno, Maternal diabetes mellitus and infant malformations. *Obstet. Gynecol.* **100**, 925 (2002). doi: [10.1016/S0029-7844\(02\)02242-1](#); PMID: 12423854
20. G. M. Shaw, E. M. Velie, D. Schaffer, Risk of neural tube defect-affected pregnancies among obese women. *JAMA* **275**, 1093 (1996). doi: [10.1001/jama.1996.03530380035028](#); PMID: 8601928
21. E. J. Lammer, L. E. Sever, G. P. Oakley Jr., Valproic acid. *Teratology* **35**, 465 (1987). doi: [10.1002/tera.1420350319](#); PMID: 3114906
22. L. McLeod, J. G. Ray, Prevention and detection of diabetic embryopathy. *Community Genet.* **5**, 33 (2002). doi: [10.1159/000064629](#); PMID: 14960898
23. J. G. Ray, T. E. O'Brien, W. S. Chan, Preconception care and the risk of congenital anomalies in the offspring of women with diabetes mellitus: A meta-analysis. *QJM* **94**, 435 (2001). doi: [10.1093/qjmed/94.8.435](#); PMID: 11493721
24. G. M. Shaw *et al.*, Neural tube defects associated with maternal periconceptional dietary intake of simple sugars and glycemic index. *Am. J. Clin. Nutr.* **78**, 972 (2003). PMID: 14594784
25. D. K. Waller *et al.*, Are obese women at higher risk for producing malformed offspring? *Am. J. Obstet. Gynecol.* **170**, 541 (1994). PMID: 8116710
26. M. M. Werler, C. Louik, S. Shapiro, A. A. Mitchell, Prepregnant weight in relation to risk of neural tube defects. *JAMA* **275**, 1089 (1996). doi: [10.1001/jama.1996.03530380031027](#); PMID: 8601927
27. K. A. Hendricks, O. M. Nuno, L. Suarez, R. Larsen, Effects of hyperinsulinemia and obesity on risk of neural tube defects among Mexican Americans. *Epidemiology* **12**, 630 (2001). doi: [10.1097/00001648-200111000-00009](#); PMID: 11679789
28. K. J. Meador *et al.*, In utero antiepileptic drug exposure: Fetal death and malformations. *Neurology* **67**, 407 (2006). doi: [10.1212/01.wnl.0000227919.81208.b2](#); PMID: 16894099
29. H. Kanai, A. Sawa, R.-W. Chen, P. Leeds, D.-M. Chuang, Valproic acid inhibits histone deacetylase activity and suppresses excitotoxicity-induced GADPH nuclear accumulation and apoptotic death in neurons. *Pharmacogenomics J.* **4**, 336 (2004). doi: [10.1038/sj.tpj.6500269](#); PMID: 15289798
30. E. Yildirim *et al.*, Valproate administration to mice increases histone acetylation and 5-lipoxygenase content in the hippocampus. *Neurosci. Lett.* **345**, 141 (2003). doi: [10.1016/S0304-3940\(03\)00490-7](#); PMID: 12821190
31. N. D. Greene, P. Stanier, G. E. Moore, The emerging role of epigenetic mechanisms in the etiology of neural tube defects. *Epigenetics* **6**, 875 (2011). doi: [10.4161/epi.6.7.16400](#); PMID: 21613818
32. W. Lin *et al.*, Proper expression of the Gcn5 histone acetyltransferase is required for neural tube closure in mouse embryos. *Dev. Dyn.* **237**, 928 (2008). doi: [10.1002/dvdy.21479](#); PMID: 18330926
33. J. P. M. Barbera *et al.*, Folic acid prevents exencephaly in Cited2 deficient mice. *Hum. Mol. Genet.* **11**, 283 (2002). doi: [10.1093/hmg/11.3.283](#); PMID: 11823447
34. C. J. Phiel *et al.*, Histone deacetylase is a direct target of valproic acid, a potent anticonvulsant, mood stabilizer, and teratogen. *J. Biol. Chem.* **276**, 36734 (2001). doi: [10.1074/jbc.M101287200](#); PMID: 11473107
35. A. Drugan, A. Weissman, M. I. Evans, Screening for neural tube defects. *Clin. Perinatol.* **28**, 279, vii (2001). doi: [10.1016/S0095-5108\(05\)70083-X](#); PMID: 11499052
36. R. M. Bowman, D. G. McLone, J. A. Grant, T. Tomita, J. A. Ito, Spina bifida outcome: A 25-year prospective. *Pediatr. Neurosurg.* **34**, 114 (2001). doi: [10.1159/000056005](#); PMID: 11359098
37. N. S. Adzick, Fetal surgery for myelomeningocele: trials and tribulations. *J. Pediatr. Surg.* **47**, 273 (2012). doi: [10.1016/j.jpedsurg.2011.11.021](#); PMID: 22325376
38. M. Dennis, M. A. Barnes, The cognitive phenotype of spina bifida meningomyelocele. *Dev Disabil Res Rev* **16**, 31 (2010). doi: [10.1002/ddrr.89](#); PMID: 20419769
39. MRC Vitamin Study Research Group, Prevention of neural tube defects: Results of the Medical Research Council Vitamin Study. *Lancet* **338**, 131 (1991). doi: [10.1016/0140-6736\(91\)90133-A](#); PMID: 1677062
40. R. J. Berry *et al.*, Prevention of neural-tube defects with folic acid in China. China-U.S. N. Engl. J. Med. **341**, 1485 (1999). doi: [10.1056/NEJM19991113412001](#); PMID: 10559448
41. M. A. Canfield *et al.*, Changes in the birth prevalence of selected birth defects after grain fortification with folic acid in the United States: Findings from a multi-state population-based study. *Birth Defects Res. A Clin. Mol. Teratol.* **73**, 679 (2005). doi: [10.1002/bdra.20210](#); PMID: 16240378
42. M. A. Honein, L. J. Paulozzi, T. J. Mathews, J. D. Erickson, L. Y. Wong, Impact of folic acid fortification of the US food supply on the occurrence of neural tube defects. *JAMA* **285**, 2981 (2001). doi: [10.1001/jama.285.23.2981](#); PMID: 11410096
43. L. J. Williams *et al.*, Prevalence of spina bifida and anencephaly during the transition to mandatory folic acid fortification in the United States. *Teratology* **66**, 33 (2002). doi: [10.1002/tera.10060](#); PMID: 12115778
44. P. De Wals *et al.*, Reduction in neural-tube defects after folic acid fortification in Canada. *N. Engl. J. Med.* **357**, 135 (2007). doi: [10.1056/NEJMoa067103](#); PMID: 17625125
45. J. S. López-Camelo *et al.*, Reduction of birth prevalence rates of neural tube defects after folic acid fortification in Chile. *Am. J. Med. Genet. A* **135A**, 120 (2005). doi: [10.1002/ajmg.a.30651](#); PMID: 15846825
46. J. A. Piedrahita *et al.*, Mice lacking the folic acid-binding protein Folb1 are defective in early embryonic development. *Nat. Genet.* **23**, 228 (1999). doi: [10.1038/13861](#); PMID: 10508523
47. J. Gelineau-van Waes *et al.*, Embryonic development in the reduced folate carrier knockout mouse is modulated by maternal folate supplementation. *Birth Defects Res. A Clin. Mol. Teratol.* **82**, 494 (2008). doi: [10.1002/bdra.20453](#); PMID: 18383508
48. J. Momb *et al.*, Deletion of Mthfd1l causes embryonic lethality and neural tube and craniofacial defects in mice. *Proc. Natl. Acad. Sci. U.S.A.* **110**, 549 (2013). doi: [10.1073/pnas.1211199110](#); PMID: 23267094
49. M. J. Harris, Insights into prevention of human neural tube defects by folic acid arising from consideration of mouse mutants. *Birth Defects Res. A Clin. Mol. Teratol.* **85**, 331 (2009). doi: [10.1002/bdra.20552](#); PMID: 19117321
50. B. S. Mosley *et al.*, Neural tube defects and maternal folate intake among pregnancies conceived after folic acid fortification in the United States. *Am. J. Epidemiol.* **169**, 9 (2009). doi: [10.1093/aje/kwn331](#); PMID: 18953063
51. J. D. Gray *et al.*, Functional interactions between the LRP6 WNT co-receptor and folate supplementation. *Hum. Mol. Genet.* **19**, 4560 (2010). doi: [10.1093/hmg/ddq384](#); PMID: 20843827
52. A. Marean, A. Graf, Y. Zhang, L. Niswander, Folic acid supplementation can adversely affect murine neural tube closure and embryonic survival. *Hum. Mol. Genet.* **20**, 3678 (2011). doi: [10.1093/hmg/ddr289](#); PMID: 21693562
53. E. B. Hook, A. E. Czeizel, Can terathanasia explain the protective effect of folic-acid supplementation on birth defects? *Lancet* **350**, 513 (1997). doi: [10.1016/S0140-6736\(97\)01342-1](#); PMID: 9274597
54. C. C. Y. Li *et al.*, A sustained dietary change increases epigenetic variation in isogenic mice. *PLoS Genet.* **7**, e1001380 (2011). doi: [10.1371/journal.pgen.1001380](#); PMID: 21541011
55. J. W. Hollingsworth *et al.*, In utero supplementation with methyl donors enhances allergic airway disease in mice. *J. Clin. Invest.* **118**, 3462 (2008). PMID: 18802477
56. M. J. Whitrow, V. M. Moore, A. R. Rumbold, M. J. Davies, Effect of supplemental folic acid in pregnancy on childhood asthma: A prospective birth cohort study. *Am. J. Epidemiol.* **170**, 1486 (2009). doi: [10.1093/aje/kwp315](#); PMID: 19880541
57. F. J. H. Magdelijns, M. Momms, J. Penders, L. Smits, C. Thijs, Folic acid use in pregnancy and the development of atopy, asthma, and lung function in childhood. *Pediatrics* **128**, e135 (2011). doi: [10.1542/peds.2010-1690](#); PMID: 21690114
58. M. J. Harris, D. M. Juriloff, An update to the list of mouse mutants with neural tube closure defects and advances toward a complete genetic perspective of neural tube closure. *Birth Defects Res. A Clin. Mol. Teratol.* **88**, 653 (2010). doi: [10.1002/bdra.20676](#); PMID: 20740593
59. D. M. Juriloff, M. J. Harris, Hypothesis: The female excess in cranial neural tube defects reflects an epigenetic drag of the inactivating X chromosome on the molecular mechanisms of neural fold elevation. *Birth Defects Res. A Clin. Mol. Teratol.* **94**, 849 (2012). doi: [10.1002/bdra.23036](#); PMID: 22753363
60. C. Pyrgaki, P. Trainor, A.-K. Hadjantonakis, L. Niswander, Dynamic imaging of mammalian neural tube closure. *Dev. Biol.* **344**, 941 (2010). doi: [10.1016/j.ydbio.2010.06.010](#); PMID: 20558153
61. J. B. Wallingford, R. M. Harland, Neural tube closure requires Dishevelled-dependent convergent extension of the midline. *Development* **129**, 5815 (2002). doi: [10.1242/dev.00123](#); PMID: 12421719
62. H. Morita *et al.*, Cell movements of the deep layer of non-neural ectoderm underlie complete neural tube closure in *Xenopus*. *Development* **139**, 1417 (2012). doi: [10.1242/dev.073239](#); PMID: 22378637
63. H. W. Van Straaten, H. C. Janssen, M. C. Peeters, A. J. Copp, J. W. Hekking, Neural tube closure in the chick embryo is multiphasic. *Dev. Dyn.* **207**, 309 (1996). doi: [10.1002/\(SICI\)1097-0177\(199611\)207:3<309::AID-AJ8A>3.0.CO;2-L](#); PMID: 8922530
64. H. W. Van Straaten, I. Sieben, J. W. Hekking, Multistep role for actin in initial closure of the mesencephalic neural groove in the chick embryo. *Dev. Dyn.* **224**, 103 (2002). doi: [10.1002/dvdy.10078](#); PMID: 11984878
65. E. A. Jones *et al.*, Dynamic in vivo imaging of postimplantation mammalian embryos using whole

- embryo culture. *Genesis* **34**, 228 (2002). doi: [10.1002/gene.10162](#); pmid: [12434332](#)
66. R. Massarwa, L. Niswander, In toto live imaging of mouse morphogenesis and new insights into neural tube closure. *Development* **140**, 226 (2013). doi: [10.1242/dev.085001](#); pmid: [23175632](#)
 67. M. J. Harris, D. M. Juriloff, Mouse mutants with neural tube closure defects and their role in understanding human neural tube defects. *Birth Defects Res. A Clin. Mol. Teratol.* **79**, 187 (2007). doi: [10.1002/bdra.20333](#); pmid: [17177317](#)
 68. J. D. Hildebrand, P. Soriano, Shroom, a PDZ domain-containing actin-binding protein, is required for neural tube morphogenesis in mice. *Cell* **99**, 485 (1999). doi: [10.1016/S0092-8674\(00\)81537-8](#); pmid: [10589677](#)
 69. L. M. Lanier *et al.*, Mena is required for neurulation and commissure formation. *Neuron* **22**, 313 (1999). doi: [10.1016/S0896-6273\(00\)81092-2](#); pmid: [10069337](#)
 70. A. J. Koleske *et al.*, Essential roles for the Abl and Arg tyrosine kinases in neurulation. *Neuron* **21**, 1259 (1998). doi: [10.1016/S0896-6273\(00\)80646-7](#); pmid: [9883720](#)
 71. S. L. Haigo, J. D. Hildebrand, R. M. Harland, J. B. Wallingford, Shroom induces apical constriction and is required for hinge-point formation during neural tube closure. *Curr. Biol.* **13**, 2125 (2003). doi: [10.1016/j.cub.2003.11.054](#); pmid: [14680628](#)
 72. J. Roffers-Agarwal, J. B. Xanthos, K. A. Kragtorp, J. R. Miller, Enabled (Xena) regulates neural plate morphogenesis, apical constriction, and cellular adhesion required for neural tube closure in *Xenopus*. *Dev. Biol.* **314**, 393 (2008). doi: [10.1016/j.ydbio.2007.12.010](#); pmid: [18201691](#)
 73. D. T. Fox, M. Peifer, Abelson kinase (Abl) and RhoGEF2 regulate actin organization during cell constriction in *Drosophila*. *Development* **134**, 567 (2007). doi: [10.1242/dev.02748](#); pmid: [17202187](#)
 74. J. B. Wallingford, Planar cell polarity and the developmental control of cell behavior in vertebrate embryos. *Annu. Rev. Cell Dev. Biol.* **28**, 627 (2012). doi: [10.1146/annurev-cellbio-092910-154208](#); pmid: [22905955](#)
 75. J. N. Murdoch, A. J. Copp, The relationship between sonic hedgehog signaling, cilia, and neural tube defects. *Birth Defects Res. A Clin. Mol. Teratol.* **88**, 633 (2010). doi: [10.1002/bdra.20686](#); pmid: [20544799](#)
 76. S. C. Goetz, K. V. Anderson, The primary cilium: A signalling centre during vertebrate development. *Nat. Rev. Genet.* **11**, 331 (2010). doi: [10.1038/nrg2774](#); pmid: [20395968](#)
 77. D. Huangfu *et al.*, Hedgehog signalling in the mouse requires intraflagellar transport proteins. *Nature* **426**, 83 (2003). doi: [10.1038/nature02061](#); pmid: [14603322](#)
 78. I. E. Zohn, K. V. Anderson, L. Niswander, Using genomewide mutagenesis screens to identify the genes required for neural tube closure in the mouse. *Birth Defects Res. A Clin. Mol. Teratol.* **73**, 583 (2005). doi: [10.1002/bdra.20164](#); pmid: [15971254](#)
 79. P. Ybot-Gonzalez, P. Cogram, D. Gerrelli, A. J. Copp, Sonic hedgehog and the molecular regulation of mouse neural tube closure. *Development* **129**, 2507 (2002). pmid: [11973281](#)
 80. E. C. Oh, N. Katsanis, Cilia in vertebrate development and disease. *Development* **139**, 443 (2012). doi: [10.1242/dev.050054](#); pmid: [22223675](#)
 81. C. V. Logan, Z. Abdel-Hamed, C. A. Johnson, Molecular genetics and pathogenic mechanisms for the severe ciliopathies: Insights into neurodevelopment and pathogenesis of neural tube defects. *Mol. Neurobiol.* **43**, 12 (2011). doi: [10.1007/s12035-010-8154-0](#); pmid: [21110233](#)
 82. T. W. Vogel, C. S. Carter, K. Abode-Iyamah, Q. Zhang, S. Robinson, The role of primary cilia in the pathophysiology of neural tube defects. *Neurosurg. Focus* **33**, E2 (2012). doi: [10.3171/2012.6.FOCUS12222](#); pmid: [23025443](#)
 83. T. J. Park, S. L. Haigo, J. B. Wallingford, Ciliogenesis defects in embryos lacking inturned or fuzzy function are associated with failure of planar cell polarity and Hedgehog signaling. *Nat. Genet.* **38**, 303 (2006). doi: [10.1038/ng1753](#); pmid: [16493421](#)
 84. R. S. Gray *et al.*, The planar cell polarity effector Fuz is essential for targeted membrane trafficking, ciliogenesis and mouse embryonic development. *Nat. Cell Biol.* **11**, 1225 (2009). doi: [10.1038/ncb1966](#); pmid: [19767740](#)
 85. J. H. Seo *et al.*, Mutations in the planar cell polarity gene, Fuzzy, are associated with neural tube defects in humans. *Hum. Mol. Genet.* **20**, 4324 (2011). doi: [10.1093/hmg/ddr359](#); pmid: [21840926](#)
 86. Z. Kibar *et al.*, Mutations in VANGL1 associated with neural-tube defects. *N. Engl. J. Med.* **356**, 1432 (2007). doi: [10.1056/NEJMoa060651](#); pmid: [17409324](#)
 87. J. B. Wallingford, R. M. Harland, *Xenopus* Dishevelled signaling regulates both neural and mesodermal convergent extension: Parallel forces elongating the body axis. *Development* **128**, 2581 (2001). pmid: [11493574](#)
 88. J. Wang *et al.*, Dishevelled genes mediate a conserved mammalian PCP pathway to regulate convergent extension during neurulation. *Development* **133**, 1767 (2006). doi: [10.1242/dev.02347](#); pmid: [16571627](#)
 89. P. Ybot-Gonzalez *et al.*, Convergent extension, planar-cell-polarity signalling and initiation of mouse neural tube closure. *Development* **134**, 789 (2007). doi: [10.1242/dev.000380](#); pmid: [17229766](#)
 90. M. Marin-Padilla, Study of the vertebral column in human craniorhachischisis. The significance of the notochordal alterations. *Acta Anat. (Basel)* **63**, 32 (1966). doi: [10.1159/000142778](#); pmid: [5911674](#)
 91. I. Kirilova *et al.*, Expression of the sonic hedgehog gene in human embryos with neural tube defects. *Teratology* **61**, 347 (2000). doi: [10.1002/\(SICI\)1096-9926\(200005\)61:5<347::AID-TERA6>3.0.CO;2-#](#); pmid: [10777830](#)
 92. G. W. E. Santen *et al.*, Mutations in SWI/SNF chromatin remodeling complex gene ARID1B cause Coffin-Siris syndrome. *Nat. Genet.* **44**, 379 (2012). doi: [10.1038/ng.2217](#); pmid: [22426309](#)
 93. Y. Tsurusaki *et al.*, Mutations affecting components of the SWI/SNF complex cause Coffin-Siris syndrome. *Nat. Genet.* **44**, 376 (2012). doi: [10.1038/ng.2219](#); pmid: [22426308](#)
 94. D. C. Hargreaves, G. R. Crabtree, ATP-dependent chromatin remodeling: Genetics, genomics and mechanisms. *Cell Res.* **21**, 396 (2011). doi: [10.1038/cr.2011.32](#); pmid: [21358755](#)
 95. L. Wang *et al.*, Relation between hypomethylation of long interspersed nucleotide elements and risk of neural tube defects. *Am. J. Clin. Nutr.* **91**, 1359 (2010). doi: [10.3945/ajcn.2009.28858](#); pmid: [20164316](#)
 96. N. D. Greene, A. J. Copp, Inositol prevents folate-resistant neural tube defects in the mouse. *Nat. Med.* **3**, 60 (1997). doi: [10.1038/nm0197-60](#); pmid: [8986742](#)
 97. J. G. Ray *et al.*, Vitamin B12 and the risk of neural tube defects in a folic-acid-fortified population. *Epidemiology* **18**, 362 (2007). doi: [10.1097/01.ede.0000257063.77411.e9](#); pmid: [17474166](#)
 98. A. C. Dey *et al.*, Maternal and neonatal serum zinc level and its relationship with neural tube defects. *J. Health Popul. Nutr.* **28**, 343 (2010). doi: [10.3329/jhpn.v28i4.6040](#); pmid: [20824977](#)
 99. M. Eiraku *et al.*, Self-organizing optic-cup morphogenesis in three-dimensional culture. *Nature* **472**, 51 (2011). doi: [10.1038/nature09941](#); pmid: [21475194](#)
 100. H. Suga *et al.*, Self-formation of functional adeno-hypophysis in three-dimensional culture. *Nature* **480**, 57 (2011). doi: [10.1038/nature10637](#); pmid: [22080957](#)
 101. P. W. Yoon *et al.*, The National Birth Defects Prevention Study. *Public Health Rep.* **116** (suppl. 1), 32 (2001). doi: [10.1093/phr/116.S1.32](#); pmid: [11889273](#)
 102. C. Lee, H. M. Scherr, J. B. Wallingford, Shroom family proteins regulate gamma-tubulin distribution and microtubule architecture during epithelial cell shape change. *Development* **134**, 1431 (2007). doi: [10.1242/dev.02828](#); pmid: [17329357](#)

Acknowledgments: This review grew from conversations at the 7th International Conference on Neural Tube Defects, sponsored by the National Institute of Child Health and Human Development. We thank V. Grier and E. Stauber for help with the manuscript and C. Fees and C. Lee for movies. This work was supported by grants from the NIH: R01NS058979 (L.A.N.), R01NS050249 (G.M.S.), R01NS076465 (R.H.F.), P01HD067244 (R.H.F. and G.M.S.), and 5R01GM074104 (J.B.W.). J.B.W. and L.A.N. are investigators of the Howard Hughes Medical Institute. The 8th International Conference on Neural Tube Defects will be held 7 to 10 October 2013. Contact rfinnell@austin.utexas.edu for more details.

10.1126/science.1222002

A Black Hole Nova Obscured by an Inner Disk Torus

J. M. Corral-Santana,^{1,2*} J. Casares,^{1,2} T. Muñoz-Darias,³ P. Rodríguez-Gil,^{1,2} T. Shahbaz,^{1,2} M. A. P. Torres,^{4,5} C. Zurita,^{1,2} A. A. Tyndall^{6,7,8}

Stellar-mass black holes (BHs) are mostly found in x-ray transients, a subclass of x-ray binaries that exhibit violent outbursts. None of the 50 galactic BHs known show eclipses, which is surprising for a random distribution of inclinations. Swift J1357.2–093313 is a very faint x-ray transient detected in 2011. On the basis of spectroscopic evidence, we show that it contains a BH in a 2.8-hour orbital period. Further, high-time-resolution optical light curves display profound dips without x-ray counterparts. The observed properties are best explained by the presence of an obscuring toroidal structure moving outward in the inner disk, seen at very high inclination. This observational feature should play a key role in models of inner accretion flows and jet collimation mechanisms in stellar-mass BHs.

Stellar-mass black holes (BHs) are fundamental to our knowledge of supernova explosions and stellar evolution (1). In ~45 years of x-ray astronomy, only 18 BHs have

been dynamically confirmed in the Milky Way, whereas ~32 other x-ray binaries are suspected to contain a BH because they have similar x-ray properties (2). BHs orbiting massive donor stars can produce x-ray eclipses even at moderately low inclinations, as exemplified by the bright, persistent, extragalactic x-ray binary M33 X-7 (3). Conversely, none of the ~50 galactic BH transients with low-mass donors show eclipses, even though ~10 are expected for an isotropic distribution of inclinations (4). This implies that selection effects prevent high-inclination BH transients from being detected, and the most commonly used explanation calls for obscuration of the x-rays by a flared accretion disk. Consequently, a large population of faint high-inclination BHs seems to be missed by current x-ray surveys.

The very faint x-ray transient Swift J1357.2–093313 was detected by the Swift Burst Alert Telescope (BAT) in January 2011. We used the 2.5-m Isaac Newton Telescope and the 4.2-m William Herschel Telescope (WHT) to obtain spectroscopic observations of Swift J1357.2–093313 during the outburst episode between 25 February and 13 April 2011. The averaged spectra (Fig. 1) show a remarkably broad double-peaked H α emission line, with a full width at half maximum (FWHM) of ~3300 km s^{−1}. The current widest H α emission profile is observed in XTE J1118+480 (FWHM ~2500 km s^{−1}) (5), an 8-solar mass (M_{\odot}) BH in a 4 hour orbit seen at 68° inclination (6). Larger projected velocities require a more massive BH, a shorter orbital period, a higher inclination angle, or a combination of these three parameters. A double-peaked profile is the signature of gas orbiting in a Keplerian accretion disk geometry (7), with the peak-to-peak separation driven by the projected velocities at the outer edge of the disk. From the H α profiles, we measured a weighted average double-peak separation of 1790 ± 67 km s^{−1}. This can be used to estimate the radial velocity semi-amplitude, K_c , of the companion star in x-ray transients (8, 9), yielding a value of $K_c \geq 690$ km s^{−1} (10). Furthermore, the radial velocities of the H α wings are modulated with a 2.8 ± 0.3 -hour period (Fig. 1), due to the motion of the inner accretion disk around the binary's center of mass. The 2.8-hour orbital period, combined with our limit to the projected velocity amplitude of the donor star, imply a mass function [i.e., an absolute lower limit to the mass of the compact object (10)] of $f(M_c) > 3.0 M_{\odot}$ at a 95.4% confidence level, and hence the confirmation of a BH because it exceeds the maximum mass possible for a neutron star (11).

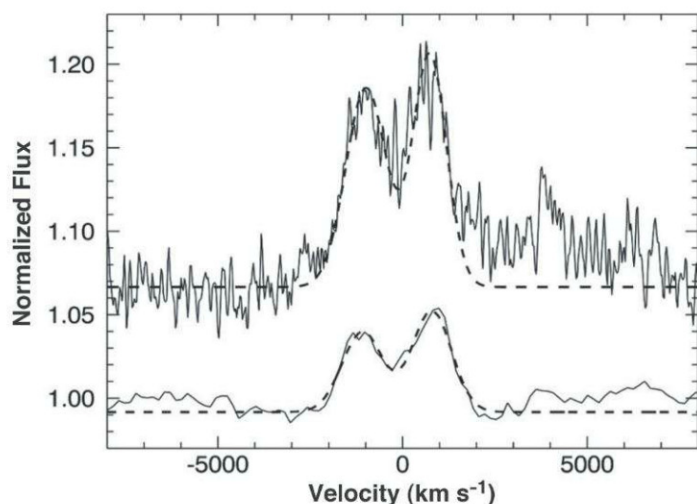
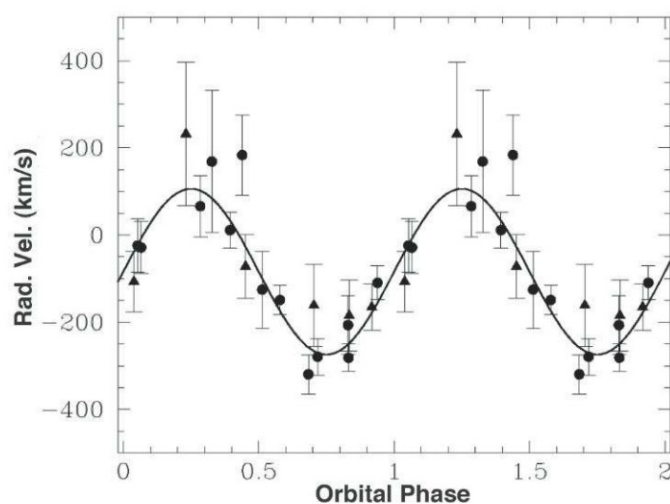


Fig. 1. Average H α emission line profiles and radial velocity curve of the H α emission line folded on the 2.8-hour period. **(Left)** The line weakens from equivalent widths = 6 to 9 Å on 25 to 27 February to 2.1 Å on 19 March 2011. A vertical offset has been applied for clarity. The H α line is the only strong emission feature detected in the optical spectra. Two Gaussian fits to the



double-peaked profiles are also shown (dashed lines). **(Right)** The velocities were obtained using a double Gaussian passband with a separation of 2600 km s^{−1}. Phase zero corresponds to heliocentric Julian date (HJD) 2455640.588. Solid circles indicate WHT velocities from 19 March, and solid triangles indicate INT velocities on 25 to 27 February. The best sine fit is shown (solid line).

¹Instituto de Astrofísica de Canarias, E-38205 La Laguna, S/C de Tenerife, Spain. ²Departamento de Astrofísica, Universidad de La Laguna E-38206 La Laguna, S/C de Tenerife, Spain. ³School of Physics and Astronomy, University of Southampton, Southampton SO17 1BJ, UK. ⁴SRON, Netherlands Institute for Space Research, 3584 CA, Utrecht, Netherlands. ⁵Harvard-Smithsonian Center for Astrophysics, 60 Garden Street, Cambridge, MA 02138, USA. ⁶Jodrell Bank Centre for Astrophysics, University of Manchester, Manchester M13 9PL, UK. ⁷European Southern Observatory, Alonso de Córdova 3107 Casilla 19001, Santiago, Chile. ⁸Isaac Newton Group of Telescopes, Apartado de Correos 321 E-38700, S/C de La Palma, Spain.

*To whom correspondence should be addressed. E-mail: jcorral@iac.es

Optical imaging observations were taken using the 0.82-m IAC80, the 1.2-m Mercator (MT), the 2.0-m Liverpool (LT) and the INT telescopes on 16 nights between March and July 2011 (table S1) during the smooth decay from outburst. We used very short exposure times on six of the nights, resulting in time resolutions ranging from 7 to 22 s. This was crucial to reveal the fast variability structure in the light curves, which unveils the presence of striking dipping variability (Fig. 2). Further, the high time resolution allowed us to resolve the complex structure of the dip profiles into multiple irregular eclipse-like features (Fig. 2C). In order to explore the timing prop-

erties of the dips, we computed Lomb-Scargle periodograms of the high-time-resolution data (Fig. 3). The power density spectra (PDS) reveal a strong peak produced by the dip recurrence period (DRP), which migrates from 2.3 to 7.5 min over our 69-day baseline. We found no evidence for modulation on the 2.8-hour orbital period over the entire photometric database.

The dipping activity in Swift J1357.2–093313 is reminiscent of neutron star x-ray dippers (12), where the dips are interpreted as the occultation of the central x-ray source by an azimuthally structured outer disk rim seen at $\sim 70^\circ$ inclination (12). However, unlike the behavior of known

x-ray dippers, the short repeatability time scale observed in Swift J1357.2–093313 (~ 2 to 8 min, which is a tiny fraction of the orbital period) and the changing recurrence period of the optical dips indicate that the eclipsing material is not phase-locked to the disk rim. Instead, the dips in Swift J1357.2–093313 can be produced only by fast and regular occultations of bright optically thick regions by a vertically extended structure well within the disk. Further, the FWHM duration of the dips is $\sim 50\%$ of their recurrence time, implying that the obscuring geometry extends $\sim 180^\circ$; i.e., an inner disk torus of variable height (perhaps tilted with respect to the binary plane) or a warp.

Several scenarios can in principle explain the formation of inner disk structures. Numerical simulations performed for extreme mass ratio systems show that x-ray irradiation by the central source can generate a torque that triggers a twist or warp (13). The precession of the warp generates a superhump modulation at approximately the orbital period, which is substantially longer than our DRP. Alternatively, the Bardeen-Petterson effect around a rapidly rotating compact object can cause a tilted accretion disk to warp into the equatorial plane at a few tens of gravitational radii (R_g 's) and naturally produce photometric modulations (14). However, under the assumption that the DRP reflects the Keplerian frequency of the obscuring wall, this would be placed at much larger distances ($\sim 10^3$ to $10^4 R_g$) than predicted by Lense-Thirring simulations (15, 16). Also, our observations of an increasing DRP provide the signature of a traveling wave propagating outward (Fig. 3).

The detection of optical dips requires the observer's line of sight to be close to the plane of the binary orbit; also the remarkable dipping amplitude of up to 0.8 magnitude (mag) implies grazing eclipses of a compact source with a 50% reduction in flux, which suggest large inclinations $i \geq 70^\circ$. Why doesn't the companion star eclipse the optical source at these high inclinations? Unlike neutron star x-ray binaries, Swift J1357.2–093313 has a very extreme mass ratio $q = M_c/M_x < 0.06$, where M_c and M_x stand for the mass of the companion star and the compact object, respectively (10). Assuming a typical disk extending up to the tidal truncation radius (17) and with scale height $\alpha = 12^\circ$ (18), the small q results in a donor star radius comparable to or smaller than the disk's outer rim. Thus, the central disk regions are never eclipsed by the donor star even at the extreme scenario of an edge-on geometry (fig. S3). In addition, regardless of the inner disk's elevation, the donor star is always sheltered from irradiation by the outer disk, preventing the production of orbitally modulated optical light curves. We estimate that the donor is consistent with a slightly evolved M4.5 star with $M_c = 0.24 M_\odot$ and $R_c = 0.29 R_\odot$ (10).

To further constrain the binary inclination, we searched for the presence of x-ray eclipses or dips in the public Rossi X-ray Timing Explorer (RXTE) archive between 2 February and 2 April 2011,

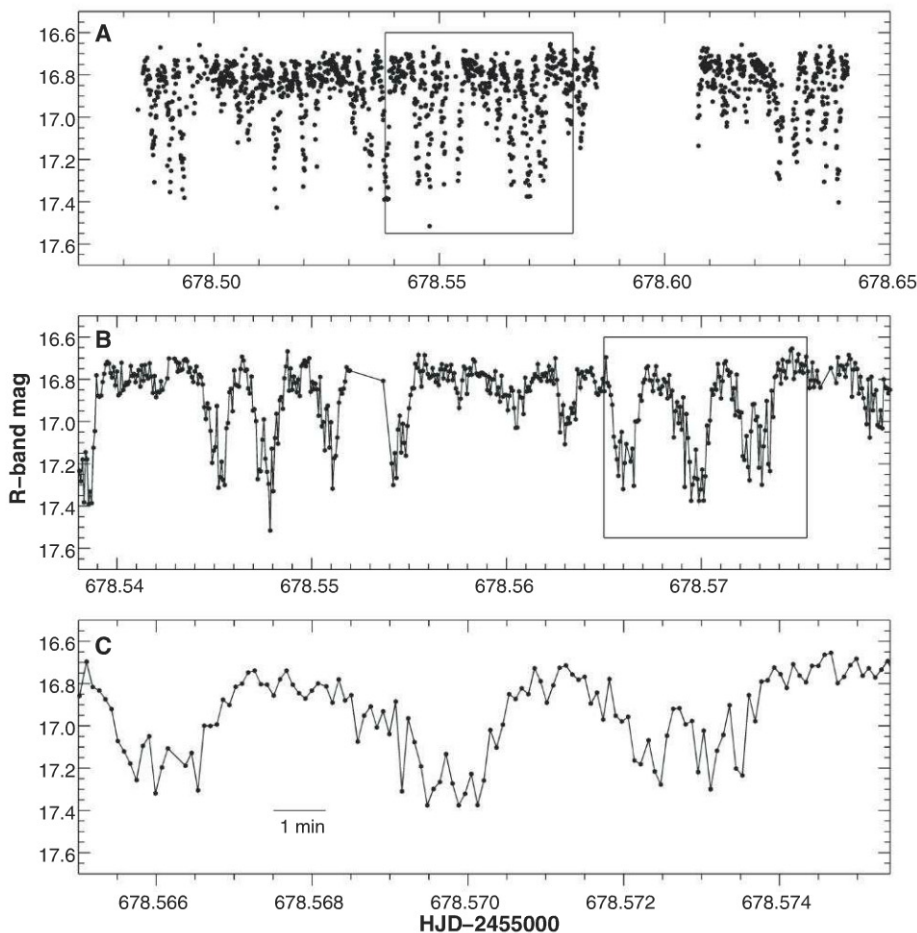


Fig. 2. The optical light curve of Swift J1357.2–093313 taken on 26 April 2011 with the INT. (A) The time resolution is 7 s, whereas the total duration of the observing run was 3.8 hours. Regular dips cause a drop in brightness of up to ≈ 0.8 mag. (B) A closeup of the box indicated in (A) with a length of 1 hour. Dips have a characteristic (FWHM) size of 2 min and recur every 4 min, hence their duty cycle is $\sim 50\%$, which is substantially larger than the typical 10 to 30% duty cycles observed in neutron star dippers. The depth of the dips also appears modulated, with a time scale of ~ 30 min. (C) A 15-min closeup of the box indicated in (B). The complex structure of the dip profiles indicates that the obscuring region is clumpy and has considerable structure. Large intensity drops of 0.4 mag ($\sim 30\%$ reduction in flux) are seen on time scales not resolved by our 7-s time resolution, implying that the eclipsed region is very compact. Alternatively, it may be composed of a distribution of small emission knots. Assuming that the DRP is driven by the orbital frequency of a vertical disk annulus around a $10 M_\odot$ BH, its Keplerian velocity is $\sim 3150 \text{ km s}^{-1}$. Our 7-s time resolution, therefore, sets an upper limit to the size of the eclipsed optical region (or individual emitting knots) of $\sim 0.03 R_\odot$. This is $\sim 2\%$ the size of a typical accretion disk extending to the tidal truncation radius (17) in a 2.8-hour BH binary. Each of our 16 night light curves displays similar dipping activity, but it is only resolved in detail on the 6 nights sampled at high time resolution.

but could not find any (10). Eclipses of x-ray photons scattered by a disk corona are typically seen in neutron star x-ray binaries at high $i \gtrsim 80^\circ$ (19, 20). However, these may be too shallow and hardly detectable in Swift J1357.2–093313, given the very small size of the donor star and the inner disk torus as compared to that of a putative disk corona. We also note that no signature of dips, eclipses, or modulations was detected in Swift/XRT data (21).

At a distance of ~ 1.6 kpc (10), Swift J1357.2–093313 has an unusually weak x-ray peak luminosity $L_x \sim 1.7 \times 10^{35}$ erg s $^{-1}$. The x-ray-to-optical luminosity ratio L_x (2 to 11 keV)/ L_{opt} (3000 to 7000 Å) ~ 57 is also atypically low for an x-ray transient in outburst (22). These properties are reminiscent of accretion disk corona sources, where the central engine is hidden from

view and only x-rays scattered into our line of sight by material above the disk plane can be seen. The unique features of Swift J1357.2–093313 (namely, its very low x-ray luminosity, striking optical dips, lack of orbital modulation, and extremely broad H α profile) can thus be explained by orientation effects in an edge-on geometry. However, at variance with the commonly accepted scenario, based on Milgrom's model (23), our observations reveal that the central BH is hidden by an inner toroidal structure rather than the outer disk rim. Orientation effects are also invoked to explain the observable properties of active galactic nuclei (AGNs), where Seyfert 2 objects are thought to be edge-on AGNs obscured by an opaque torus (24). In this framework, it is tempting to view Swift J1357.2–093313 as a scaled-down version of the Seyfert 2 scenario, where distinct observ-

able properties are a consequence of geometrically thick inner disk structures seen at very high inclination.

Inner disk doughnuts might be ubiquitous in erupting x-ray binaries, at least during the hard state, when there is emission from compact jets [see (25) for a review on BH states]: a state in which Swift J1357.2–093313 remained through the entire outburst (10, 21, 26, 27). This observational feature may be a key to understand the poorly known accretion-ejection connection and the collimation of jet outflows (28) observed during the transition from the hard to the soft state. Standard mechanisms for jet production require both high angular velocities and strong poloidal magnetic fields which, in turn, depend on the disk height. Geometrically thick, inner disk regions such as that observed in Swift J1357.2–093313 provide the best environment for jet formation (29). Incidentally, a radio detection of Swift J1357.2–093313 was reported during outburst, presumably associated with compact jet emission (27). In this regard, it has been proposed that (irradiation-induced) equatorial disk winds develop during BH soft states but not in the jet/hard x-ray state (30). The presence of inner vertical structures is relevant to this picture because it prevents a large irradiation of the outer disk, thus providing an explanation for the absence of equatorial winds in the hard state. This scenario is consistent with the results reported in (21), which imply that the accretion disk in Swift J1357.2–093313 is not irradiated.

The detection of an edge-on BH has been possible because of its proximity. With a maximum flux of 30 mCrab in the 15- to 50-keV band, Swift J1357.2–093313 was barely detected by the BAT onboard Swift (31); were it placed just farther than ~ 1.9 kpc, it would have not reached a 3σ detection. In addition, with a galactic latitude $b = +50^\circ$, it is located in the halo at ~ 1.2 kpc above the galactic plane, where the absorption column N_H is minimal. Other edge-on BHs sitting on the galactic plane would certainly be affected by interstellar extinction, which makes their outbursts difficult to detect by soft x-ray wide-field cameras such as the RXTE All-Sky Monitor.

Some of these may be associated with the increasing population of very faint x-ray transients, a class of x-ray transients recently detected (32). Clearly, the fortuitous short distance and the dramatic optical dips have led to the detection and characterization of Swift J1357.2–093313, a prototype of the hitherto missing population of high-inclination BH x-ray transients.

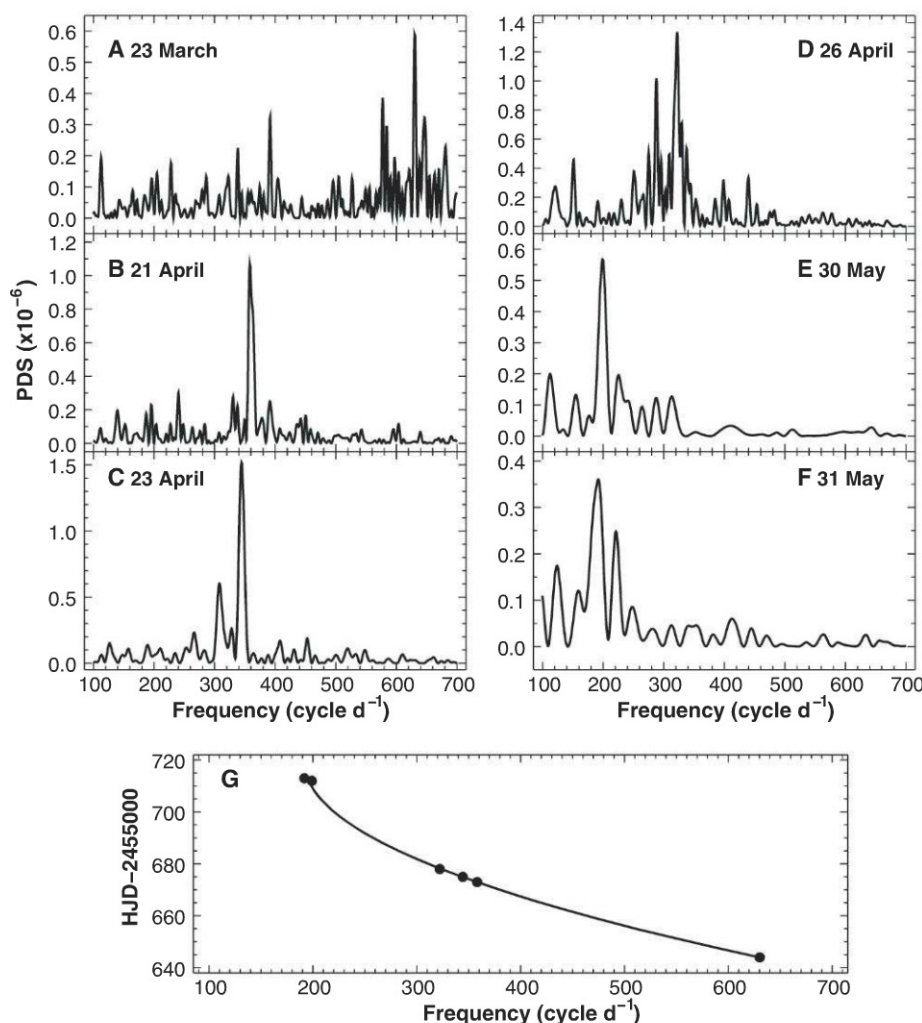


Fig. 3. Time evolution of the optical DRP. (A to F) The panels display the PDS of the six high-time-resolution nights. The highest peak shifts from 2.3 min (~ 630 cycles day $^{-1}$) to 7.5 min (~ 192 cycles day $^{-1}$) over 69 days. (G) The frequency shift as a function of time with the best parabolic fit (solid line): $\nu_{\text{DRP}} = 7.7 \times 10^{-2} T^2 - 111.218 T + 40192.4$, with ν_{DRP} the DRP frequency, $T = \text{HJD} - 2455000$ and HJD representing the HJD of the observation. Assuming that the DRP period reflects the Keplerian frequency of a particular disk annulus in the gravitational field of a $10 M_\odot$ BH, this frequency corresponds to just ≈ 1600 Schwarzschild radii. Further, the 2.3-min DRP on 23 March is produced at $0.12 R_\odot$, whereas the 7.5-min DRP on 31 May is at $0.27 R_\odot$. Consequently, the disk annulus responsible for the DRP has moved outward by $0.15 R_\odot$ in 69 days at an average speed of 17 m s^{-1} .

References and Notes

1. C. L. Fryer, V. Kalogera, *Astrophys. J.* **554**, 548 (2001).
2. F. Özel, D. Psaltis, R. Narayan, J. E. McClintock, *Astrophys. J.* **725**, 1918 (2010).
3. J. A. Orosz et al., *Nat. Phys.* **449**, 872 (2007).
4. R. Narayan, J. E. McClintock, *Astrophys. J.* **623**, 1017 (2005).
5. M. A. P. Torres et al., *Astrophys. J.* **612**, 1026 (2004).
6. D. M. Gelino et al., *Astrophys. J.* **642**, 438 (2006).

7. J. Smak, *Acta Astronom.* **19**, 155 (1969).
8. J. A. Orosz, C. D. Bailyn, R. A. Remillard, J. E. McClintock, C. B. Foltz, *Astrophys. J.* **436**, 848 (1994).
9. J. A. Orosz, C. D. Bailyn, *Astrophys. J.* **446**, L59 (1995).
10. See the supplementary materials on Science Online.
11. V. Kalogera, G. Baym, *Astrophys. J.* **470**, L61 (1996).
12. N. E. White, K. O. Mason, *Space Sci. Rev.* **40**, 167 (1985).
13. S. B. Foulkes, C. A. Haswell, J. R. Murray, *Mon. Not. R. Astron. Soc.* **366**, 1399 (2006).
14. J. M. Bardeen, J. A. Petterson, *Astrophys. J.* **195**, L65 (1975).
15. J. Lense, H. Thirring, *Phys. Z.* **19**, 156 (1918).
16. A. Ingram, C. Done, P. C. Fragile, *Mon. Not. R. Astron. Soc.* **397**, L101 (2009).
17. A. King, in *X-ray Binaries*, W. H. G. Lewin, J. van Paradijs, E. P. J. van den Heuvel, Eds. (Cambridge Univ. Press, Cambridge, 1997), p. 419.
18. J. A. de Jong, J. van Paradijs, T. Augusteijn, *Astron. Astrophys.* **314**, 484 (1996).
19. J. Frank, A. R. King, J.-P. Lasota, *Astron. Astrophys.* **178**, 137 (1987).
20. J. van Paradijs, M. van der Klis, H. Pedersen, *Astron. Astrophys. Suppl. Ser.* **76**, 185 (1988).
21. M. Armas-Padilla, N. Degenaar, D. M. Russell, R. Wijnands, *Mon. Not. R. Astron. Soc.* **428**, 3083 (2013).
22. J. van Paradijs, J. E. McClintock, in *X-ray Binaries*, W. H. G. Lewin, J. van Paradijs, E. P. J. van den Heuvel, Eds. (Cambridge Univ. Press, Cambridge, 1997), p. 58.
23. M. Milgrom, *Astron. Astrophys.* **67**, L25 (1978).
24. R. Antonucci, *Astron. Astrophys. Ann. Rev.* **31**, 473 (1993).
25. J. E. McClintock, R. A. Remillard, in *Compact Stellar X-ray Sources*, W. H. G. Lewin, M. van der Klis, Eds. (Cambridge Univ. Press, Cambridge, 2006), p. 157.
26. H. A. Krimm, J. A. Kennea, S. T. Holland, *The Astronomer's Telegram* **3142**, 1 (2011).
27. G. R. Sivakoff, J. C. A. Miller-Jones, H. A. Krimm, *The Astronomer's Telegram* **3147**, 1 (2011).
28. M. Livio, G. I. Ogilvie, J. E. Pringle, *Astrophys. J.* **512**, 100 (1999).
29. D. L. Meier, *Astrophys. J.* **548**, L9 (2001).
30. G. Ponti et al., *Mon. Not. R. Astron. Soc.* **422**, L11 (2012).
31. H. A. Krimm et al., *The Astronomer's Telegram* **3138**, 1 (2011).
32. A. R. King, R. Wijnands, *Mon. Not. R. Astron. Soc.* **366**, L31 (2006).

Acknowledgments: This work made use of the Image Reduction and Analysis Facility (IRAF) and the MOLLY software developed by T. R. Marsh. We thank P. Charles, G. Ponti, and D. M. Russell for their useful comments; G. Pérez and M. Leal for their help with fig. S3 and movie S1; and I. Negueruela and C. González-Fernández for obtaining the Intermediate Dispersion Spectrograph (IDS) spectra. Based on

observations made with the INT and WHT, operated by the Isaac Newton Group; the LT, operated by the Liverpool John Moores University with financial support from the UK Science and Technology Facilities Council; and the MT, operated by the University of Leuven and the Observatory of Geneva. All of them are installed at the Spanish Observatorio del Roque de Los Muchachos (on the island of La Palma) of the Instituto de Astrofísica de Canarias (IAC). The photometry taken on 26 April 2011 is based on observations made with the INT under the Spanish IAC Director's Discretionary Time. T.M.D. acknowledges funding via a European Union Marie Curie Intra-European Fellowship under contract no. 2011-301355. This research was supported by the Spanish Ministerio de Ciencia e Innovación (MICINN) under grant AYA2010-18080 and partly funded by the Spanish MICINN under the Consolider-Ingenio 2010 Program grant CSD2006-00070: "First science with the GTC" (www.iac.es/consolider-ingenio-gtc/).

Supplementary Materials

www.sciencemag.org/cgi/content/full/339/6123/1048/DC1

Supplementary Text

Figs. S1 to S3

Table S1

References (33–50)

Movie S1

31 July 2012; accepted 20 December 2012

10.1126/science.1228222

Quantitative Magneto-Mechanical Detection and Control of the Barkhausen Effect

J. A. J. Burgess,^{1,2} A. E. Fraser,¹ F. Fani Sani,^{1,2} D. Vick,² B. D. Hauer,¹ J. P. Davis,^{1,2} M. R. Freeman^{1,2*}

Quantitative characterization of intrinsic and artificial defects in ferromagnetic structures is critical to future magnetic storage based on vortices or domain walls moving through nanostructured devices. Using torsional magnetometry, we observe finite size modifications to the Barkhausen effect in the limiting case of a single vortex core interacting with individual pointlike pinning sites in a magnetic thin film. The Barkhausen effect in this limit becomes a quantitative two-dimensional nanoscale probe of local energetics in the film. Tailoring the pinning potential using single-point focused ion beam implantation demonstrates control of the effect and points the way to integrated magneto-mechanical devices incorporating quantum pinning effects.

The Barkhausen effect refers to the stochastic jumps in magnetization resulting from the pinning of magnetic domain patterns (1). Of current interest is how the phenomenon is modified at the smallest scale and the consequent technological implications. Thin-film magnetic disks exhibit a ground-state vortex (2–4) and offer a convenient platform to study a single vortex core. The magnetic vortex core is equivalent to a zero-dimensional domain wall and is often restricted to a radius of less than 10 nanometers (5). The high density of exchange energy within the core enhances local interactions (6–8). A single pointlike pinning site, together with a vortex core, constitutes the simplest sys-

tem to exhibit the Barkhausen effect. Previous work has shown indirect signs of the Barkhausen effect for the vortex state. Local variation in films has been found to cause a stick-slip motion (9) and to increase the frequencies of dynamic modes of the vortex (10–13).

Technologically, domain-wall pinning, and consequently Barkhausen effects, present an opportunity to enhance spintronic memory (14) and construct magnetic logic devices (15, 16). In wire geometries, film imperfections affect domain-wall velocity and energy loss (17), whereas thermal motion of wall structures in wire kinks has been exploited to learn about nonadiabatic spin torque (18). Artificial control of pinning potentials will be important for device applications (16), and focused ion beam modification (19) is emerging as a leading technique.

Nanomechanical torque magnetometry (20, 21) provides an ideal method of measuring minute magnetization (M) changes with minimal influ-

ence on the sample (Fig. 1A). The device is constructed as a paddle supported by thin rods that act as a torsion spring. A single 1- μm -diameter, 42-nm-thick, permalloy disk exhibiting a vortex ground state is fabricated on the paddle. As the field (H) is increased, the vortex core is deflected orthogonally to the field direction, moving it through the film. This permits a torque to be applied to the in-plane magnetic moment by an out-of-plane field, inducing a deflection of the paddle linearly proportional to the magnetization. The deflection is measured by a laser interferometer (21). Energetic interactions between the core and imperfections in the film—thickness variations, grain boundaries, or material impurities—alter the energy cost of shifting the core, leading to concomitant variations in the differential magnetic susceptibility, dM/dH (Fig. 1B). During pinning, the differential susceptibility is suppressed but, crucially, does not vanish, whereas transitions between pinning sites appear as steep sections.

At room temperature all intersite transitions appear continuous and reversible; however, at $T = 77$ K, some transition states become minor hysteresis loops. Bistable states are masked at room temperature by thermally activated intersite hopping. When the hopping rate exceeds the measurement bandwidth (~ 30 Hz), a time-averaged magnetization, weighted by the occupancy of the participating states, is recorded. Investigation at intermediate temperatures shows the convergence of the experimental bandwidth and the hopping frequency as the thermal noise slows (Fig. 2A). This makes the mechanism for the emergence of hysteresis at low temperature clear. Stopping at fixed fields around the hysteresis loop allows traces of Barkhausen telegraph noise to be captured (Fig. 2B). Incrementing the field demonstrates that the lifetimes of the states have strong field dependence. Computation of the lifetimes of the states from telegraph noise

¹Department of Physics, University of Alberta, 4-181 Centennial Centre for Interdisciplinary Science, Edmonton, Alberta T6G 2E1, Canada. ²National Institute for Nanotechnology, 11421 Saskatchewan Drive, Edmonton, Alberta T6G 2M9, Canada.

*To whom correspondence should be addressed. E-mail: mark.freeman@ualberta.ca

traces enables calculation of hopping energy barriers for varied temperatures and fields. An Arrhenius relation is used to describe the dynamics $\tau = f_0^{-1} \exp(\Delta E/k_B T)$ (with $f_0 = 200$ MHz approximating the gyrotropic mode frequency). For separate data runs, the measured energy barrier and hysteresis loop position change slightly, indicating very fine scale instability in the hopping pathway. In the example traces shown in Fig. 2C, the barrier at which occupancy of the two sites is equal is found to be ~ 0.14 eV in the 80- and 90-K traces, whereas it is ~ 0.1 eV in the 60-K trace.

In a perfect disk, the deflection of the core by the applied bias field would lead to a straight path orthogonal to the field. However, the imperfections that introduce pinning and telegraph noise present the possibility of two-dimensional (2D) path deviations from the ideal path. Add-

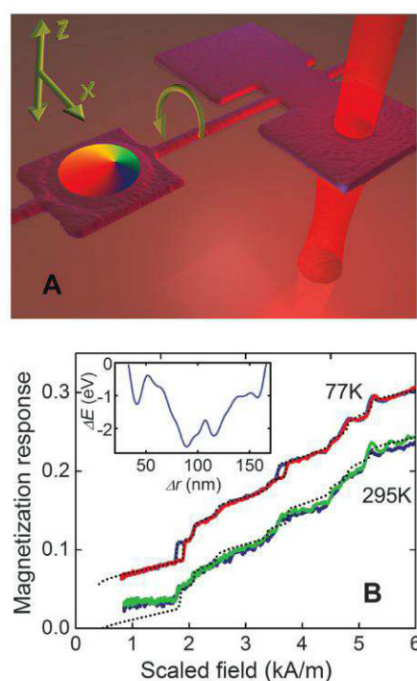


Fig. 1. Device schematic and magnetization curves showing the Barkhausen effect. **(A)** A silicon nitride nanomechanical torque magnetometer holding a ferromagnetic disk is read out using laser interferometry. Inducing magnetization with a static field in-plane (along x) and applying an AC out-of-plane (z) field drives the torsional resonance of the paddle with an amplitude proportional to the magnetization. **(B)** Low-field M - H loops show the influence of pinning sites on dM/dH . At 77 K, bistable states appear in the up (red) and down (blue) sweeps, and at 295 K (offset for clarity) up (green) and down (blue) sweeps are identical. Magnetic field is rescaled as $H_{\text{scaled}} = H [M_S(T=0)/M_S(T)]$ to normalize the field position of features independently of temperature (25, 31). An analytic fit (dotted line), including thermal effects (22), to the 77-K data is used to extract the disorder potential (inset). Recomputing using the same potential at room temperature, the hopping rates exceed the measurement bandwidth and mask the bistability.

ing a second in-plane orthogonal field, H_y , to the primary bias field, H_x , allows 2D measurements (Fig. 3A). Using secondary field values equivalent to path shifts on the nanometer scale to explore a prominent minor hysteresis loop shows the strong influence of the 2D distribution. On the low-field side of the loops, a single site with a clear circular interaction profile dominates. On the high-field side, multiple pinning sites can be identified by counting the distinct magnetization levels in the minor hysteresis loops.

To perform a quantitative analysis of the M - H curves in 1D and 2D, a deformable vortex pinning model was developed (22, 23) based on the rigid vortex model (24, 25) and the two-vortex model (26, 27). This model captures the field dependence of both the core position and the

flexing of the disk magnetization in response to the presence of imperfections, whether they are strong enough to locally trap the vortex or merely modify its progression across the disk (22) (fig. S3). More details are in the supplementary materials (22) and in (23), which also contains extensive evaluation of model performance against micromagnetic simulation. The model may be applied by fitting to the measured magnetization data, enabling the extraction of a quantitative pinning potential. Consequently, this allows computation of potential energy barriers separating bistable states and the associated thermal dynamics. The steps necessary to accurately fit the model to the data are described in the supplementary materials (22). This fitting approach is applied to Fig. 1B to extract a quantitative

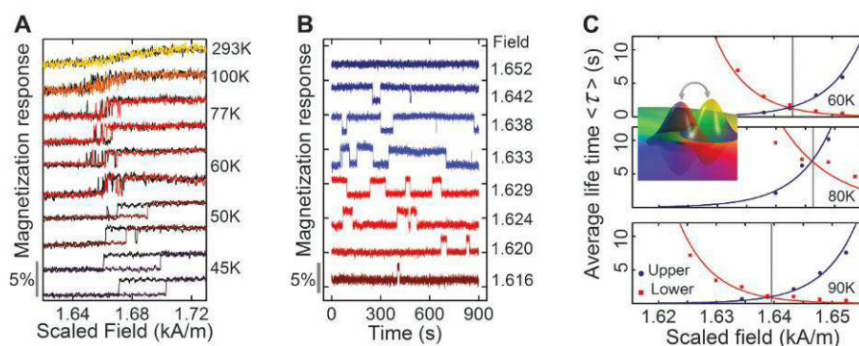


Fig. 2. Barkhausen telegraph noise across a bistable transition. **(A)** The strong temperature dependence of minor hysteresis is probed over a bistable state (the first minor loop in Fig. 1B) with a field sweep rate of $0.45 \text{ Am}^{-1}\text{s}^{-1}$. **(B)** At 77 K and various fixed fields (labeled in kA/m), telegraph noise traces show strong field dependence. The gray bar indicates the normalized magnetization scale. **(C)** For three temperatures the average lifetimes of the upper and lower states are calculated as a function of field using an Arrhenius fit to the observed lifetime distribution of telegraph noise traces. Analytical estimates of the lifetimes computed from the vortex pinning model show that the two sites are separated by ~ 10 nm in y . For equal state occupancy, the barriers range between 100 and 140 meV. The inset is a cartoon depicting the hopping process.

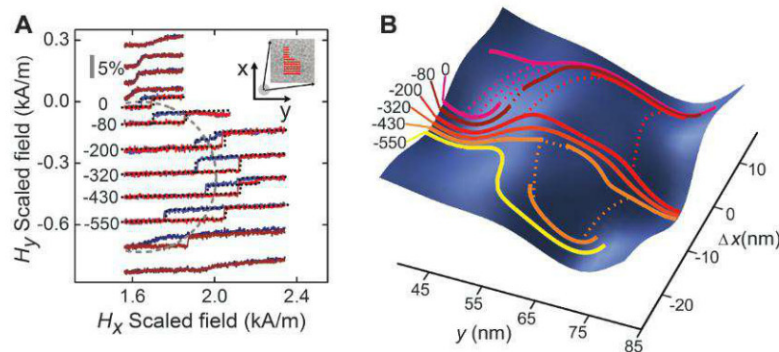


Fig. 3. Quantitative 2D mapping of the pinning potential. **(A)** Field sweeps taken with various secondary, H_y , field values (labeled in A/m) probe the landscape around a strong pinning site. The circular profile of the central site is clearly visible; a dashed line indicates a circle with radius 10 nm computed analytically, assuming no pinning. The inset is a cartoon of the idealized paths overlaid on a representative 50-nm-square transmission electron microscopy (TEM) image showing the grain structure of the permalloy disk. The gray bar indicates the normalized magnetization scale. **(B)** A 2D potential is constructed that yields minimum energy paths (solid lines) and estimated hopping trajectories (dashed lines) with profiles matching those extracted from the hysteresis loops in (A). The field values are labeled in A/m. For the $H_y = 0$ path, the broad overlap of bistable paths provides a multitude of diagonal hopping paths with energy barriers in the 100- to 200-meV range, consistent with Fig. 2C.

potential as a function of the real, pinned position of the core. Typical pinning site energies between 0.6 and 2.0 eV are found. Fitting to the measured field evolution of the state lifetimes shown in Fig. 2C results in two pinning sites spaced out by approximately 10 nm with a steep barrier. Considering the size limitations on energetic profiles imposed by the core, this implies a diagonal hopping path.

Analysis in 2D presents additional challenges. For any single magnetization trace, the potential extracted is a 1D projection of the defect potential encountered along the 2D path of minimum energy (22) (fig. S4). From each loop shown in Fig. 3A, a 1D potential was extracted. Subsequently, a 2D potential (Fig. 3B) was constructed that yields minimum-energy path profiles that match each extracted 1D potential when the appropriate secondary, H_y , field value is included. The details of constraining the constructed 2D potential can be found in the supplement-

tary materials (22). This provides an estimate of the 2D pinning site distribution probed by the vortex core.

A better idea of the morphology of the natural pinning may be gleaned from the 2D data. The strongest individual sites used in the reconstruction are 2.0 to 2.5 eV deep, whereas the weakest are ~ 0.3 eV, corroborating the range found in the 1D fit. Site sizes range from 7 to 10 nm in standard deviation, matching closely with the 7.3-nm standard deviation of the simulated exchange energy distribution of a vortex core in this size of disk (fig. S5). Any defect profile will be convolved with the energy profile of the core, indicating that the pinning sites are typically very small, effectively pointlike up to a few nanometers in width.

The minimum energy paths in the 2D constructed potential shown in Fig. 3B reveal the complexity of the situation. Minor hysteresis can arise for transitions between bistable positions along the same path or between separate paths. Both types of hopping are observed. The existence of two paths raises the possibility of hysteresis loops where the path on the sweep up is different from that on the sweep down. This is seen in Fig. 3A in the $H_y = -430$ A/m and $H_y = -200$ A/m loops, where the computed paths imply that the core traverses one side of the repulsive site on the sweep up and the other side on the sweep down. Near $H_y = 0$ ($x = 0, y = 50$ nm), a variety of low-barrier (100 to 200 meV) hopping trajectories exist between paths. The diagonal hopping trajectories accessible are consistent with the field values and variability observed in the hopping (Fig. 2C), as are the barrier heights and site separations. The complexity of the paths leads to the richness of features exhibited in the minor loops in Fig. 3A. Conversely, only by considering every subtle feature and change between adjacent hysteresis loops is the reconstruction of the 2D potential possible. The hysteresis and analytical modeling approach presented here is compatible with dynamical pinning techniques (10, 11, 13), and a combined study could extract complementary measurements of potential well shapes with additional information, such as local dissipation.

The detailed understanding of the quasistatic and low-speed stochastic dynamics of the vortex core in its natural pinning potential motivates detailed exploration of artificial texturing of the local magnetic energy to create magneto-mechanical devices. The concept is demonstrated by the addition of three stronger pinning sites introduced by ion milling fine dimples into the surface. Very low current (0.3 pA), fast-shuttered (40 ms) point exposures of a focused gallium ion beam ($\sim 70,000$ Ga⁺ ions) were used (22). This is a very much scaled-down version of the creation of artificial pinning sites as holes through the disk that eliminate the vortex core (28, 29). Here, the vortex core is maintained but reduced in energetic cost by the ion damage. Ion damage-based sites, in principle, are continuously adjustable start-

ing from zero pinning strength. Here, one dimple was placed ~ 110 nm from the disk center, whereas on the opposite side of the disk two dimples were placed at ~ 200 and 280 nm to enable identification of the chirality of the vortex state. All dimples were placed along the y axis, where previous measurements had characterized the natural pinning potential. The modified magnetization response as the core passes through the pinning site is shown in Fig. 4A. Even at room temperature, strong minor hysteresis loops mark the entrance and exit points of the core from the dimple. Exploring the opposite side of the disk, similarly dramatic changes occur (Fig. 4B), including clean minor hysteresis from direct transitions between the proximal dimples, as seen with dual holes (28). Applying the model, good fits are found for Gaussian pinning sites at 110, 215, and 300 nm, with depths between 17 and 21 eV and a common standard deviation of 18 nm. This pinning site strength is equivalent to the complete suppression of magnetization in a volume equivalent to a cylinder ~ 6 nm in radius through the thickness of the disk. The physical thinning of the disk at the dimple, ~ 2 nm depth by atomic force microscopy (fig. S2), or dilution of magnetic material by Ga is insufficient. This suggests that the Ga⁺ ions disrupt the exchange interaction. Assuming linear response, the efficacy of magnetic potential well excavation is ~ 0.3 meV per implanted ion. In this polycrystalline sample, artificial pinning sites down to the natural energetic corrugation will remain detectable. However, in a single crystal sample, energetic scales well below this should be accessible. Variable strength of pinning with preservation of the core structure indicates the possibility for pointillist rendering of a full, quantitative 2D energy landscape. Recent work demonstrates the applicability of very weak gradient dose pinning (16).

The technological potential of controlled magnetic pinning spans applications from spin transfer oscillator devices to integrated magneto-mechanical memories. With demonstrated sensitivities for measurement and modification that extrapolate to the meV level, the techniques for characterization and control reported here offer a route all the way down to the range of artificial corrugations relevant to quantum devices exploiting tunneling of the magnetization (30).

References and Notes

1. H. Barkhausen, *Phys. Z.* **20**, 401 (1919).
2. R. P. Cowburn, D. K. Koltsov, A. O. Adeyeye, M. E. Welland, D. M. Tricker, *Phys. Rev. Lett.* **83**, 1042 (1999).
3. J. Raabe, R. Pulwey, R. Sattler, T. Schweinböck, J. Zweck, D. Weiss, *J. Appl. Phys.* **88**, 4437 (2000).
4. T. Shinjo, T. Okuno, R. Hassdorf, K. Shiget, T. Ono, *Science* **289**, 930 (2000).
5. A. Wachowiak et al., *Science* **298**, 577 (2002).
6. H. Min, R. D. McMichael, J. Miltat, M. D. Stiles, *Phys. Rev. B* **83**, 064411 (2011).
7. D. Toscano, S. A. Leonel, R. A. Dias, P. Z. Coura, B. V. Costa, *J. Appl. Phys.* **109**, 076104 (2011).
8. F. A. Apolonio, W. A. Moura-Melo, F. P. Crisafulli, A. R. Pereira, R. L. Silva, *J. Appl. Phys.* **106**, 084320 (2009).
9. T. Uhlig et al., *Phys. Rev. Lett.* **95**, 237205 (2005).

Fig. 4. Control of the Barkhausen effect. (A) Point exposures of Ga⁺ ions disrupt ordering in the perm-alloy film, creating strongly interacting artificial pinning sites. The three added pinning sites are visible with a linear remapping of the grayscale to a color scale in a contrast-enhanced scanning electron microscopy image of the torsional paddle (inset, top left). The modified magnetization response exhibits prominent hysteresis between the up (red) and down (blue) field sweeps as the vortex is driven over the single dimple. The observed pinning is modeled accurately (dotted black line) by a Gaussian pinning potential (inset, bottom right). (B) The double dimple also shows strong artificially induced bistability, including hysteretic transitions directly from dimple to dimple (inset, top left). The two dimples may be modeled as Gaussian sites (inset, bottom right) with width and depths very similar to the single dimple.

10. R. L. Compton, P. A. Crowell, *Phys. Rev. Lett.* **97**, 137202 (2006).
11. R. L. Compton, T. Y. Chen, P. A. Crowell, *Phys. Rev. B* **81**, 144412 (2010).
12. J. S. Kim *et al.*, *Phys. Rev. B* **82**, 104427 (2010).
13. T. Y. Chen, A. T. Galkiewicz, P. A. Crowell, *Phys. Rev. B* **85**, 180406 (2012).
14. S. S. P. Parkin, M. Hayashi, L. Thomas, *Science* **320**, 190 (2008).
15. D. A. Allwood *et al.*, *Science* **309**, 1688 (2005).
16. J. H. Franken, H. J. M. Swagten, B. Koopmans, *Nat. Nanotechnol.* **7**, 499 (2012).
17. H. Min, R. D. McMichael, M. J. Donahue, J. Miltat, M. D. Stiles, *Phys. Rev. Lett.* **104**, 217201 (2010).
18. M. Eltschka *et al.*, *Phys. Rev. Lett.* **105**, 056601 (2010).
19. C. Chappert *et al.*, *Science* **280**, 1919 (1998).
20. J. Moreland, *J. Phys. D Appl. Phys.* **36**, R39 (2003).
21. J. P. Davis *et al.*, *J. Appl. Phys.* **109**, 07D309 (2011).
22. Supplementary materials are available on Science Online.
23. J. A. J. Burgess, J. E. Losby, M. R. Freeman, <http://arxiv.org/abs/1208.3797> (2012).
24. K. Y. Guslienko, V. Novosad, Y. Otani, H. Shima, K. Fukamichi, *Phys. Rev. B* **65**, 024414 (2001).
25. J. A. J. Burgess *et al.*, *Phys. Rev. B* **82**, 144403 (2010).
26. K. Y. Guslienko *et al.*, *J. Appl. Phys.* **91**, 8037 (2002).
27. K. L. Metlov, K. Y. Guslienko, *J. Magn. Magn. Mater.* **242**, 1015 (2002).
28. M. Rahm, J. Stahl, W. Wegscheider, D. Weiss, *Appl. Phys. Lett.* **85**, 1553 (2004).
29. M. Rahm, R. Höllinger, V. Umansky, D. Weiss, *J. Appl. Phys.* **95**, 6708 (2004).
30. R. Zarzuela, S. Vélaz, J. M. Hernandez, J. Tejada, V. Novosad, *Phys. Rev. B* **85**, 180401 (2012).
31. G. Mihajlovic *et al.*, *Appl. Phys. Lett.* **96**, 112501 (2010).

Acknowledgments: This work was supported by the Natural Sciences and Engineering Research Council, Canada, the Canadian Institute for Advanced Research, the Informatics Circle of Research Excellence, Canada Research Chairs, the Integrated Nanosystems Research Facility, the Canadian

Foundation for Innovation, nanoAlberta, and the National Institute for Nanotechnology. The samples were fabricated using the electron microscopy facilities of the National Institute for Nanotechnology and Infrastructure of the Centre for Nanoscale Physics and Nanomaterials Research at the University of Alberta. J.B. thanks the Alberta Ingenuity Foundation/Alberta Innovates for support. We are grateful to W. Hiebert, J. Losby, Z. Diao, M. Malac, and V. Sauer for many discussions; to P. Li for TEM work; and to D. Fortin for technical assistance.

Supplementary Materials

www.sciencemag.org/cgi/content/full/science.1231390/DC1
Materials and Methods
Supplementary Text
Figs. S1 to S7
Movies S1 to S3
References (32–40)

11 October 2012; accepted 17 December 2012

Published online 17 January 2013;
10.1126/science.1231390

Coherence and Indistinguishability of Single Electrons Emitted by Independent Sources

E. Bocquillon,¹ V. Freulon,¹ J.-M. Berroir,¹ P. Degiovanni,² B. Plaças,¹ A. Cavanna,³ Y. Jin,³ G. Fève^{1*}

The on-demand emission of coherent and indistinguishable electrons by independent synchronized sources is a challenging task of quantum electronics, in particular regarding its application for quantum information processing. Using two independent on-demand electron sources, we triggered the emission of two single-electron wave packets at different inputs of an electronic beam splitter. Whereas classical particles would be randomly partitioned by the splitter, we observed two-particle interference resulting from quantum exchange. Both electrons, emitted in indistinguishable wave packets with synchronized arrival time on the splitter, exited in different outputs as recorded by the low-frequency current noise. The demonstration of two-electron interference provides the possibility of manipulating coherent and indistinguishable single-electron wave packets in quantum conductors.

As with photons, the wave-particle duality plays a crucial role in the propagation of electrons in quantum conductors. The wave nature of electrons can be revealed in interference experiments (1–3) probing the single-particle coherence of electron sources through the measurement of the average electrical current. The corpuscular nature of charge carriers is apparent when measuring fluctuations of the electrical current (4). Yet, some experiments cannot be understood within the wave or the corpuscular description. This is the case when two-particle interference effects related to the exchange between two indistinguishable particles take

place. Such experiments have proven particularly interesting—both from a fundamental standpoint, as they require a full quantum treatment, and because the on-demand generation of indistinguishable partners is at the heart of quantum information protocols (5). Information coding in few-electron states that propagate ballistically in quantum conductors (6) thus requires the production of coherent and indistinguishable single-particle wave packets emitted by several synchronized but otherwise independent emitters. The collision of two particles emitted at two different inputs of a beam splitter can be used to measure their degree of indistinguishability. In the case of bosons, indistinguishable partners always exit in the same output (Fig. 1). Fermionic statistics leads to the opposite behavior: Particles exit in different outputs. The bunching of indistinguishable photons has been observed by recording the coincidence counts between two detectors placed at the outputs of the beam splitter as a function of the time delay τ between the arrival times of the photons on the splitter. Bunching shows up in a dip in the coincidence counts, the Hong-Ou-

Mandel (HOM) dip (7), when τ is varied. The reduction of the coincidence counts directly measures the overlap between the single-particle states at the input. It is maximum when the arrivals are synchronized and can be suppressed when the delay becomes larger than the wave-packet widths.

The production of indistinguishable partners is challenging, and their generation by independent sources has only recently been achieved in optics (8). In one-dimensional quantum conductors, a continuous stream of indistinguishable electrons can be produced by applying a dc voltage bias to two different electronic reservoirs. Because of fermionic statistics, each source fills the electronic states up to the chemical potential $-eV$, and identical electron beams are generated. With the use of such sources, the π exchange phase of indistinguishable fermions has been measured in the above-described collider geometry (9) and in a two-particle interferometer based on a Mach-Zehnder geometry (10, 11). However, as these sources generate a continuous beam of electrons, they do not reach the single-particle resolution of their optical analog, and two-particle interference cannot be interpreted as resulting from the overlap between two single-particle wave packets. The manipulation of single-particle states thus requires replacement of dc emitters by triggered ac emitters that generate a single-electron wave packet at a well-defined time.

When dealing with electrons, one can benefit from the charge quantization of a small quantum dot enforced both by Coulomb interaction and fermionic statistics to trigger the emission of particles one by one (12–16). Moreover, the edge channels of the quantum Hall effect provide an ideal test bench to implement optic-like experiments with electron beams in condensed matter, as electron propagation is ballistic, one-dimensional, and chiral. We will consider here a mesoscopic capacitor (12), which comprises a small quantum dot capacitively coupled to a metallic top gate and tunnel coupled to a single edge channel by a quantum point contact of variable transmission D . By applying a square-wave periodic radiofrequency excitation on the top gate, whose

¹Laboratoire Pierre Aigrain, Ecole Normale Supérieure, CNRS (UMR8551), Université Pierre et Marie Curie, Université Paris Diderot, 24 rue Lhomond, 75231 Paris Cedex 05, France. ²Université de Lyon, Fédération de Physique André Marie Ampère, CNRS—Laboratoire de Physique de l'Ecole Normale Supérieure de Lyon 46 Allée d'Italie, 69364 Lyon Cedex 07, France. ³CNRS—Laboratoire de Photonique et de Nanostructures Route de Nozay, 91460 Marcoussis, France.

*To whom correspondence should be addressed. E-mail: feve@lpa.ens.fr

peak-to-peak amplitude matches the dot addition energy, $2eV_{\text{exc}} \approx \Delta$, a quantized current resulting from the emission of a single electron followed by a single hole is generated (12). Beyond average current measurements, this emitter has been characterized through the study of current correlations on short times (17–20) as well as partition noise measurements (21) in the electronic analog of the Hanbury-Brown and Twiss geometry (22, 23). These measurements have demonstrated that, for escape times smaller than half the period of the excitation drive, exactly a single-electron and a single-hole excitation were successively emitted at each period. Moreover, the tunnel emission of single particles from a discrete dot level should lead to electron and hole wave functions described by exponentially decaying wave packets (24, 25): $\phi(t) = \frac{1}{\sqrt{\tau_e}} \Theta(t - t_0) e^{\frac{\Delta(t-t_0)}{2\hbar}} e^{-\frac{t-t_0}{2\tau_e}}$,

where $\Theta(t)$ is the step function, $\Delta/2$ is the energy of emitted electrons and holes, and t_0 is the emission trigger that can be tuned with an accuracy of a few picoseconds. Measurements of the average current $\langle I(t) \rangle$ (12) and short-time correlations $\langle I(t)I(t+\tau) \rangle$ (17) have confirmed that the probability of single-particle detection (that is, the envelope of the wave packet) was following this exponential decay. However, these measurements are only sensitive to the squared modulus of the wave function, $|\phi(t)|^2$, and as such, do not probe the coherence of the electronic wave packet related to the phase relationship between $\phi(t)$ and $\phi^*(t')$ (for $t \neq t'$) and encoded in the off-diagonal components (coherences) of the density matrix $\rho(t, t') = \phi(t)\phi^*(t')$.

When two such emitters are used at the two inputs of an electronic beam splitter, the coherence and indistinguishability of two single electronic wave packets can be probed by two-electron interference (25–27). Considering the electron emission sequence, each emitter generates an electronic wave packet $|\phi_i\rangle$ ($i = 1, 2$) above the Fermi energy at each input of the splitter set at transmission

$T = 1/2$. The probability $P(1,1)$ that the two particles exit in different outputs is related to the overlap between wave packets: $P(1,1) = \frac{1}{2}[1 + |\langle \phi_1 | \phi_2 \rangle|^2]$. An opposite sign occurs in the expression of the probability that both particles exit in the same output, $P(0,2) + P(2,0) = \frac{1}{2}[1 - |\langle \phi_1 | \phi_2 \rangle|^2]$. These signs are related to the exchange phase of π for fermions; they would be opposite for bosons. For fermions, the coincidence counts for indistinguishable particles would thus be doubled compared to the classical case (Fig. 1). However, single-shot detection of ballistic electrons in condensed matter is not available. Antibunching is thus probed not by coincidence counts but rather by low-frequency fluctuations of the electrical current in the outputs related to the fluctuations of the number of transmitted particles: $\langle \delta N_3^2 \rangle = \langle \delta N_4^2 \rangle = \frac{1}{2}[1 - |\langle \phi_1 | \phi_2 \rangle|^2]$. Repeating this two-electron collision at frequency f and considering the successive emission of one electron and one hole per period, the low-frequency current noise at the output is then given by (25)

$$S_{33} = S_{44} = e^2 f \times [1 - |\langle \phi_1 | \phi_2 \rangle|^2] \quad (1)$$

$$= e^2 f \times [1 - |\int dt \phi_1(t) \phi_2^*(t)|^2] \quad (2)$$

The single-electron wave packets ϕ_i in Eq. 2 differ from the states generated by applying a time-dependent voltage $V_i(t)$ on each electronic reservoir connected to inputs $i = 1, 2$ and cannot be generated by such classical drive [in which case, the two inputs in Eq. 2 can be reduced to a single one by the proper gauge transformation that shifts the potentials by $V(t) = V_2(t)$]. For perfectly indistinguishable states, $\phi_2(t) = \phi_1(t)$, a complete suppression of the output noise is obtained. By delaying by time τ the emission of one particle with respect to the other, $\phi_2(t) = \phi_1(t + \tau)$, the full random partitioning of classical particles $S_{33} = S_{44} = e^2 f$ can be recovered (Fig. 1). It is thus convenient to consider the noise normalized by

the classical random partitioning $q = S_{44}/e^2 f$, which equals for exponentially decaying wave packets

$$q = 1 - e^{-|\tau|/\tau_e} \quad (3)$$

Equation 3 is valid at zero temperature, or when the Fourier components of the wave functions $\tilde{\phi}_i(\omega)$ have no overlap with the thermal excitations: $\tilde{\phi}_i(\omega) = 0$ for $\hbar\omega \approx k_B T$. Otherwise, the random partitioning is also affected by antibunching with the thermal excitations, so that $S_{44} \leq e^2 f$ (21). However, if one measures the normalized value of the excess noise Δq between the situations where both sources are switched on and switched off, simulations describing the source in the Floquet scattering formalism (20, 28) show that Δq is accurately described by Eq. 3 for moderate temperatures $k_B T \ll \Delta$.

The circuit (Fig. 2), is realized in a two-dimensional electron gas at a AlGaAs/GaAs heterojunction, of nominal density $n = 1.9 \times 10^{15} \text{ m}^{-2}$ and mobility $\mu = 2.4 \times 10^6 \text{ cm}^2 \text{ V}^{-1} \text{ s}^{-1}$. A strong magnetic field $B = 2.68 \text{ T}$ is applied so as to work in the quantum Hall regime at filling factor $\nu = 3$ ($\nu = 3$ is chosen because, in this sample, the splitter transparency T becomes energy dependent at higher values of the magnetic field). Two mesoscopic capacitors with identical addition energies $\Delta = 1.4 \text{ K}$ (much larger than the electronic temperature $T = 100 \text{ mK}$) are used as electron and hole emitters and placed at a 3- μm distance from a quantum point contact used as an electronic beam splitter at transmission $T = \frac{1}{2}$. Single-charge emission in the outer edge channel is triggered with a square excitation at frequency $f = 2.1 \text{ GHz}$ with average emission times set to $\tau_{e,1} = \tau_{e,2} = 58 \pm 7 \text{ ps}$, corresponding to a transmission $D_1 = D_2 = 0.45 \pm 0.05$. The low-frequency partition noise is measured at output 4. Figure 3 presents the measurements of Δq as a function of the time delay τ between the two sources. We observe a dip in the noise measurements for zero time delay and a plateau for longer

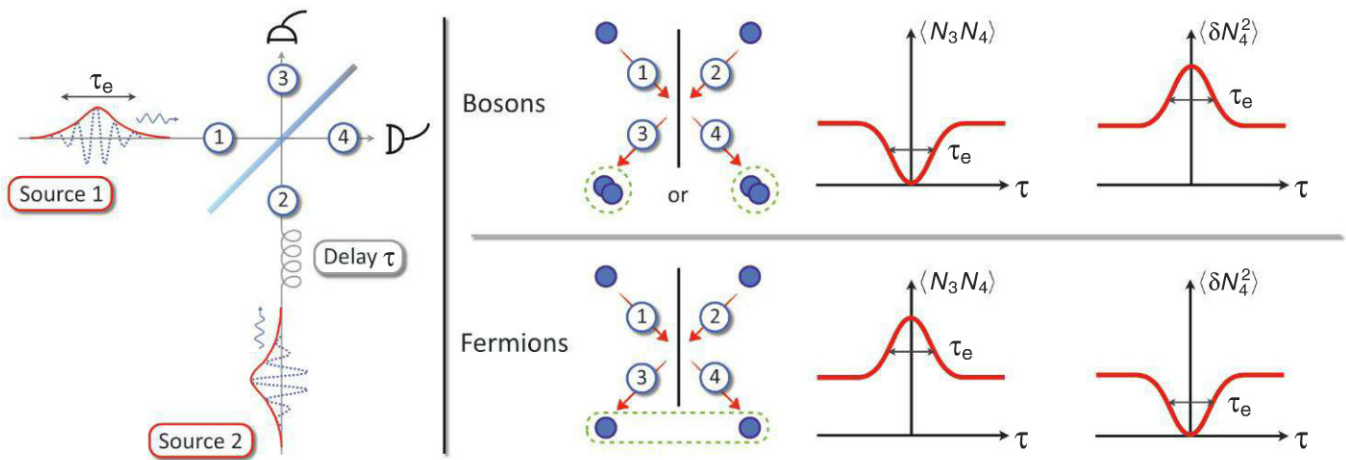


Fig. 1. Sketch of the experiment. Two single-particle wave packets of width τ_e are emitted at inputs 1 and 2 and partitioned on a splitter. Coincident counts $\langle N_3 N_4 \rangle$ and fluctuations $\langle \delta N_4^2 \rangle$ can be recorded at the outputs 3 and 4 as a function of the tunable delay τ . Indistinguishable bosons always exit in the same output. This

results in a suppression of the coincidence count and a doubling of the fluctuations at zero delay compared to the partitioning of classical particles obtained for $\tau \gg \tau_e$. An opposite behavior is expected for indistinguishable fermions (doubling of the coincidence counts and suppression of the fluctuations).

time delays. The noise values Δq are normalized by the value of the noise on the plateau. The sum of the partition noises for each source can also be measured by switching off each source alternately. This random partition noise is represented on Fig. 3 by the blurry blue line, whose extension represents the error bar. As expected, it agrees with Δq for large time delays.

The dip observed for short time delay is analogous to the HOM dip but is related here to the antibunching of single indistinguishable fermions; we thus call it the Pauli dip. It reflects our ability to produce single-particle states emitted by two different emitters with some degree of indistinguishability. The states are not perfectly identical, as shown by the fact that the dip does not go to zero. Coulomb repulsion between electrons and between holes on the splitter could also be responsible for a dip in the low-frequency noise. However, this effect can be ruled out by using the long time-delay limit, $\tau \approx 240$ ps. In this limit, the arrival of one electron is synchronized with the arrival of a hole in the other input. A random partitioning is observed (Fig. 3), although Coulomb attraction between electrons and holes would also predict a dip in the low-frequency noise (as the transmitted charge is always zero when electrons and holes exit in the same output). The dip around zero time delay can be well fitted by the ex-

pression $\Delta q = 1 - \gamma e^{-\frac{\tau - \tau_0}{\tau_c}}$ expected for two exponentially decaying wave packets but with a non-unit overlap γ . We find $\tau_c = 62 \pm 10$ ps, $\gamma = 0.45 \pm 0.05$, and $\tau_0 = 13 \pm 6$ ps, consistent with the 10-ps accuracy of the synchronization between sources. As noted above, these results can be compared with a numerical simulation of Δq in the Floquet scattering formalism, which we denote $\Delta q_F(\tau)$. For identical emission parameters of both sources, Floquet theory predicts a unit overlap at zero time delay, $\Delta q_F(\tau = 0) = 0$. The red trace in Fig. 3 represents $\Delta q = 1 - \gamma[1 - \Delta q_F(\tau)]$, which imposes a non-unit overlap γ in the Floquet scattering formalism. It reproduces well the shape of the dip with the following parameters: $\gamma = 0.5$, $D_1 = D_2 = 0.4$, $\Delta_1 = \Delta_2 = 1.4$ K, and $T = 100$ mK.

This non-unit overlap can be attributed to two different origins. First, it could stem from some small differences in the emission energies related to small differences in the static potential of each dot. Using Eq. 2, a reduction to a 50% overlap can be obtained by shifting one level relative to the other by energy $\Delta/10$. The value of the static potential is fixed with a better accuracy, but small variations could occur within the several hours of measurement time for each point. The second possibility is related to the decoherence of single-electron wave packets during propagation toward the splitter (which could arise from Coulomb interaction with the adjacent edge channel). In a simple treatment of the wave-packet decoherence, the pure state $\phi_1(t)$ is replaced by the density matrix $\rho_1(t, t') = \phi_1(t)\phi_1^*(t')D_1(t, t')$, where $D_1(t, t')$ is a decoherence factor (27, 29). We have $D_1(t, t) = 1$, such

that the average current $\langle I(t) \rangle$ is not affected, but $D_1(t, t') \rightarrow 0$ for $|t - t'| \rightarrow \infty$, suppressing the coherence of the electronic wave packet. In that case, Eq. 2 becomes

$$\Delta q = 1 - \text{Tr}[\rho_1 \rho_2] \quad (4)$$

$$= 1 - \int dt dt' \phi_1(t) \phi_1^*(t') D_1(t, t') \times \phi_2^*(t) \phi_2(t') D_2(t, t') \quad (5)$$

Equation 5 exemplifies the fact that the noise suppression stems from a two-particle interference effect encoded in the off-diagonal components of the density matrices ρ_i , i.e., on the coherence of the electronic wave packet. Assuming

$D_1(t, t') = D_2(t, t') = e^{-\frac{|t - t'|}{\tau_c}}$ in Eq. 5, we find

analytically that the overlap depends on the ratio between the intrinsic coherence time of the wave packet τ_c and the coherence time τ_c associated with the propagation along the edge: $\gamma = \frac{\tau_c/(2\tau_c)}{1 + \tau_c/(2\tau_c)}$. For $\tau_c \ll \tau_c$, the effects of decoherence can be neglected but in the opposite limit, $\tau_c \gg \tau_c$, the overlap is completely suppressed and the classical partitioning is recovered. In this case, electrons are rendered distinguishable through their interaction with the environment. Within this picture, our measurement of the overlap is compatible with $\tau_c \approx 100$ ps. Such decoherence effects underline the necessity to reach the subnanosecond time scale in electron emission to be able to generate indistinguishable electron wave packets.

The observed Pauli dip in the low-frequency noise of the output current for short time delays

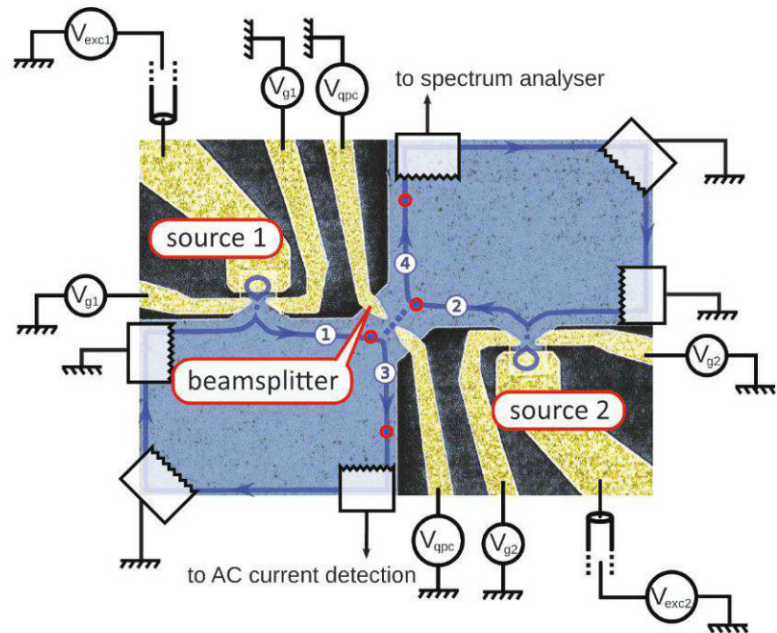


Fig. 2. Sketch of the sample based on a scanning electron microscope image. The electron gas is represented in blue. Two single-electron emitters are located at inputs 1 and 2 of a quantum point contact used as a single-electron beam splitter. Transparencies D_1 and D_2 and static potentials of dots 1 and 2 are tuned by gate voltages $V_{g,1}$ and $V_{g,2}$. Electron and hole emissions are triggered by excitation drives $V_{exc,1}$ and $V_{exc,2}$. The transparency of the beam splitter partitioning the inner edge channel (blue line) is tuned by gate voltage V_{qpc} and set at $T = 1/2$. The average ac current generated by sources 1 and 2 is measured on output 3, and the low-frequency output noise S_{44} is measured on output 4.

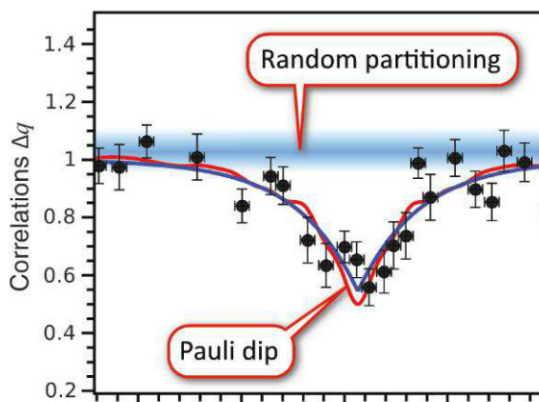


Fig. 3. Excess noise Δq as a function of the delay τ and normalized by the value on the plateau observed for long delays. The blurry blue line represents the sum of the partition noise of both sources. The blue trace is an exponential fit by $\Delta q = 1 - \gamma e^{-\frac{|\tau - \tau_0|}{\tau_c}}$. The red trace is obtained by using Floquet scattering theory, which includes finite temperature effects.

between the arrival times of electrons at a beam splitter is a signature of two-particle interference, which demonstrates the possibility of generating coherent and indistinguishable single-electron wave packets with independent sources. It provides the possibility of controlled manipulation of single-electron states in quantum conductors, with applications in quantum information processing, but could also be used to fully reconstruct the wave function of a single electron (24, 30) and thus quantitatively address the propagation of a single excitation propagating in a complex environment.

References and Notes

1. Y. Ji *et al.*, *Nature* **422**, 415 (2003).
2. P. Roulleau *et al.*, *Phys. Rev. Lett.* **100**, 126802 (2008).
3. M. Yamamoto *et al.*, *Nat. Nanotechnol.* **7**, 247 (2012).
4. Y. Blanter, M. Büttiker, *Phys. Rep.* **336**, 1 (2000).
5. E. Knill, R. Laflamme, G. J. Milburn, *Nature* **409**, 46 (2001).
6. A. Bertoni, P. Bordone, R. Brunetti, C. Jacoboni, S. Reggiani, *Phys. Rev. Lett.* **84**, 5912 (2000).
7. C. K. Hong, Z. Y. Ou, L. Mandel, *Phys. Rev. Lett.* **59**, 2044 (1987).
8. J. Beugnon *et al.*, *Nature* **440**, 779 (2006).
9. R. C. Liu, B. Odom, Y. Yamamoto, S. Tarucha, *Nature* **391**, 263 (1997).
10. P. Samuelsson, E. V. Sukhorukov, M. Büttiker, *Phys. Rev. Lett.* **92**, 02685 (2004).
11. I. Neder *et al.*, *Nature* **448**, 333 (2007).
12. G. Fève *et al.*, *Science* **316**, 1169 (2007).
13. M. D. Blumenthal *et al.*, *Nat. Phys.* **3**, 343 (2007).
14. C. Leicht *et al.*, *Semicond. Sci. Technol.* **26**, 055010 (2011).
15. S. Hermelin *et al.*, *Nature* **477**, 435 (2011).
16. R. P. G. McNeil *et al.*, *Nature* **477**, 439 (2011).
17. A. Mahé *et al.*, *Phys. Rev. B* **82**, 201309(R) (2010).
18. M. Albert, C. Flindt, M. Büttiker, *Phys. Rev. B* **82**, 041407(R) (2010).
19. T. Jonckheere, T. Stoll, J. Rech, T. Martin, *Phys. Rev. B* **85**, 045321 (2012).
20. F. D. Parmentier *et al.*, *Phys. Rev. B* **85**, 165438 (2012).
21. E. Bocquillon *et al.*, *Phys. Rev. Lett.* **108**, 196803 (2012).
22. M. Henny *et al.*, *Science* **284**, 296 (1999).
23. W. D. Oliver, J. Kim, R. C. Liu, Y. Yamamoto, *Science* **284**, 299 (1999).
24. C. Grenier *et al.*, *New J. Phys.* **13**, 093007 (2011).
25. T. Jonckheere, J. Rech, C. Wahl, T. Martin, *Phys. Rev. B* **86**, 125425 (2012).
26. S. Ol'khovskaya, J. Splettstoesser, M. Moskalets, M. Büttiker, *Phys. Rev. Lett.* **101**, 166802 (2008).
27. G. Fève, P. Degiovanni, T. Jolicœur, *Phys. Rev. B* **77**, 035308 (2008).
28. M. Moskalets, P. Samuelsson, M. Büttiker, *Phys. Rev. Lett.* **100**, 086601 (2008).
29. P. Degiovanni, C. Grenier, G. Fève, *Phys. Rev. B* **80**, 241307(R) (2009).
30. G. Haack, M. Moskalets, J. Splettstoesser, M. Büttiker, *Phys. Rev. B* **84**, 081303 (2011).

Acknowledgments: This work is supported by the Agence Nationale de la Recherche grant "1shot," ANR-2010-BLANC-0412.

9 November 2012; accepted 18 December 2012

Published online 24 January 2013;

10.1126/science.1232572

InP Nanowire Array Solar Cells Achieving 13.8% Efficiency by Exceeding the Ray Optics Limit

Jesper Wallentin,¹ Nicklas Anttu,¹ Damir Asoli,² Maria Huffman,² Ingvar Åberg,² Martin H. Magnusson,² Gerald Siefer,³ Peter Fuss-Kailuweit,³ Frank Dimroth,³ Bernd Witzigmann,⁴ H. Q. Xu,^{1,5} Lars Samuelson,¹ Knut Deppert,¹ Magnus T. Borgström^{1*}

Photovoltaics based on nanowire arrays could reduce cost and materials consumption compared with planar devices but have exhibited low efficiency of light absorption and carrier collection. We fabricated a variety of millimeter-sized arrays of p-type/intrinsic/n-type (p-i-n) doped InP nanowires and found that the nanowire diameter and the length of the top n-segment were critical for cell performance. Efficiencies up to 13.8% (comparable to the record planar InP cell) were achieved by using resonant light trapping in 180-nanometer-diameter nanowires that only covered 12% of the surface. The share of sunlight converted into photocurrent (71%) was six times the limit in a simple ray optics description. Furthermore, the highest open-circuit voltage of 0.906 volt exceeds that of its planar counterpart, despite about 30 times higher surface-to-volume ratio of the nanowire cell.

Nanostructures are currently being investigated for next-generation photovoltaic (PV) architectures as a means of lowering cost (1) through the use of abundant materials (2) or to improve light trapping (3). Nanowire (NW) arrays could provide substantial reductions in material consumption as well as production costs for III-V-based solar cells, in part because they can be monolithically grown on low-cost substrates such as silicon (4). However, proof of concepts of III-V NW-based PV

(5–9), have had limited efficiencies in the 3 to 5% range.

The efficiency of NW-based solar cells is often limited by light absorption, especially when the NWs have subwavelength dimensions. In a ray optics description, the maximum fraction of normally incident sunlight that could be absorbed and converted to a photocurrent is proportional to the surface coverage of the active material. However, theoretical modeling based on wave optics has predicted resonant light trapping in sub-200-nm-diameter NW arrays (10–12), which would allow bulklike photocurrent generation with just a fraction of the materials consumption. Experimental studies have been confined to NW arrays with either large-diameter wires (13, 14) or high surface coverage (9). Another limitation is that crystal surfaces typically have a high density of defects that act as potential recombination centers, and nanostructured devices have high surface-to-volume

(S/V) ratios. Surface recombination could explain the hitherto observed relatively low open-circuit voltages (V_{oc}) in NW-based PV cells (8, 9).

Here, we demonstrate how these challenges can be overcome and report on a NW array solar cell with 13.8% efficiency. Although the 180-nm-diameter InP NWs only cover 12% of the surface, they deliver 83% of the photocurrent density obtained in planar InP solar cells (15, 16). Furthermore, the highest V_{oc} exceeds that of the InP planar record cell (15, 16), despite about 30 times higher S/V ratio in our NW-based PV cell. By using three-dimensional (3D) optical modeling, we provide insight into the origins of the high performance of our solar cells, as well as guidelines to how they further can be improved.

We chose InP not only because of its direct band gap of 1.34 eV (925 nm wavelength-equivalent), suitable for the solar spectrum but also because it allows in situ etching with HCl during NW growth to prevent short-circuiting from radial overgrowth (17). The InP NWs in our solar cells were epitaxially grown with an axially defined p-type/intrinsic/n-type (p-i-n) doped structure (7) and have a length of ~ 1.5 μm . We used a nanoimprint technique to arrange gold seed particles in arrays (18). (Fig. 1, A to C). Different sizes and array pitches of the Au seeds were used, resulting in samples with different NW diameters (130 to 190 nm) and array pitches (470 or 500 nm). To reduce reflection, we removed the metal seed particles after growth by using wet etching and defined a top contact with a silicon oxide insulating layer and a transparent conducting oxide (TCO) (7). Last, the 1-mm-by-1-mm cells and metal contact pads were defined with optical lithography (Fig. 1C), with each sample containing a few solar cells. Details of the samples (table S1) and their fabrication are given in the supplementary materials (19).

Characterization of the solar cells (Fig. 1D) revealed very good performance in comparison with other InP PV architectures (Table 1). At 1-sun

¹Solid State Physics, Lund University, Box 118, 22100 Lund, Sweden. ²Sol Voltaics AB, Ideon Science Park, Scheelevägen 17, 22370 Lund, Sweden. ³Fraunhofer ISE, Heidenhofstrasse 2, D-79110 Freiburg, Germany. ⁴University of Kassel, Wilhelmshoeher Allee 71, 34121, Kassel, Germany. ⁵Key Laboratory for the Physics and Chemistry of Nanodevices and Department of Electronics, Peking University, Beijing 100871, China.

*To whom correspondence should be addressed. E-mail: magnus.borgstrom@ftf.lth.se

(1000 W/m²) illumination, measured in ambient air at the Fraunhofer ISE CalLab reference setup, our best cell (from sample A) shows a conversion efficiency $\eta = 13.8\%$ and a photocurrent density $J_{sc} = 24.6 \text{ mA/cm}^2$. Because our calculation of J_{sc} accounts for the full (unmetalized) cell area rather than the NW surface coverage only, it can be compared with that of the best reported planar InP cell [$J_{sc} = 29.5 \text{ mA/cm}^2$ (15, 16)] and the theoretical limit of 34.5 mA/cm^2 [assuming that each incident photon with energy above the InP band gap generates one electron-hole pair (19)]. Thus, our cell reaches 83% of the best reported planar J_{sc} despite covering only 12% of the surface area. Our axially defined NW solar cell outperforms similar cells based on core-shell NWs

with a surface coverage of 27% (9), as well as several other next-generation PV architectures (Table 1). Our results demonstrate that ray optics is not appropriate for describing the interaction of light with these subwavelength structures, because the maximum J_{sc} in the ray optics picture, 4.2 mA/cm^2 (12% of the theoretical limit, 34.5 mA/cm^2), is almost six times lower than the J_{sc} of our best cell. Alternatively, a hypothetical calculation on the single-NW level, using the NW cross-sectional area, would give a physically impossible efficiency above 100%. Thus, light that would travel between the NWs in a ray optics description was absorbed efficiently in the experimental cell. To more accurately study the absorption of light in the NW solar cell, we used full 3D electro-

magnetic optical modeling (figs. S1 to S3) (20). The validity of our approach is confirmed by comparing the calculated absorptance spectrum of the NWs in the record cell and its measured external quantum efficiency (EQE) (Fig. 2A). The values and general trends of these two spectra agree well, although the calculated absorptance is greater than the measured EQE throughout the spectrum. This discrepancy can be attributed to the absorption modeling not taking into account any carrier losses. We also show the measured EQE of a 130-nm-diameter NW solar cell (sample D) (blue solid line in Fig. 2A) and note that the EQE increases slowly above the band gap energy (925 nm in wavelength). The relatively weak coupling leads to weak absorption of long-wavelength photons into these small-diameter NWs (21).

We identified two key design parameters that influence the performance of our solar cells: the NW diameter and the length of the top n-segment. We show (Fig. 2B) the calculated absorption versus NW diameter assuming a constant NW length (1.4 μm) and array pitch (470 nm). The absorption increases with increasing diameter until it saturates around 180 nm, in line with previous modeling of unprocessed NW arrays (10). Experimentally we also saw improvement in the measured average J_{sc} from 14.0 mA/cm^2 (sample D) to 17.4 mA/cm^2 (B) when increasing the diameter from 130 to 180 nm for the same n-segment growth time of 3 min. To reach the highest J_{sc} (sample A), we also shortened the n-segment as described below. For the 180-nm diameter, the remaining 7% of the available sunlight (red area in Fig. 2B) could in principle be captured by increasing the NW length. In this work, we chose to keep the length as constant as possible in order to investigate other parameters.

The second key design parameter is the length of the top n-segment. The 3D simulations indicate that the strongest optical generation of carriers occurs near the top of the NWs (Fig. 3A). Because of the high doping, the recombination losses in the top n-segment are expected to be high. We experimentally varied the n-segment growth time (Fig. 3B) and found that reducing the nominal n-segment length from 180 (sample B) to 60 (A) nm increased the average J_{sc} by 39%. Conversely, an increase to 360 nm (sample C) reduced the average J_{sc} by 34%. These three samples are also indicated in Fig. 2B, showing that the reduction in n-segment length actually increased J_{sc} more

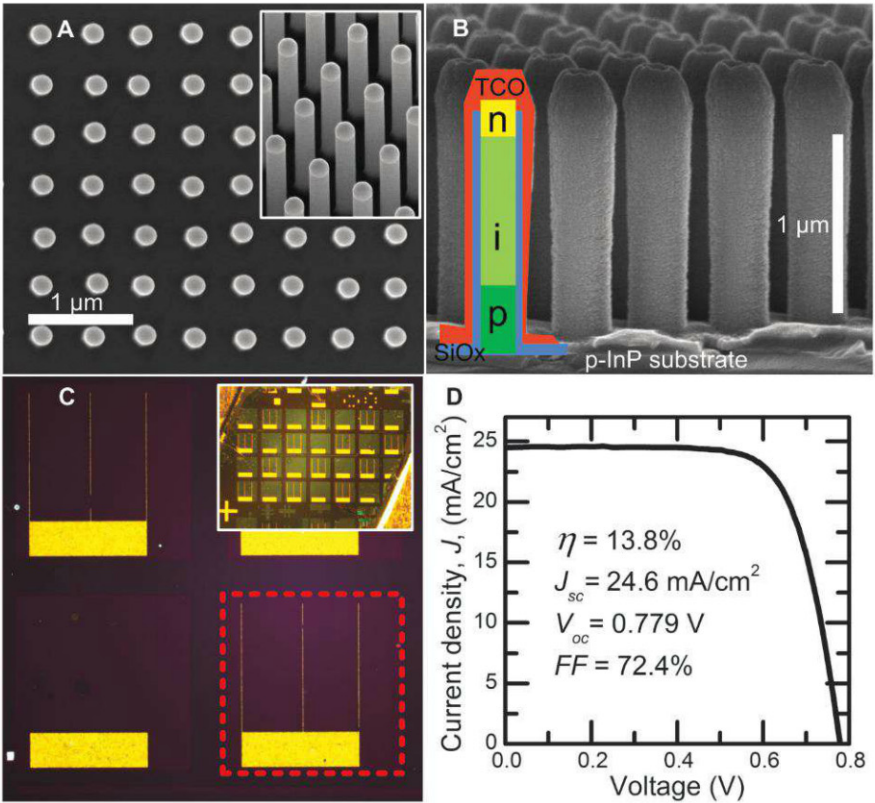


Fig. 1. Characterization of NW-array solar cells: (A) 0° and 30° (inset) tilt scanning electron microscopy (SEM) images of as-grown NWs with a surface coverage of 12%. (B) SEM image of processed NWs. The superimposed schematics illustrate the silicon oxide (SiO_x, blue), TCO (red), and the p-i-n doping layers in the NWs. (C) Optical microscope image of NW solar cells. The dashed red line highlights the border of a 1-mm-by-1-mm cell. (Inset) A sample with four-by-seven cells. (D) The 1-sun J-V curve for the highest-efficiency cell (sample A).

Table 1. A comparison of the performance of InP PV architectures, as well as reported efficiencies of selected next-generation PV architectures, under 1-sun illumination. The listed devices show variation in cell area and measurement conditions.

	Active area coverage (%)	Relative active volume (%)	J_{sc} (mA/cm ²)	V_{oc} (V)	Fill factor (%)	Efficiency 1 sun (%)
Axial InP NW - this work, A	12	5	24.6	0.779	72.4	13.8
Sample E	11	5	18.2	0.906	78.6	13.0
Planar InP (15, 16)	100	100	29.5	0.878	85.4	22.1
Core-shell InP NW (9)	27	14	13.7	0.43	57	3.37
Dye-sensitized (27)	100		17.66	0.935	74	12.3
Organic (16)	100		10.08	1.53	68.5	10.6
Colloidal quantum dot (28)	100		20.1	0.605	58	7.0

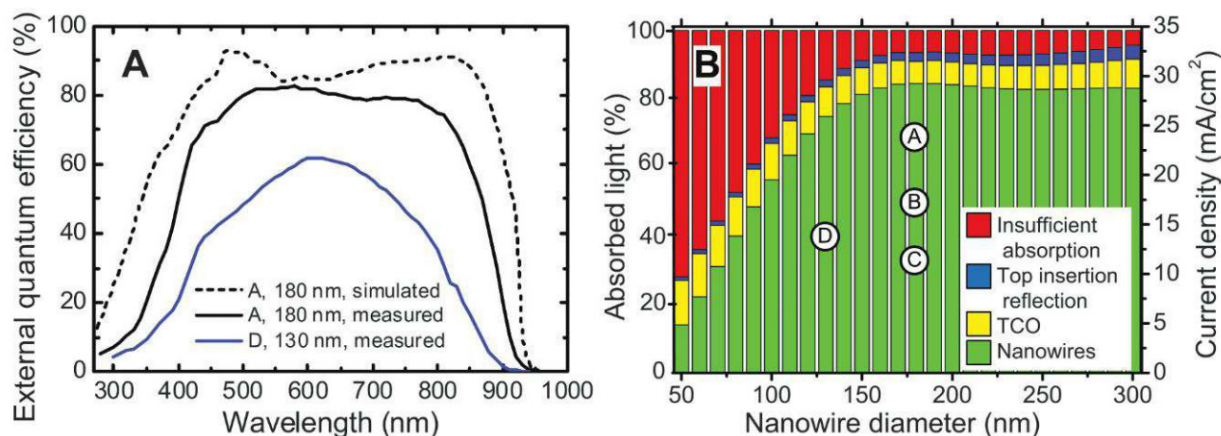


Fig. 2. Absorption in NW solar cells (A) Measured EQE of cells from samples A (180-nm diameter) and D (130 nm), with the simulated EQE of sample A assuming that all carriers generated in the whole NW (including the top n-segment) contribute to J_{sc} . (B) Simulated absorbed light as a fraction of

the solar spectrum above the InP band gap and calculated J_{sc} versus NW diameter. Different optical losses are also shown (fig. S2). The markers indicate the experimentally measured average J_{sc} of samples A, B, C, and D (1-, 3-, 6-, and 3-min n-segment growth times, respectively).

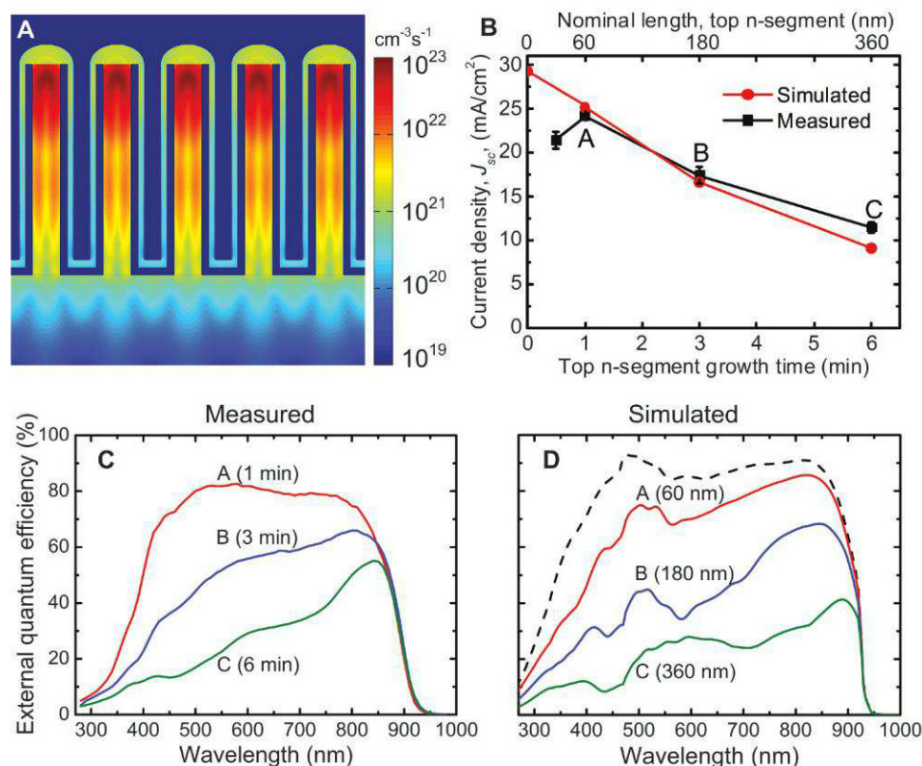


Fig. 3. Solar cell performance dependence on top n-segment length. (A) Simulated optical generation rate of electron-hole pairs in the y-z cross section of sample A for x polarized incident light (19). (B) Measured and simulated J_{sc} versus n-segment growth time (19). The error bars are one standard deviation. (C) Measured EQE of cells from samples A (n-segment growth time, 1 min), B (3 min), and C (6 min). (D) Simulated EQE of samples A (60-nm n-segment length), B (180 nm), and C (360 nm), together with the simulated EQE for sample A without losses (dashed line).

than the increase in diameter from 130 to 180 nm. With a 30-nm n-segment, the photocurrent was reduced, possibly because some slightly shorter NWs were not properly contacted.

To understand these experimental findings, we expanded our purely optical model by assuming that all carriers generated in the n-region are lost and calculated the resulting J_{sc} (Fig. 3B)

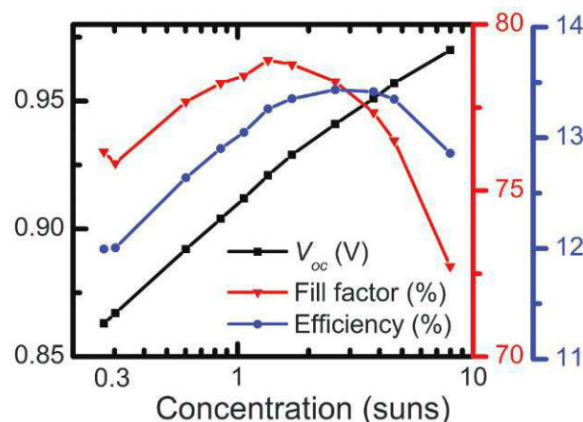
and EQE (Fig. 3D). Although this simple model neglects the effects of graded doping profiles, carrier diffusion, and electrical fields, it reproduces the experimental data well. Primarily the short-wavelength light is lost, because it is most strongly absorbed at the top. We note that the modeled spectra contain sharper peaks compared with the experimental EQE (Fig. 3C). This dif-

ference probably stems from small variations in NW diameter, length position, and doping profile, which occur naturally in the experimental cells.

Next, we discuss the ability of our solar cells in transferring the photogenerated charge carriers to the contacts. The highest V_{oc} that we observed, 0.906 V, measured in sample E that has 13.0% efficiency, exceeds that of the planar InP record cell (15) (Table 1). In contrast, the highest-efficiency, highest-current sample, A, shows a substantially lower V_{oc} , 0.779 V. The relative variation in V_{oc} between our samples is typically greater than that for J_{sc} . Because the dimensions of the NWs in these samples are similar, we believe that this is due to variations in the contact-formation process. We therefore anticipate larger cells to show similar J_{sc} but lower V_{oc} than our best cells.

The highest V_{oc} , 0.906 V, is notable considering that the depletion region, estimated by the nominally 650-nm-long i-region, is several times longer than the NW diameter (190 nm). InP NWs have a relatively low surface-recombination velocity (22), with values as low as 170 cm/s reported for undoped InP NWs (23). Because we did not use any intentional surface passivation or high-band gap window layer, we suggest three possible origins to the high V_{oc} values observed in our NW-based solar cells in comparison to planar cells. First, the crystal structure in InP NWs is typically a mixture of wurtzite and zinc blende (7). Because wurtzite InP has an 80-meV higher band gap than the bulk zinc blende, this could at most produce an 80-mV increase in V_{oc} (24, 25). Second, the carriers are confined to the NW cross-sectional area rather than the cell area, which means that the saturation current density, J_0 , as measured by using the cell area, could be reduced by a factor of 0.12. With the formula $V_{oc} = (kT/q)\ln(J_{sc}/J_0)$ (where k is the Boltzmann constant, T is the absolute temperature, and q is the elemental charge), we can estimate this enhancement to 55 mV. Third, there could be a radial charge separation of electrons and holes, resulting from

Fig. 4. Characterization of cell from sample E under concentrated illumination.



effects such as surface pinning (26). Additional experiments are needed to understand the high V_{oc} .

Because multijunction III-V PV is currently being deployed for concentrator PV—where large-area, low-cost optics are used to collect sunlight and focus it onto small, high-performance solar cells—we have also investigated the performance of the cell with highest V_{oc} (sample E) under concentration (Fig. 4). The V_{oc} increases logarithmically as expected up to 0.97 V. However, the fill factor decreases, which indicates a series resistance, possibly originating from the TCO or the small contact area of the NW tips. The efficiency under concentrated illumination for this cell therefore peaks at 13.4% at 2.6 suns. The angular dependence, which is important for diffuse light conditions, has not been investigated experimentally, but previous simulations have indicated weak angular dependence up to 40° (12).

Lastly, we assess the technical maturity of our design. We fabricated seven working cells on the same sample (average efficiency of 12.0% with standard deviation of 1.4%) and reproduced

similar results in separate growth and processing batches. The best sample was stored 2 months in ambient air before the measurement, and the degradation in absolute efficiency of somewhat older samples is less than 0.5% over a period of 6 months. This design should be readily scalable to wafer-sized cells and be useful for similar optoelectronic devices such as photodetectors.

References and Notes

- W. U. Huynh, J. J. Dittmer, A. P. Alivisatos, *Science* **295**, 2425 (2002).
- B. O'Regan, M. Grätzel, *Nature* **353**, 737 (1991).
- A. Polman, H. A. Atwater, *Nat. Mater.* **11**, 174 (2012).
- T. Mårtensson et al., *Nano Lett.* **4**, 1987 (2004).
- C. Colombo, M. Heiß, M. Grätzel, A. Fontcuberta i Morral, *Appl. Phys. Lett.* **94**, 173108 (2009).
- J. F. Wang, M. S. Gudiksen, X. Duan, Y. Cui, C. M. Lieber, *Science* **293**, 1455 (2001).
- M. T. Borgström et al., *IEEE J. Sel. Top. Quantum Electron.* **17**, 1050 (2011).
- E. C. Garnett, M. L. Brongersma, Y. Cui, M. D. McGehee, *Annu. Rev. Mater. Res.* **41**, 269 (2011).
- H. Goto et al., *Appl. Phys. Express* **2**, 035004 (2009).
- J. Kupec, R. L. Stoop, B. Witzigmann, *Opt. Express* **18**, 27589 (2010).

- L. Hu, G. Chen, *Nano Lett.* **7**, 3249 (2007).
- N. Anttu, H. Q. Xu, *J. Nanosci. Nanotechnol.* **10**, 7183 (2010).
- M. D. Kelzenberg et al., *Nat. Mater.* **9**, 368 (2010).
- E. Garnett, P. D. Yang, *Nano Lett.* **10**, 1082 (2010).
- C. J. Keavney, V. E. Haven, S. M. Vernon, in *Photovoltaic Specialists Conference, 1990, Conference Record of the Twenty First IEEE* (IEEE, Piscataway, NJ, 1990), vol. 1, pp. 141–144.
- M. A. Green, K. Emery, Y. Hishikawa, W. Warta, E. D. Dunlop, *Prog. Photovolt. Res. Appl.* **20**, 606 (2012).
- M. T. Borgström et al., *Nano Research* **3**, 264 (2010).
- T. Mårtensson et al., *Nano Lett.* **4**, 699 (2004).
- See supplementary materials on Science Online.
- N. Anttu, H. Q. Xu, *Phys. Rev. B* **83**, 165431 (2011).
- P. M. Wu, N. Anttu, H. Q. Xu, L. Samuelson, M. E. Pistol, *Nano Lett.* **12**, 1990 (2012).
- S. Münch et al., *Nanotechnology* **21**, 105711 (2010).
- H. J. Joyce et al., *Nano Lett.* **12**, 5325 (2012).
- A. Mishra et al., *Appl. Phys. Lett.* **91**, 263104 (2007).
- O. J. Glembocki, H. Piller, in *Handbook of Optical Constants of Solids*, E. D. Palik, Ed. (Academic Press, Orlando, FL, 1985), pp. 503–516.
- M. H. M. van Weert et al., *Appl. Phys. Lett.* **88**, 043109 (2006).
- A. Yella et al., *Science* **334**, 629 (2011).
- A. H. Ip et al., *Nat. Nano* **7**, 577 (2012).

Acknowledgments: This work was performed within the Nanometer Structure Consortium at Lund University (nmC@LU) and was supported by the Swedish Research Council (Vetenskapsrådet), by the Knut and Alice Wallenberg Foundation, by the Swedish Energy Agency, and by the European Union program AMON-RA (214814). This Report is based on a project that was funded by E.ON AG as part of the E.ON International Research Initiative. We thank M. Graczyk for nanoimprint lithography and S. Lehmann for transmission electron microscopy.

Supplementary Materials

www.sciencemag.org/cgi/content/full/science.1230969/DC1
Materials and Methods
Figs. S1 to S3
Table S1
References (29–33)

1 October 2012; accepted 17 December 2012

Published online 17 January 2013;

10.1126/science.1230969

Synchronous Change of Atmospheric CO₂ and Antarctic Temperature During the Last Deglacial Warming

F. Parrenin,^{1*} V. Masson-Delmotte,² P. Köhler,³ D. Raynaud,¹ D. Paillard,² J. Schwander,⁴ C. Barbante,^{5,6} A. Landais,² A. Wegner,^{3†} J. Jouzel²

Understanding the role of atmospheric CO₂ during past climate changes requires clear knowledge of how it varies in time relative to temperature. Antarctic ice cores preserve highly resolved records of atmospheric CO₂ and Antarctic temperature for the past 800,000 years. Here we propose a revised relative age scale for the concentration of atmospheric CO₂ and Antarctic temperature for the last deglacial warming, using data from five Antarctic ice cores. We infer the phasing between CO₂ concentration and Antarctic temperature at four times when their trends change abruptly. We find no significant asynchrony between them, indicating that Antarctic temperature did not begin to rise hundreds of years before the concentration of atmospheric CO₂, as has been suggested by earlier studies.

Analyses of polar ice cores have shown that the concentration of atmospheric CO₂ (aCO₂) and surface air temperature

are closely related and that they have risen and fallen in tandem over most of the past 800,000 years. However, whether changes of temperature

occurred first and how large that lead may have been have been topics of considerable controversy. The most highly resolved aCO₂ record during the last deglacial warming, Termination I (TI), is from the European Project for Ice Coring in Antarctica (EPICA) Dome C (EDC) ice core (1, 2). In this record, aCO₂ appears to lag local Antarctic temperature (AT) by 800 ± 600 years at the onset of TI, in agreement with an earlier study on the Vostok and Taylor Dome ice cores, which identified a lag of 600 ± 400 years at the end of the

¹Laboratoire de Glaciologie et Géophysique de l'Environnement (CNRS/UJF), Grenoble, France. ²Laboratoire des Sciences du Climat et de l'Environnement (CEA/CNRS/UVSQ-IPSL), Gif-sur-Yvette, France. ³Alfred Wegener Institute for Polar and Marine Research, Bremerhaven, Germany. ⁴Physics Institute, University of Bern, Bern, Switzerland. ⁵Department of Environmental Sciences, University of Venice, Venice, Italy. ⁶Institute for the Dynamics of Environmental Processes—CNR, University of Venice, Venice, Italy.

*Corresponding author. E-mail: parrenin@ujf-grenoble.fr

†Present address: Byrd Polar Research Center, Ohio State University, Columbus, OH, USA.

past three terminations (3). However, uncertainties in the relative timing of $\delta^{15}\text{N}$ and AT remain for two reasons. First, air is trapped in fallen snow only when it has recrystallized enough to create enclosed cavities, typically at a depth of 50 to 120 m below the surface (depending on site conditions), at the bottom of the so-called firn. This results in a depth difference (Δdepth , see Fig. 1) between synchronous events recorded in the ice matrix and in the trapped gas bubbles or hydrates (4, 5). We used air $\delta^{15}\text{N}$ data from the EDC ice core to determine the past Lock-In Depth (LID), which is the depth at which air in the ice is permanently trapped. The LID estimates are transformed to Δdepth estimates, using a constant

firm average density and a modeled vertical thinning function. Our approach is further validated with two independent methods. Second, using only the isotopic record from one ice core produces a noisy reconstruction of past temperature variations in Antarctica. We used a stack of AT variations based on five synchronized ice cores.

Figure 2 illustrates an approach similar to previous studies (1, 3) to deduce Δdepth , based on firn densification modeling (6) to estimate the past LID and average firm density, and on ice flow modeling (7) to estimate the vertical thinning of ice layers. The past LID can also be estimated using the fact that in the firn, below a convective zone where the air is freely mixed,

gravitational fractionation enriches the $\delta^{15}\text{N}$ of N_2 proportionally to the height of the diffusive column (8, 9). There is no convective zone today at EDC (10). Assuming a persistent absence of such a convective zone during TI and using the $\delta^{15}\text{N}$ data from the EDC ice core (11), we can estimate the LID during TI. Then, assuming that the average firm density did not vary and using a one-dimensional ice flow model (7) to assess layer thinning, the LID can be converted to Δdepth (Fig. 2 and supplementary materials).

One caveat of our method arises from our assumption of the absence of a convective zone during the past, which is known to reach more than 20 m in low-accumulation windy sites today (12). For verification, we used two independent approaches. First, we synchronized EDC to the EPICA Dronning Maud Land (EDML) and Talos Dome (TALDICE) ice cores both in the gas (using CH_4) and ice (using volcanic events) phases (5). The Δdepth at EDC can be estimated from Δdepth at EDML and TALDICE (Fig. 1). The latter is evaluated from firn modeling but, because the accumulation is about three times higher at EDML or TALDICE than at EDC, an error on the past LID at EDML or TALDICE has an impact at EDC that is about three times smaller (5). Second, we used the bipolar seesaw hypothesis (13), which suggests that a rapid temperature rise in Greenland occurs synchronous to a maximum in AT, and a rapid temperature fall occurs synchronous to a minimum. This hypothesis has been proven by relative dating of ice cores around the Laschamp geomagnetic event (14). We assumed that the fast CH_4 transitions in EDC can be taken as proxies of rapid Greenland temperature changes, thus revealing three tie points during TI (Fig. 3). The fact that it is possible, with a very simple mathematical model (15), to construct from the EDC ice isotope record a Greenland-like temperature time-series, correctly capturing stadial-interstadial transitions (corresponding to the extrema of the EDC ice isotope record) makes it very likely that the bipolar seesaw pattern is robust during these rapid transitions. These independent methods, either based on the synchronization of EDC to EDML and TALDICE or on the bipolar seesaw hypothesis, confirm our $\delta^{15}\text{N}$ method for TI within their 1σ confidence intervals, suggesting that the convective zone indeed was absent or nearly absent during TI at EDC.

We therefore built a new gas chronology based on filtered $\delta^{15}\text{N}$ data (supplementary materials). The reason why we based our new gas chronology only on the $\delta^{15}\text{N}$ method is twofold. First, the $\delta^{15}\text{N}$ method allows us to produce a continuous gas age scale along TI, whereas the other two methods give only three tie points (at times when CH_4 varies abruptly: the onset of the Bölling oscillation, the onset of the Younger Dryas, and the onset of the Holocene) and in particular cannot provide constraints for the onset of TI. Second, apart from the zero-convective-zone assumption, the $\delta^{15}\text{N}$ method has the smallest analytical uncertainty (Fig. 2).

Fig. 1. Scheme illustrating the deduction of Δdepth at EDC from ice (volcanic) and gas (CH_4) synchronization to the EDML or TALDICE ice cores and evaluation of Δdepth at EDML or TALDICE.

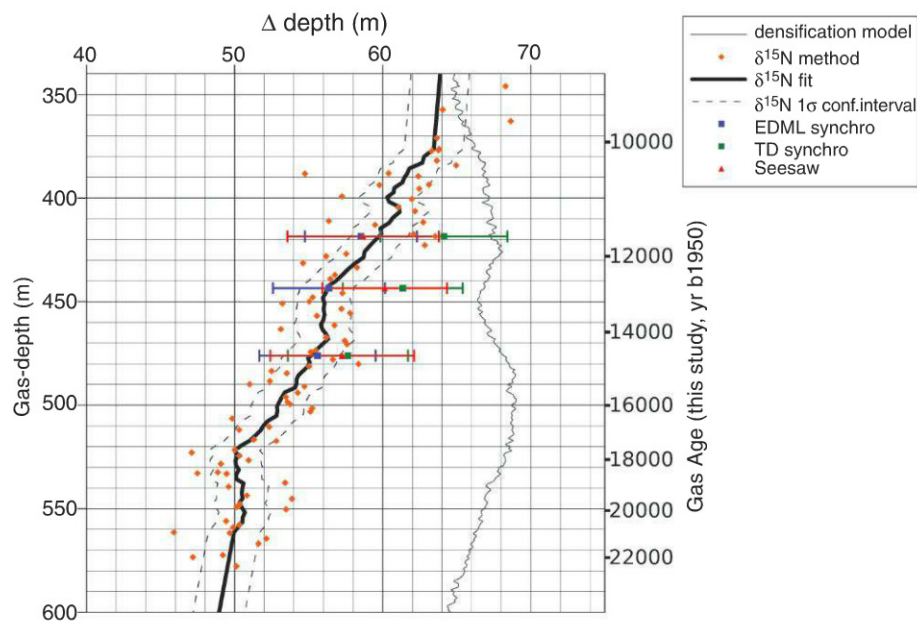
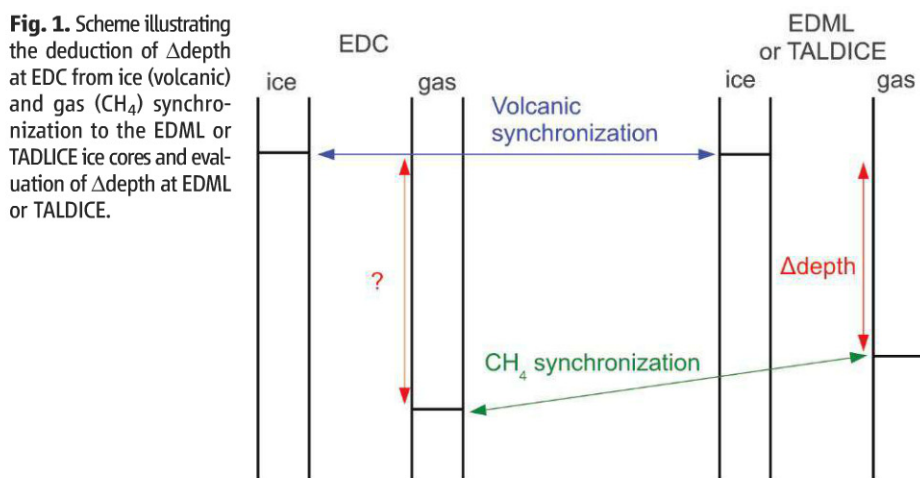


Fig. 2. Estimation of Δdepth along the EDC ice core using different methods: purely based on modeling (densification and ice flow, gray line), based on $\delta^{15}\text{N}$ data and ice flow modeling (orange dots), based on the synchronization to the EDML ice core (blue square), based on synchronization to the TALDICE ice core (green square), or based on the bipolar seesaw hypothesis (red triangle). The black line is a fit (supplementary materials) to the $\delta^{15}\text{N}$ estimates, and the dashed lines represent its 1σ confidence interval. The estimation of 1σ uncertainties is described in (5) and in the supplementary materials. yr b1950, years before 1950.

The three approaches— $\delta^{15}\text{N}$, synchronization to EDML and TALDICE, and seesaw methods—all disagree with the firm densification model simulation for EDC (Fig. 2), which probably lacks important processes affecting densification under glacial conditions, such as the effect of increased concentrations of impurities (16).

A second step to examine the phasing between aCO_2 and AT during TI is to produce an accurate record of AT during the past [an Antarctic Temperature Stack (ATS)]. To do this, we stacked (supplementary materials) the isotopic temperature reconstructions from five different ice cores (EDC, Vostok, Dome Fuji, TALDICE, and EDML) after the synchronization of these ice cores to the EDC record. This stacking process considerably reduces the noise in comparison to the single EDC record (Fig. 4): The standard deviation of ATS to its 220-year moving average is 0.20°C , whereas it is 0.52°C for the EDC temperature record (with both ATS and the EDC temperature record being resampled every 20 years).

The temporal variations of aCO_2 and AT across TI (Fig. 4) on our chronology are highly correlated (Pearson correlation coefficient of 0.993 for a 20-year resampled time series). Both records can be accurately fitted by a six-point linear function (Fig. 4 and supplementary materials). We infer the aCO_2 -AT phasing at the four break points using a Monte-Carlo algorithm (supplementary materials): the onset of TI (10 ± 160 years, 1σ , aCO_2 leads), the onset of the Bølling oscillation (-260 ± 130 years, AT leads), the onset of the Younger Dryas (60 ± 120 years, aCO_2 leads), and the onset of the Holocene (-500 ± 90 years, AT leads). The uncertainty takes into account the uncertainty in the determination of the break points and the uncertainty in the determination of Δdepth . The only significant aCO_2 -AT lags are observed at the onsets of the Bølling oscillation and the Holocene. It should be noted that during these two events, the associated sharp increases in aCO_2 were probably larger and more abrupt than the signals recorded in the ice core, due to the diffusion in the gas recording process (17). This atmosphere-ice core difference biases our break point determination toward younger ages. If we use these fast increases to determine the break points in aCO_2 , we find a lag of -10 ± 130 years (1σ) for the Bølling onset and -130 ± 90 years (1σ) for the Holocene onset; that is, no significant phasing. If, instead of using aCO_2 we use the radiative forcing of aCO_2 (18) [$\text{rCO}_2 = 5.35 \text{ W/m}^2 \ln(\text{CO}_2/280 \text{ parts per million by volume})$], the inferred phasing is not significantly changed (Fig. 4).

Our evaluation of the aCO_2 -AT phasing for TI differs from the 800 ± 200 year (lead of AT) estimate for TIII (19), based on the hypothesis that $\delta^{40}\text{Ar}$ of air is a gas proxy for local temperature. We cannot exclude the possibility that the aCO_2 -AT phasing is different for TI and TIII. However, if as recently suggested (16) the LID is influenced by the impurity content of the firm, $\delta^{40}\text{Ar}$, which, as $\delta^{15}\text{N}$, follows a gravitational

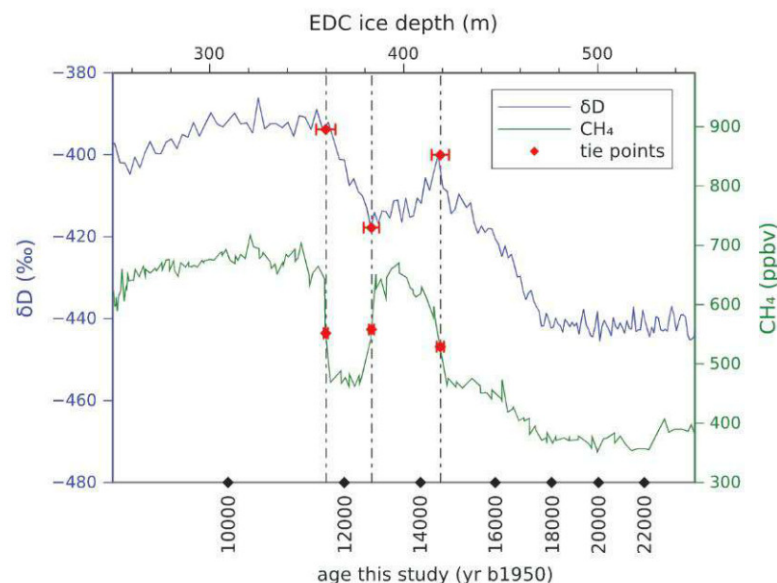


Fig. 3. The bipolar seesaw hypothesis allows us to derive three Δdepth estimates at EDC during the last deglacial warming, using the 100-year resampled δD record (28) and the CH_4 record (29). Error bars on the depths of tie points are 1σ . The EDC gas depth scale is linearly stretched according to the tie points.

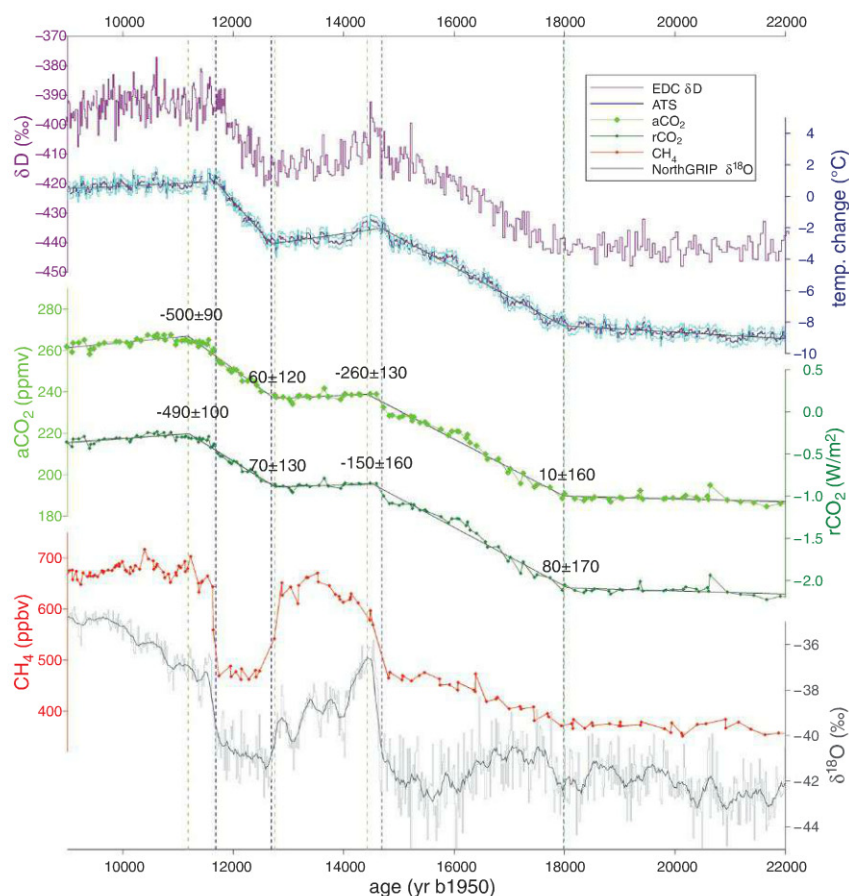


Fig. 4. Various climate time series during TI. Shown are δD from EDC (28) (purple), ATS (dark blue, this study) and confidence interval (light blue), aCO_2 from EDC (1, 2) (light green), rCO_2 (dark green), atmospheric CH_4 from EDC (29) (red), and Greenland $\delta^{18}\text{O}$ from NorthGRIP (gray) onto the GICC05 age scale (27) with a 220-year running average (dark gray). The solid lines represent the best six-point linear fit of ATS, aCO_2 , and rCO_2 (supplementary materials). The vertical dashed lines mark the four break points in ATS (blue) and in aCO_2 (green), where we evaluated the aCO_2 -AT and the rCO_2 -AT phase lags (black numbers). The new EDC age scale is described in the supplementary materials.

enrichment, should be paced by changes in dust concentration. During TIII, the change in dust occurs earlier than the change in ice isotope at both EDC and Vostok (figs. S7 and S8), whereas these two records are approximately in phase during TI (fig. S8). This could explain why the Vostok $\delta^{40}\text{Ar}$ record is in advance with respect to the aCO_2 record, without contradicting our finding of synchronous changes in aCO_2 and AT. During TII at EDC (fig. S8), on the other hand, the change in $\delta^{15}\text{N}$ occurs at a deeper depth than the change in dust. Dust concentration therefore cannot be the only factor influencing the LID.

Our results are also in general agreement with a recent 0- to 400-year aCO_2 -AT average lag estimate for TI (20), using a different approach. Although this study does not make any assumption about the convective zone thickness, it is based on coastal cores, which might be biased by local changes in ice sheet thickness; and firn densification models, which may not be valid for past conditions (see the supplementary materials for a more detailed discussion).

Our chronology and the resulting aCO_2 -AT phasing strengthens the hypothesis that there was a close coupling between aCO_2 and AT on both orbital and millennial time scales. The aCO_2 rise could contribute to much of the AT change during TI, even at its onset, accounting for positive feedbacks and polar amplification (21), which magnify the impact of the relatively weak rCO_2 change (Fig. 4) that alone accounts for $\sim 0.6^\circ\text{C}$ of global warming during TI (21). Invoking changes in the strength of the Atlantic meridional overturning circulation is no longer required to explain the lead of AT over aCO_2 (22).

Given the importance of the Southern Ocean in carbon cycle processes (23), one should not exclude the possibility that aCO_2 and AT are interconnected through another common mechanism such as a relationship between sea ice cover and ocean stratification. Although the tight link between aCO_2 and AT suggests a major common mechanism, reviews of carbon cycle processes suggest a complex association of numerous independent mechanisms (2, 23).

Changes in aCO_2 and AT were synchronous during TI within uncertainties. Our method, based on air ^{15}N measurements to determine the ice/gas depth shift, is currently being used in the construction of a common and optimized chronology for all Antarctic ice cores (24, 25). The assumption that no convective zone existed at EDC during TI might be tested in the future by using Kr and Xe isotopes (26). Further studies on the firn are needed to understand the causes of the past variations of the LID, such as the possible impact of impurity concentrations on the densification velocity. Although our study was focused on the relative timing of TI climatic records extracted from Antarctic ice cores, there is now the need to build a global chronological framework for greenhouse gases, temperature reconstructions, and other climate proxies at various locations (22). Although the timings of the Bølling, Younger Dryas,

and Holocene onsets as visible in the methane records are now well constrained by a layer-counted Greenland chronology (27), determining the timing of the onset of TI in Antarctic records remains challenging. Modeling studies using coupled carbon cycle-climate models will be needed to fully explore the implications of this synchronous change of AT and aCO_2 during TI in order to improve our understanding of natural climate change mechanisms.

References and Notes

1. E. Monnin *et al.*, *Science* **291**, 112 (2001).
2. A. Lourantou *et al.*, *Global Biogeochem. Cycles* **24**, GB2015 (2010).
3. H. Fischer, M. Wahlen, J. Smith, D. Mastoianni, B. Deck, *Science* **283**, 1712 (1999).
4. L. Loulergue *et al.*, *Clim. Past* **3**, 527 (2007).
5. F. Parrenin *et al.*, *Clim. Past* **8**, 1239 (2012).
6. C. Goujon, J.-M. Barnola, C. Ritz, *J. Geophys. Res.* **108**, ACL10/1-10 (2003).
7. F. Parrenin *et al.*, *Clim. Past* **3**, 243 (2007).
8. H. Craig, Y. Horibe, T. Sowers, *Science* **242**, 1675 (1988).
9. T. A. Sowers, M. Bender, D. Raynaud, Y. L. Korotkevich, *J. Geophys. Res.* **97**, 15683 (1992).
10. A. Landais *et al.*, *Quat. Sci. Rev.* **25**, 49 (2006).
11. G. B. Dreyfus *et al.*, *Quat. Sci. Rev.* **29**, 28 (2010).
12. J. P. Severinghaus *et al.*, *Earth Planet. Sci. Lett.* **293**, 359 (2010).
13. T. F. Stocker, S. J. Johnsen, *Paleoceanography* **18**, 1 (2003).
14. G. M. Raisbeck, F. Yiou, J. Jouzel, T. F. Stocker, *Clim. Past* **3**, 541 (2007).
15. S. Barker *et al.*, *Science* **334**, 347 (2011).
16. M. Hörhold *et al.*, *Earth Planet. Sci. Lett.* **325–326**, 93 (2012).
17. P. Köhler, G. Knorr, D. Buiron, A. Lourantou, J. Chappellaz, *Clim. Past* **7**, 473 (2011).
18. G. Myhre, E. J. Highwood, K. P. Shine, F. Stordal, *Geophys. Res. Lett.* **25**, 2715 (1998).
19. N. Caillon *et al.*, *Science* **299**, 1728 (2003).
20. J. B. Pedro, S. O. Rasmussen, T. D. van Ommen, *Clim. Past* **8**, 1213 (2012).

21. P. Köhler *et al.*, *Quat. Sci. Rev.* **29**, 129 (2010).
22. J. D. Shakun *et al.*, *Nature* **484**, 49 (2012).
23. H. Fischer *et al.*, *Quat. Sci. Rev.* **29**, 193 (2010).
24. L. Bazin *et al.*, *Clim. Past Discuss.* **8**, 5963 (2012).
25. D. Veres *et al.*, *Clim. Past Discuss.* **8**, 6011 (2012).
26. J. P. Severinghaus, A. Grachev, B. Luz, N. Caillon, *Geochim. Cosmochim. Acta* **67**, 325 (2003).
27. A. Svensson *et al.*, *Clim. Past* **4**, 47 (2008).
28. J. Jouzel *et al.*, *Science* **317**, 793 (2007).
29. L. Loulergue *et al.*, *Nature* **453**, 383 (2008).

Acknowledgments: We thank O. Watanabe, B. Stenni, and EPICA community members for giving access to, respectively, the DF1, TALDICE, and EDM1 isotopic data; L. Loulergue, D. Buiron, and T. Blunier for giving access to, respectively, the EDC-EDML, TALDICE, and GRIP CH_4 data; G. Dreyfus for giving access to the $\delta^{15}\text{N}$ isotopic data; and G. Delaygue, J. Chappellaz, S. Barker, and A. Ganopolski for helpful discussions. This work greatly benefited from constructive comments by two anonymous reviewers. This work had support from the French Agence Nationale de la Recherche (project ANR-07-BLAN-0125 "Dome A" and ANR-09-SYSC-001 "ADAGE"). This work is a contribution to EPICA, a joint European Science Foundation/European Commission scientific program, funded by the European Union and by national contributions from Belgium, Denmark, France, Germany, Italy, the Netherlands, Norway, Sweden, Switzerland, and the United Kingdom. Main logistical support was provided by the Institut Paul Emile Victor and the Programma Nazionale Ricerche in Antartide at Dome C. We thank the technical teams in the field and at the different laboratories. This is EPICA publication no. 291.

Supplementary Materials

www.sciencemag.org/cgi/content/full/339/6123/1060/DC1
Materials and Methods
Supplementary Text
Figs. S1 to S8
Tables S1 to S7
Database S1

20 June 2012; accepted 9 January 2013
10.1126/science.1226368

Genomic Diversity and Evolution of the Head Crest in the Rock Pigeon

Michael D. Shapiro,^{1*} Zev Kronenberg,² Cai Li,^{3,4} Eric T. Domyan,¹ Hailin Pan,³ Michael Campbell,² Hao Tan,³ Chad D. Huff,^{2,5} Haofu Hu,³ Anna I. Vickrey,¹ Sandra C. A. Nielsen,⁴ Sydney A. Stringham,¹ Hao Hu,⁵ Eske Willerslev,⁴ M. Thomas P. Gilbert,^{4,6} Mark Yandell,² Guojie Zhang,³ Jun Wang^{3,7,8*}

The geographic origins of breeds and the genetic basis of variation within the widely distributed and phenotypically diverse domestic rock pigeon (*Columba livia*) remain largely unknown. We generated a rock pigeon reference genome and additional genome sequences representing domestic and feral populations. We found evidence for the origins of major breed groups in the Middle East and contributions from a racing breed to North American feral populations. We identified the gene *EphB2* as a strong candidate for the derived head crest phenotype shared by numerous breeds, an important trait in mate selection in many avian species. We also found evidence that this trait evolved just once and spread throughout the species, and that the crest originates early in development by the localized molecular reversal of feather bud polarity.

Since the initial domestication of the rock pigeon in Neolithic times (1), breeders have selected striking differences in behavior, vocalizations, skeletal morphology, feather ornaments, colors, and color patterns to establish over 350 breeds (2). In many cases, the number and magnitude of differences among breeds are

more characteristic of macroevolutionary changes than of changes within a single species (2, 3). Indeed, Charles Darwin was so fascinated by domestic pigeons that he repeatedly called attention to this dramatic example of diversity within a species to communicate his ideas about natural selection (3, 4).

The genetic architecture for many derived traits in pigeons is probably relatively simple (5, 6), probably more so than that for interspecific trait variation among many wild species,

¹Department of Biology, University of Utah, Salt Lake City, UT 84112, USA. ²Department of Human Genetics, University of Utah, Salt Lake City, UT 84112, USA. ³BGI-Shenzhen, Shenzhen, 518083, China. ⁴Centre for GeoGenetics, Natural History Museum of Denmark, University of Copenhagen, Øster Voldgade 5-7, 1350 Copenhagen, Denmark. ⁵Department of Epidemiology, University of Texas M. D. Anderson Cancer Center, Houston, TX 77030, USA. ⁶Ancient DNA Laboratory, Murdoch University, Perth, Western Australia 6150, Australia. ⁷Department of Biology, University of Copenhagen, DK-1165 Copenhagen, Denmark. ⁸Novo Nordisk Foundation Center for Basic Metabolic Research, University of Copenhagen, DK-1165 Copenhagen, Denmark.

*To whom correspondence should be addressed. E-mail: mike.shapiro@utah.edu (M.D.S.); wangj@genomics.org.cn (J.W.)

because breeders often focus on qualitative rather than quantitative variation; this increases the chance of identifying genes responsible for differences among breeds. Additionally, several morphological traits show similar patterns of variation in different breeds, making it possible to test whether the same or different genes underlie similar phenotypes. Despite these advantages, the pigeon is underused as a model for the molecular genetic basis of avian variation because of the paucity of genetic and genomic resources for this bird.

We examined genomic diversity, genetic structure, and phylogenetic relationships among domestic breeds and feral populations (free-living birds descended from escaped domestics) of the rock pigeon. The pigeon reference genome was sequenced from a male Danish tumbler with the Illumina HiSeq 2000 platform, and we also resequenced 40 additional *Columba livia* genomes

to 8- to 26-fold coverage (38 individuals from 36 domestic breeds and two feral pigeons) (7). Genome-wide nucleotide diversity in the rock pigeon ($\pi = 3.6 \times 10^{-3}$) and the mutation rate estimate in the pigeon lineage (1.42×10^{-9} substitutions per site per year $\pm 2.60 \times 10^{-12}$ SE) are comparable to those of other avian species (8, 9). The observed heterozygosity indicates a large effective population size for the rock pigeon of $N_e \approx 521,000$; demographic inferences based on the allele frequency spectrum indicate that, aside from a very recent bottleneck, N_e has been remarkably stable over the past 1.5 million generations (7).

Patterns of linkage disequilibrium (LD) are indicative of haplotype sizes and genome-wide recombination rates and inform decisions about genetic mapping strategies. Using genotype data from the 40 resequenced *C. livia* genomes, we

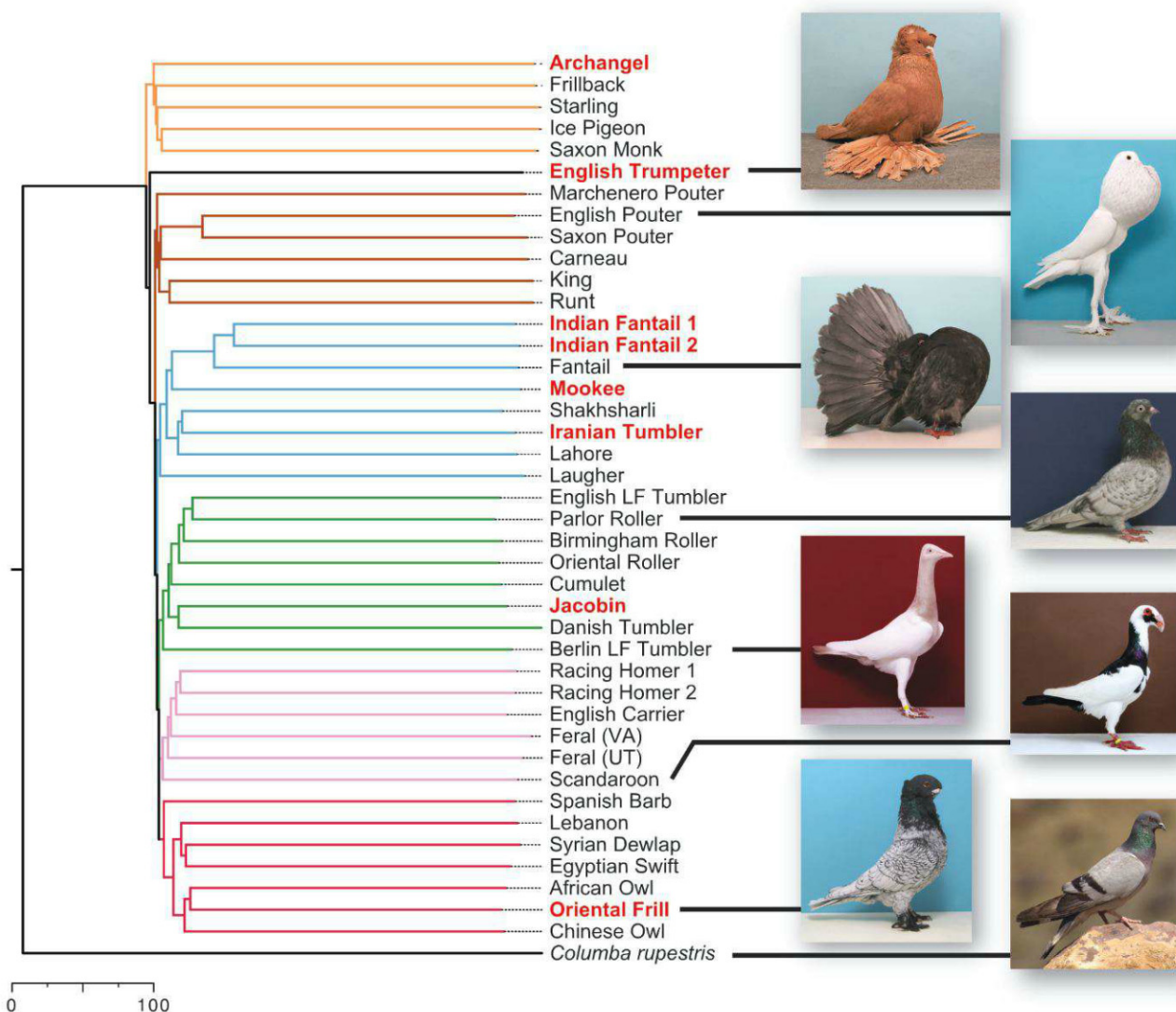


Fig. 1. Relationships among rock pigeons and the hill pigeon *C. rupestris*. A consensus neighbor-joining tree based on 1.48 million genomic SNPs and 1000 bootstrap replicates (see fig. S16 for bootstrap support) is shown. Branches are colored according to traditional breed groups (12) and/or geographic affinities: orange, toy breeds; brown, pouters and utility breeds;

light blue, Indian and Iranian breeds; green, tumblers and highflyers; pink, homers and wattle breeds; red, Mediterranean and owl breeds; black, voice characteristics (14). Bold red lettering indicates breeds with the head crest phenotype. Scale bar, Euclidean distance. [Photo credits: T. Hellmann (domestic breeds) and M. V. Shreeram (*C. rupestris*)]

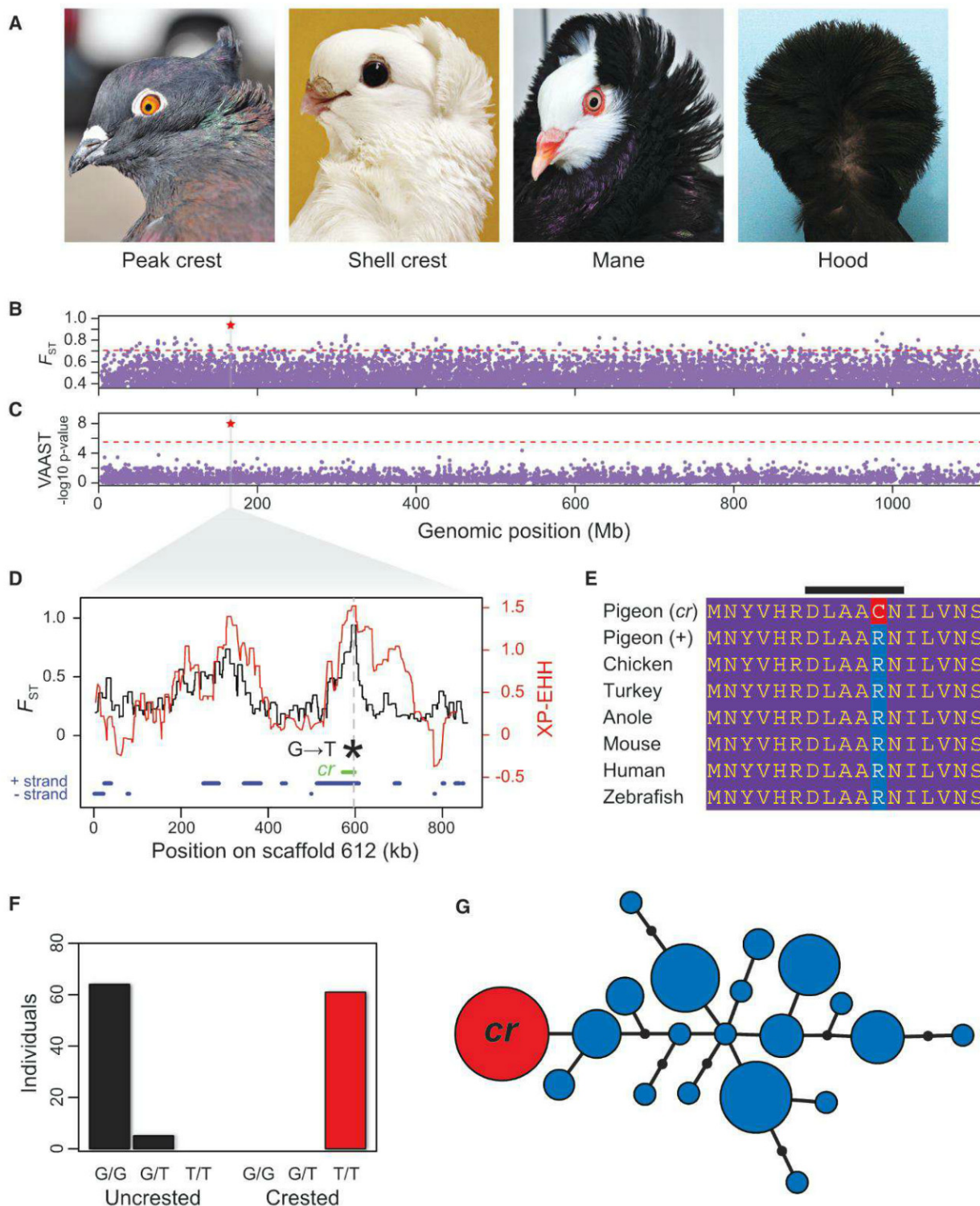


Fig. 2. *EphB2* is associated with the derived head crest phenotype. **(A)** Head crests are variable among breeds (left to right: Indian fantail, Old German owl, Old Dutch capuchin, Jacobin). **(B)** F_{ST} between crested and uncrested pigeons, with maximum value for individual SNPs plotted for nonoverlapping 100-kb windows across the genome. Red star, window with the highest score. Dashed red line, top 1% of scores. **(C)** Genome-wide VAAST scan. Each dot represents a single gene. Red star, gene with the highest score. Dashed red line, genome-wide significance cutoff. **(D)** Magnification of scaffold 612 in shaded region of **(B)** and **(C)**. Black trace, maximum F_{ST} between crested and uncrested birds over a 300-SNP window. Red trace, unstandardized cross-population extended haplotype homozygosity (XP-EHH); higher values are evidence of selection (see fig. S21, genome-wide plot). Dashed

vertical line, position of the lone genome-wide significant VAAST hit. Green bar, the 27.4-kb haplotype shared by all crested birds, includes only the *EphB2* gene. Blue bars, gene predictions on + and – DNA strands. **(E)** The *cr* mutation induces a charge-changing amino acid substitution; black bar, highly conserved DLAARN motif of catalytic loop. **(F)** Genotypes of 159 birds from 79 breeds at the *cr* locus are perfectly associated with the crest phenotype under a recessive model. **(G)** Network diagram of the minimal 11-kb haplotype shared by all resequenced rock pigeons with the *cr* mutation (also see fig. S23). Many haplotypes contain the + allele (blue), but only one contains the *cr* SNP (red). The sizes of the circles are proportional to the number of chromosomes containing a haplotype. Line segments represent single-nucleotide differences. [Jacobin photo credit: T. Hellmann]

found that mean “useful LD” (10) (coefficient of determination, $r^2 > 0.3$) decays in 2.2 kb (fig. S10J). This suggests that we should expect little LD between typical pairs of genes in an analysis across breeds; thus, the pigeon is well suited for association-mapping strategies.

We leveraged our whole-genome data to determine breed relationships, using 1.48 million variable loci. A neighbor-joining tree rooted on *C. rupestris*, the sister species of *C. livia* (11), yielded several well-supported groups (Fig. 1 and fig. S16). Notably, the two feral pigeons grouped with the wattle and homer breeds (Fig. 1, pink branches), supporting the idea that escaped racing homers are probably major contributors to feral populations (12). As with many domesticated species, pigeon evolution is probably not exclusively linear or hierarchical (12). We therefore examined genetic structure among breeds by analyzing 3950 loci with ADMIXTURE (13) and found a best model fit at $K = 1$ (a single population, where K is the number of assumed ancestral populations). However, higher values of K can also be biologically informative (figs. S17 to S20). Our analysis includes some of the oldest lineages of domestic pigeons and breeds that were not exported from the Middle East until the late 19th or early 20th centuries (14), providing information about likely geographic origins of breeds and their exchange along ancient trade routes (7).

Derived traits in domesticated birds tend to evolve along a predictable temporal trajectory, with color variation appearing in the earliest stages of domestication, followed by plumage and structural (skeletal and soft tissue) variation, and finally behavioral differences (2). One of the genetically simplest derived traits of pigeons is the head crest. Head crests are common ornaments in many bird species (2) and are important display structures in mate selection (15). In pigeons, head crests consist of neck and occipital feathers with reversed growth polarity, so that the feathers grow toward the top of the head instead of down the neck. Crests can be as small and simple as a peak of feathers or as elaborate as the hood of the Jacobin, which envelops the head (Fig. 2A). Classical genetics experiments suggest that the head crest segregates as a simple Mendelian recessive trait (6, 14). Moreover, previous studies suggest that the same locus controls the presence of a crest in numerous breeds, either with alternative alleles at this locus or additional modifier loci controlling the extent of crest development (6, 14).

We resequenced eight individuals with head crests to directly test whether the same mutation controls crest development in different breeds. We sorted genomic variants from birds with and without head crests into separate bins and calculated allele frequency differentiation (F_{ST}) across the genome (Fig. 2B). We identified a region of high differentiation between crested and uncrested birds in the pigeon ortholog of *Ephrin receptor B2* (*EphB2*; $F_{ST} = 0.94$, top hit genome-wide;

fig. S22A) (Fig. 2D). The role of *EphB2* in feather growth is not known, but it plays important roles in tissue patterning and morphogenesis and is a member of a receptor tyrosine kinase family that mediates development of the feather cytoskeleton (16, 17). All eight crested birds were homozygous for a T nucleotide at scaffold 612, position 596613 (hereafter, the *cr* allele), whereas uncrested birds were heterozygous ($n = 3$) or homozygous ($n = 30$, including the uncrested outgroup *C. rupestris*) for the putatively ancestral C nucleotide (the + allele). These results were consistent with the known simple recessive architecture of the trait and implicated a common polymorphism associated with head crest development in multiple breeds with different genetic histories (Fig. 1). This trend extended well beyond our resequencing panel: We genotyped an additional 61 crested birds from 22 breeds and 69 uncrested birds from 57 breeds, and found a perfect association between *cr/cr* genotype and the crest phenotype (Fig. 2F). By treating the genomes of crested and uncrested birds as separate populations, we also found suggestive evidence for positive selection around the *cr* allele using cross-population extended haplotype homozygosity analysis (Fig. 2D and figs. S21 and S22B).

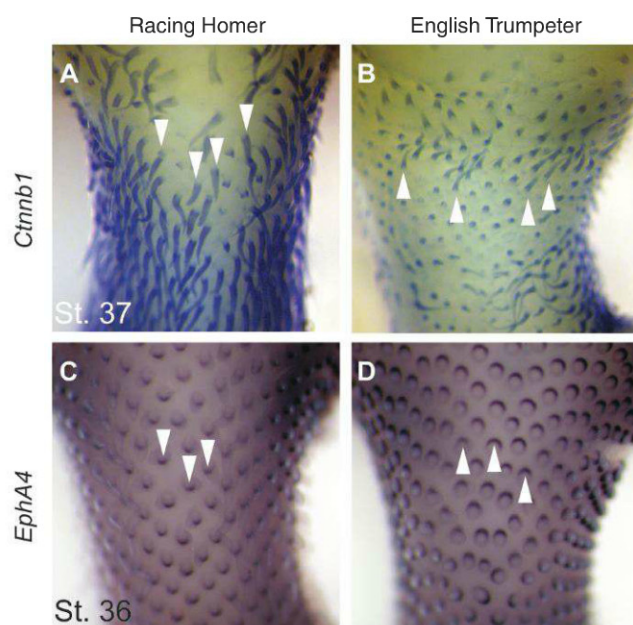
We then used the Variant Annotation, Analysis, and Search Tool [VAAST (18)] to investigate the pigeon genomes for additional coding changes associated with the head crest phenotype. This identified one gene with genome-wide significance: *EphB2*, and specifically the *cr* single-nucleotide polymorphism (SNP) ($P_{\text{genome}} = 2.0 \times 10^{-8}$) (Fig. 2, C and D). The *cr* allele has a predicted charge-changing arginine (basic) to cysteine (polar uncharged) transition in the catalytic

loop of the intracellular tyrosine kinase domain of *EphB2* (Fig. 2E). This amino acid position is invariant among other vertebrates, suggesting strong purifying selection for conserved protein function. The same DLAARN to DLAACN motif change we observe in *EphB2* is sufficient to abrogate kinase activity in human and mouse orthologs of the protein tyrosine kinase ZAP-70, and in both mammals and pigeons the mutant phenotypes are inherited recessively (19). Hence, the pigeon *cr* mutation probably abrogates kinase activity in *EphB2* and disrupts downstream signal propagation, consistent with the high VAAST score for this gene. *EphB2* is therefore a convincing candidate for the *cr* locus of classical pigeon genetics (5–7, 14).

In several wild and domesticated species, the repeated evolution of a derived trait has occurred by selection on the same gene, possibly owing to the repeated selection on the same allele or haplotype (20–22). Similarly, the *cr* SNP is part of a 27.4-kb haplotype that is shared by all crested pigeons, suggesting that the mutation occurred just once and spread to multiple breeds by introgression among domestic breeds, or was selected repeatedly from a standing variant in wild rock pigeons (Fig. 2G and fig. S23; the core haplotype containing the *cr* mutation is reduced to 11 kb when uncrested heterozygotes are included). The only gene present in the shared *cr* haplotype is *EphB2* (Fig. 2D, green bar), although at this time we cannot rule out the presence of regulatory variants that might alter the expression of another gene. Crested members of the toy, fantail, Iranian, Jacobin, and owl breed groups are not more closely related to each other than to uncrested breeds (Fig. 1). Nevertheless, members of these groups had head crests

Fig. 3. Feather bud polarity is reversed in the *cr* mutant.

(A and B) Expression of the feather structural gene *Ctnnb1* reveals the direction of outgrowth of early feather buds. St., Hamburger-Hamilton embryonic stage. (A) Neck and occipital head expression of *Ctnnb1* in an embryo of the uncrested racing homer. Feather buds point downward along the contour of the head and neck (arrowheads). (B) Occipital feather buds point upward in the equivalent region of the crested English trumpeter, indicating morphological reversal of feather orientation. (C and D) Expression of the polarity marker *EphA4* was assayed at an earlier developmental stage to test whether feather placodes, the ectodermal thickenings that give rise to feather buds, are also reversed. (C) Polarity marker *EphA4* is expressed posteriorly (arrowheads) in feather placodes of the racing homer. (D) The polarity of placodes is reversed in the English trumpeter. Expression of *EphB2* in the skin is weak and unpolarized at this stage in both morphs (fig. S26).



hundreds of years ago (14), so some of these introgression events must have occurred in the distant past. Breeds with a wide variety of crest phenotypes share the same derived allele; therefore, allelic variation at the *cr* locus alone does not control all aspects of crest development (14). Other genetic and developmental factors beyond this locus must contribute to variation in crest morphology, akin to the presumed complex genetic architecture of species-level divergence in feather ornaments (2).

In crested pigeons, feather placode polarity and bud outgrowth are inverted during embryogenesis (Fig. 3). Expression of *EphB2* is not polarized in early placodes (fig. S26), so the effects of the *cr* mutation on feather polarity are probably exerted earlier in development. Why might the crest phenotype be limited to the head and neck? In Naked neck chicken mutants, regionalized production of retinoic acid allows uniform up-regulation of *Bmp7* expression to change skin phenotypes in the neck but not the body (23). Similarly, the head crests of several chicken breeds, in which feathers are elongated but do not have a reversed growth trajectory as in pigeons, are localized to the top of the head, probably due to ectopic expression of *Hox* positional cues (24). Together these examples provide evidence for regionalization of the developing head and neck skin in the chicken. We propose that analogous mechanisms might underlie skin regionalization in the pigeon and allow *cr* to change feather polarity in the occiput and neck, but not elsewhere.

Our study of domestic rock pigeons illustrates how combining comparative genomics and population-based analyses forwards our understanding of genetic relationships and the genomic basis of traits. Many of the traits that vary

among pigeon breeds also vary among wild species of birds and other animals (2, 25); thus, pigeons are a model for identifying the genetic basis of variation in traits of general interest. Moreover, variation in many traits in domestic pigeons, including the head crest phenotype described here, is constructive rather than regressive: Breeds derived from the ancestral rock pigeon possess traits that the ancestor does not have. Although adaptive regressive traits are important, the genetic basis of constructive traits in vertebrates remains comparatively poorly understood. The domestic pigeon is thus a promising model with which to explore the genetic architecture of derived, constructive phenotypes in a bird that is amenable to genetic, genomic, and developmental investigation.

References and Notes

1. A. C. Driscoll, D. W. Macdonald, S. J. O'Brien, *Proc. Natl. Acad. Sci. U.S.A.* **106** (Suppl. 1), 9971 (2009).
2. T. D. Price, *Genetica* **116**, 311 (2002).
3. C. Darwin, *On the Origin of Species by Means of Natural Selection* (John Murray, London, 1859).
4. C. Darwin, *The Variation of Animals and Plants Under Domestication* (John Murray, London, 1868), vol. 1.
5. T. H. Morgan, *Biol. Bull.* **21**, 215 (1911).
6. A. Sell, *Breeding and Inheritance in Pigeons* (Schober Verlags-GmbH, Hengersberg, Germany, 1994).
7. See the supplementary materials on Science Online.
8. C. N. Balakrishnan, S. V. Edwards, *Genetics* **181**, 645 (2009).
9. H. Ellegren *et al.*, *Nature* **491**, 756 (2012).
10. J. Aerts *et al.*, *Cytogenet. Genome Res.* **117**, 338 (2007).
11. K. P. Johnson *et al.*, *Auk* **118**, 874 (2001).
12. S. A. Stringham *et al.*, *Curr. Biol.* **22**, 302 (2012).
13. D. H. Alexander, J. Novembre, K. Lange, *Genome Res.* **19**, 1655 (2009).
14. W. M. Levi, *The Pigeon* (Levi Publishing, Sumpter, SC, ed. 2 revised, 1986).
15. T. Amundsen, *Trends Ecol. Evol.* **15**, 149 (2000).
16. I. W. McKinnell, H. Makarenkova, I. de Curtis, M. Turmaine, K. Patel, *Dev. Biol.* **270**, 94 (2004).

17. R. N. Kelsh, M. L. Harris, S. Colanesi, C. A. Erickson, *Semin. Cell Dev. Biol.* **20**, 90 (2009).
18. M. Vandell *et al.*, *Genome Res.* **21**, 1529 (2011).
19. M. E. Elder *et al.*, *J. Immunol.* **166**, 656 (2001).
20. P. F. Colosimo *et al.*, *Science* **307**, 1928 (2005).
21. N. B. Sutter *et al.*, *Science* **316**, 112 (2007).
22. A. S. Van Laere *et al.*, *Nature* **425**, 832 (2003).
23. C. Mou *et al.*, *PLoS Biol.* **9**, e1001028 (2011).
24. Y. Wang *et al.*, *PLoS ONE* **7**, e34012 (2012).
25. L. F. Baptista, J. E. Gomez Martinez, H. M. Horblit, *Acta Zoologica Mex.* **25**, 719 (2009).

Acknowledgments: We thank the University of Washington Burke Museum for the *C. rupestris* tissue sample (UWBM 59803); J. Oldham, K. Wright, the Utah Pigeon Club, the National Pigeon Association, and A. and H. O. Christiansen for domestic pigeon samples; D. Clayton for feral samples; and D. Clayton, M. Horvath, D. Kingsley, R. Nielsen, and W. Warren for discussion and comments. Supported by a Burroughs Wellcome Fund Career Award in the Biomedical Sciences, NSF CAREER DEB-1149160, University of Utah Research Foundation (M.D.S.); NIH training grant T32GM007464 (S.A.S.); NIH training grant T32HD07491 (E.T.D.); an NSF EDEN internship (A.I.V.); NIH/NHGRI R01HG004694 and NIH ARRA GO RC2HG005619 (M.Y.); and the Danish National Research Foundation (M.T.P.G. and E.W.). We acknowledge a computer time allocation from the Center for High Performance Computing at the University of Utah. This whole-genome shotgun project has been deposited at DDBJ/EMBL/GenBank under accession no. AKCR00000000 (the first version described here is AKCR01000000; raw reads, SRA052637); RNA-seq data for annotation, accession no. GSE39333; and raw reads for resequenced genomes, accession no. SRA054391.

Supplementary Materials

www.sciencemag.org/cgi/content/full/science.1230422/DC1
Materials and Methods
Supplementary Text
Figs. S1 to S27
Tables S1 to S28
References (26–72)

19 September 2012; accepted 7 December 2012
Published online 31 January 2013;
10.1126/science.1230422

KNOX2 Genes Regulate the Haploid-to-Diploid Morphological Transition in Land Plants

Keiko Sakakibara,^{1,2,3,4*} Sayuri Ando,^{3,4} Hoichong Karen Yip,⁵
Yosuke Tamada,^{4,6} Yuji Hiwatashi,^{4,6†} Takashi Murata,^{4,6} Hironori Deguchi,¹
Mitsuyasu Hasebe,^{3,4,6} John L. Bowman^{2,5*}

Unlike animals, land plants undergo an alternation of generations, producing multicellular bodies in both haploid (1n: gametophyte) and diploid (2n: sporophyte) generations. Plant body plans in each generation are regulated by distinct developmental programs initiated at either meiosis or fertilization, respectively. In mosses, the haploid gametophyte generation is dominant, whereas in vascular plants—including ferns, gymnosperms, and angiosperms—the diploid sporophyte generation is dominant. Deletion of the class 2 KNOTTED1-LIKE HOMEBOX (KNOX2) transcription factors in the moss *Physcomitrella patens* results in the development of gametophyte bodies from diploid embryos without meiosis. Thus, KNOX2 acts to prevent the haploid-specific body plan from developing in the diploid plant body, indicating a critical role for the evolution of KNOX2 in establishing an alternation of generations in land plants.

Plants have a life cycle characterized by alternation between two generations, haploid (gametophyte) and diploid (sporophyte),

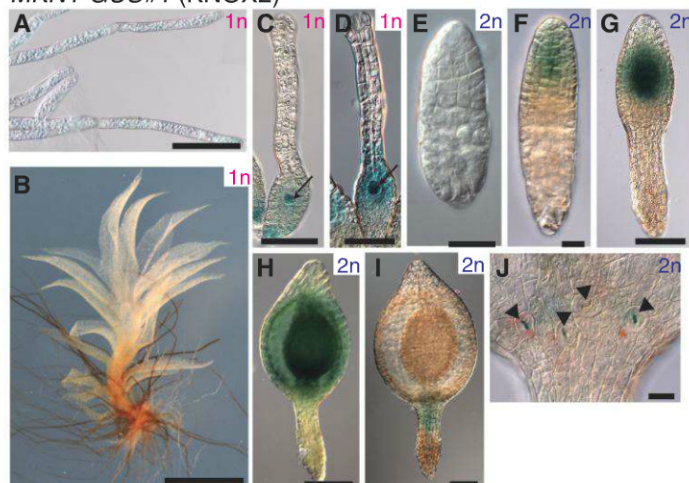
where each phase develops a multicellular body (1, 2). The gametophyte produces gametes—sperm (or pollen) and egg cells—and may be the domi-

nant photosynthetic generation, as in liverworts, mosses, and hornworts. The sporophyte produces haploid spores via meiosis and is the dominant photosynthetic generation in the vascular plants. The alternation of generations in land plants results in the possibility that tissue differentiation in each generation is governed by different genetic programs, initiated by either fertilization (haploid to diploid) or meiosis (diploid to haploid). Land plants probably evolved from a freshwater algal ancestor, with a life cycle similar to

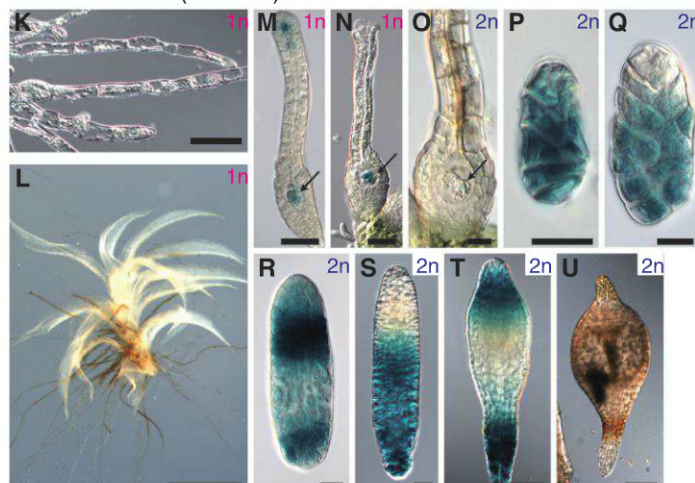
¹Department of Biological Science, Graduate School of Science, Hiroshima University, Higashi-Hiroshima 739-8526, Japan. ²School of Biological Sciences, Monash University, Melbourne, Victoria 3800, Australia. ³ERATO, Japan Science and Technology Agency, Okazaki 444-8585, Japan. ⁴National Institute for Basic Biology, Okazaki 444-8585, Japan. ⁵Section of Plant Biology, University of California, Davis, One Shields Avenue, Davis, CA 95616, USA. ⁶School of Life Science, The Graduate University for Advanced Studies, Okazaki 444-8585, Japan.

*To whom correspondence should be addressed. E-mail: john.bowman@monash.edu (J.L.B.); bara@hiroshima-u.ac.jp (K.S.)
†Present address: National Plant Phenomics Centre, Institute of Biological, Environmental and Rural Sciences, Aberystwyth University, Aberystwyth, SY23 3EB, UK.

MKN1-GUS#1 (KNOX2)



MKN6-GUS#5 (KNOX2)



MKN2-GUS#1 (KNOX1)

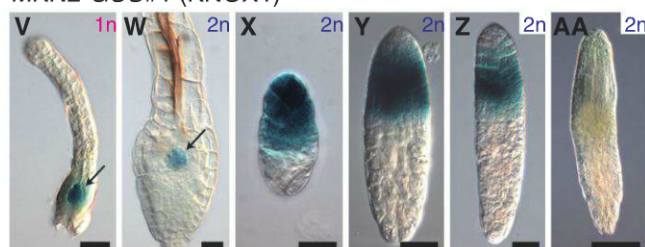


Fig. 1. Expression patterns of *Physcomitrella* KNOX2 genes. Blue staining documents GUS activity derived from translational fusions into endogenous KNOX loci. (A to J) *MKN1-GUS#1*, (K to U) *MKN6-GUS#5*, and (V to AA) *MKN2-GUS#1* (KNOX1) lines. Protonemata and gametophores of the gametophyte (A and B, K and L), archegonial tissues with egg mother cells (C and M, arrows), and unfertilized egg cells (D and N, arrows) of gametophyte generation. *MKN1-GUS* expression in embryos (E), sporogenous precursor cells (F), sporogenous tissues (G and H), seta (I), and stomatal cells (J, arrowheads) in sporophytes. *MKN6-GUS* expression in the zygote (O, arrow), young embryos (P to R), older developing sporophytes (S and T), and a mature sporangium (U). *MKN2-GUS* expression in the egg mother cell (V, arrow), the zygote (W, arrow), and apical regions of young (X to Z) and older developing sporophytes (AA). Sporophytes were removed from archegonia and gametophores in (E) to (I), (P) to (U), and (X) to (AA). Scale bars,

100 μ m (A, G to I, K, T, U, and AA); 1 mm (B and L); 50 μ m (C, D, M, N, and Z); and 20 μ m (E, F, J, O to S, and V to Y). Ploidy level is indicated in the upper right corner of each panel.

extant charophycean algae, the algal taxa most closely related to land plants (3–5). These algae have multicellular haploid bodies that produce gametes, and after fertilization, the diploid zygote directly undergoes meiosis to produce haploid spores. The multicellular diploid sporophyte generation of land plants is thought to have evolved through a delay in zygotic meiosis, with extensive mitotic cell divisions between the formation of the zygote and the production of spores via meiosis (1). Thus, the diploid sporophyte generation of land plants evolved from an ancestral single-celled diploid generation.

The genetic mechanisms regulating the multicellular diploid generation of land plants are presently unknown, but their origin may lie in the genetic machinery regulating the sexual cycle of land plant ancestors. Chlorophyta are a green algal clade with a sister relationship to charophycean algae plus land plants (4). In *Chlamydomonas*, a unicellular chlorophyte, the haploid-to-diploid transition is regulated by a pair of related TALE (three-amino acid length extension) class homeodomain protein-encoding genes (6–8). The two gamete types, “plus” and “minus,” express two homeodomain genes, *GSP1* (encoding a BELL-related TALE homeodomain protein) and *GSM1* [encoding a KNOTTED1-LIKE HOMEBOX (KNOX)-related TALE homeodomain protein], respectively (7). On their own, each of the two en-

coded proteins is cytoplasmic, but upon gamete fusion, the proteins physically interact and translocate into the nucleus to regulate zygotic gene expression (7). Loss-of-function *GSP1* alleles result in a failure to activate the diploid genetic program with zygotes reentering the haploid program, whereas gain-of-function alleles can ectopically activate the diploid program during the haploid phase of the life cycle (6, 8). Lee *et al.* have proposed that KNOX-TALE genes in land plants are candidates for regulating aspects of the alternation of generations (7).

In contrast to Chlorophyta, land plant genomes encode two subfamilies of KNOX genes, class 1 (KNOX1) and class 2 (KNOX2), resulting from a gene duplication in the lineage leading to land plants (9). KNOX1 genes are regulators of sporophytic (diploid) meristematic genes, but the functions of KNOX2 genes are unknown (10). We used translational fusions with the β -glucuronidase (*GUS*) reporter gene to investigate the spatiotemporal expression patterns of the two *Physcomitrella* KNOX2 genes, *MKN1* (AF285148) and *MKN6* (XM_001765523) (11, 12), throughout both gametophyte and sporophyte generations (fig. S1) (13, 14). In the gametophyte generation, GUS activity was not detected for either *MKN1* or *MKN6* in the protonemata (the early filamentous growth phase) or the gametophores (leafy shoots from which reproductive structures develop) (Fig. 1, A,

B, K, and L, and fig. S2), similar to *Physcomitrella* KNOX1 genes (11). In all of the haploid tissue we examined, we detected GUS activity in only the egg mother cell, the surrounding archegonial tissues, and mature eggs before fertilization (Fig. 1, C, D, M, N, and V).

In the sporophyte generation, we first detected a signal in the *MKN6-GUS* line in the zygote (Fig. 1O) and later throughout young embryos (Fig. 1P), with the signal diminishing in the apical region during apical cell divisions (Fig. 1Q). Subsequently, we identified GUS activity throughout the embryo (Fig. 1R); at later stages of sporophyte development, we detected a signal in a complex pattern in several tissues, including the seta and foot (Fig. 1, S to U). In contrast, the *MKN1-GUS* signal was more restricted during sporophyte development (Fig. 1E), with signal in the endotheicum, a tissue that gives rise to sporogenous precursor cells (Fig. 1, F and G), and later in sporogenous tissues (Fig. 1H) and a few tissues of the mature sporophyte (Fig. 1, I and J). These sporophytic patterns of *Physcomitrella* KNOX2 expression are initially overlapping with those of KNOX1 in the zygote (Fig. 1W), then complementary in the young embryo (Fig. 1X), and again overlapping in sporogenous tissues of developing sporophyte (Fig. 1, Y to AA) (11), such that all sporophytic meristematic cells expressed at least one KNOX gene.

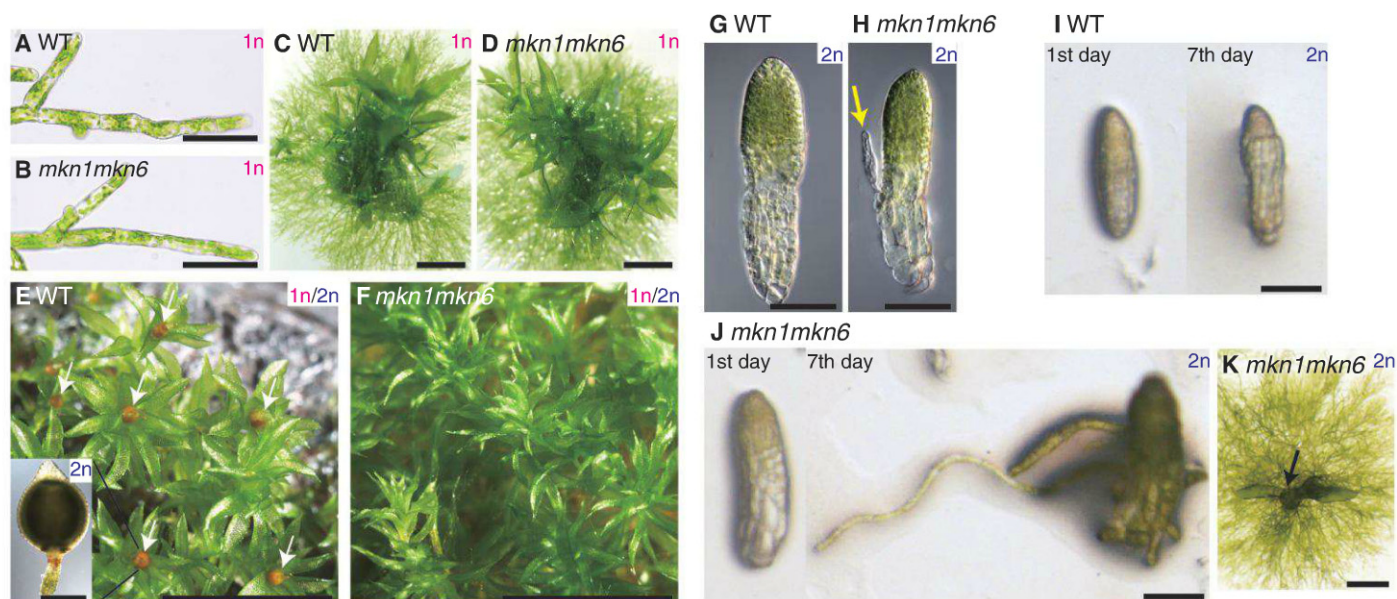


Fig. 2. Embryogenesis in KNOX2 deletion lines is suspended with haploid-like tissues produced in the diploid generation. (A to D) Gametophytes of the wild type (A and C) and double-deletion line *mkn1mkn6*#12 (B and D). Protonemata (A and B) and gametophyte tissues 2 weeks after culturing of protonemata (C and D) of WT and *mkn1mkn6* lines. (E to F) Haploid gametophores 8 weeks after gametangia induction of the wild type (E) and the *mkn1mkn6* deletion line (F). Arrows in (E) indicate mature diploid sporangia. The inset in (E) depicts a maturing WT sporophyte 6 weeks after gametangia induction. (G) Wild-type sporophyte 4 weeks after gametangia induction. (H)

Sporophyte in the *mkn1mkn6* deletion line 6 weeks after gametangia induction. Protruding filamentous tissues were observed in 50% (19 of 38) of embryos (arrow). (I to K) Embryo culture after removal from archegonia in the wild type (I) and *mkn1mkn6* deletion lines (J and K). (I) Wild-type embryos on the first day (left) and after 1 week (right) in culture. (J) *mkn1mkn6* embryos on the first day (left) and after 1 week (right) in culture. (K) Protonemata with gametophores derived from *mkn1mkn6* embryos after 16 days in culture (arrow). Scale bars, 100 μ m (A, B, and G to J); 1 mm (C, D, and K); 5 mm (E and F); and 500 μ m [inset in (E)]. Ploidy level is indicated in the upper right corner of each panel.

Because the two *Physcomitrella* KNOX2 genes are closely related paralogs (9, 11) and their expression patterns partially overlap, we constructed single- and double-deletion mutants (fig. S3). Consistent with their expression patterns, the deletion of both KNOX2 genes did not affect the phenotype of the gametophytic (1n) protonema and gametophore morphologies (Fig. 2, A to D). However, no mature sporangia developed in the *mkn1mkn6* deletion line (Fig. 2, E and F, and table S1), with development of sporophytes suspended at the 4-week embryo stage (Fig. 2, G and H, and table S1). The *mkn1mkn6* embryos often had protruded filamentous structures, similar in morphology to protonemata or rhizoids, cell types normally produced only in the haploid generation (Fig. 2H). To further characterize the defects in sporophyte development, we cultured *mkn1mkn6* and wild-type (WT) embryos on plate media without plant hormones. Notably, the filamentous structures that emerged from *mkn1mkn6* sporophytes continued to grow, forming protonemal tissues resembling that of a WT gametophyte within 1 week (Fig. 2J and Table 1). Subsequently, gametophore buds developed from the mutant protonemal filaments approximately 2 weeks after incubation (Fig. 2K), again, similar to a WT gametophyte (Fig. 2C). Gametophores produced via *mkn1mkn6* embryos formed gametangia at a similar frequency as the wild type, with the antheridia and archegonia producing functional sperms and

eggs, respectively (table S2). Self-fertilization resulted in embryos arrested at the same stage as the original *mkn1mkn6* lines. However, the growth of gametophyte-like bodies derived from *mkn1mkn6* embryos is not indistinguishable from WT embryos, with a reduced frequency of gametophore initiation and possible differences in sizes of protonemal filament cells noted (fig. S4 and tables S3 and S4). Thus, some developmental epigenetic modifications may not be properly reset in protonemata that differentiated directly from embryonic tissues. Consistent with their expression patterns, the phenotype of single-gene knockouts of *mkn6* was similar to the double mutant, whereas *mkn1* single mutants showed no dramatic phenotype, indicating that *MKN6* expression (Fig. 1, E and P to R) is critical to maintain sporophyte identity (Table 1 and table S1).

The irregular transition from sporophyte to gametophyte without meiosis is called apospory. In mosses, apospory can be induced, with protonemata and leafy gametophores (gametophytic tissues) developing from setae (sporophytic tissues) that have been severed (15). The opposite irregular transition from gametophyte to sporophyte without fertilization is called apogamy. Apogamy and apospory have been observed to occasionally take place under both natural environmental and experimental conditions in nonseed plants (16, 17). As the number of chromosomes in the sporophyte (2n) is double that of the gametophyte

Table 1. Protonemal tissue formation in *mkn6* and *mkn1mkn6* embryos after 1 week in culture. *n* represents the number of embryos examined. Intact embryos were isolated from archegonia and incubated on BCD plates (14) including 1 mM CaCl₂ and 0.8% agar for 1 week.

Cell lines	Protonemal tissue formation (%)	<i>n</i>
Wild type	0	26
<i>mkn1mkn6</i> #12	87.0	23
<i>mkn1</i> #5-8	0	7
<i>mkn1</i> #7-8	0	6
<i>mkn6</i> #8	100	10
<i>mkn6</i> #11	86.7	15

(1n), an aposporously produced gametophyte should have 2n chromosomes (18).

To determine the ploidy of protonemata developing from *mkn1mkn6* embryos, we measured the DNA content of cell nuclei. Chloronemal cells, including apical cells, of *Physcomitrella* spend most of the cell cycle in the G₂/M phase (19); therefore, the amount of nuclear DNA in the haploid (1n) controls—WT and *mkn1mkn6* chloronemal apical cells—is at a 2C level. Importantly, when we analyzed apical cells of protonemata growing from *mkn1mkn6* sporophytes, the average nuclear intensity was close to double (4C) that of the controls (Fig. 3 and fig. S5). These results

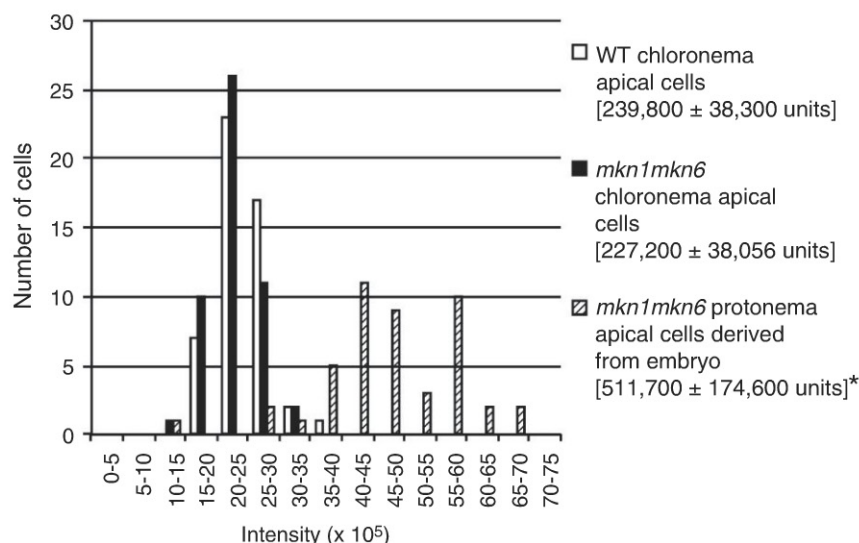


Fig. 3. Ploidy of protonemal apical cells in WT and *mkn1mkn6* deletion lines. Comparison of nuclear DNA content (as calculated from fluorescence of nuclei stained with 4',6-diamidino-2-phenylindole) of interphase apical cells of chloronema in the WT gametophyte (white; $n = 50$ cells), the *mkn1mkn6* deletion line gametophyte (black; $n = 50$), and interphase apical cells in the protonema-like tissues derived from the embryo of the *mkn1mkn6* line (stripes; $n = 50$). Average values and standard deviations are shown. The asterisk indicates significant differences relative to WT chloronemata ($P < 0.001$, Mann-Whitney U test).

indicate that deletion of *Physcomitrella* KNOX2 genes results in apospory, a haploid phenotype developing from a diploid body. This phenotype, combined with the expression pattern of these genes throughout sporophyte development (Fig. 1), indicates that KNOX2 transcription factors function to repress the haploid generation developmental genetic program during the diploid generation of sporophyte development.

In contrast to apospory observed in KNOX2 mutants, inactivation of the *Physcomitrella* polycomb repressive complex 2 (PRC2) results in apogamy, the development of a sporophyte body plan in a haploid gametophyte. Mutations in either *Physcomitrella patens* *CURLY LEAF* (*PpCLF*) or *Physcomitrella patens* *FERTILIZATION-INDEPENDENT ENDOSPERM* (*PpFIE*), both of which are predicted to encode components of PRC2 based on sequence similarities, result in fertilization-independent, sporophyte-like bodies from branches of gametophytic protonemal filaments and the induction of sporophyte-specific gene expression (e.g., KNOX1) in gametophyte buds (20, 21). Thus, polycomb-mediated repressive chromatin modification throughout the genome is required to maintain gametophyte identity through repression of the sporophyte genetic program. In contrast to PRC2, a global regulator of facultative chromatin that acts to repress target genes, KNOX2 is a specific transcription factor family that regulates the alternation of generations in land plants.

In land plants, KNOX1 and KNOX2 proteins heterodimerize with proteins encoded by BELL-class TALE genes to affect gene expression (22–24). Furthermore, KNOX expression in the *Physco-*

mitrella egg cell may function as KNOX expression in *Chlamydomonas* gametes. In the flowering plant *Arabidopsis thaliana*, the four KNOX2 genes (*KNAT3*, *KNAT4*, *KNAT5*, and *KNAT7*) are broadly expressed in the sporophyte body (2n) (25, 26). Intriguingly, loss-of-function alleles of *knat3* partially suppress phenotypes induced by ectopic expression of a BELL gene, *BLH1*, in the embryo sac (1n) (27), indicating that *KNAT3* is expressed in WT embryo sacs. Conversely, three of the four *Physcomitrella* BELL genes were primarily expressed in the antheridia, archegonial tissues, and/or the sporophyte (fig. S6). We speculate that gamete-specific expression of KNOX and BELL genes to initiate zygotic gene expression may be conserved more broadly throughout plants.

The KNOX1 and KNOX2 subfamilies arose after the divergence of the Chlorophyta and land plant lineages. The evolution of a multicellular diploid generation from an ancestral single-celled zygotic diploid generation required the maintenance of continued mitotic divisions after fertilization and repression of the haploid developmental program during development of the diploid generation. We hypothesize that in the common ancestor of land plants, KNOX1 genes acquired functions in the maintenance of sporophytic meristematic cells, as evidenced by loss-of-function phenotypes in both flowering plants (e.g., *Arabidopsis*) and a moss (*Physcomitrella*), and KNOX2 genes evolved to maintain diploid differentiation by suppression of the gametophytic development program. Thus, KNOX1/KNOX2 duplication facilitated the evolution of more complex gene regulatory networks to perform two critical roles in the diploid phase of the alternation of generations and was instru-

mental in the establishment of a multicellular diploid generation in land plants.

References and Notes

1. F. O. Bower, *Origin of a Land Flora: A Theory Based on the Facts of Alternation* (MacMillan, London, 1908).
2. W. F. B. Hofmeister, *On the Germination, Development, and Fructification of the Higher Cryptogamia, and on the Fructification of the Coniferae* (Ray Society, London, 1862).
3. K. G. Karol, R. M. McCourt, M. T. Cimino, C. F. Delwiche, *Science* **294**, 2351 (2001).
4. L. A. Lewis, R. M. McCourt, *Am. J. Bot.* **91**, 1535 (2004).
5. L. E. Graham, *Origin of Land Plants* (Wiley, New York, 1993).
6. H. Zhao, M. Lu, R. Singh, W. J. Snell, *Genes Dev.* **15**, 2767 (2001).
7. J.-H. Lee, H. Lin, S. Joo, U. Goodenough, *Cell* **133**, 829 (2008).
8. Y. Nishimura, T. Shikanai, S. Nakamura, M. Kawai-Yamada, H. Uchimiya, *Plant Cell* **24**, 2401 (2012).
9. K. Mukherjee, L. Brocchieri, T. R. Bürglin, *Mol. Biol. Evol.* **26**, 2775 (2009).
10. A. Hay, M. Tsiantis, *Development* **137**, 3153 (2010).
11. K. Sakakibara, T. Nishiyama, H. Deguchi, M. Hasebe, *Evol. Dev.* **10**, 555 (2008).
12. S. D. Singer, N. W. Ashton, *Plant Cell Rep.* **26**, 2039 (2007).
13. R. A. Jefferson, T. A. Kavanagh, M. W. Bevan, *EMBO J.* **6**, 3901 (1987).
14. Supplementary materials and methods are available on Science Online.
15. N. Pringsheim, *Monatsber. K. Akad. Wiss. Berlin* **1876**, 425 (1876).
16. C. E. Allen, *Bot. Rev.* **1**, 269 (1935).
17. W. N. Steil, *Bot. Rev.* **5**, 433 (1939).
18. E. Strasburger, *Ann. Bot. (London)* **8**, 281 (1894).
19. M. Ishikawa et al., *Plant Cell* **23**, 2924 (2011).
20. A. Mosquana et al., *Development* **136**, 2433 (2009).
21. Y. Okano et al., *Proc. Natl. Acad. Sci. U.S.A.* **106**, 16321 (2009).
22. M. Bellaoui et al., *Plant Cell* **13**, 2455 (2001).
23. J. Hackbusch, K. Richter, J. Müller, F. Salami, J. F. Uhrig, *Proc. Natl. Acad. Sci. U.S.A.* **102**, 4908 (2005).
24. H. M. S. Smith, I. Boschke, S. Hake, *Proc. Natl. Acad. Sci. U.S.A.* **99**, 9579 (2002).
25. K. A. Serikawa, A. Martinez-Laborda, H. S. Kim, P. C. Zambryski, *Plant J.* **11**, 853 (1997).
26. E. Truemit, K. R. Siemerling, S. Hodge, V. Grbic, J. Haseloff, *Plant Mol. Biol.* **60**, 1 (2006).
27. G. C. Pagnussat, H. J. Yu, V. Sundaresan, *Plant Cell* **19**, 3578 (2007).

Acknowledgments: We thank Y. Kabeya for technical assistance of flow cytometry; C. L. Volk Murayama for translation of references; D. R. Smyth, Y. Eshed, M. Shimamura, and T. Nishiyama for critical comments on the manuscript; and the Model Plant Research Facility of the National Institute for Basic Biology for experimental facilities. This research was partly supported by grants from the Ministry of Education, Culture, Sports, Science and Technology (MEXT); the Japan Society for the Promotion of Science (JSPS) KAKENHI grant (to K.S., Y.T., H.D., and M.H.); and the Australian Research Council grant FF0561326 (J.L.B.). K.S. was a JSPS research fellow. Sequence data associated with this manuscript have been submitted to the DNA Data Bank of Japan.

Supplementary Materials

www.sciencemag.org/cgi/content/full/339/6123/1067/DC1
Materials and Methods
Figs. S1 to S6
Tables S1 to S7
References (28–35)

12 September 2012; accepted 10 January 2013
10.1126/science.1230082

Mps1 and Ipl1/Aurora B Act Sequentially to Correctly Orient Chromosomes on the Meiotic Spindle of Budding Yeast

Régis E. Meyer,¹ Seoyoung Kim,^{1,2*} David Obeso,^{1,2†} Paul D. Straight,^{3‡} Mark Winey,³ Dean S. Dawson^{1,2§}

The conserved kinases Mps1 and Ipl1/Aurora B are critical for enabling chromosomes to attach to microtubules so that partner chromosomes will be segregated correctly from each other, but the precise roles of these kinases have been unclear. We imaged live yeast cells to elucidate the stages of chromosome-microtubule interactions and their regulation by Ipl1 and Mps1 through meiosis I. Ipl1 was found to release kinetochore-microtubule (kMT) associations after meiotic entry, liberating chromosomes to begin homologous pairing. Surprisingly, most chromosome pairs began their spindle interactions with incorrect kMT attachments. Ipl1 released these improper connections, whereas Mps1 triggered the formation of new force-generating microtubule attachments. This microtubule release and reattachment cycle could prevent catastrophic chromosome segregation errors in meiosis.

In order to be segregated properly, partner chromosomes must attach to microtubules that emanate from opposite poles of the spindle—a configuration referred to as bioriented. Chromosomes become bioriented in a multistep process (fig. S1A) that involves the release and reattachment of kMT connections that would lead to chromosome segregation errors (1). A surveillance mechanism, the spindle checkpoint, delays progression out of metaphase until incorrect kinetochore-microtubule (kMT) connections be-

come corrected (2). Meiosis I, which involves the segregation of homologous chromosomes, presents extra challenges to the biorientation machinery (fig. S1). Ipl1 (Aurora B in mammals) and Mps1 are implicated in several aspects of chromosome segregation in meiosis and mitosis (3–6). Their failures lead to the generation of aneuploid cells. Paradoxically, tumor cells with abnormal chromosome compositions can be especially sensitive to their inactivation (7, 8). Although both kinases are required to biorient chromosomes, their functional relationship is unclear. Aurora B is known to destabilize kMT associations. Mps1 has been suggested to modulate Aurora B activity in mammals and both to couple and sever kMT connections in yeast (1, 9).

Mps1 has been difficult to study because it is involved in multiple functions (4). We took advantage of a separation-of-function allele (*mps1-R170S*) to determine the role of Mps1 in meiotic chromosome segregation (fig. S2A). This allele exhibited only mild defects during mitosis (which is consistent with a defective spindle checkpoint) but catastrophic failures during meiosis (fig. S2,

B and C). The *mps1-R170S* mutation is in a region outside of the kinase domain implicated in chromosome biorientation, presumably by mediating interactions between the kinase and key substrates (10). In fact, *mps1-R170S* mutants, like *ipl1* mutants, errantly moved both homologous partners to the same pole at meiosis I (meiosis I non-disjunction, or NDJ) in over half the meioses (fig. S2D). This elevated NDJ was not due to failure to form kMT attachments (fig. S3). To explain this defect, we investigated kMT connections, which are regulated at two points in meiosis I (fig. S1A). The first occurs as cells enter meiosis with their centromeres clustered near the single spindle pole body (SPB, the microtubule organizing center). This cluster, termed the Rabl cluster (11), disperses in prophase as homologous chromosomes begin pairing (12, 13). *ipl1-mn* (“mn” for meiotic-null) mutants, in contrast to *mps1-R170S*, and two other *mps1* mutant alleles (fig. S4A) exhibited a striking phenotype: Centromeres never dispersed from the SPB (Fig. 1A). In mitosis, Ipl1 triggers kMT release by phosphorylating target proteins. Blocking Ipl1 kinase activity prevented release of the cluster (fig. S4B). In *ipl1* mutants, the cluster could be released by destabilizing microtubules (Fig. 1B) or by disrupting the kinetochore, by inducing transcription through the centromere (Fig. 1C) (14) or depleting a kinetochore protein (fig. S4C), demonstrating the Rabl cluster is maintained by kMTs. The failure of *ipl1* mutants to release clustered centromeres was not due to a delay in meiotic progression because the cells exhibited hallmarks of meiotic progression while the Rabl persisted (Fig. 1D). Thus, Ipl1—but not Mps1—mediates programmed release of the Rabl cluster by reversing kMT attachments.

The failure of *ipl1* mutants to release the Rabl cluster predicts that their meiotic non-disjunctions will be toward this “old” SPB. Tagging SPBs with a fluorescent protein allowed old and new SPBs to be distinguished (fig. S5). Randomly segregating chromosomes (*spo11*) non-disjoined equally, but *ipl1* non-disjoined to the old SPB

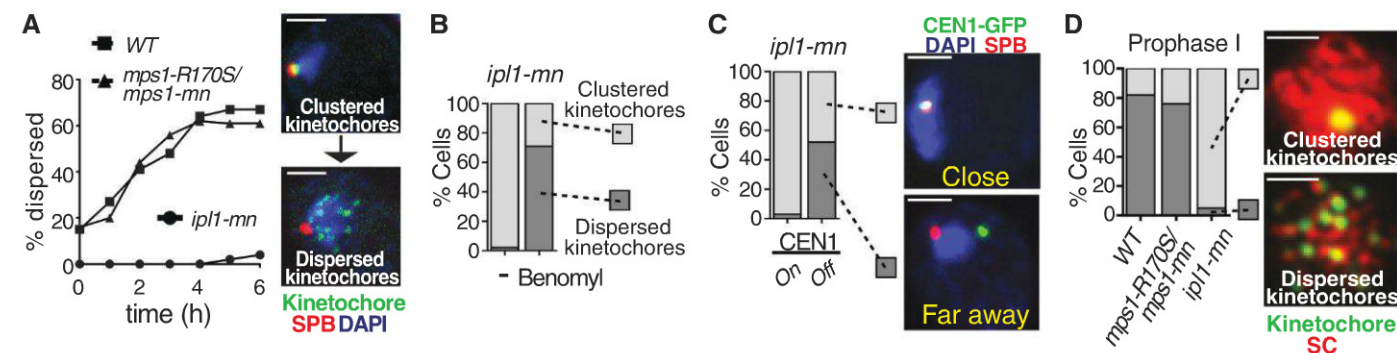


Fig. 1. Ipl1 is necessary to release centromeres from the SPB in meiotic prophase. (A) Dispersion of kinetochores was monitored in wild-type (square), *ipl1-mn* (circle), and *mps1-R170S/mps1-mn* (triangle) cells carrying SPB (Spc42-DsRed) and kinetochore (Mtw1-GFP) markers. Cells with one SPB and dispersed kinetochores were counted ($n \geq 100$ cells). $T = 0$ represents the time at which cells were switched to sporulation medium. (B) As in (A), *ipl1-mn* diploid cells with clustered (light gray) or dispersed kinetochores (dark gray) were analyzed ($n \geq 100$ cells) with or without ad-

dition of benomyl. (C) Separation of *CEN1*–green fluorescent protein (GFP) from the SPBs (Spc42-DsRed) was monitored in *ipl1-mn* cells with or without inactivation of *CEN1* (materials and methods, supplementary materials). Separation was scored as either close to ($<0.75 \mu\text{m}$, light gray) or far away from the SPB ($\geq 0.75 \mu\text{m}$, dark gray) ($n \geq 30$ cells). (D) Cells with Zip1 staining were scored for having clustered (light gray) or dispersed (dark gray) kinetochores 3 hours after meiotic induction ($n \geq 38$ cells). Cells were stained with antibodies to GFP (*MTW1-GFP*; green) and Zip1 (red). Scale bar, $2 \mu\text{m}$.

(Fig. 2A). Surprisingly, this was also true of *mps1* mutants. This result could be explained if in wild-type cells, most attachments of chromosomes were monopolar, and to the older SPB, and were then corrected by Mps1. Indeed, we found that in 85% of cells, when new spindles formed both homologs were mono-oriented and biased for attachment to the older pole (Fig. 2, B and C). Thus, in wild-type cells most chromosome pairs begin pro-metaphase in a monopolar configuration, which is then corrected. We found a higher density

of microtubules radiating from the old pole of new spindles, which may explain this bias (fig. S6). To investigate the roles of Ipl1 and Mps1 in reorienting monopolar attachments, we used *ipl1-as5* or *mps1-as1* alleles that could be inactivated with inhibitors after prophase (fig. S7). Inactivation of either Ipl1 or Mps1 lead to very high NDJ (70 and 90%, respectively) (Fig. 2D), which correlates well with the proportion of chromosomes that begin metaphase mono-oriented (85%) (Fig. 2B) and is consistent with roles for both in reorien-

tating chromosomes. An alternate explanation—that in these mutants, homologous chromosomes cannot be separated—was eliminated (fig. S8).

In wild-type meioses, the spindle is short, and the chromosomes become bioriented quickly (Fig. 2B), making it difficult to monitor reorientation events. Thus, we monitored reorientation in *spo11Δ* mutants, which have longer spindles (15) and do not tether their homologous partners with chiasmata. Because these univalent chromosomes can attach to only one microtubule (16),

Fig. 2. Chromosomes begin pro-metaphase with monopolar spindle attachments. (A) NDJ of *CEN1* toward the new (light gray) or old SPB (dark gray) was determined in anaphase I cells ($n \geq 60$ cells) homozygous for *CEN1-GFP* and expressing Spc42-RedStar, which differentiates old from new SPBs (fig. S5). An example of NDJ to the old SPB is shown. (B) The frequency of mono- or bipolar orientation of *CEN1-GFP* on newly formed spindles (Spc42-DsRed) was observed by means of time-lapse imaging (5-min intervals). The first frame with a bipolar spindle is $t = 0$. Cells with *CEN1-GFP* overlapping one pole were scored as mono-oriented (dark gray) and between poles as bi-oriented (light gray) ($n = 29$ cells). (C) Association of mono-oriented *CEN1-GFP* with the old (dark gray) or new SPB (light gray) measured in diploid cells carrying *GAL4-ER*, *GAL-NDT80*, homozygous *CEN1-GFP*, and *SPC42-RedStar* after release from prophase arrest (β -estradiol addition) (fig. S5). Cells with short spindles were scored (0.75 to 1.5 μm) ($n = 104$ cells). (D) Non-disjunction after inactivation of Ipl1-as5 or Mps1-as1. Cells were released from prophase in the presence or absence of inhibitor. Disjunction (light gray) or NDJ (dark gray) of *CEN1-GFP* was scored at anaphase I. Scale bar, 2 μm .

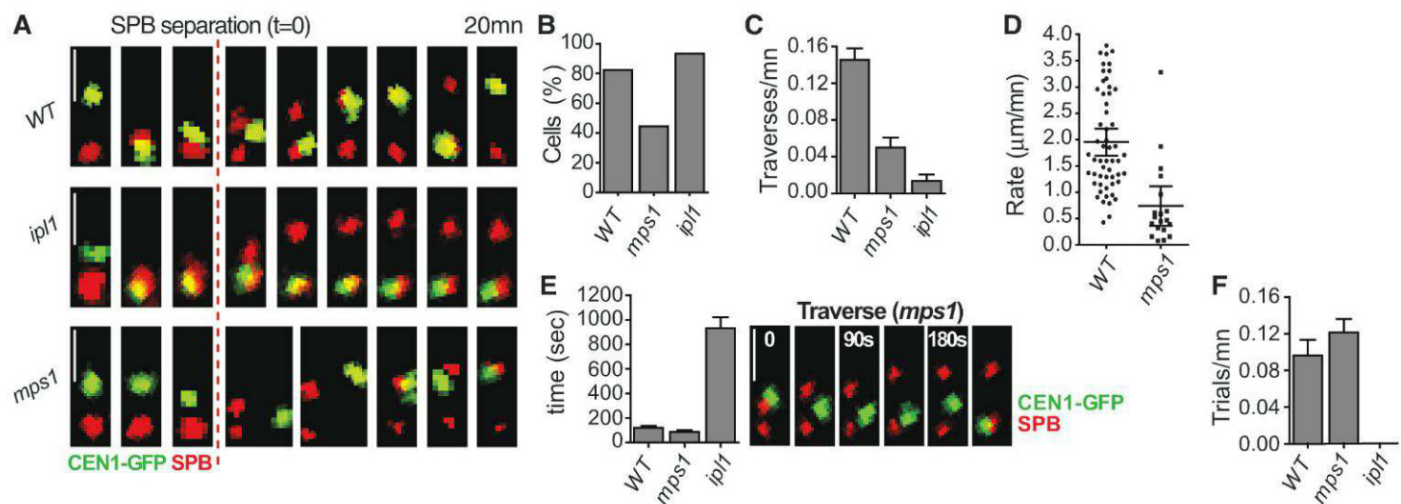
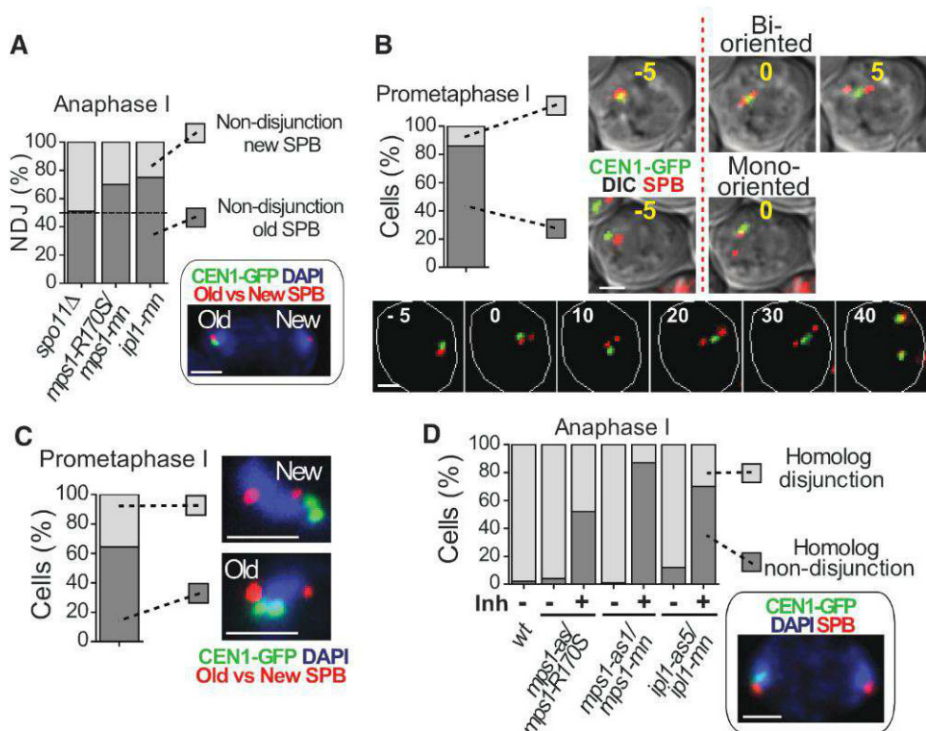


Fig. 3. Ipl1 and Mps1 have different roles in re-orientation. (A to F) *spo11Δ* [wild-type(WT)], *spo11Δ mps1-as1/mps1-mn* (*mps1*) or *spo11Δ ipl1-as5/ipl1-mn* (*ipl1*) cells with one *CEN1-GFP*-tagged chromosome and expressing Spc42-DsRed were observed by means of time-lapse imaging during meiosis at 2-min [(A), (B), and (E)] or 45-s intervals [(C), (D), and (F)] after release from prophase arrest, with or without inhibitor (fig. S7). (A) Images from representative cells ($t = 0$ represents first frame with SPB separation). (B) Cells in which *CEN1*

migrated to SPBs before spindle formation. (C) After release from the SPB, complete migrations of *CEN1* to the opposite SPB were quantified as traverses. (D) The speed for crossing the spindle was evaluated for each individual traverse ($n = 55$ cells for WT, $n = 19$ cells for *mps1-as1*). (Bottom) An *mps1-as1* mutant showing back-and-forth movements. Scale bar, 2 μm . (E) Dwell-time of *CEN1* at SPBs. (F) Migrations away from and then back to the same SPB (trials).

we reasoned they should exhibit cycles of microtubule attachment and detachment in futile attempts to biorient, optimizing our opportunity to quantify this process (fig. S9A). In both controls and *ipl1* mutants, upon the exit from prophase the dispersed centromeres migrated toward the SPBs before spindle formation (Fig. 3, A and B). In contrast, *mps1* mutants were defective in this movement. In wild-type cells, once the spindle was formed the centromeres traversed from one pole to pole (Fig. 3, A and C) at a rate of about 2 $\mu\text{m}/\text{min}$ (Fig. 3E); similar to the 1.5 $\mu\text{m}/\text{min}$ estimated for kinetochores with end-on attachments to microtubules in mitotic cells (17). The centromeres also made “trial” excursions, in which they left one pole, lingered, and then returned (Fig. 3A). Both *mps1* and *ipl1* mutants exhibited very few traverses (Fig. 3, A and C). In *ipl1* cells, once centromeres arrived at a pole they remained there indefinitely (Fig. 3E). In contrast, in *mps1* mutants the centromeres were released from the SPB and began excursions as efficiently as wild-type controls (Fig. 3E), but they could not efficiently traverse the spindle (Fig. 3C), instead making futile trial excursions (Fig. 3F). In rare cases in which centromeres traversed the spindle, the traverses were slow and featured back-and-forth movements and pauses characteristic of kinetochores with lateral microtubule attachments

(figs. S9 and S10) (17). In *mps1* mutants, many kinetochores in each cell failed to migrate completely to the poles before anaphase (fig. S11). Nonetheless, these kinetochores remained close to the poles as they separated at anaphase and were not left at the mid-zone as lagging chromosomes, suggesting that *mps1* mutants are proficient in forming kMT attachments.

Similar assays were used to evaluate the behavior of homologous chromosome pairs tethered by chiasmata (*SPO11*). As in the single chromosome assay, *mps1* mutants were proficient in releasing monopolar attachments, but chromosome pairs could not move efficiently across the spindle or biorient (figs. S12 and S13). A comparison of *mps1* mutants to a spindle checkpoint mutant revealed that the migration defects of *mps1* mutants are not due to a loss of the spindle checkpoint (figs. S12 and S13).

The chromosome behavior in the *mps1* mutants was characteristic of a failure to convert side-on attachments—which in yeast appear unable to support rapid, processive movements (17)—into end-on kMT attachments, which do. A hallmark of end-on attachment formation is the association of the Duo/Dam complex with the outer kinetochore (18). If *mps1* mutants are defective in forming end-on attachments, then Dam1 should exhibit reduced colocalization with kinetochores. Indeed,

the *mps1* cells were significantly reduced in colocalization of Dam1 with kinetochores (Fig. 4A).

We conclude that Ipl1 and Mps1 act sequentially. Ipl1 is required for releasing kMT attachments, whereas Mps1 is required to promote new force-generating end-on attachments that allow released chromosomes to be moved back toward the opposite pole (Fig. 4B). Prior work has suggested that Aurora B and Mps1 have shared phenotypes because they regulate each other (19). The fact that *ipl1* mutants have no dramatic defect in poleward migration and *mps1* mutants are able to release kMT attachments efficiently suggests that, at least in budding yeast meiosis, each kinase can perform its function independently of the other, a conclusion supported by the finding that in mitosis, the kinase activity of each does not appear dependent on the other (20). However, we cannot eliminate the possibility that cross-phosphorylation might enhance these functions or promote activities beyond those reported here.

In yeast, Mps1 is known to phosphorylate multiple proteins that could have roles in kMT function, including the kinetochore components Dam1, Ndc80, Cnn1, and Spc105 (9, 21–23), but how phosphorylation of these potential targets contributes to meiotic biorientation remains an unanswered question. Mammalian meiotic chromosomes also experience multiple incorrect attachments that must be corrected by Mps1 and Aurora B (3, 24). The elucidation of the manner in which Mps1 promotes biorientation in meiosis, and the identification of a conserved region of the Mps1 kinase critical for this activity, should refine the search for its key targets in this process.

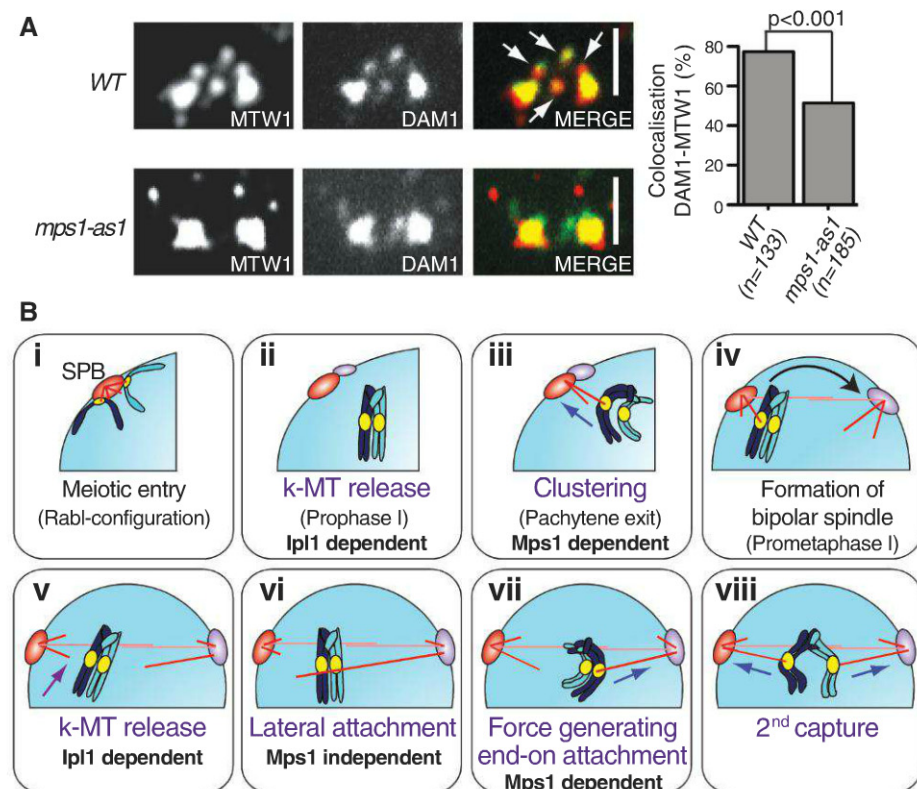


Fig. 4. Mps1 is necessary to generate end-on attachment during meiosis I. (A) Colocalization of Mtw1-RFP and Dam1-GFP were observed in spread nuclei from WT or *mps1-as1/mps1-mn* (*mps1-as1*) chromosome spreads after release from prophase arrest with addition of inhibitor (fig. S7). The proportion of chromosomes (Mtw1) located between the SPBs with Dam1 overlapping staining (white arrow) was determined. The difference between WT and *mps1* mutant is significant (Fischer's test, $P < 0.001$). Scale bar, 2 μm . (B) Model showing kinetochore behaviors in meiosis and the roles of Ipl1 and Mps1.

References and Notes

1. T. U. Tanaka, *EMBO J.* **29**, 4070 (2010).
2. L. Nezi, A. Musacchio, *Curr. Opin. Cell Biol.* **21**, 785 (2009).
3. K. Hached *et al.*, *Development* **138**, 2261 (2011).
4. X. Liu, M. Winey, *Annu. Rev. Biochem.* **81**, 561 (2012).
5. A. L. Marston, A. Amon, *Nat. Rev. Mol. Cell Biol.* **5**, 983 (2004).
6. S. Ruchaud, M. Carmena, W. C. Earnshaw, *Nat. Rev. Mol. Cell Biol.* **8**, 798 (2007).
7. R. Colombo *et al.*, *Cancer Res.* **70**, 10255 (2010).
8. S. M. Lens, E. E. Voest, R. H. Medema, *Nat. Rev. Cancer* **10**, 825 (2010).
9. M. M. Shimogawa *et al.*, *Curr. Biol.* **16**, 1489 (2006).
10. Y. Araki *et al.*, *J. Cell Biol.* **189**, 41 (2010).
11. C. R. Cowan, P. M. Carlton, W. Z. Cande, *Rabl Organization and the Bouquet*, *Plant Physiol.* **125**, 532 (2001).
12. A. Hayashi, H. Ogawa, K. Kohno, S. M. Gasser, Y. Hiraoka, *Genes Cells* **3**, 587 (1998).
13. Q. Jin, E. Trelles-Sticken, H. Scherthan, J. Loidl, *J. Cell Biol.* **141**, 21 (1998).
14. A. Hill, K. Bloom, *Mol. Cell Biol.* **7**, 2397 (1987).
15. M. A. Shonn, R. McCarroll, A. W. Murray, *Science* **289**, 300 (2000).
16. M. Winey, G. P. Morgan, P. D. Straight, T. H. Giddings Jr., D. N. Mastronarde, *Mol. Biol. Cell* **16**, 1178 (2005).
17. K. Tanaka, E. Kitamura, Y. Kitamura, T. U. Tanaka, *J. Cell Biol.* **178**, 269 (2007).
18. J. F. Maure *et al.*, *Curr. Biol.* **21**, 207 (2011).
19. W. Lan, D. W. Cleveland, *J. Cell Biol.* **190**, 21 (2010).
20. J. F. Maure, E. Kitamura, T. U. Tanaka, *Curr. Biol.* **17**, 2175 (2007).
21. L. J. Bock *et al.*, *Nat. Cell Biol.* **14**, 614 (2012).
22. S. Kemmler *et al.*, *EMBO J.* **28**, 1099 (2009).
23. N. London, S. Ceto, J. A. Ranish, S. Biggins, *Curr. Biol.* **22**, 900 (2012).
24. T. S. Kitajima, M. Ohsugi, J. Ellenberg, *Cell* **146**, 568 (2011).

Acknowledgments: We thank S. Jaspersen for critically reading the manuscript; K. Benjamin, S. Biggins, M. Dresser, M. Knop, K. Nasmyth, and A. Straight for providing strains and reagents; and current and past laboratory members for reagents and discussions of our work. P.D.S. was supported in part by NIH training grant GM-07135. This work was supported by March of Dimes Birth Defects Foundation

grant FY98.409/FY99.617 to M.W. and NSF grant 0950005 and NIH grant GM087377 to D.D. Data used in this paper are available in the supplementary materials.

Supplementary Materials

www.sciencemag.org/cgi/content/full/science.1232518/DC1
Materials and Methods

Figs. S1 to S13
Tables S1 and S2
References (25–48)

8 November 2012; accepted 15 January 2013
Published online 31 January 2013;
10.1126/science.1232518

Genome-Wide Quantitative Enhancer Activity Maps Identified by STARR-seq

Cosmas D. Arnold, Daniel Gerlach, Christoph Stelzer, Łukasz M. Boryń, Martina Rath, Alexander Stark*

Genomic enhancers are important regulators of gene expression, but their identification is a challenge, and methods depend on indirect measures of activity. We developed a method termed STARR-seq to directly and quantitatively assess enhancer activity for millions of candidates from arbitrary sources of DNA, which enables screens across entire genomes. When applied to the *Drosophila* genome, STARR-seq identifies thousands of cell type-specific enhancers across a broad continuum of strengths, links differential gene expression to differences in enhancer activity, and creates a genome-wide quantitative enhancer map. This map reveals the highly complex regulation of transcription, with several independent enhancers for both developmental regulators and ubiquitously expressed genes. STARR-seq can be used to identify and quantify enhancer activity in other eukaryotes, including humans.

Enhancers (1) are DNA sequences that recruit transcription factors (TFs) to regulate the transcription of target genes in a cell type-specific manner, thereby governing development and physiology (2). Despite their importance, enhancer discovery has remained challenging, and rather few enhancers have been described and functionally characterized (3). Two types of recently developed methods enable genome-wide enhancer predictions via enhancer-associated chromatin features (4). Deep sequencing of deoxyribonuclease I-hypersensitive sites [DHS-seq (5)] or formaldehyde-assisted isolation of regulatory elements sequencing [FAIRE-seq (6)] allows the mapping of open chromatin, and chromatin immunoprecipitation followed by deep sequencing [ChIP-seq (7, 8)] enables the detection of regulator

(e.g., TF or cofactor) binding sites and enhancer-associated histone modifications [e.g., histone 3 (H3) Lys⁴ monomethylation (H3K4me1) or H3 Lys²⁷ acetylation (H3K27ac)]. These methods, however, do not provide a direct functional or quantitative readout of enhancer activity, which requires reporter assays that infer enhancer strength from the abundance of reporter transcripts [e.g., by means of luciferase or barcodes (9, 10)]. Such assays, however, do not scale to the millions of tests required for genome-wide enhancer identification.

To comprehensively identify sequences that function as transcriptional enhancers in a direct, quantitative, and genome-wide manner, we developed STARR-seq (self-transcribing active regulatory region sequencing). Because enhancers can function independently of their relative positions (1), we placed candidate sequences downstream of a minimal promoter (Fig. 1A), such that active enhancers transcribe themselves, and each enhancer's strength is reflected by its abundance among cellular RNAs. This direct coupling of

candidate sequences to enhancer activity allows the parallel assessment of millions of DNA fragments from arbitrary sources.

We cloned a genome-wide reporter library from randomly sheared genomic DNA of the *Drosophila melanogaster* reference strain (11) (fig. S1). This library contained at least 11.3 million independent candidate fragments with a median length of ~600 base pairs (bp) as revealed by paired-end sequencing (fig. S2A). It covered 96% of the non-repetitive genome at least 10-fold and was sufficiently complex to represent the entire 169 Mb *D. melanogaster* genome (fig. S2, B to E). We transfected the library (fig. S2F) into *Drosophila* S2 cells, isolated polyadenylated RNA, and selectively reverse-transcribed, polymerase chain reaction (PCR)-amplified, and paired-end sequenced the candidate fragments. After mapping the sequences to the genome, we quantified the enrichment over input for each position (Fig. 1B and fig. S3).

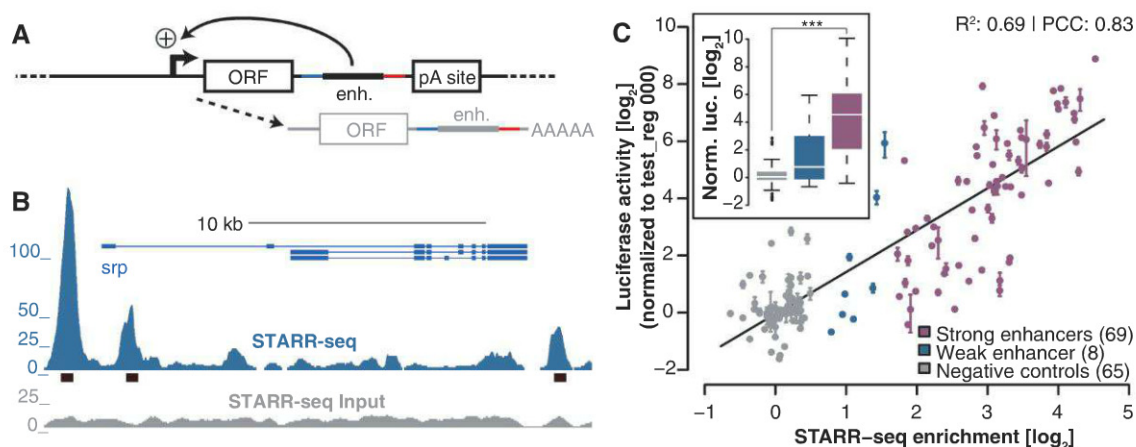
This yielded 5499 regions that were significantly enriched ["peaks"; $P \leq 0.001$, binomial test; empirical false discovery rate (FDR) = 1.8%; Fig. 1B and fig. S4A] at various genomic positions, including weak and strong (1953 with \geq threefold enrichment) enhancers over a wide dynamic range (fig. S5A). A biological replicate showed a Pearson correlation coefficient (r) of 0.92 for the peak summits, which indicated that STARR-seq is highly reproducible (figs. S6, A, B, and E, and S7, A, B, and G).

To validate STARR-seq, we tested 77 peaks chosen across a wide range of enrichments and 65 negative controls by luciferase assays. Our assays showed that 81% (62 out of 77) of the peaks but only 14% (9 out of 65) of the negative controls were at least two times the baseline ($P < 0.05$, t test; see detailed sensitivity and specificity analyses in figs. S8 to S11). STARR-seq enrichment and

Research Institute of Molecular Pathology (IMP), 1030 Vienna, Austria.

*To whom correspondence should be addressed. E-mail: stark@starklab.org

Fig. 1. STARR-seq genome-wide quantitative enhancer discovery. (A) STARR-seq reporter setup [enh., enhancer candidate; ORF, open-reading frame (here: GFP); pA site, polyadenylation site; +, transcriptional activation]. (B) STARR-seq (blue) and input (gray) fragment densities in the *srp* locus. Black boxes denote predicted enhancers ("peaks"). (C) STARR-seq and luciferase signals are linearly correlated: R^2 , coefficient of determination and Pearson correlation coefficient (PCC or r). [Error bars indicate two independent biological replicates; (Inset) the same data as a boxplot; *** $P \leq 0.001$, Wilcoxon rank-sum test; $n = 65, 8$, and 69.]



luciferase activity were strongly linearly related over the entire range of enrichment values ($r = 0.83$; Fig. 1C), which established STARR-seq as a quanti-

tative assay applicable to millions of fragments for the genome-wide identification of enhancers that substantially outperforms methods based on chro-

matin features (figs. S9 to S11). We did not find any evidence that the location of candidates inside the transcript would bias their assessment:

Fig. 2. Complexity of gene regulation. (A) Enrichment and depletion of different enhancer strengths (left) and enhancer number (right) in specific gene categories versus all genes. (B) STARR-seq enhancers and fragment densities in the *Act5C* and *shn* loci. (C) Gene expression versus the number and the combined strengths of enhancers per gene locus (bins of 100 genes).

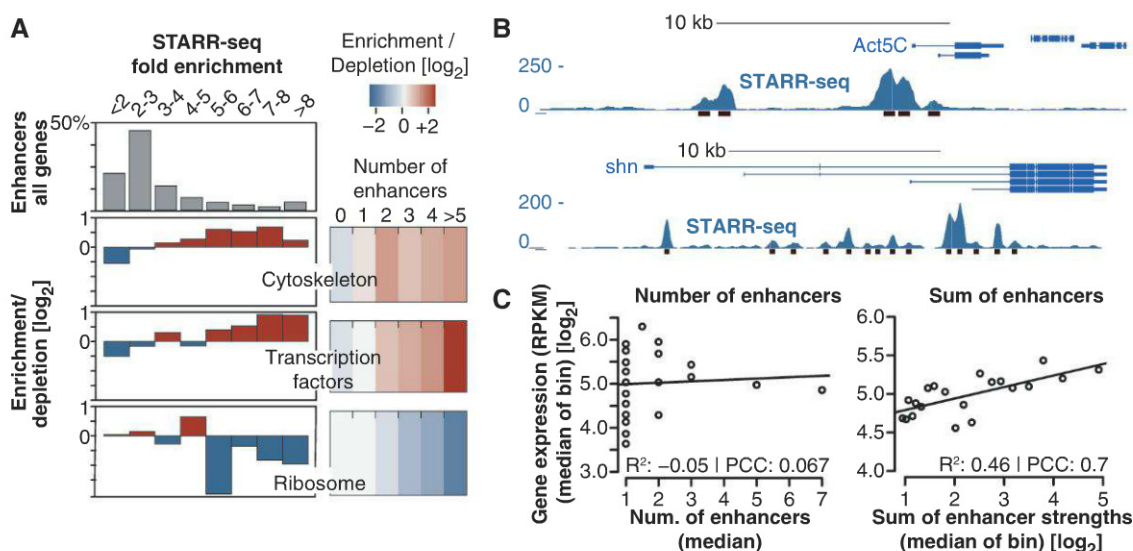
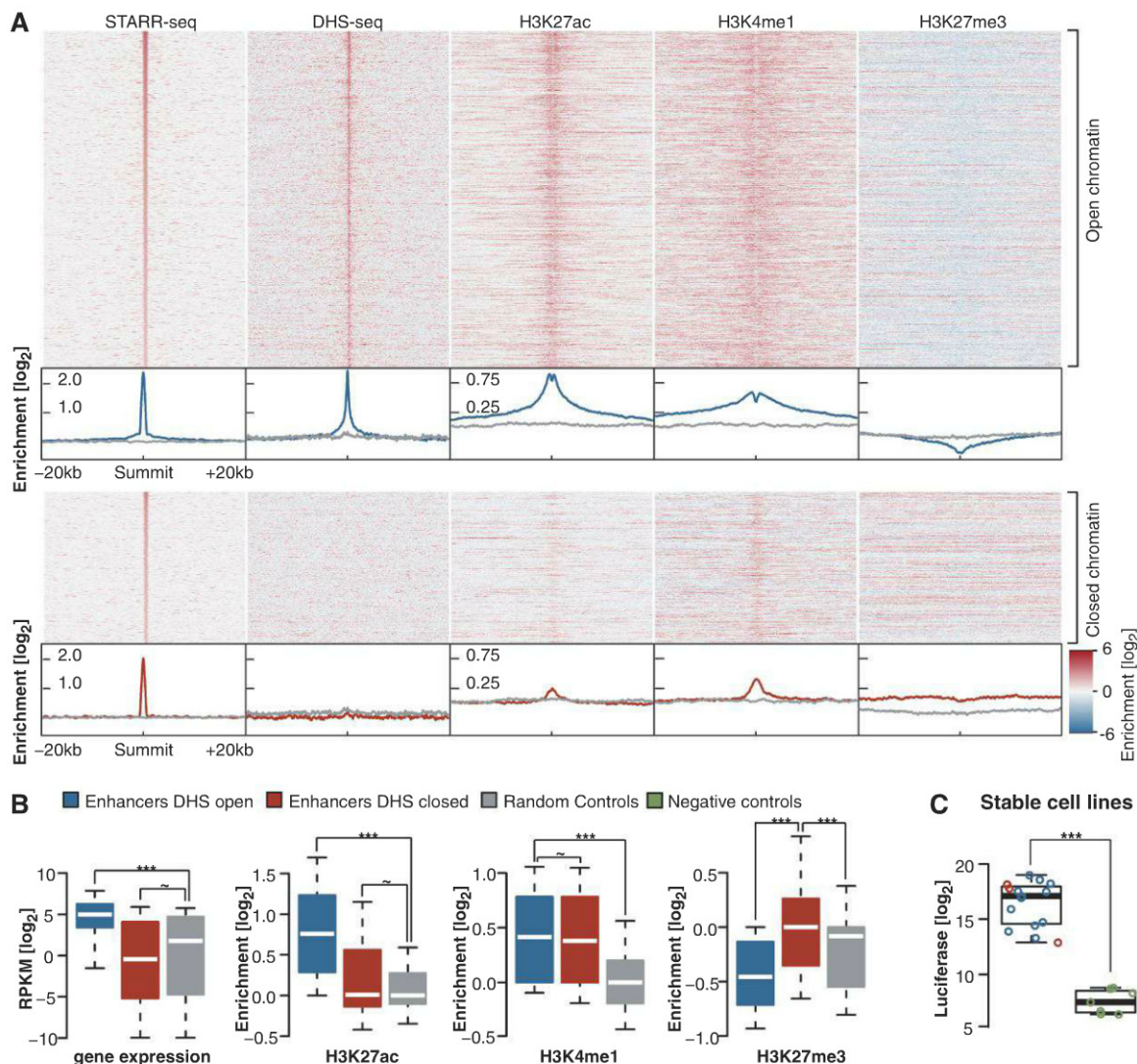


Fig. 3. Regulation of enhancer activity at the chromatin level. (A) Histone modifications (modEncode) at STARR-seq enhancers separated into open ($P \leq 0.05$, binomial test) and closed ($P > 0.05$) classes by DHS-seq (rows within each class sorted by STARR-seq P value). (B) Boxplots for STARR-seq enhancers in open (blue) and closed (red) chromatin indicating flanking gene expression (RPKM) and H3K27ac, H3K4me1, and H3K27me3 enrichments compared with a random control (gray) ($***P \leq 0.001$, $\sim P > 0.05$, Wilcoxon rank-sum test; $n = 1349, 604$, and 500). (C) Luciferase assays of stable cell lines with genomically integrated reporter constructs for open (blue) and closed (red) S2 STARR-seq enhancers and negative controls (green; $***P \leq 0.001$, Wilcoxon rank-sum test; $n = 15, 7$; see fig. S21 for details).



STARR-seq and luciferase assays agreed for sequences that, in their endogenous genomic contexts, occur upstream or within transcribed regions (fig. S12A). Moreover, more than 99% of all enhancers were supported similarly by fragments from both strands (figs. S12C and S13F), and even sequences that contained transcript-destabilizing elements were not substantially depleted during STARR-seq (fig. S12B).

The majority (55.6%) of identified enhancers were located within introns, especially in the first intron (37.2%), and in intergenic regions (22.6%) (fig. S13, A and B), consistent with predictions based on chromatin features (12, 13) (figs. S13, A and B, and S14). To our surprise, 4.5% overlapped annotated transcription start sites (TSSs), which suggested that these sequences can both initiate transcription and enhance transcription from a remote TSS (fig. S13E). Indeed, as expected for bona fide enhancers, all tested (7 out of 7) TSS proximal regions activated luciferase expression irrespective of their relative orientation toward the luciferase TSS (fig. S13F).

The strongest enhancers were next to housekeeping genes such as enzymes (e.g., *Cct1*; enhancer rank no. 3) or constituents of the cytoskeleton (e.g., *Actin5C*; no. 31; Fig. 2, A and B) and also developmental regulators such as the TFs *luna* (no. 37), *shn* (no. 46), *pnt* (no. 49), or the fly fibroblast growth factor receptor *hrl* (no. 45) (Fig. 2B). In fact, the strongest enhancer was located in the intron of the TF *zfh1* (fig. S15), and 18 of

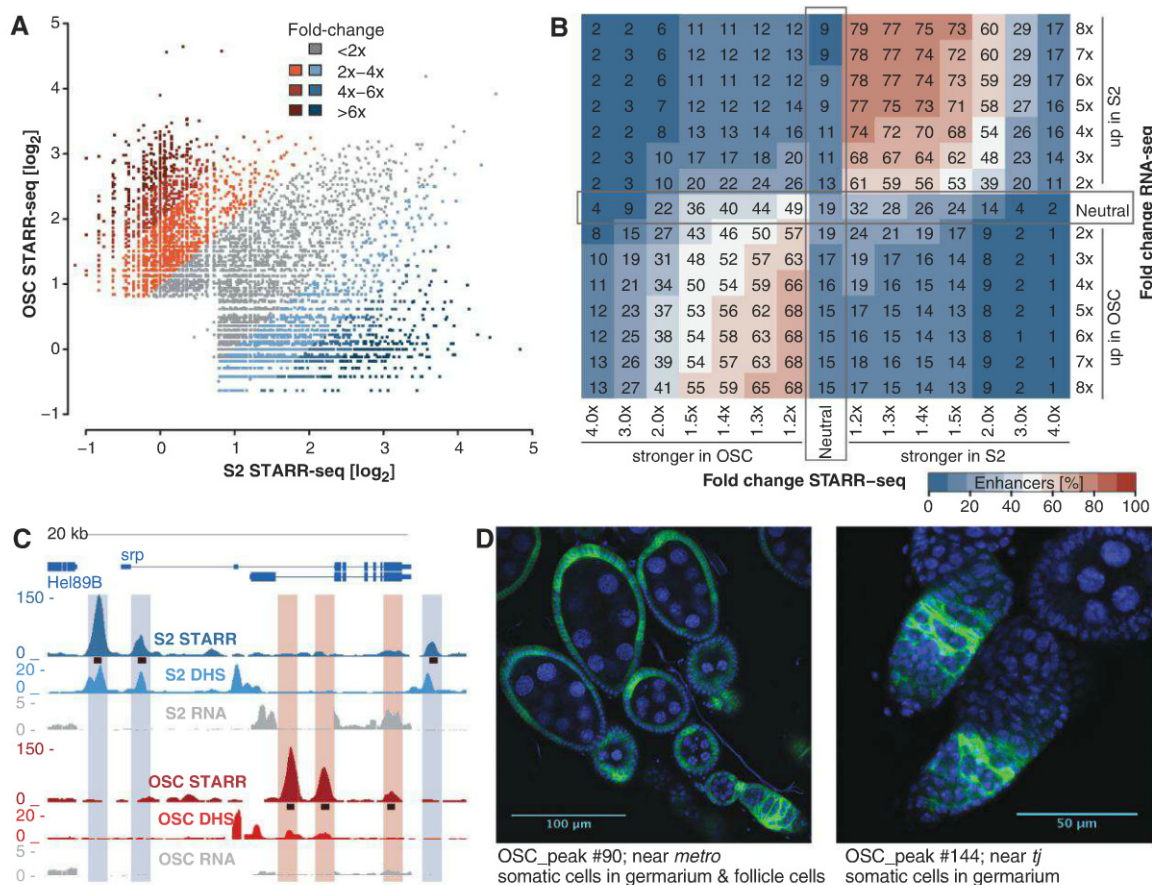
the top 100 and 364 of all strong enhancers were in TF gene loci. The only prominent class of genes with poorly ranking enhancers was the ribosomal protein genes (e.g., *RpS3*, rank 760) (Fig. 2A), presumably because their enhancers require a TCT motif-containing core promoter (14).

Even in a single cell type, many genes appeared to be regulated by several independently functioning enhancers (e.g., *shn*): 203 gene loci (see supplementary materials) contained five or more enhancers and 26 loci, 10 or more (Fig. 2A). Moreover, 434 genes had at least two and 56 had three or more enhancers within 2 kb of the TSS, including 14 TFs but also 30 housekeeping genes such as *Actin5C* (Fig. 2A). The sum of the enhancer strengths per gene correlated well with gene expression levels on average ($r = 0.7$; Fig. 2C), which directly linked gene expression to enhancer activity. Together, these findings suggest that transcription of a large number of genes, including ubiquitously expressed housekeeping genes, is complex and controlled by numerous enhancers per gene, even in a single cell type. These enhancers presumably function additively or redundantly to ensure robustness (15, 16).

STARR-seq assesses the ability of DNA sequences to enhance transcription in a heterologous context, whereas the complementary DHS-seq and ChIP-seq determine enhancer-associated characteristics in the endogenous genomic context. We performed DHS-seq in S2 cells (figs. S16, A, C, and D, and S17, A and B) and found

that the majority (69%) of strong STARR-seq enhancers were accessible (DHS enrichment $P \leq 0.05$, binomial test; Fig. 3A), and all weak enhancers showed above-random DHS enrichment on average (fig. S18), which suggests that they are active in their endogenous contexts. However, 604 (31%) strong STARR-seq enhancers were not accessible ("closed chromatin"; Fig. 3A) and occurred next to genes (e.g., the Hox TFs; fig. S19) expressed at significantly lower levels than genes next to open STARR-seq enhancers (25-fold difference; $P < 2.2 \times 10^{-16}$, Wilcoxon rank-sum test; Fig. 3B). Open and closed enhancers both function in luciferase assays and show the same linear correlation between STARR-seq and luciferase signals (fig. S20), which suggests that sequences with enhancer potential can be silenced in their endogenous contexts, presumably at the chromatin level. Indeed, in contrast to open STARR-seq enhancers, closed enhancers are not marked by H3K27ac, a histone modification associated with active enhancers, but lie in broad domains of repressive H3K27me3 (Fig. 3A and fig. S19), suggestive of Polycomb-mediated repression (17) or a poised enhancer state (18). It is noteworthy that both open and closed enhancers are marked to similar extents by H3K4me1, which labels enhancers irrespective of their activity (19, 20) (Fig. 3A). The precise labeling of closed enhancers by H3K4me1 is particularly evident for Hox genes (fig. S19) and holds genome-wide (Fig. 3, A and B), which suggests that

Fig. 4. Identification of cell type-specific enhancers. (A) STARR-seq enrichments in S2 cells versus OSCs. (B) Enhancer activities and gene expression levels change consistently between cell types (fraction of enhancers for each gene expression class; details in fig. S26). (C) STARR-, DHS-, and RNA-seq tracks for S2 cells and OSCs at the *srp* locus (black bars, STARR-seq enhancers). (D) In vivo validation of predicted OSC enhancers in ovaries of transgenic flies (OSC enhancers → Gal4; UAS-CD8-GFP; green, GFP; blue for DNA, 4',6'-diamidino-2-phenylindole). See fig. S29 for details and all 13 tested candidates.



these sequences are recognized as functional enhancers, yet actively repressed.

To test the functionality of STARR-seq enhancers when integrated into the genome, we created 22 stable S2 cell lines each carrying stably integrated luciferase reporter constructs with an enhancer (15 lines) or a negative fragment (fig. S21). All enhancers, including three out of three closed enhancers, showed strong luciferase activity, whereas none of the negative controls did (Fig. 3C and fig. S21). For all, the luciferase activity was constant over a course of 4 weeks, measured 3, 5, and 7 weeks after integration (fig. S21). The activity of the three closed enhancers suggests that their endogenous inactive state might depend on the genomic context and/or on regulatory activities in S2 precursor cells. This shows that enhancers identified by ectopic assays, such as STARR-seq, can function when integrated into a chromosomal context, even if they are silenced endogenously.

We next applied STARR-seq to *Drosophila* adult ovarian somatic cells [OSCs (21)] and identified a comparable number of enhancers (4682; $P \leq 0.001$, binomial test; FDR = 0.2%) with similar characteristics (figs. S4B; S5B; S6, C to E; S12D; S13, C and D; and S22, A to C). Out of 8659 enhancers found in S2 cells or OSCs, 5404 (62.4%) changed at least twofold and 2138 (24.7%) at least fourfold between both cell types (Fig. 4A, and figs. S23 and S24, A and D), and luciferase assays confirmed these differences quantitatively ($r = 0.85$; fig. S24, B and C). Changes in enhancer strengths between the two cell types were reflected in the differential mRNA abundance (fig. S25) of the flanking genes (Fig. 4, B and C, and fig. S26): 74% of all enhancers near genes that are fourfold up-regulated in S2 cells appear stronger in S2 cells, whereas only 16% appear stronger in OSCs and vice versa (66% versus 19%). This establishes a direct link between quantitative differences in genome-wide enhancer strengths and differential gene expression. Up to 19% of cell type-specific enhancers were accessible in the cell-type in which they were not active (fig. S27). We also observed 514 genes for which individual enhancers changed more than twofold between cell types, whereas the sum of enhancer activities and the gene expression levels remained constant (<twofold change; fig. S28).

As OSCs have been derived from adult *Drosophila* ovaries and retained marker gene expression and other functional aspects of their in vivo counterparts (21), we assessed the activity of 13 OSC STARR-seq enhancers in ovaries of transgenic flies with site-specifically integrated transcriptional reporter constructs. In these flies, 85% (11 out of 13) of the enhancers but none of five control regions were active (Fig. 4D and fig. S29).

Here, we present STARR-seq, which complements ChIP-seq and DHS-seq as the third principal method to study transcriptional regulatory elements in entire genomes. It is unique in its ability to assess enhancer strengths quantitatively and to discover regulatory elements directly based on their ability to enhance transcription, even when silenced

endogenously. Applied to two *Drosophila* cell types, it revealed thousands of cell type-specific enhancers with a broad range of strengths and provided the first genome-wide quantitative enhancer activity maps in any organism. STARR-seq is widely applicable to screening arbitrary sources of DNA in any cell type or tissue that allow the efficient introduction of reporter constructs (e.g., by plasmid transfection). This includes human HeLa cells, for which we confirm the quantitative nature of STARR-seq and its ability to identify enhancers that function in luciferase assays independent of their chromatin states and, thus, more reliably than previous methods (figs. S30 and S31). STARR-seq should be widely applied to many cell types across organisms to annotate cell type-specific gene regulatory elements and functionally assess noncoding mutations.

References and Notes

1. J. Banerji, S. Rusconi, W. Schaffner, *Cell* **27**, 299 (1981).
2. M. Levine, *Curr. Biol.* **20**, R754 (2010).
3. J. O. Yáñez-Cuna, E. Z. Kvon, A. Stark, *Trends Genet.* **29**, 11 (2013).
4. N. D. Heintzman *et al.*, *Nature* **459**, 108 (2009).
5. A. P. Boyle *et al.*, *Cell* **132**, 311 (2008).
6. K. J. Gaulton *et al.*, *Nat. Genet.* **42**, 255 (2010).
7. D. S. Johnson, A. Mortazavi, R. M. Myers, B. Wold, *Science* **316**, 1497 (2007).
8. G. Robertson *et al.*, *Nat. Methods* **4**, 651 (2007).
9. A. Melnikov *et al.*, *Nat. Biotechnol.* **30**, 271 (2012).
10. R. P. Patwardhan *et al.*, *Nat. Biotechnol.* **30**, 265 (2012).
11. M. D. Adams *et al.*, *Science* **287**, 2185 (2000).
12. P. V. Kharchenko *et al.*, *Nature* **471**, 480 (2011).
13. modENCODE Consortium *et al.*, *Science* **330**, 1787 (2010).

14. T. J. Parry *et al.*, *Genes Dev.* **24**, 2013 (2010).
15. M. W. Perry, A. N. Boettiger, M. Levine, *Proc. Natl. Acad. Sci. U.S.A.* **108**, 13570 (2011).
16. N. Frankel *et al.*, *Nature* **466**, 490 (2010).
17. L. A. Boyer *et al.*, *Nature* **441**, 349 (2006).
18. A. Rada-Iglesias *et al.*, *Nature* **470**, 279 (2011).
19. M. P. Creighton *et al.*, *Proc. Natl. Acad. Sci. U.S.A.* **107**, 21931 (2010).
20. S. Bonn *et al.*, *Nat. Genet.* **44**, 148 (2012).
21. K. Saito *et al.*, *Nature* **461**, 1296 (2009).

Acknowledgments: We thank H. K. Akyüz, M. Pagani, K. Schernhuber, D. Spies, H. Tagoh, M. Busslinger, S. Westermann, J. M. Peters, J. Zuber (IMP), J. Brennecke and group, U. Elling [Institute of Molecular Biotechnology (IMBA)], and the IMP/IMBA BioOptics and Graphics Services for help. Deep sequencing was performed at the CSF Next-Generation Sequencing Unit (<http://csf.ac.at>); Vienna Tile (VT) lines were obtained from the Dickson laboratory via the Vienna *Drosophila* RNAi Center (<http://stockcenter.vdrc.at>). C.D.A., L.M.B., and M.R. are supported by a European Research Council (ERC) Starting Grant (no. 242922) awarded to A.S. Basic research at the IMP is supported by Boehringer Ingelheim GmbH. C.D.A. and A.S. are authors on a patent application for STARR-seq (EP 12 004 520.8) filed by Boehringer Ingelheim International GmbH. All constructs are available from the authors subject to a Material Transfer Agreement. All deep sequencing data are available at www.starklab.org and GEO (series accession number GSE40739).

Supplementary Materials

www.sciencemag.org/cgi/content/full/science.1232542/DC1
Materials and Methods
Figs. S1 to S31
Tables S1 to S12
References (22–48)

9 November 2012; accepted 8 January 2013
Published online 17 January 2013;
10.1126/science.1232542

Genomic Analysis of Non-*NF2* Meningiomas Reveals Mutations in *TRAF7*, *KLF4*, *AKT1*, and *SMO*

Victoria E. Clark,¹ E. Zeynep Erson-Omay,¹ Akdes Serin,¹ Jun Yin,² Justin Cotney,² Koray Özdoğan,³ Timuçin Avcı,⁴ Jie Li,⁵ Phillip B. Murray,¹ Octavian Henegariu,¹ Saliha Yilmaz,¹ Jennifer Moliterno Günel,⁶ Genevieve Carrión-Grant,¹ Baran Yılmaz,⁷ Conor Grady,¹ Bahattin Tanrikulu,⁷ Mehmet Bakırcıoğlu,¹ Hande Kaymakçalan,⁸ Ahmet Okay Caglayan,¹ Leman Sencar,¹ Emre Ceyhan,¹ A. Fatih Atik,⁷ Yaşar Bayrı,⁷ Hanwen Bai,¹ Luis E. Kolb,¹ Ryan M. Hebert,¹ S. Bulent Omay,¹ Ketu Mishra-Gorur,¹ Murim Choi,² John D. Overton,⁹ Eric C. Holland,¹⁰ Shrikant Mane,^{2,9} Matthew W. State,¹¹ Kaya Bilgüvar,¹ Joachim M. Baehring,¹² Philip H. Gutin,⁶ Joseph M. Piepmeyer,¹³ Alexander Vortmeyer,⁵ Cameron W. Brennan,¹⁴ M. Necmettin Pamir,³ Türker Kılıç,¹⁵ Richard P. Lifton,^{2,16} James P. Noonan,^{2,17} Katsuhito Yasuno,¹ Murat Günel^{1,18*}

We report genomic analysis of 300 meningiomas, the most common primary brain tumors, leading to the discovery of mutations in *TRAF7*, a proapoptotic E3 ubiquitin ligase, in nearly one-fourth of all meningiomas. Mutations in *TRAF7* commonly occurred with a recurrent mutation (K409Q) in *KLF4*, a transcription factor known for its role in inducing pluripotency, or with *AKT1*^{E17K}, a mutation known to activate the PI3K pathway. *SMO* mutations, which activate Hedgehog signaling, were identified in ~5% of non-*NF2* mutant meningiomas. These non-*NF2* meningiomas were clinically distinctive—nearly always benign, with chromosomal stability, and originating from the medial skull base. In contrast, meningiomas with mutant *NF2* and/or chromosome 22 loss were more likely to be atypical, showing genomic instability, and localizing to the cerebral and cerebellar hemispheres. Collectively, these findings identify distinct meningioma subtypes, suggesting avenues for targeted therapeutics.

Meningiomas, arising from the meninges of the central nervous system, are the most common primary brain tumors,

with a prevalence of ~170,000 cases in the United States (1). Although most are histologically classified as benign (grade I), about 10% represent

atypical (grade II) or anaplastic (grade III) forms. Meningiomas frequently invade surrounding brain and critical neurovascular structures, often causing neurological deficits and requiring surgical intervention. Loss of *Neurofibromin 2* (*merlin*, *NF2*) is found in 40 to 60% of sporadic meningiomas (2), but the genetic architecture of the remainder remains obscure, limiting options for the development of rational therapies.

To comprehensively characterize the genomics of meningioma and to gain further insight into molecular mechanisms of tumor formation, we performed genome-wide genotyping and exome sequencing (average depth of coverage 255-fold) of 50 previously nonirradiated grade I (*n* = 39) and grade II (*n* = 11) meningiomas and matched normal DNA (3) (table S1). For the meningiomas in which matching blood samples were available (*n* = 39), the mean number of protein-altering somatic mutations was 7.2 (range 1 to 15), a considerably smaller number compared with malignant tumors (table S2). We next searched for genes with significantly more somatic mutations than expected by chance (fig. S1). Besides *NF2*, we identified increased mutation burden in *TNF receptor-associated factor 7* (*TRAF7*), *Krupple-like factor 4* (*KLF4*), *v-akt murine thymoma viral oncogene homolog 1* (*AKT1*), and *Smoothed, frizzled family receptor* (*SMO*) (as a group, referred to as *non-NF2* mutant hereafter) (Fig. 1). Mutations in these genes were mutually exclusive of *NF2* mutations. In addition, we identified single muta-

tions in genes previously reported to play a role in other neoplasias, including *CREBBP*, *PIK3CA* (R108H variant), *PIK3R1* (deletion p.306-307), and *BRCAl* as well as two *SMARCB1* mutations, which coexisted with *NF2* loss and have previously been reported in meningiomas (4) (table S3).

We next performed targeted resequencing of these top five genes, along with chromosome 22 copy-number analysis, in an independent set of 250 unirradiated meningiomas (204 grade I and 46 high-grade meningiomas) (fig. S2). In the combined analysis of 300 meningiomas, we identified coding mutations in one of these five genes and/or evidence for chromosome 22 loss in 237 (79%) (Fig. 2A and table S3). *NF2* mutations were present in 108 (36%). *TRAF7* mutations, which were always exclusive of *NF2* mutations [mutual exclusivity *P* value (*P_{me}*) = 2.55×10^{-17} (5)], were observed in nearly one-fourth of the meningiomas examined (*n* = 72). *TRAF7* is a proapoptotic N-terminal RING and zinc finger

domain protein with E3 ubiquitin ligase activity that contains seven WD40 repeats in its C terminus (6). *TRAF7* interacts with several molecules, such as MEKK3, through these WD40 repeats, affects multiple signaling pathways, including NF- κ B, and targets ubiquitination of proteins including c-FLIP, an antiapoptotic molecule (7). It is notable that 67 of the 72 *TRAF7* mutations, including 15 recurrent mutations, all map to the WD40 domains (Fig. 2B).

In the transcription factor *KLF4*, we identified a recurrent K409Q mutation, which almost always co-occurred with *TRAF7* mutations [*n* = 31; co-occurrence *P* value (*P_{co}*) = 2.50×10^{-20}] and were exclusive of *NF2* mutations (*P_{me}* = 3.77×10^{-7}). *KLF4* is expressed in meningiomas (fig. S3). *KLF4* regulates differentiation of several cell types and is best known as one of four genes that together promote reprogramming of differentiated somatic cells into pluripotent stem cells (8). Deletion of the *KLF4* DNA binding

¹Departments of Neurosurgery and Genetics, Yale Program in Brain Tumor Research, Yale School of Medicine, New Haven, CT 06510, USA. ²Department of Genetics, Yale School of Medicine, New Haven, CT 06510, USA. ³Department of Neurosurgery, Acibadem University School of Medicine, Istanbul 34848, Turkey. ⁴Dr. Orhan Öcalgiray Molecular Biology-Biotechnology and Genetics Research Center, Istanbul Technical University, Maslak 34469, Istanbul, Turkey. ⁵Department of Pathology, Yale School of Medicine, New Haven, CT 06510, USA. ⁶Department of Neurosurgery and Brain Tumor Center, Memorial Sloan-Kettering Cancer Center, New York, NY 10065, USA. ⁷Department of Neurosurgery, Marmara University School of Medicine, Istanbul 34854, Turkey. ⁸Department of Genetics and Bioinformatics, Bahcesehir University, Istanbul 34353, Turkey. ⁹Center for Genome Analysis, Yale School of Medicine, West Haven, CT 06516, USA. ¹⁰Departments of Cancer Biology and Genetics, Neurosurgery, Neurology, and Surgery, Brain Tumor Center, Memorial Sloan-Kettering Cancer Center, New York, NY 10065, USA. ¹¹Departments of Genetics and Psychiatry, Yale Program on Neurogenetics and Child Study Center, Yale School of Medicine, New Haven, CT 06510, USA. ¹²Departments of Neurology, Neurosurgery, and Internal Medicine, Yale Program in Brain Tumor Research and Yale Brain Tumor Center, Yale School of Medicine, New Haven, CT 06510, USA. ¹³Department of Neurosurgery, Yale Program in Brain Tumor Research and Yale Brain Tumor Center, Yale School of Medicine, New Haven, CT 06510, USA. ¹⁴Department of Neurosurgery and Brain Tumor Center, Human Oncology and Pathogenesis Program, Memorial Sloan-Kettering Cancer Center, New York, NY 10065, USA. ¹⁵Department of Neurosurgery, Bahcesehir University School of Medicine, Istanbul 34349 Turkey. ¹⁶Department of Internal Medicine, Howard Hughes Medical Institute, Yale School of Medicine, New Haven, CT 06510, USA. ¹⁷Kavli Institute for Neuroscience, Yale School of Medicine, New Haven, CT 06520, USA. ¹⁸Yale Program on Neurogenetics, Yale School of Medicine, New Haven, CT 06510, USA.

*To whom correspondence should be addressed. E-mail: murat.gunel@yale.edu

Tumor	Grade	Chr22 loss	NF2	TRAF7	AKT1	KLF4	SMO
MN-95	1	Yes					
MN-290	1	Yes					
MN-1041	1	Yes					
MN-1047	1	Yes					
MN-1137	1	Yes					
MN-47	1	Yes	p.Q453X				
MN-52	1	Yes	p.F256fs				
MN-71	1	Yes	p.T59fs				
MN-81	1	Yes	p.Q65fs				
MN-169	1	Yes	p.E460X				
MN-288	1	Yes	p.K17_M29del				
MN-291	1	Yes	p.I210fs				
MN-293	1	Yes	p.Q459X				
MN-294	1	Yes	c.363+1G>C				
MN-297	1	Yes	p.K99fs				
MN-301	1	Yes	p.W41fs				
MN-306	1	Yes	p.K44X				
MN-1091	1	Yes	p.L14fs				
MN-1133	1	Yes	p.Y207fs				
MN-26	1			p.C388Y	p.E17K		
MN-105	1			p.R641C	p.E17K		
MN-292	1			p.Q637H	p.E17K		
MN-191	1			p.K615E		p.K409Q	
MN-201	1			p.L580del		p.K409Q	
MN-249	1			p.R641C		p.K409Q	
MN-1025	1			p.G536S		p.K409Q	
MN-1066	1			p.N520S		p.K409Q	
MN-303	1			p.S561N			
MN-206	1			p.G390E			
MN-304	1			p.R653Q			
MN-305	1			p.G536S			
MN-1053	1			p.E353insFRRDAS			
MN-1045	1						p.L412F
MN-1132	1						p.W535L
MN-164	2	Yes					
MN-22	2	Yes	c.115-1G>A				
MN-54	2	Yes	p.Q319X				
MN-96	2	Yes	p.L14fs				
MN-97	2	Yes	p.M426fs				
MN-171	2	Yes	p.L208P				
MN-295	2	Yes	p.E103fs				
MN-298	2	Yes	p.V24fs				
MN-1054	2	Yes	p.R262X				
MN-16	2	Yes		p.T145M	p.E17K		
MN-1144	2	Yes		p.F337S			

Fig. 1. Exome sequencing identifies meningioma subgroups based on mutually exclusive mutation profiles.

domain blocks differentiation and induces self-renewal in hematopoietic cells (9). The recurrently mutated KLF4 residue, K409, lies within the first zinc finger and makes direct DNA contact in the major groove of the DNA binding motif (9) (Fig. 2C and fig. S4).

The known neoplasia-related recurrent mutation, *AKT1*^{E17K}, was identified in 38 meningiomas. Although the *AKT1*^{E17K} mutation co-occurred with *TRAF7* mutations in 25 of the 38 tumors ($P_{co} = 3.90 \times 10^{-9}$), it was exclusive of the *KLF4*^{K409Q} ($P_{me} = 1.18 \times 10^{-2}$) and *NF2* mutations, except in one case ($P_{me} = 2.70 \times 10^{-7}$). The *AKT1*^{E17K} mutation has been shown to activate PI3K/AKT

signaling (10) and was readily detectable by immunohistochemistry using an antibody specific for this mutation (fig. S3).

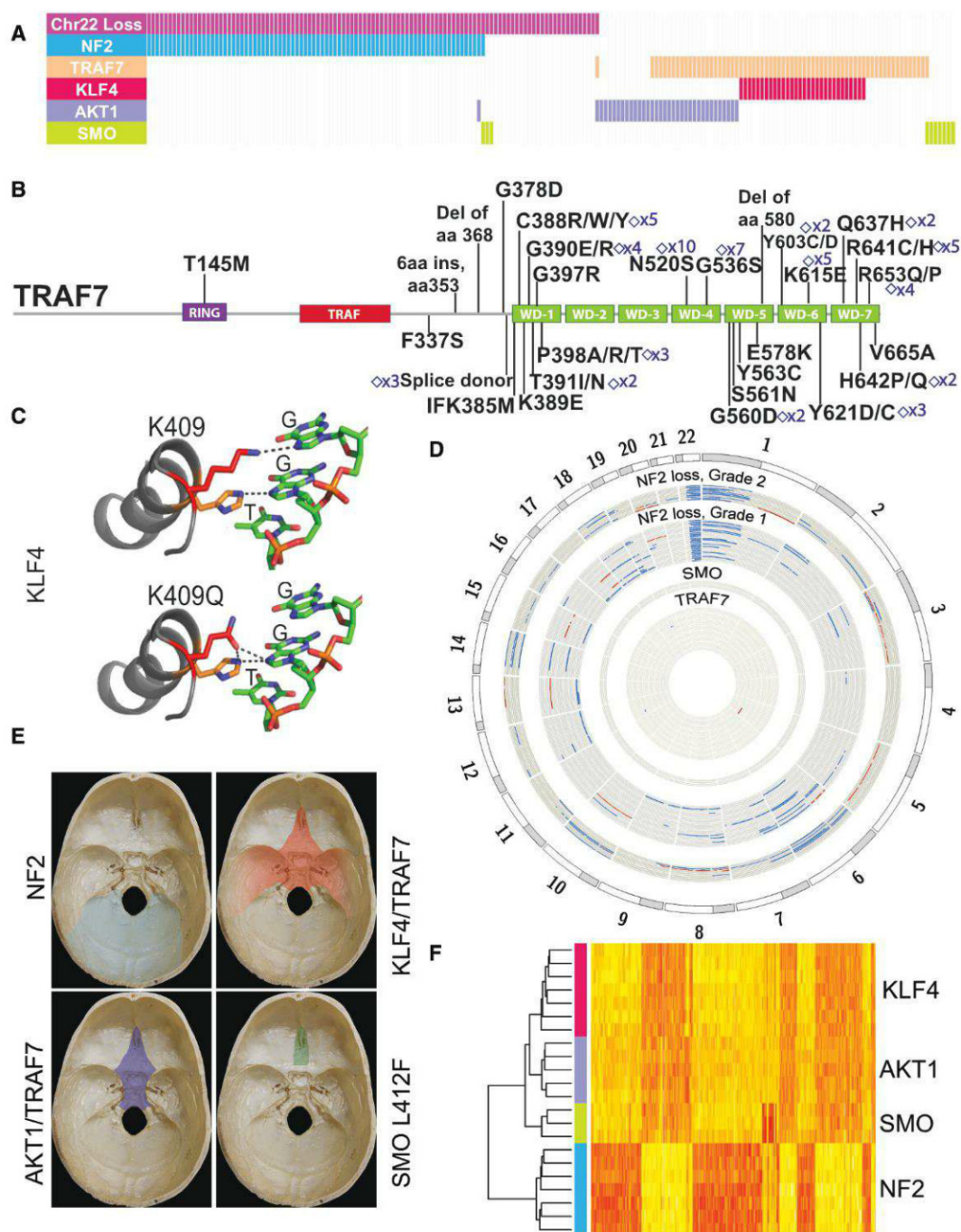
Finally, in 11 tumors, we identified mutations in *SMO*, which is expressed in meningiomas (fig. S5). These mutations include a recurrent L412F variant in seven meningiomas and a previously reported W535L mutation, which has been shown to result in activation of Hedgehog signaling in basal cell carcinoma (11). Eight of these *SMO* mutations were mutually exclusive of mutations in the other four genes ($P_{me} = 1.24 \times 10^{-2}$).

We next evaluated chromosomal instability. Chromosome 22 loss, observed in 149 tumors,

was the most common event and was strongly associated with the presence of coding *NF2* mutations ($P_{co} = 1.32 \times 10^{-47}$). These were also significantly associated with higher grade meningiomas [$P = 5.90 \times 10^{-5}$; odds ratio (OR) = 3.54]. Higher-grade tumors also showed an increased number of large-scale chromosomal abnormalities (Fig. 2D and fig. S6) (6.9 versus 1.7 events per tumor) and an increased rate of *NF2* mutations ($P = 0.03$; OR = 1.96) and were observed more frequently in males than females ($P = 6.45 \times 10^{-4}$; OR = 2.93).

Given these observations pointing to distinct tumor subtypes based on mutation profiles, we

Fig. 2. Genomic architecture of meningiomas. (A) *NF2*, *TRAF7*, and *SMO* coding mutations along with recurrent *AKT1*^{E17K} and *KLF4*^{K409Q} variants reveal meningioma subtypes with mutually exclusive profiles. Analysis for chromosome 22 copy number is also shown. Each bar represents a grade I meningioma sample; 191 samples are depicted. (B) *TRAF7* mutations, which are identified in 72 of 300 meningiomas analyzed, are clustered within its WD40 domains. The count of recurrent mutations, which are denoted by diamonds, is indicated. (C) The recurrent *KLF4*^{K409Q} mutation is located within the first zinc finger domain, which makes direct DNA contact. (D) Circos plot of large-scale genomic abnormalities identified (blue: deletion, red: amplification). Whereas all *NF2*/*chr22loss* meningiomas (outer circles, $n = 41$, including $n = 30$ with coding *NF2* mutations) show chromosome 22 loss, which is typically associated with further chromosomal abnormalities in grade II tumors ($n = 11$, including $n = 8$ with coding *NF2* mutations), genomic stability is a hallmark of grade I *non-NF2* tumors (inner circles, $n = 36$). (E) Along the skull base, *NF2*/*chr22loss* meningiomas originate from the lateral and posterior regions, whereas the vast majority of anterior and medial meningiomas are *non-NF2* mutant. (F) Unsupervised hierarchical clustering of gene expression profiles defines two major benign meningioma subgroups, those with *NF2*/*chr22loss* and *non-NF2* mutant tumors. Each subgroup reveals differential H3K27ac and gene expression profiles (figs. S10 to S14 and tables S5 to S8).



examined whether the mutation spectrum correlated with anatomical distribution and histological subtype. We initially grouped cerebral meningiomas into those originating along the skull base or those present in the cerebral hemispheres (Fig. 2E, fig. S7, and table S4). Interestingly, tumors with *NF2* mutations and/or chromosome 22 loss (*NF2/chr22loss*) were predominantly found in the hemispheres ($P = 9.22 \times 10^{-14}$; OR = 6.74) with nearly all posterior cerebral (parieto-occipital), cerebellar, or spinal meningiomas being *NF2/chr22loss* tumors (fig. S8). For the meningiomas originating from the skull base, we observed a difference between those originating from medial versus lateral regions. The vast majority of *non-NF2* meningiomas were medial ($P = 4.36 \times 10^{-8}$; medial versus lateral OR = 8.80), whereas the lateral and posterior skull base meningiomas had *NF2/chr22loss* ($P = 1.55 \times 10^{-12}$; OR = 23.11). Meningiomas with only the recurrent *SMO* L412F mutation ($n = 5$) all localized to the medial anterior skull base, near the midline. This is particularly interesting because mutations in Hedgehog signaling result in holoprosencephaly, the midline failure of embryonic forebrain to divide into two hemispheres (12).

Mutational profiles also were correlated with histological diagnoses. For example, all of the meningiomas with a “secretory” component ($n = 12$), which follow a more aggressive clinical course owing to increased brain swelling,

carried both *TRAF7* and *KLF4* mutations ($P_{co} = 6.02 \times 10^{-12}$) (fig. S9).

Consistent with these clinical observations, unsupervised hierarchical clustering of meningiomas based on gene expression and chromatin immunoprecipitation for H3K27 acetylation followed by sequencing (H3K27ac ChIP-seq) analyses confirmed clustering into *NF2/chr22loss* versus *non-NF2* mutant subgroups (Fig. 2F and figs. S10 and S11) and revealed several molecules whose acetylation and expression was specific to a subtype (tables S5 and S6). For these differentially expressed genes, there was a strong correlation between expression and ChIP-seq data (fig. S12). Among the *non-NF2* meningiomas, *SMO* mutants were clearly defined by increased expression and activation of the Hedgehog pathway (fig. S13 and tables S7 and S8).

These results clearly identify meningioma subgroups, distinguishing them based on their mutually exclusive distribution of mutations, distinct potential for chromosomal instability and malignancy, anatomical location, histological appearance, gene expression, and H3K27ac profile. Our results show that the mutational profile of a meningioma can largely be predicted based on its anatomical position, which in turn may predict likely drug response (e.g., Hedgehog inhibitors for midline tumors). This may prove relevant for surgically unresectable, recurrent, or invasive meningiomas and could spare patients surgery or irradiation, an independent risk factor for progression of these generally benign tumors.

References and Notes

1. J. Wiemels, M. Wrensch, E. B. Claus, *J. Neurooncol.* **99**, 307 (2010).
2. M. J. Riemenschneider, A. Perry, G. Reifenberger, *Lancet Neurol.* **5**, 1045 (2006).
3. Materials and methods are available as supplementary materials on Science Online.
4. U. Schmitz *et al.*, *Br. J. Cancer* **84**, 199 (2001).
5. Q. Cui, *PLoS ONE* **5**, e13180 (2010).
6. L. G. Xu, L. Y. Li, H. B. Shu, *J. Biol. Chem.* **279**, 17278 (2004).
7. T. Bouwmeester *et al.*, *Nat. Cell Biol.* **6**, 97 (2004).
8. K. Takahashi *et al.*, *Cell* **131**, 861 (2007).
9. A. Schuetz *et al.*, *Cell. Mol. Life Sci.* **68**, 3121 (2011).
10. J. D. Carpten *et al.*, *Nature* **448**, 439 (2007).
11. J. Xie *et al.*, *Nature* **391**, 90 (1998).
12. E. Roessler *et al.*, *Nat. Genet.* **14**, 357 (1996).

Acknowledgments: We are grateful to the patients and their families who have contributed to this study. This study was supported by the Gregory M. Kiez and Mehmet Kutman Foundation. R.P.L. is an investigator of the Howard Hughes Institute. V.E.C. is supported by NIH T32GM07205. All somatic mutations identified through exome sequencing of meningiomas are reported in the supplementary materials and submitted to the Catalogue of Somatic Mutations in Cancer (COSMIC) database (<http://cancer.sanger.ac.uk/cancergenome/projects/cosmic>, submission ID COSP30702). Yale University has filed a provisional patent application based on the results of this study.

Supplementary Materials

www.sciencemag.org/cgi/content/full/science.1233009/DC1
Materials and Methods
Figs. S1 to S14
Tables S1 to S8
References (13–27)

24 May 2012; accepted 15 January 2013
Published online 24 January 2013;
10.1126/science.1233009

Unraveling the Mechanism of Protein Disaggregation Through a ClpB-DnaK Interaction

Rina Rosenzweig,^{1,2,3*} Shoeib Moradi,¹ Arash Zarrine-Afsar,² John R. Glover,¹ Lewis E. Kay^{1,2,3,4*}

HSP-100 protein machines, such as ClpB, play an essential role in reactivating protein aggregates that can otherwise be lethal to cells. Although the players involved are known, including the DnaK/DnaJ/GrpE chaperone system in bacteria, details of the molecular interactions are not well understood. Using methyl–transverse relaxation–optimized nuclear magnetic resonance spectroscopy, we present an atomic-resolution model for the ClpB-DnaK complex, which we verified by mutagenesis and functional assays. ClpB and GrpE compete for binding to the DnaK nucleotide binding domain, with GrpE binding inhibiting disaggregation. DnaK, in turn, plays a dual role in both disaggregation and subsequent refolding of polypeptide chains as they emerge from the aggregate. On the basis of a combined structural-biochemical analysis, we propose a model for the mechanism of protein aggregate reactivation by ClpB.

The 580-kD hexameric ClpB molecular chaperone is a bacterial adenosine 5'-triphosphate (ATP)-dependent protein-remodeling machine that rescues stress-damaged proteins trapped in an aggregated state and plays a key role in thermotolerance development and in cell recovery after acute stress (1–3). Aggregate reactivation requires the collaboration of a second ATP-dependent mo-

lecular chaperone system, Hsp70/DnaK (1, 4–7). DnaK binding to client proteins is, in turn, regulated by co-chaperones DnaJ and GrpE through modulation of the DnaK ATPase cycle (8). A molecular picture of the ClpB-DnaK complex is critical to elucidate the mechanism of protein disaggregation, yet this system has proven recalcitrant to detailed structural studies.

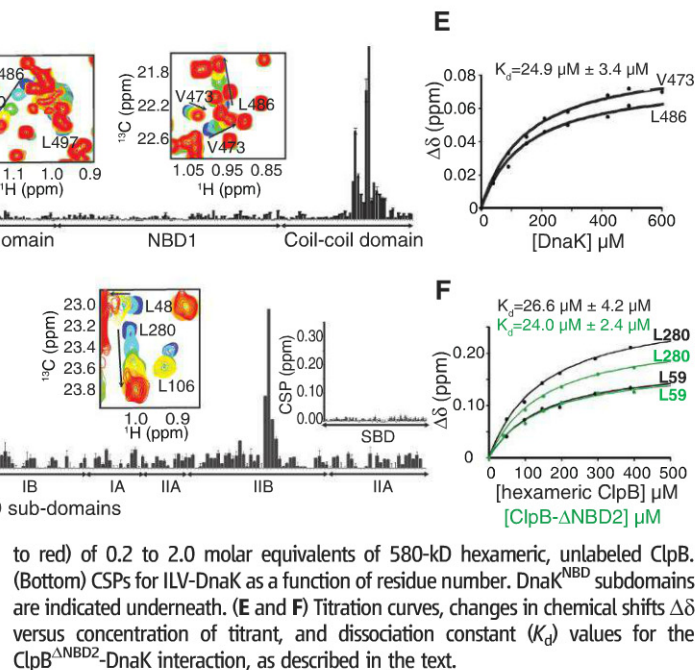
Nuclear magnetic resonance (NMR) spectroscopy is especially suited to characterize protein complexes at atomic detail, even if the interactions are weak and transient. Methyl–transverse relaxation–optimized spectroscopy (TROSY)-based experiments (9) and labeling schemes, whereby Ile, Leu, and Val methyl groups are ¹³CH₃-labeled in an otherwise highly deuterated background (referred to as ILV-protein) (10), have enabled NMR studies of large molecular systems (11, 12), such as those involved in disaggregation. Using these methods, we set out to elucidate the DnaK binding site on the ClpB chaperone.

Because of the large size of each monomer of ClpB (97 kD), NMR spectra of the ILV-labeled protein overlapped, precluding detailed analyses of the full-length molecule (fig. S1). We separately analyzed two monomeric fragments, including (i) ClpB^{ΔNBD2}, comprising the N-terminal domain (NTD), nucleotide binding domain 1 (NBD1), and the coil-coil domain (CCD), and (ii) nucleotide

¹Department of Biochemistry, University of Toronto, Toronto, Ontario M5S 1A8, Canada. ²Department of Chemistry, University of Toronto, Toronto, Ontario M5S 3H6, Canada. ³Department of Molecular Genetics, University of Toronto, Toronto, Ontario M5S 1A8, Canada. ⁴Program in Molecular Structure and Function, Hospital for Sick Children, Toronto, Ontario M5G 1X8, Canada.

*To whom correspondence should be addressed. E-mail: rina.rosenzweig@utoronto.ca (R.R.); kay@pound.med.utoronto.ca (L.E.K.)

Fig. 1. Interaction between ClpB CCD and DnaK NBD as detected by NMR. **(A)** Monomer structure of ClpB [Protein Data Base (PDB): 1QVR] (30) highlighting each domain. Residues with CSPs upon addition of DnaK are colored orange. **(B)** (Top) Selected regions of ^{13}C - ^1H HMQC data sets of ILV-ClpB $^{\Delta\text{NBD2}}$ in the absence (blue) or as a function of increasing concentrations (cyan to red) of 0.2 to 2.5 molar equivalents of unlabeled DnaK. Arrows indicate directions of peak movement. (Bottom) Magnitudes of CSPs for ILV-ClpB $^{\Delta\text{NBD2}}$ at the endpoint of titration with DnaK are shown as black bars for each residue. ClpB $^{\Delta\text{NBD2}}$ domains are indicated underneath. **(C)** Structural representation of DnaK chaperone, with residues showing significant CSPs highlighted in orange (see fig. S4C for details). The lid section of the SBD is shown in green. **(D)** (Top) Selected regions of HMQC spectra of ILV-DnaK in the absence (blue) and with increasing concentrations (cyan



to red) of 0.2 to 2.0 molar equivalents of 580-kD hexameric, unlabeled ClpB. (Bottom) CSPs for ILV-DnaK as a function of residue number. DnaK $^{\text{NBD}}$ subdomains are indicated underneath. **(E and F)** Titration curves, changes in chemical shifts $\Delta\delta$ versus concentration of titrant, and dissociation constant (K_d) values for the ClpB $^{\Delta\text{NBD2}}$ -DnaK interaction, as described in the text.

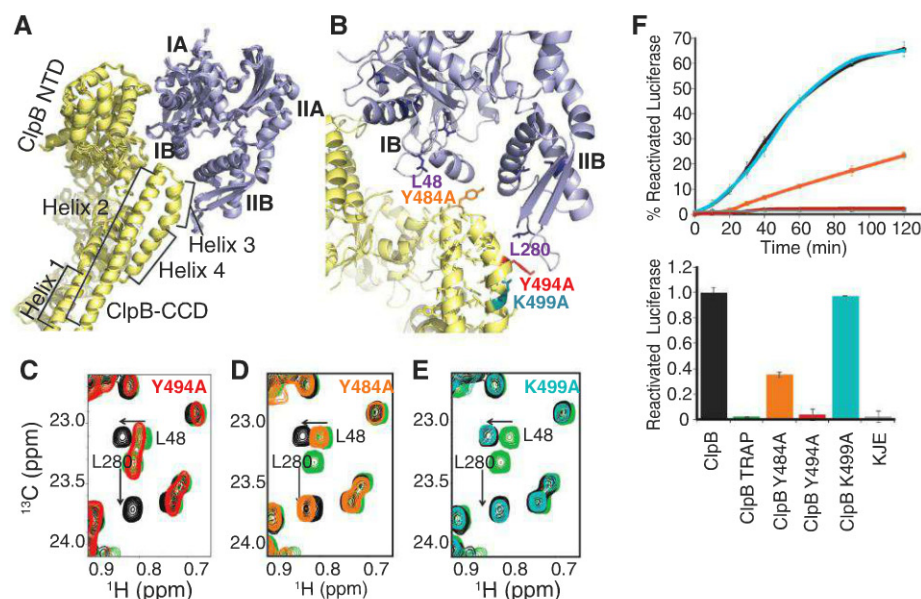


Fig. 2. Structural model for the ClpB-DnaK complex. **(A)** Ensemble of 10 lowest-energy HADDOCK structures for the ClpB $^{\Delta\text{NBD2}}$ -DnaK complex. **(B)** Cartoon diagram of the lowest-energy structure from HADDOCK with detailed view on binding surface. **(C to E)** Key ClpB residues in contact with DnaK were mutated to Ala (Y494A-red, Y484A-orange, and K499A-blue) and complex formation was monitored by HMQC experiments that exploit a methyl-TROSY effect. CSPs for DnaK L48 and L280 from the unbound (green) to fully bound forms of DnaK (black) are shown in each spectrum as a reference. **(F)** (Top) Reactivation of luciferase aggregates monitored in the presence of indicated ClpB mutants and the DnaK/DnaJ/GrpE (K/J/E) chaperone system. (Bottom) Reactivated luciferase after 120 min as a fraction of wt-ClpB reactivation. Standard errors of three independent assays are shown.

binding domain 2 (NBD2) (Fig. 1A). Of the two segments, only ILV-ClpB $^{\Delta\text{NBD2}}$ showed chemical-shift perturbations (CSPs) upon titration with unlabeled DnaK (Fig. 1B and fig. S1). Consistent with functional analyses of CCD mutants (13

and cross-linking results (14), the most prominent CSPs were mapped to specific residues in helices 2 and 3 of ClpB CCD (Fig. 1, A and B, and fig. S2), with several residues in the ClpB NTD showing very minor changes. To identify which

DnaK residues participate in binding, additional titrations were performed with unlabeled hexameric ClpB added to ILV-DnaK, forming a 650-kD complex. The DnaK chaperone contains a pair of domains: an N-terminal nucleotide binding domain (NBD) and a C-terminal substrate binding domain (SBD) (Fig. 1C) that undergo substantial conformational changes during the ATPase-coupled substrate binding and release cycle of DnaK (15–18). CSPs of DnaK establish that NBD subdomains IB and IIB bind ClpB (Fig. 1D and fig. S3), whereas ClpB binding to the SBD was not detected (Fig. 1D and fig. S4). ^{15}N - ^1H TROSY-HSQC (heteronuclear single-quantum coherence) experiments on smaller fragments such as a complex of ^{15}N -labeled DnaK $^{\text{NBD}}$ and ClpB $^{\text{NBD1-CCD}}$ (fig. S4; 100-kD complex) confirmed and extended the ClpB interaction surface to the cleft between subdomains IB and IIB of DnaK and the extended loop of IIB. Similar binding affinities were obtained from the titration of ILV-ClpB $^{\Delta\text{NBD2}}$ with unlabeled-DnaK (Fig. 1E) and from titrations of ILV-DnaK with equivalent concentrations of either unlabeled hexameric ClpB or unlabeled monomeric ClpB $^{\Delta\text{NBD2}}$ (Fig. 1F and table S1), suggesting a 1:1 ClpB $_6$:DnaK stoichiometry (19).

Paramagnetic relaxation enhancement (PRE) experiments (20, 21) were used to measure long-range distances between each of the components of the DnaK $^{\text{NBD}}$ -ClpB $^{\text{NBD1-CCD}}$ (or DnaK $^{\text{NBD2}}$ -ClpB $^{\Delta\text{NBD2}}$) complex with nitroxide spin probes attached to one of residues 77, 222, 479, or 502 of ClpB (fig. S5). These distances were used in combination with CSPs as restraints in the flexible docking program HADDOCK (22, 23) (table S2), with the resulting 95 docked structures (root mean

square deviation 0.41 Å) (table S3) revealing details of the DnaK NBD interaction with ClpB CCD (Fig. 2A). To cross-validate the ClpB-DnaK

structural model, Y484 and Y494 in the ClpB CCD, potentially forming hydrogen bonds with R55 and K285 of DnaK subdomains IB and IIB,

respectively (Fig. 2B), were mutated to Ala in ClpB^{ANBD2} and the interaction with DnaK monitored by NMR. Figure 2C illustrates a region of the ¹³C-¹H HMQC (heteronuclear multiple-quantum coherence) map of ILV-DnaK unbound (green) or bound to wild-type (wt)-ClpB^{ANBD2} (black), overlaid on the spectrum obtained when ClpB^{Y494A} is substituted for wt-ClpB^{ANBD2} (red). The superposition of “red” and “green” peaks establishes that complex formation does not occur with the Y494A mutant. Consistent with our model, CSPs for L280 and other methyl-containing probes of ILV-DnaK subdomain IIB titrated similarly for both wt-ClpB^{ANBD2} and ClpB^{Y484A}, indicating that the Y484A mutation does not disrupt contacts with subdomain IIB. By contrast, L48 (Fig. 2D) and other probes from ILV-DnaK subdomain IB showed no shifts upon addition of ClpB^{Y484A}, establishing that the Y484A mutation eliminates contacts with DnaK subdomain IB. Finally, ClpB^{K499A}, with position 499 located outside the DnaK binding surface, interacted with DnaK as the wild-type protein (Fig. 2E).

We tested the effect of these ClpB mutants on protein disaggregation by monitoring reactivation of aggregated firefly luciferase (Fig. 2F) and α -glucosidase (fig. S6). Both require tight collaboration between ClpB and DnaK chaperones, which we predicted depends on their physical interaction. ClpB^{K499A} (hexamer), whose binding to DnaK is indistinguishable from that of wt-ClpB, was fully active in reactivation. However, as expected from the impaired binding observed by NMR, ClpB^{Y484A} displayed a 65% reduction in reactivation compared to wt-ClpB. ClpB^{Y494A}, which did not bind DnaK in our NMR experiments, was correspondingly incapable of luciferase reactivation (Fig. 2F). None of the ClpB mutants showed defects in hexamer assembly or unfolding/translocation of nonaggregated unfolded protein (fig. S7).

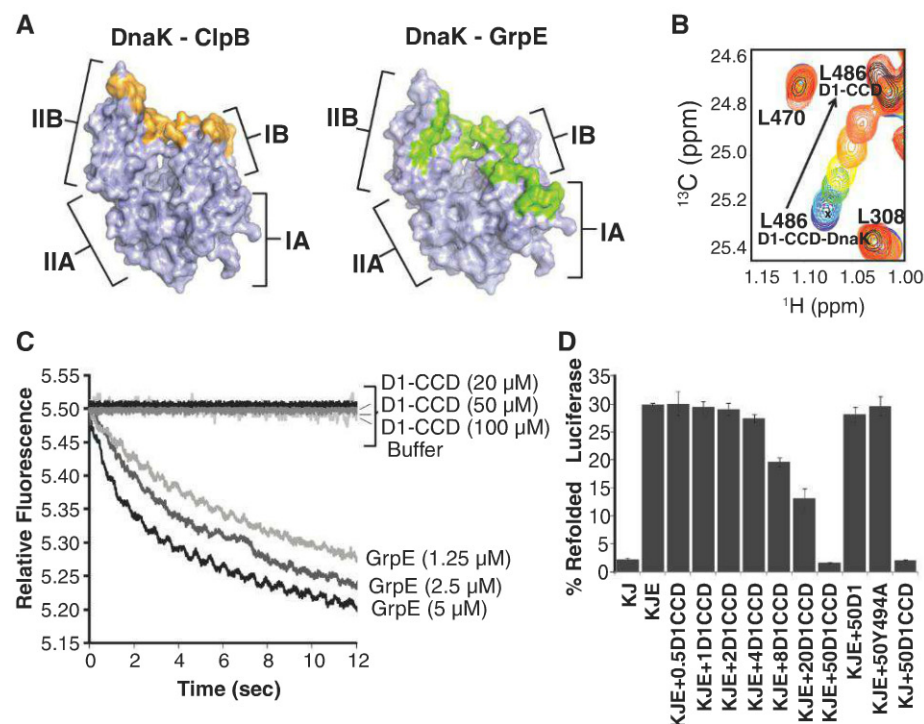


Fig. 3. The interaction of ClpB with DnaK competes with GrpE, yet does not induce nucleotide release. (A) DnaK residues that interact with ClpB (orange) and DnaK residues within 5 Å of GrpE [PDB: 1DKG (24)] in green. Subdomains are labeled for clarity. (B) Equimolar complex of ILV-ClpB^{NBD1-CCD} and unlabeled DnaK (D1-CCD-DnaK, blue) was titrated with increasing concentrations of unlabeled GrpE, shifting peaks to their unbound position (D1-CCD, red). Peaks in black are from a spectrum of unbound NBD1-CCD. (C) Effect of GrpE or ClpB^{NBD1-CCD} on nucleotide exchange rates of DnaK as monitored by stopped flow fluorimetry. (D) Percent luciferase refolding from soluble aggregates in the presence of the indicated chaperones. Addition of ClpB^{NBD1-CCD} (D1CCD) inhibits refolding by the DnaK/DnaJ/GrpE (K/J/E) chaperone system, whereas addition of ClpB^{NBD1} (D1) or CCD mutant Y494A (Y494A), which does not interact with DnaK, has no effect.

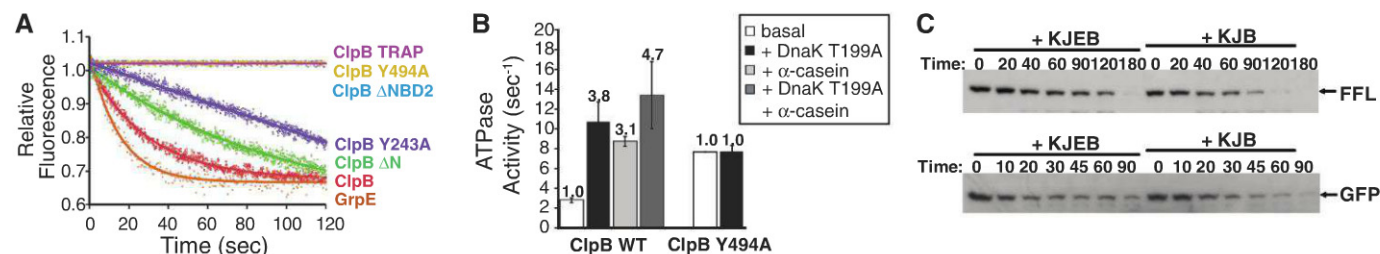


Fig. 4. The role of ClpB-DnaK collaboration in aggregate reactivation. (A) Dissociation of DnaK-RCLMA complex by the indicated proteins in the presence of ATP. The concentration of dimeric GrpE and hexameric ClpB were equivalent. (B) ATPase activity of ClpB is enhanced through interaction with DnaK or substrate α -casein. Rate of ClpB ATP hydrolysis was measured in the absence of other proteins (white bars), with DnaK^{T199A} (black bars), with α -casein (light gray bars), or with both (dark gray bars). The higher basal ATPase activity of ClpB^{T199A} (31), which does not bind DnaK, was not stimulated in the presence of DnaK. (C) Coupled disaggregation/degradation reactions of aggregated firefly luciferase

(FFL) and GFP (green fluorescent protein) by DnaK/DnaJ/GrpE/BAP/ClpB (KJEB) or DnaK/DnaJ/BAP/ClpB (KJB) monitored by Western blotting. Disaggregation rates are enhanced in the absence of GrpE. (D) Mechanistic model for collaboration between ClpB and DnaK systems in protein disaggregation.

The ClpB interaction with DnaK involves an extended loop in subdomain IIB (Figs. 2, A and B, and 3A) that also plays an important role in the binding of DnaK to the nucleotide exchange factor GrpE (Fig. 3A). Additionally, both ClpB and GrpE interact with the cleft between DnaK subdomains IB and IIB (Fig. 3A). Given these similarities, we determined whether GrpE and ClpB compete for DnaK binding. Addition of GrpE to an ILV-ClpB^{NBD1-CCD}-unlabeled DnaK complex caused shifting of cross peaks from residues in ClpB^{NBD1-CCD} to their unbound position, confirming that GrpE and ClpB bind to the same surface of DnaK (Fig. 3B).

The GrpE interaction with DnaK leads to nucleotide dissociation and subsequent substrate release from DnaK (24). We tested whether ClpB-DnaK binding would also result in nucleotide release using the nucleotide MABA-ADP, which displays a decrease in fluorescence upon release from DnaK (25). Although increasing concentrations of GrpE enhanced adenosine 5'-diphosphate (ADP) release rates, ClpB^{NBD1-CCD} could not stimulate ADP release from DnaK (Fig. 3C) or affect DnaJ-mediated DnaK ATP hydrolysis rates in the absence of GrpE (fig. S8).

Given that ClpB^{NBD1-CCD} competes with GrpE for DnaK binding without promoting nucleotide exchange, we asked whether ClpB^{NBD1-CCD} binding could hinder DnaK/DnaJ/GrpE-dependent refolding of heat-denatured substrates. Indeed, addition of ClpB^{NBD1-CCD} reduced the yield of DnaK-reactivated luciferase or malate dehydrogenase MDH, with complete inhibition at a 50:1 ClpB^{NBD1-CCD}:GrpE ratio (Fig. 3D and fig. S8) that reflects the lower affinity of CCD relative to GrpE for DnaK.

Aggregate reactivation requires transfer of DnaK-bound client proteins to ClpB to facilitate protein disaggregation. Involvement of GrpE at this stage would disrupt the DnaK-ClpB interaction, substantially decreasing the efficiency of the disaggregation reaction. Thus, we explored the possibility of an alternative ClpB-dependent substrate release mechanism by monitoring the rates of RCMLa (reduced carboxymethylated lactalbumin) release from DnaK as a function of GrpE or ClpB variants (Fig. 4A). Surprisingly, ClpB could induce RCMLa release from DnaK nearly as efficiently as GrpE. When using ClpB^{Y243A}, a translocation-pore-deficient mutant, substrate release rates were reduced, indicating that the translocation activity of ClpB plays a role in this process. When an ATP-hydrolysis-deficient mutant, ClpB^{TRAP}, was used, no substrate release occurred, demonstrating a high dependence on ClpB ATPase activity and that binding to ClpB in and of itself is insufficient to promote substrate release from DnaK.

Given that ClpB ATPase activity is essential for substrate release from DnaK, we asked whether the ClpB-DnaK interaction has a functional role by tuning ClpB ATP turnover rates. ClpB ATP hydrolysis rates were measured in the presence or absence of either the substrate casein or a

DnaK^{T199A} variant that cannot hydrolyze ATP. Interaction with either casein or DnaK separately increased ClpB ATP turnover rates between three- and fourfold, with a fivefold increase when both DnaK and α -casein were added (Fig. 4B and fig. S7). Furthermore, ClpB CCD can convert ClpB from a repressed state to an activated state in a DnaK-dependent manner (14). Thus, direct interaction of ClpB CCD with DnaK increases ClpB ATPase activity, which in turn enhances ClpB substrate threading power.

The DnaK chaperone system is active both upstream of ClpB, where it aids in extracting polypeptides from aggregates (26), and downstream, where DnaK/DnaJ/GrpE refold polypeptide chains that emerge from the ClpB lumen (5). We tested whether GrpE is required in the initial steps of the disaggregation reaction by performing disaggregation assays with and without this co-chaperone in a manner that eliminates the need for downstream GrpE-dependent refolding by using (i) a modified version of ClpB, termed BAP (3), that binds to the ClpP protease and transfers substrates emerging from the BAP central pore directly to ClpP for degradation or (ii) wt-ClpB/DnaK/DnaJ in combination with refolding chaperones GroEL/ES. In both cases, the presence of GrpE was detrimental to disaggregation (Fig. 4C and fig. S9). This reflects the competition between GrpE and ClpB for DnaK binding that leads to premature release of ClpB from the aggregate. Thus, the biological function of GrpE is solely downstream of the DnaK-ClpB disaggregation reaction. Indeed, GrpE is reversibly inactivated during heat shock (27, 28), which explains the ability of ClpB and DnaK to solubilize cellular aggregates without interference from GrpE under stress conditions.

We propose a mechanism by which the ClpB and DnaK chaperone systems reactivate insoluble protein aggregates (Fig. 4D). DnaK/DnaJ act during the early stages of aggregate reactivation, exposing peptide segments that then serve as the initiating points for disaggregation (29). These exposed segments of the aggregated protein are brought to the substrate-processing central pore of ClpB through direct interaction between the DnaK NBD and ClpB CCD. Association of either DnaK or substrate with ClpB leads to its activation, with nucleotide turnover rates greatly amplified in the presence of both. Activated ClpB then pulls on exposed regions of peptide chains in the aggregate, progressively unfolding and threading them through its axial channel (3). Once unfolded substrates emerge from the ClpB central pore, they either refold spontaneously or are recovered by the DnaK/DnaJ/GrpE system.

References and Notes

1. D. A. Parsell, A. S. Kowal, M. A. Singer, S. Lindquist, *Nature* **372**, 475 (1994).
2. Y. Sanchez, S. L. Lindquist, *Science* **248**, 1112 (1990).
3. J. Weibezahn *et al.*, *Cell* **119**, 653 (2004).
4. J. R. Glover, S. Lindquist, *Cell* **94**, 73 (1998).
5. P. Goloubinoff, A. Mogk, A. P. Zvi, T. Tomoyasu, B. Bukau, *Proc. Natl. Acad. Sci. U.S.A.* **96**, 13732 (1999).
6. A. Mogk *et al.*, *EMBO J.* **18**, 6934 (1999).
7. K. Motohashi, Y. Watanabe, M. Yoshida, M. Yoshida, *Proc. Natl. Acad. Sci. U.S.A.* **96**, 7184 (1999).
8. M. P. Mayer, B. Bukau, *Cell. Mol. Life Sci.* **62**, 670 (2005).
9. V. Tugarinov, P. M. Hwang, J. E. Ollerenshaw, L. E. Kay, *J. Am. Chem. Soc.* **125**, 10420 (2003).
10. V. Tugarinov, L. E. Kay, *J. Biomol. NMR* **28**, 165 (2004).
11. R. Sprangers, L. E. Kay, *Nature* **445**, 618 (2007).
12. I. Gelis *et al.*, *Cell* **131**, 756 (2007).
13. M. Miot *et al.*, *Proc. Natl. Acad. Sci. U.S.A.* **108**, 6915 (2011).
14. F. Seyffer *et al.*, *Nat. Struct. Mol. Biol.* **19**, 1347 (2012).
15. K. M. Flaherty, C. DeLuca-Flaherty, D. B. McKay, *Nature* **346**, 623 (1990).
16. M. Sriram, J. Osipiuk, B. Freeman, R. Morimoto, A. Joachimiak, *Structure* **5**, 403 (1997).
17. A. Zhuravleva, E. M. Clerico, L. M. Gierasch, *Cell* **151**, 1296 (2012).
18. R. Kityk, J. Kopp, I. Sinning, M. P. Mayer, *Mol. Cell* **48**, 863 (2012).
19. See supplementary materials on Science Online.
20. J. L. Battiste, G. Wagner, *Biochemistry* **39**, 5355 (2000).
21. T. L. Religa, R. Sprangers, L. E. Kay, *Science* **328**, 98 (2010).
22. C. Dominguez, R. Boelens, A. M. Bonvin, *J. Am. Chem. Soc.* **125**, 1731 (2003).
23. S. J. de Vries *et al.*, *Proteins* **69**, 726 (2007).
24. C. J. Harrison, M. Hayer-Hartl, M. Di Liberto, F. Hartl, J. Kuriyan, *Science* **276**, 431 (1997).
25. Y. Groemping *et al.*, *J. Mol. Biol.* **305**, 1173 (2001).
26. C. Schlieker, I. Tews, B. Bukau, A. Mogk, *FEBS Lett.* **578**, 351 (2004).
27. J. P. Grimshaw, I. Jelesarov, H. J. Schönfeld, P. Christen, *J. Biol. Chem.* **276**, 6098 (2001).
28. Y. Groemping, J. Reinstein, *J. Mol. Biol.* **314**, 167 (2001).
29. T. Haslberger *et al.*, *Nat. Struct. Mol. Biol.* **15**, 641 (2008).
30. S. Lee *et al.*, *Cell* **115**, 229 (2003).
31. T. Haslberger *et al.*, *Mol. Cell* **25**, 247 (2007).

Acknowledgments: We thank J. Forman-Kay for providing laboratory space and for valuable discussions, R. Muhandiram for NMR support, and M. Latham for helpful discussions. wt-ClpB and GroEL/ES constructs were generously provided by F. Tsai (Baylor College of Medicine, Texas) and A. Horwich (Yale School of Medicine, Connecticut). R.R. acknowledges the European Molecular Biology Organization (ALTF-570-2010) and the Government of Canada (Banting) for postdoctoral fellowships. L.E.K. holds a Canada Research Chair in Biochemistry. This work was supported by a grant from the Canadian Institutes of Health Research. Coordinates for the ClpB-DnaK complex are available as supplementary material.

Supplementary Materials

www.sciencemag.org/cgi/content/full/science.1233066/DC1
Materials and Methods
Figs. S1 to S9
Tables S1 to S3
References (32–66)
Coordinates for ClpB-DNA complex

21 November 2012; accepted 23 January 2013
Published online 7 February 2013;
10.1126/science.1233066

Sex Differences in the Gut Microbiome Drive Hormone-Dependent Regulation of Autoimmunity

Janet G. M. Markle,^{1,2} Daniel N. Frank,³ Steven Mortin-Toth,¹ Charles E. Robertson,⁴ Leah M. Feazel,³ Ulrike Rolle-Kampczyk,⁵ Martin von Bergen,^{5,6,7} Kathy D. McCoy,⁸ Andrew J. Macpherson,⁸ Jayne S. Danska^{1,2,9*}

Microbial exposures and sex hormones exert potent effects on autoimmune diseases, many of which are more prevalent in women. We demonstrate that early-life microbial exposures determine sex hormone levels and modify progression to autoimmunity in the nonobese diabetic (NOD) mouse model of type 1 diabetes (T1D). Colonization by commensal microbes elevated serum testosterone and protected NOD males from T1D. Transfer of gut microbiota from adult males to immature females altered the recipient's microbiota, resulting in elevated testosterone and metabolomic changes, reduced islet inflammation and autoantibody production, and robust T1D protection. These effects were dependent on androgen receptor activity. Thus, the commensal microbial community alters sex hormone levels and regulates autoimmune disease fate in individuals with high genetic risk.

Genome-wide studies have identified common polymorphisms associated with autoimmune disease risk, including causal variants implicated in immune regulation. These analyses have not addressed the impact of two other critical modifiers of autoimmunity: sexual dimorphism and environmental factors. The incidences of many autoimmune syndromes display a strong female bias (1–3), yet the mechanisms of sex-mediated immune regulation are poorly understood. Findings of incomplete concordance in monozygotic twins and a recent rise in autoimmune disease incidence in developed countries (4) indicate a causal role of environmental factors

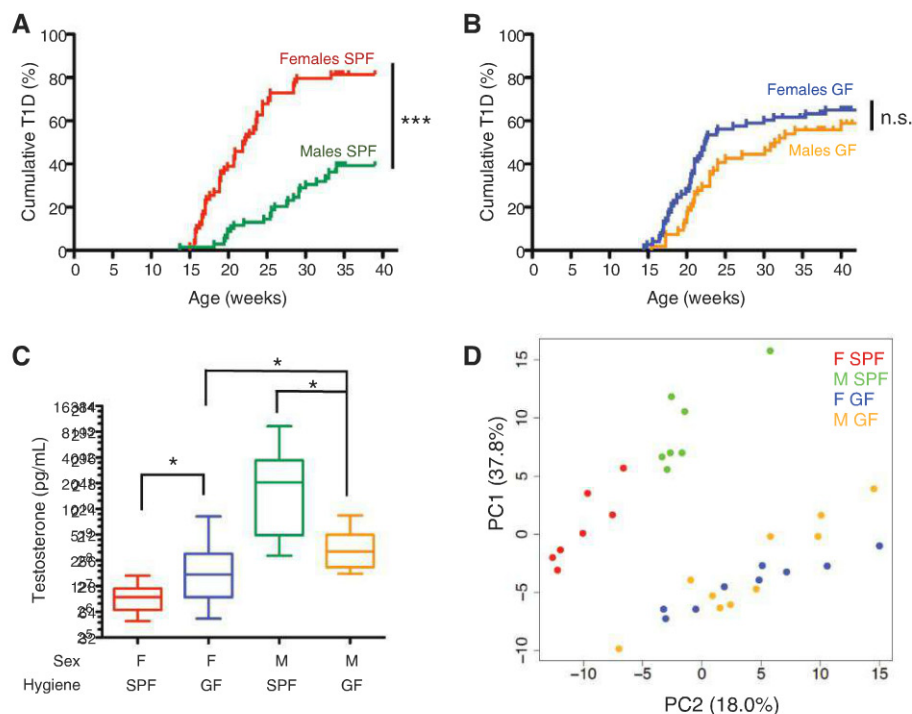
in disease. We have identified a direct interaction between sex hormones and microbial exposures and show that microbiome manipulations can provoke testosterone-dependent protection from autoimmunity in a genetically high-risk rodent model.

The nonobese diabetic (NOD) mouse displays spontaneous, immune-mediated pancreatic β cell destruction, causing type 1 diabetes (T1D) with complex genetic and environmental etiology (5, 6). In NOD mice and humans, T1D is preceded by leukocyte infiltration of the pancreatic islets (insulinitis) and production of autoantibodies (Aab) to islet antigens, including insulin

(7–10). NOD T1D incidence displays a strong >2:1 female-to-male sex bias (11). Castration increases male T1D incidence (12), and androgen treatment confers protection to females (13); hence, testosterone regulation is implicated in T1D pathogenesis. Moreover, higher T1D incidence in NOD colonies is positively correlated with better hygiene status (11). Conversely, systemic immune challenge with bacterial antigens protects these animals from disease (14, 15). Thus, the NOD model enables assessment of the roles of microbial colonization and sex in the regulation of spontaneous autoimmunity in high-risk individuals.

Male NOD mice housed in specific pathogen-free (SPF) conditions were protected relative to females ($P < 10^{-4}$; Fig. 1A and table S1), in agreement with previous reports (11, 16, 17). To assess the impact of commensal microbes on T1D

Fig. 1. Sex-biased autoimmunity in the NOD mouse depends on the microbiome. (A and B) The natural history of T1D in NOD/Jsd mice in SPF or GF conditions. (A) SPF females ($n = 59$) and SPF males ($n = 69$). $***P < 0.0001$. (B) GF females ($n = 73$) and GF males ($n = 54$). $P = 0.2115$, log-rank (Mantel-Cox) comparisons of survival curves. (C) Serum testosterone concentrations were higher in GF versus SPF females ($P = 0.0248$) and lower in GF versus SPF males (asterisk represents significant differences between groups, $P = 0.0049$, Mann-Whitney test, $n \geq 10$ per group). Testosterone in GF male sera was higher than in GF female sera ($P = 0.0378$). Box plots display the median, 25th percentile, and 75th percentile; whiskers display minimum and maximum values. (D) PCA plot, generated by analysis of more than 180 serum metabolites in SPF females, SPF males, GF females, and GF males ($n \geq 6$ per group). Principal components PC1 and PC2, which explain 55.8% of the total variance observed, discriminate SPF female samples from male samples and discriminate both sexes in SPF housing from GF-housed females and males.



¹Program in Genetics and Genome Biology, Hospital for Sick Children Research Institute, Toronto, Ontario M5G 1X8, Canada. ²Department of Immunology, University of Toronto, Toronto, Ontario M5S 1A8, Canada. ³Division of Infectious Diseases, University of Colorado School of Medicine, Aurora, CO 80045, USA. ⁴Department of Molecular, Cellular, and Developmental Biology, University of Colorado, Boulder, CO 80309, USA. ⁵Department of Metabolomics, Helmholtz Center for Environmental Research, 04318 Leipzig, Germany. ⁶Department of Proteomics, Helmholtz Center for Environmental Research, 04318 Leipzig, Germany. ⁷Department of Biotechnology, Chemistry and Environmental Engineering, Aalborg University, 9000 Aalborg, Denmark. ⁸Maurice Müller Laboratories, Universitätsklinik für Viszerale Chirurgie und Medizin (UVC), University of Bern, 3008 Bern, Switzerland. ⁹Department of Medical Biophysics, University of Toronto, Toronto, Ontario M5G 2M9, Canada.

*To whom correspondence should be addressed. E-mail: jayne.danska@sickkids.ca

incidence, we rederived NOD mice into germ-free (GF) conditions and monitored GF cohorts by glucose testing. In contrast to SPF conditions (18), GF NOD males and females had similar T1D incidence ($P = 0.2115$; Fig. 1B and table S1). T1D incidence was stable under SPF conditions (fig. S1A) and was unaltered by feeding of a diet used in GF conditions (fig. S1B); therefore, the relative protection of males in the SPF setting appeared to be dependent on the presence of commensal organisms. GF NOD mice colonized with an altered Schaedler flora (ASF; eight species) displayed a sex-dependent trend ($P = 0.0878$), which suggests that this limited-diversity microbiota partially restored the sex bias in the T1D phenotype (table S1 and fig. S1C). To determine whether microbial colonization affected sex hormone levels, we quantified 17β -estradiol and testosterone in the serum of SPF and GF males and females. No hygiene-dependent effects were detected in 17β -estradiol (fig. S1D). In contrast, GF females displayed elevated testosterone relative

to SPF females ($P < 0.05$; Fig. 1C), and GF males had lower levels relative to SPF males ($P < 0.05$; Fig. 1C), indicating that commensal colonization regulated testosterone production and/or usage.

Alterations in the composition and function of the gut microbiome exert mutualistic effects on host metabolism (19). Mass spectrometry-based metabolome analyses provide high sensitivity and reliable quantification of metabolites (20, 21). To identify host metabolic changes induced by microbial colonization, we screened 183 serum metabolites using mass spectrometry methods (18). Serum metabolite levels from SPF NOD males and females and from GF males and females were analyzed to identify metabolites that differentiated these four groups (tables S2 and S3). Principal components analysis (PCA) revealed a subset of glycerophospholipid and sphingolipid metabolites that accounted for a high proportion of total variability in this data set and showed distinct clustering of SPF males and SPF females (Fig. 1D). In contrast, these metabolites

did not distinguish males and females in the GF state (Fig. 1D), revealing a role for microbiome exposure in regulating sex-specific features of the host metabolic profile. Therefore, under colonized settings, males and females either had distinct microbial communities that induced different hormonal and metabolic responses, or responded in a sex-specific manner to an identical community.

To test for gut microbiome composition differences between the sexes and for changes that might accompany maturation, we sequenced bacterial 16S ribosomal RNA (rRNA) libraries prepared from cecal contents of SPF-housed NOD males and females at weaning (3 weeks), puberty (6 weeks), and adulthood prior to T1D onset (14 weeks). PCA was applied to these data to detect age- and sex-specific phenotypes. Although weanling NOD males and females were indistinguishable from each other, sex-specific differences in microbiome composition became evident at puberty and were most apparent in adult mice

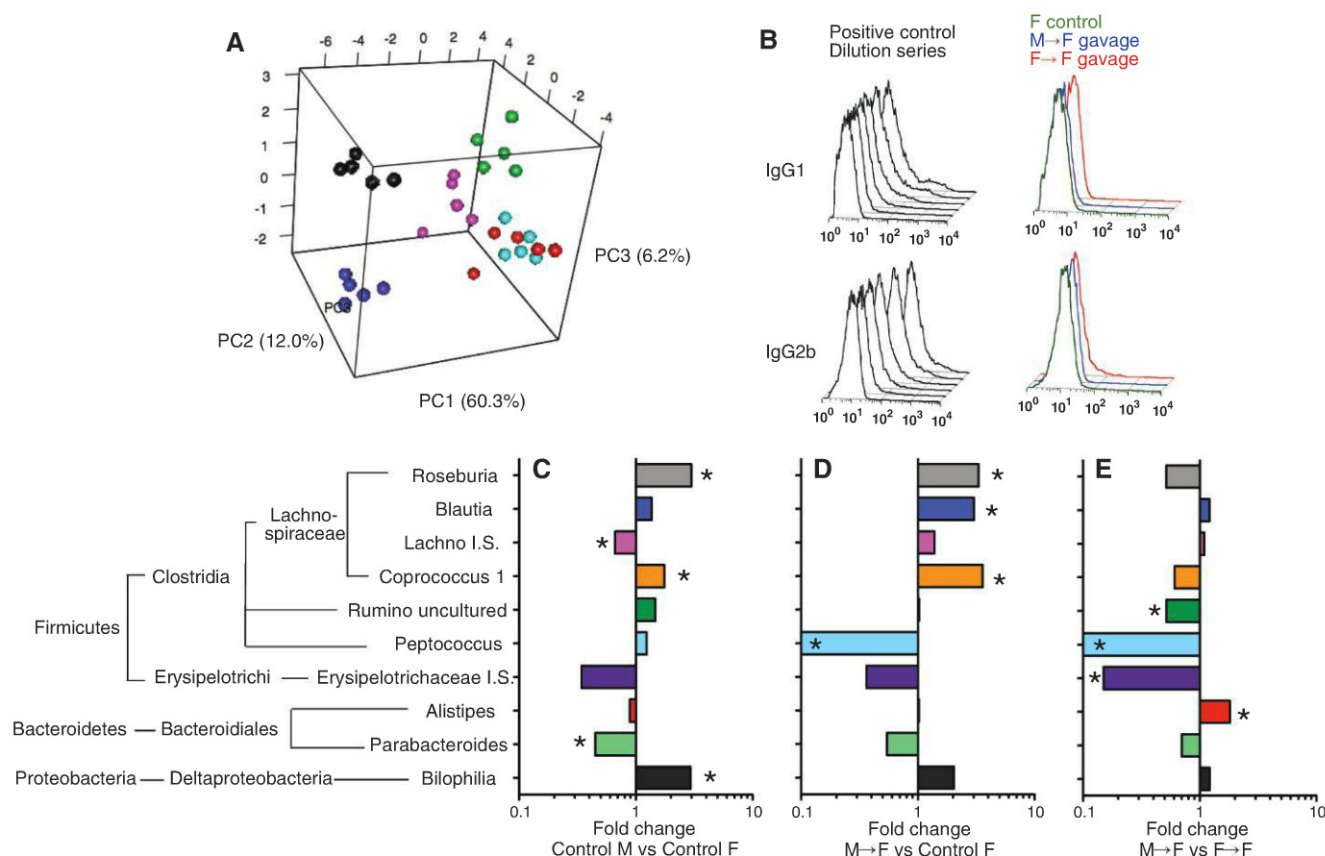
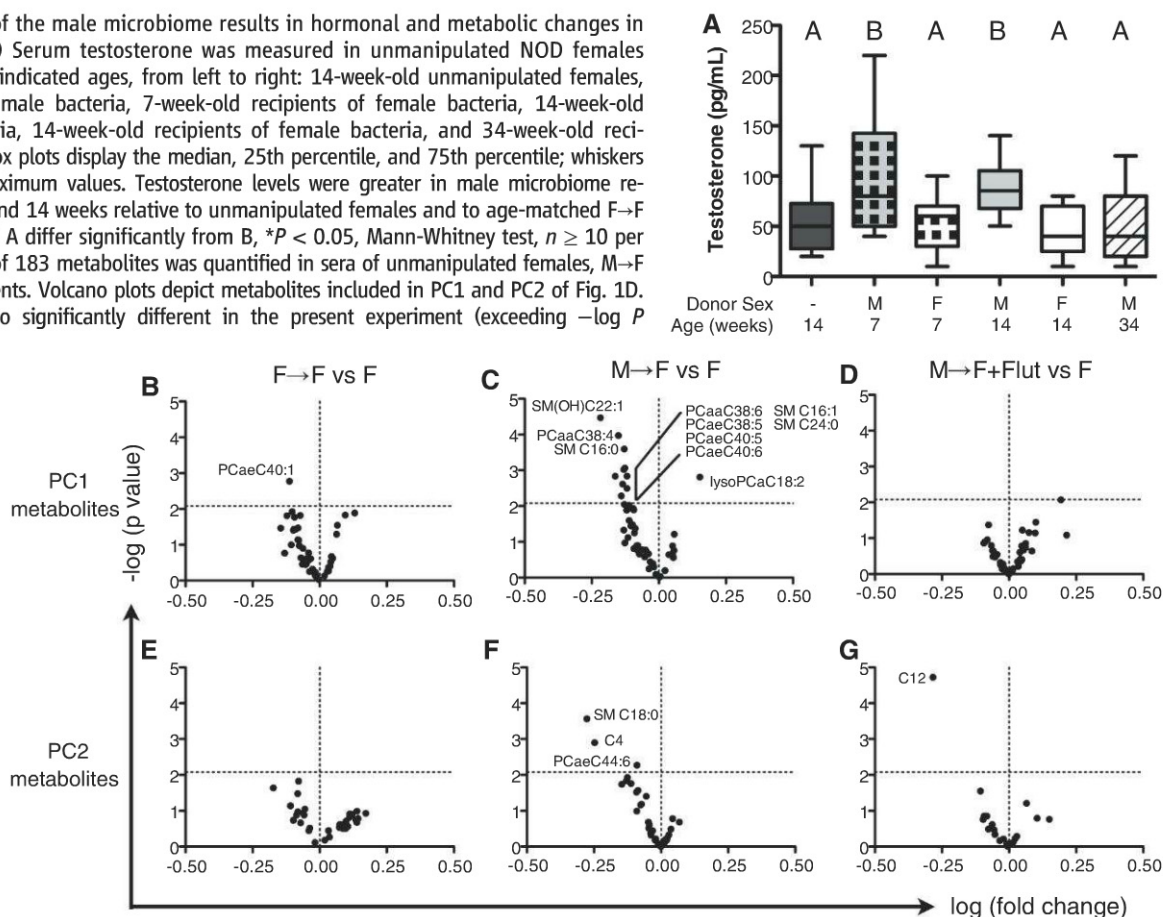


Fig. 2. Sex-specific microbiome profiles emerge after puberty, and cecal microbiome transplantation can stably alter the microbiome of the host without inducing systemic immune priming. (A) 16S bacterial rRNA sequencing was used to define the microbiome profiles of NOD male and female SPF mice at various developmental time points. PCA was used to compare the top 30 differentially abundant bacterial families across six different groups ($n = 5$ per group): 3-week-old males (turquoise), 3-week-old females (red), 6-week-old males (pink), 6-week-old females (green), 14-week-old males (blue), and 14-week-old females (black). These groups were separated by principal components PC1 to PC3, collectively explaining 78.5% of the total variance. (B) Systemic immune priming against the commensal microbiome was evaluated

in M→F, F→F, and unmanipulated female NOD mice (right histograms). No microbiome-dependent differences in commensal immunoglobulin G1 (IgG1) or IgG2b titers were detected among these groups ($n > 10$ per group; see fig. S2). Control mice were inoculated systemically with a bacterial isolate (black traces). (C to E) 16S sequencing comparisons of control males versus females at 14 weeks of age (C), female recipients of male microbiome (M→F) versus unmanipulated females (D), and female recipients of male microbiome (M→F) versus female recipients of female microbiome (F→F) (E) ($n = 5$ per control group, $n = 10$ per gavage group). Bacterial genera shown represent those found to be significantly different in at least one of these pairwise comparisons [$*P < 0.05$, two-part statistic (35); see table S6].

Fig. 3. Transplantation of the male microbiome results in hormonal and metabolic changes in the female recipient. **(A)** Serum testosterone was measured in unmanipulated NOD females and gavage recipients at indicated ages, from left to right: 14-week-old unmanipulated females, 7-week-old recipients of male bacteria, 7-week-old recipients of female bacteria, 14-week-old recipients of male bacteria, 14-week-old recipients of female bacteria, and 34-week-old recipients of male bacteria. Box plots display the median, 25th percentile, and 75th percentile; whiskers display minimum and maximum values. Testosterone levels were greater in male microbiome recipients at both 7 weeks and 14 weeks relative to unmanipulated females and to age-matched F→F recipients (groups marked A differ significantly from B, * $P < 0.05$, Mann-Whitney test, $n \geq 10$ per group). **(B to G)** A panel of 183 metabolites was quantified in sera of unmanipulated females, M→F recipients, and F→F recipients. Volcano plots depict metabolites included in PC1 and PC2 of Fig. 1D. Metabolites that were also significantly different in the present experiment (exceeding $-\log P$ threshold of 2.08) are labeled. Comparisons of metabolite levels in F→F versus F [(B) and (E)] and M→F versus F [(C) and (F)] are shown ($n \geq 5$ per group). The metabolomic assay was also applied to M→F recipients that had also been implanted with continuous-release pellets containing the AR antagonist flutamide [(D) and (G)].



(Fig. 2A). Given their similar housing conditions (18), these data indicated that sexual maturation was a major determinant of the cecal microbiome community structure. Because the relative T1D protection of males depended on commensal colonization (Fig. 1, A and B) and because mature males and females harbored distinct cecal microbiota, we asked whether manipulating the microbiota of young SPF females by transfer of cecal contents from adult donors provoked changes in microbiome composition, hormonal status, and metabolic status of the recipients.

Female NOD weanlings were gavaged twice with diluted cecal contents from either adult NOD male or NOD female donors. Systemic exposures to microbial agents can protect NOD mice from T1D (14, 22). Therefore, we tested whether gavage had unintentionally caused systemic priming that resulted in antibodies specific for the inoculated bacteria (23) (Fig. 2B). Positive control sera for this assay were prepared from mice systemically primed by intravenous injection with commensal bacteria. Low-titer commensal antibody responses were observed in control and gavaged females (Fig. 2B and fig. S2) relative to systemically primed controls. Therefore, the gavage transfer protocol did not induce systemic immune priming against cecal bacteria.

To evaluate the impacts of gavage transfers on the recipients' microbiomes, we performed 16S rRNA sequencing of cecal samples from age-

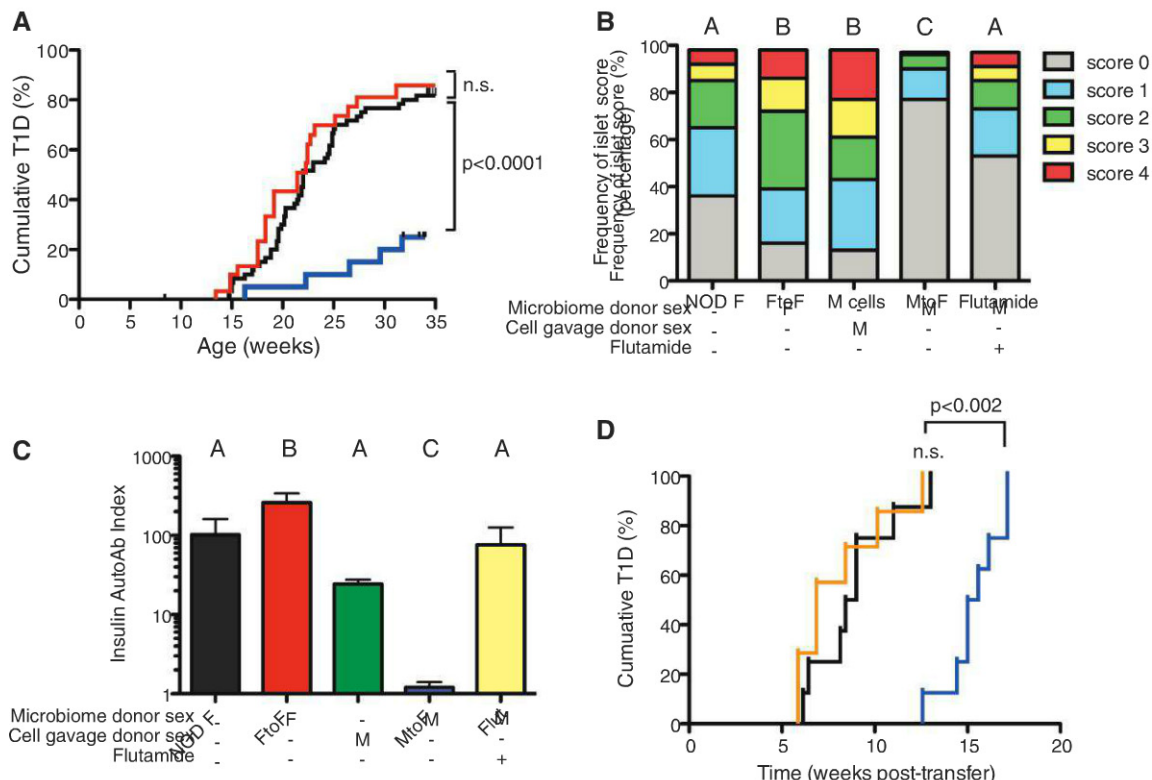
matched unmanipulated male and female controls (Fig. 2C) and from female recipients of adult male (M→F) or adult female (F→F) microbiota. Introduction of either adult male or female microbiota stably altered the recipient microbiome relative to unmanipulated female controls (Fig. 2, D and E). Some bacterial genera that were differentially represented in unmanipulated females relative to M→F gavage recipients also distinguished unmanipulated males and females (e.g., *Roseburia*, *Blautia*, *Coprococcus* 1, *Parabacteroides*, and *Bilophila*; Fig. 2, C and D, and tables S4 and S6), whereas other differences resulting from gavage of male microbiota were not "male-typical" (e.g., *Peptococcus* and *Lachno* S.S.; Fig. 2, C and D, and tables S4 and S6). Statistical analysis indicated excellent coverage of the biodiversity among these samples (fig. S3A). Thus, gavage of male microbiota into SPF-colonized weanling females altered their microbiota to a third state, distinct from both unmanipulated males and females. Although durable for ≥ 11 weeks, these gavage-induced changes were no longer evident at 34 weeks of age (fig. S3B).

Given our observations that microbial colonization status was correlated with testosterone levels (Fig. 1C), we analyzed serum testosterone in female gavage recipients of either male or female microbiota. Strikingly, at ages 7 and 14 weeks, but not at 34 weeks, the M→F gavage recipients displayed significantly increased testosterone lev-

els relative to unmanipulated adult females and to age-matched F→F recipients (Fig. 3A). The magnitude of testosterone increase produced by M→F transplant was lower than observed values in unmanipulated, age-matched SPF males (compare Fig. 1C). To determine whether this moderate elevation affected fecundity, we paired cohorts of M→F gavage recipients and unmanipulated females with stud males. Litter size and time to birth of a first litter did not differ between the two groups, which suggests that the male microbiota-dependent increase in testosterone did not impair fertility (table S6). These data show that transfer of male microbiota into young females conferred sustained testosterone elevation compatible with normal breeding behavior in recipient females.

The effect of M→F microbiome transfer on recipient testosterone levels suggested that this manipulation might exert broader metabolic influence. Therefore, we performed a serum metabolomics analysis of 14-week-old unmanipulated males and females and of M→F and F→F recipient females, with a focus on metabolites that had distinguished the sexes under SPF and GF conditions (Fig. 1D and tables S2 and S3). Transfer of male, but not female, microbiota lowered serum concentrations of glycerophospholipid and sphingolipid long-chain fatty acids (Fig. 3, B, C, E, and F), demonstrating that the sex of the microbiome donor determined metabolic out-

Fig. 4. Gavage of female NOD pups with male NOD-derived intestinal microbiome results in T1D protection, decreased insulinitis severity, and decreased insulin Aab titer by an androgen-dependent mechanism. Female NOD weanlings were gavaged with cecal bacteria from either adult NOD males or adult NOD females. (A) T1D was assessed in unmanipulated NOD females (black, $n = 59$), F→F female recipients (red, $n = 30$), and M→F recipients (blue, $n = 38$). T1D survival curves did not differ between F and F→F groups. M→F recipients were protected from T1D relative to unmanipulated females ($P < 0.0001$, log-rank test). (B) Insulinitis severity was assessed by established protocols (18) in (from left to right) unmanipulated females, recipients of the female microbiome (F→F), or recipients of the male microbiome (M→F), as well as a M→F group that simultaneously received a subcutaneous pellet secreting the AR antagonist flutamide. As a control for possible effects of male cells contaminating the gavage inoculum, females gavaged at weaning with male cells only were also included (middle histogram bar). Different letters indicate significantly different insulinitis score distributions by χ^2 test (Bonferroni-corrected $\alpha = 0.005$, $n \geq 5$ biological replicates per group). (C) Insulin Aab titer was assessed as another preclinical T1D-related phenotype. Different letters indicate significantly different group means by Mann-Whitney test (Bonferroni-corrected $\alpha = 0.005$, $n \geq 5$ per group). Error bars indicate SEM. (D) As a test for possible effects of microbiome manip-



ulation and changes in host hormonal and metabolic status on T cell diabetogenicity, 10^7 purified splenic T cells were prepared from unmanipulated NOD females (black), M→F gavage recipients (blue), or M→F gavage recipients treated with flutamide to antagonize AR signaling (orange), then transferred to 4- to 5-week-old female NOD.SCID recipients by intravenous injection. Recipients were monitored for hyperglycemia ($n > 7$ per group). The latency of T1D in NOD.SCID recipients of T cells isolated from M→F gavage recipients was greater than in recipients of T cells isolated from either unmanipulated females or from M→F gavage recipients that had been treated with flutamide ($P < 0.002$, log-rank comparisons of survival curves).

comes in the recipient. A recent report that many of these same long-chain fatty acids differed between human males and females (24) suggests evolutionary conservation of the sex-dependent effects we observed. Thus, in agreement with phylogenetic analysis of microbiome composition (Fig. 2, C to E), M→F gavage produced a metabolite distinct from that of both unmanipulated females and males.

To determine whether the testosterone elevation observed in M→F females caused the metabolite changes, we repeated the M→F gavage of weanling females and also treated these recipients with the androgen receptor (AR) antagonist flutamide, using a 60-day implant formulation. Blockade of AR signaling attenuated all of the male microbiome-specific changes in female host metabolites (Fig. 3, D and G), demonstrating that testosterone elevation caused by male microbiome transfer was critical for the generation of downstream host metabolomic phenotypes.

Because transfer of male microbiota altered recipient female hormonal and metabolic profiles, we asked whether these changes also altered the course of autoimmunity. We established co-

horts of NOD females that were either unmanipulated or gavaged at weaning with male or female microbiota, followed by blood glucose monitoring. Relative to either unmanipulated females or F→F gavage recipients, M→F recipients were strongly protected from T1D (Fig. 4A, $P < 0.0001$). Diabetes onset is preceded by progressive insulinitis (5, 6). Thus, insulinitis was assessed at 14 weeks of age in separate cohorts of unmanipulated females, F→F gavage recipients, and M→F recipients with or without flutamide treatment. Because intestinal epithelial cells are continuously sloughed into the gut lumen and are likely present in the M→F gavage inoculum, we performed an *in vivo* cytotoxicity assay (25) to verify that gavage transfer of male cellular antigens did not induce an immune response in female recipients (fig. S4). As an additional control for potential effects of male antigens in cecal preparations, another cohort of females was gavaged with sterile male cells only. Gavage of male cells did not protect against insulinitis progression, in accord with the *in vivo* cytotoxicity assay; this finding indicates that oral delivery of male antigens did not confer an im-

mune response in this model (Fig. 4B). In contrast, female recipients of male microbiota were protected from invasive insulinitis relative to both unmanipulated and F→F recipients, and the latter displayed slightly greater insulinitis severity than unmanipulated controls (Fig. 4B). Moreover, insulinitis protection conferred by M→F microbiome transfer was lost when AR signaling was antagonized by flutamide (Fig. 4B), demonstrating that testosterone activity was essential to the protection from islet inflammation.

Insulin-specific Aab, a second autoimmune phenotype in prediabetic NOD mice and humans, was quantified in the same cohorts of mice examined for insulinitis. Relative to either unmanipulated females or F→F recipients, M→F recipients displayed lower Aab titers (Fig. 4C). In agreement with our insulinitis data (Fig. 4B), Aab titers were not significantly decreased in M→F flutamide-treated mice or in recipients of male cell gavage only (Fig. 4C). Collectively, these results show that male microbiome transfer to females drove testosterone-dependent attenuation of autoimmune phenotypes and protection from T1D. To test whether the diabetogenic

potential of T cells was altered by these microbiome manipulations, we assessed the ability of T cells from unmanipulated and from M→F recipient females (with or without flutamide) to transfer T1D to lymphocyte-deficient, T1D-resistant NOD.*SCID* (severe combined immunodeficient) recipients. T cells from unmanipulated NOD females transferred T1D to 100% of NOD.*SCID* recipients within 13 weeks (Fig. 4D). In contrast, T cells from M→F mice were delayed in their ability to transfer T1D ($P < 0.002$; Fig. 4D). T cells from M→F + flutamide-treated mice transferred T1D with equivalent kinetics to the T cells from unmanipulated females (Fig. 4D). Thus, testosterone was a key mediator of male microbiota effects on the female metabolome and of the autoimmune response evident in insulinitis progression, Aab production, and the capacity of T cells to transfer diabetes to NOD.*SCID* recipients. Additional studies are needed to define the pro-autoimmune mechanisms conferred by the female intestinal microbiome that likely involve other hormone-regulated pathways.

Our results reveal that alteration of the gut microbiome composition in early life potentially suppresses autoimmunity in animals at high genetic risk for disease. Recent human data demonstrate that puberty and pregnancy shape the intestinal microbiota, provoking metabolic changes that may favor fertility and reproduction (26, 27). Similar to our findings in the NOD model, sex hormones may also modulate sexual dimorphism in human autoimmune diseases. The female-to-male bias in rheumatoid arthritis and multiple sclerosis incidence declines with older age at onset, coincident with a decline in testosterone (28, 29). In contrast, human T1D is not sex-biased, perhaps because the peak age at onset precedes puberty, with a recent rapid rise in incidence reported in children under 5 (30, 31). Our data demonstrate that microbiome alterations in young, commensally colonized mice conferred testosterone and metabolite changes sufficient to oppose genetically programmed autoimmunity while preserving fertility.

Evidence of intestinal dysbiosis in autoimmune disease patients is emerging (32, 33). As shown here and in a recent study of autoimmune demyelination (34), rodent models identify microbiome alterations as a causal factor and not merely a consequence of autoimmune disease. Improved prospective identification of children at high risk for autoimmunity through the use of genetic and immune markers could facilitate the testing of nonpathogenic microbial therapies in disease prevention and treatment.

References and Notes

- H. M. Scobie *et al.*, *PLoS Pathog.* **2**, e111 (2006).
- C. C. Whitacre, *Nat. Immunol.* **2**, 777 (2001).
- C. Ober, D. A. Loisel, Y. Gilad, *Nat. Rev. Genet.* **9**, 911 (2008).
- J. F. Bach, *N. Engl. J. Med.* **347**, 911 (2002).
- S. Makino *et al.*, *Jikken Dobutsu* **29**, 1 (1980).
- E. Leiter, M. Atkinson, *NOD Mice and Related Strains: Research Applications in Diabetes, AIDS, Cancer and Other Diseases* (Landes, Austin, TX, 1998), vol. 2.
- D. V. Serreze, E. H. Leiter, *Curr. Dir. Autoimmun.* **4**, 31 (2001).
- D. Miao, L. Yu, G. S. Eisenbarth, *Front. Biosci.* **12**, 1889 (2007).
- M. S. Anderson, J. A. Bluestone, *Annu. Rev. Immunol.* **23**, 447 (2005).
- S. Ghosh *et al.*, *Nat. Genet.* **4**, 404 (1993).
- P. Pozzilli, A. Signore, A. J. Williams, P. E. Beales, *Immunol. Today* **14**, 193 (1993).
- S. Makino, K. Kunimoto, Y. Muraoka, K. Katagiri, *Jikken Dobutsu* **30**, 137 (1981).
- H. S. Fox, *J. Exp. Med.* **175**, 1409 (1992).
- M. Harada, Y. Kishimoto, S. Makino, *Diabetes Res. Clin. Pract.* **8**, 85 (1990).
- H. Y. Qin, M. W. Sadelain, C. Hitchon, J. Lauzon, B. Singh, *J. Immunol.* **150**, 2072 (1993).
- E. A. Ivakine *et al.*, *Diabetes* **55**, 3611 (2006).
- E. A. Ivakine *et al.*, *J. Immunol.* **174**, 7129 (2005).
- See supplementary materials on Science Online.
- J. K. Nicholson *et al.*, *Science* **336**, 1262 (2012).
- T. Koal, H. P. Deigner, *Curr. Mol. Med.* **10**, 216 (2010).
- A. Oberbach *et al.*, *J. Proteome Res.* **10**, 4769 (2011).
- M. W. Sadelain, H. Y. Qin, J. Lauzon, B. Singh, *Diabetes* **39**, 583 (1990).
- E. Slack *et al.*, *Science* **325**, 617 (2009).
- K. Mittelstrass *et al.*, *PLoS Genet.* **7**, e1002215 (2011).
- J. G. Chai, E. James, H. Dewchand, E. Simpson, D. Scott, *Blood* **103**, 3951 (2004).
- O. Koren *et al.*, *Cell* **150**, 470 (2012).
- T. Yatsunenko *et al.*, *Nature* **486**, 222 (2012).
- M. F. Doran, G. R. Pond, C. S. Crowson, W. M. O'Fallon, S. E. Gabriel, *Arthritis Rheum.* **46**, 625 (2002).
- B. G. Weinshenker, *Ann. Neurol.* **36** (suppl.), S6 (1994).
- P. R. Burton *et al.*, Wellcome Trust Case Control Consortium, *Nature* **447**, 661 (2007).
- C. C. Patterson, G. G. Dahlquist, E. Gyürüs, A. Green, G. Soltész, EURODIAB Study Group, *Lancet* **373**, 2027 (2009).
- C. T. Brown *et al.*, *PLoS ONE* **6**, e25792 (2011).
- D. N. Frank, W. Zhu, R. B. Sartor, E. Li, *Trends Microbiol.* **19**, 427 (2011).
- K. Berer *et al.*, *Nature* **479**, 538 (2011).
- B. D. Wagner, C. E. Robertson, J. K. Harris, *PLoS ONE* **6**, e20296 (2011).

Acknowledgments: We thank S. Bashir for assistance with metabolomic data analysis, C. Vogel Kotter for high-throughput sequencing, and E. Simpson and M. Palmert for helpful discussions. The 16S sequence data have been submitted to the National Center for Biotechnology Information short-read archive project, accession no. SRA064044. Flow cytometry was performed in the SickKids–University Health Network Flow Cytometry Facility with funds from the Ontario Institute for Cancer Research, McEwen Centre for Regenerative Medicine, Canada Foundation for Innovation, and SickKids Foundation. Roche 454 sequencing was performed at the Centre for Applied Genomics, Hospital for Sick Children. Illumina sequencing was performed at the University of Colorado School of Medicine. Supported by Canadian Institutes of Health Research (CIHR) grant 64216 and Juvenile Diabetes Research Foundation (JDRF) grant 17-2011-520 (J.S.D.), Genome Canada (administered by Ontario Genomics Institute) (J.S.D. and A.J.M.), JDRF grant 36-2008-926 and the Genexen Foundation (A.J.M.), a CIHR Banting and Best fellowship (J.G.M.M.), and NIH grant R21HG005964 (D.N.F. and C.E.R.). J.G.M.M. and J.S.D. designed the study, analyzed data, and wrote the manuscript; J.G.M.M., D.N.F., S.M.-T., C.E.R., M.v.B., K.D.M., and A.J.M. performed experiments and analyzed data; L.M.F. and U.R.-K. performed experiments; and all authors contributed to manuscript editing.

Supplementary Materials

www.sciencemag.org/cgi/content/full/science.1233521/DC1
Materials and Methods
Figs. S1 to S4
Tables S1 to S6
References (36–58)

3 December 2012; accepted 9 January 2013

Published online 17 January 2013;

10.1126/science.1233521

Interferon- ϵ Protects the Female Reproductive Tract from Viral and Bacterial Infection

Ka Yee Fung,^{1*} Niamh E. Mangan,^{1*} Helen Cumming,¹ Jay C. Horvat,² Jemma R. Mayall,² Sebastian A. Stifter,¹ Nicole De Weerd,¹ Laila C. Roisman,^{1,3} Jamie Rossjohn,³ Sarah A. Robertson,⁴ John E. Schjenken,⁴ Belinda Parker,^{5,6} Caroline E. Gargett,^{7,8} Hong P. T. Nguyen,⁷ Daniel J. Carr,⁹ Philip M. Hansbro,² Paul J. Hertzog^{1†}

The innate immune system senses pathogens through pattern-recognition receptors (PRRs) that signal to induce effector cytokines, such as type I interferons (IFNs). We characterized IFN- ϵ as a type I IFN because it signaled via the Ifnar1 and Ifnar2 receptors to induce IFN-regulated genes. In contrast to other type I IFNs, IFN- ϵ was not induced by known PRR pathways; instead, IFN- ϵ was constitutively expressed by epithelial cells of the female reproductive tract (FRT) and was hormonally regulated. *Ifn- ϵ* -deficient mice had increased susceptibility to infection of the FRT by the common sexually transmitted infections (STIs) herpes simplex virus 2 and *Chlamydia muridarum*. Thus, IFN- ϵ is a potent antipathogen and immunoregulatory cytokine that may be important in combating STIs that represent a major global health and socioeconomic burden.

Type I interferons (IFNs) are crucial in host defense because of their antipathogen actions and ability to activate effector cells of the innate and adaptive immune responses (1, 2). The type I IFN locus contains genes encoding 13 IFN- α subtypes, IFN- β , and IFN- ω (3) whose promoters contain acute response elements [such as interferon regulatory factors (IRFs) and

NF- κ B in IFN- β], which ensure rapid induction of these genes by pattern-recognition receptor (PRR) pathways (4, 5). This locus also contains a gene, which we previously designated *IFN- ϵ* , but whose function has remained uncharacterized.

Interferon- ϵ shares only 30% amino acid homology to a consensus IFN- α sequence and to IFN- β . Therefore, we first demonstrated that

IFN- ϵ was a type I IFN by showing that it transduced signals via the *Ifnar1* and *Ifnar2* receptors (see the supplementary materials and methods) (6). Incubation of recombinant Ifn- ϵ with bone marrow-derived macrophages (BMDMs) from wild-type (WT) mice induced IFN-regulated genes (IRGs) such as *Irf7* and *2'5'oas* (which encodes oligoadenylate synthetase) (Fig. 1, A and B), whereas these IRGs were not induced in BMDMs from *Ifnar1*- or *Ifnar2*-deficient mice. Accordingly, Ifn- ϵ should be classified as a type I IFN.

We next determined whether IFN- ϵ was induced by PRR pathways. Primary BMDMs, murine embryonic fibroblasts, and the murine macrophage cell line RAW264.7 were treated with synthetic ligands of Toll-like receptors (TLRs) 2, 3, 4, 7/8, and 9; cytosolic DNA sensors or AIM2 inflammasomes potentially induced known PRR response genes such as *Ifn- β* and/or *interleukin-6* (*Il-6*) (7–9). By contrast, there was no significant change in the expression of *Ifn- ϵ* upon stimulation with these activators (Fig. 1C and fig. S1, A and B). Because all PRRs induce type I IFN expression through the activation of the IRF family of transcription factors (5), we then examined whether IRFs could directly regulate the *Ifn- ϵ* promoter. IRF-3, IRF-7, and IRF-5 induced promoter activity of *Ifn- β* , *Ifn- α* , and *p125* (5) luciferase reporters in human embryonic kidney (HEK) 293 cells (Fig. 1D). By contrast, we did not observe any alteration of *Ifn- ϵ* promoter activity (Fig. 1D). Semliki Forest virus infection of RAW264.7 cells stimulated the expression of the positive control antiviral response gene *2'5'oas*, but not *Ifn- ϵ* expression (fig. S1C). Furthermore, *Ifn- ϵ* expression was not altered during in vivo infection with herpes simplex virus 2 (HSV-2) or *Chlamydia muridarum* (see below), nor by stimulation of human endometrial cell lines with PRR ligands (fig. S1D). This lack of regulation of *Ifn- ϵ* gene expression by conventional PRR pathways is consistent with the lack of response elements for these pathways [IRFs, NF- κ B, STAT (signal transducers and activators of transcription), ISRE (interferon-stimulated response element)] in the *Ifn- ϵ* proximal promoter compared with other type I IFN genes (fig. S1E).

Because *Ifn- ϵ* was not regulated by PRR pathways, we examined its constitutive expression. The expression of *Ifn- α* and β was undetectable in all organs (Fig. 2A). Similarly, the expression of *Ifn- ϵ* was not detectable at significant levels in any organ except the uterus, cervix, vagina, and ovary (Fig. 2A). Immunohistochemistry results show that Ifn- ϵ was expressed in the luminal and glandular epithelial cells of the endometrium (Fig. 2B). In support of these data, the uterine expression levels of *Ifn- ϵ* did not differ in NOD (nonobese diabetic)/SCID (severe combined immunodeficient)/IL-2 γ ^{−/−} mice [which are deficient in mature T, B, and natural killer (NK) cells] relative to WT mice, indicating that the aforementioned cells do not express detectable levels, nor do they regulate this cytokine (fig. S1F). This finding differs from the expression of conventional type I IFNs, which are usually expressed in hemopoietic cells.

We found that *Ifn- ϵ* expression varied approximately 30-fold at different stages of the estrous cycle, with the lowest levels during diestrus and the highest at estrus (Fig. 2C). During pregnancy, uterine *Ifn- ϵ* expression was dramatically reduced at day 1.5 postcoitus (pc) and was lowest at day 4.5 pc, coincident with the time of embryo im-

plantation (Fig. 2D). *Ifn- ϵ* expression was also reduced in pseudo-pregnant mice 4.5 days pc after mating with vasectomized males (Fig. 2D), which suggests that maternal hormones, not the embryo or its products, were required for the reduction in *Ifn- ϵ* . In addition, there was a slight increase in expression of *Ifn- ϵ* (1.8- to 1.9-fold) 8 hours pc, though expression had returned to normal levels by 16 hours pc, showing that neither seminal fluid nor sperm directly suppress *Ifn- ϵ* expression (fig. S1G). Because changes in expression occur after mating with vasectomized or intact males, expression fluctuations are likely to be secondary to physiological and hormonal changes, which are known to be comparable at day 4.5 pc whether or not conception occurs. Together, these data are consistent with *Ifn- ϵ* expression being hormonally regulated. To evaluate this finding, we ovariectomized female mice and administered ovarian sex steroid hormones. Estrogen administration induced *Ifn- ϵ* expression more than sixfold (Fig. 2E). This hormonal regulation was not observed for expression of other conventional type I IFNs (10).

Expression analysis of a panel of tissues confirmed the lack of basal expression of IFN- ϵ in all organs in women, with the exception of the

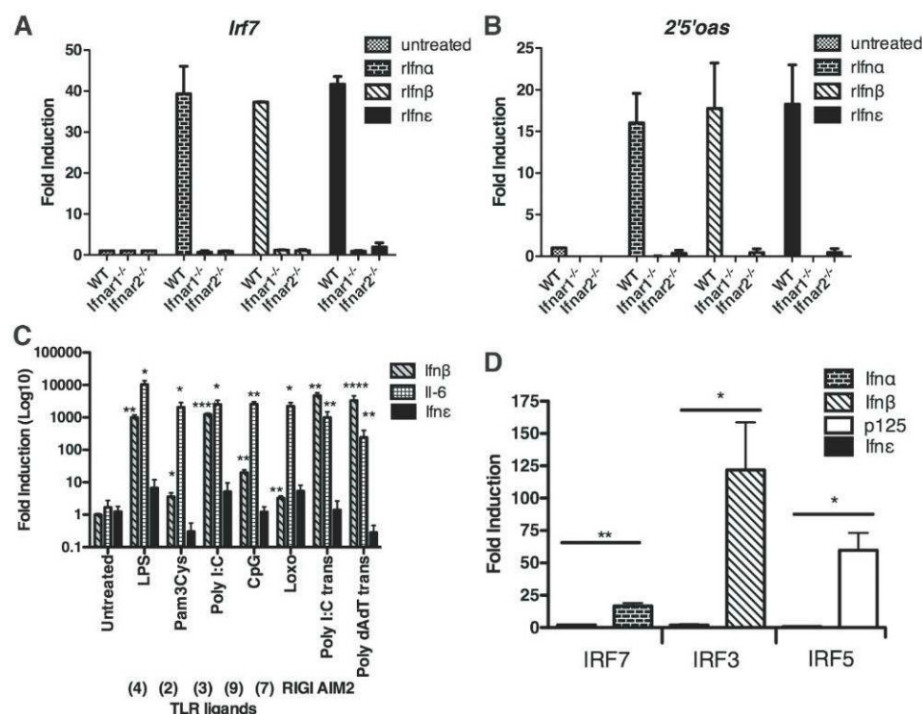


Fig. 1. Interferon- ϵ signals through the type I IFN receptor but is not induced by TLR ligands nor regulated by IRFs. (A and B) BMDMs from WT, *Ifnar1*^{−/−}, and *Ifnar2*^{−/−} C57BL/6 mice were stimulated with recombinant mouse Ifn- α 1, Ifn- β , or Ifn- ϵ (0.1 μ g/ml) for 3 hours. (A) *Irf7* and (B) *2'5'oas* expression was measured by quantitative real-time fluorescence polymerase chain reaction (qRT-PCR). Data are expressed as mean \pm SEM (error bars) of at least three independent experiments. (C) BMDMs from C57BL/6 WT mice were treated with a range of TLR ligands or transfected with Poly (I:C) and Poly (dA:dT) for 3 hours at 37°C. *Ifn- β* , *Il-6*, and *Ifn- ϵ* were measured by qRT-PCR. Data are expressed as mean \pm SEM of at least three independent experiments. (D) Luciferase reporter plasmids containing *Ifn- α* , *Ifn- β* , *p125*, or *Ifn- ϵ* were cotransfected with empty vector or IRF-3, IRF-7, or IRF-5 expression vectors into HEK293 cells. Data are expressed as mean \pm SEM. All values are means of at least three independent experiments. * P < 0.05; ** P < 0.01; *** P < 0.001; **** P < 0.0001 (unpaired Student's t test).

¹Centre for Innate Immunity and Infectious Diseases, Monash Institute of Medical Research, Monash University, Clayton, Victoria, Australia. ²Centre for Asthma and Respiratory Disease and Hunter Medical Research Institute, The University of Newcastle, Newcastle, New South Wales, Australia. ³Department of Biochemistry and Molecular Biology, Monash University, Clayton, Victoria, Australia. ⁴Robinson Institute and School of Paediatrics and Reproductive Health, University of Adelaide, South Australia, Australia. ⁵Peter MacCallum Cancer Centre, East Melbourne, Victoria, Australia. ⁶Sir Peter MacCallum Department of Oncology, The University of Melbourne, Parkville, Australia. ⁷The Ritchie Centre, Monash Institute of Medical Research, Monash University, Clayton, Victoria, Australia. ⁸Department of Obstetrics and Gynaecology, Monash University, Clayton, Victoria, Australia. ⁹Department of Ophthalmology and Department of Microbiology and Immunology, University of Oklahoma Health Sciences Center, Oklahoma City, OK, USA.

*These authors contributed equally to this work.

†To whom correspondence should be addressed. E-mail: paul.hertzog@monash.edu

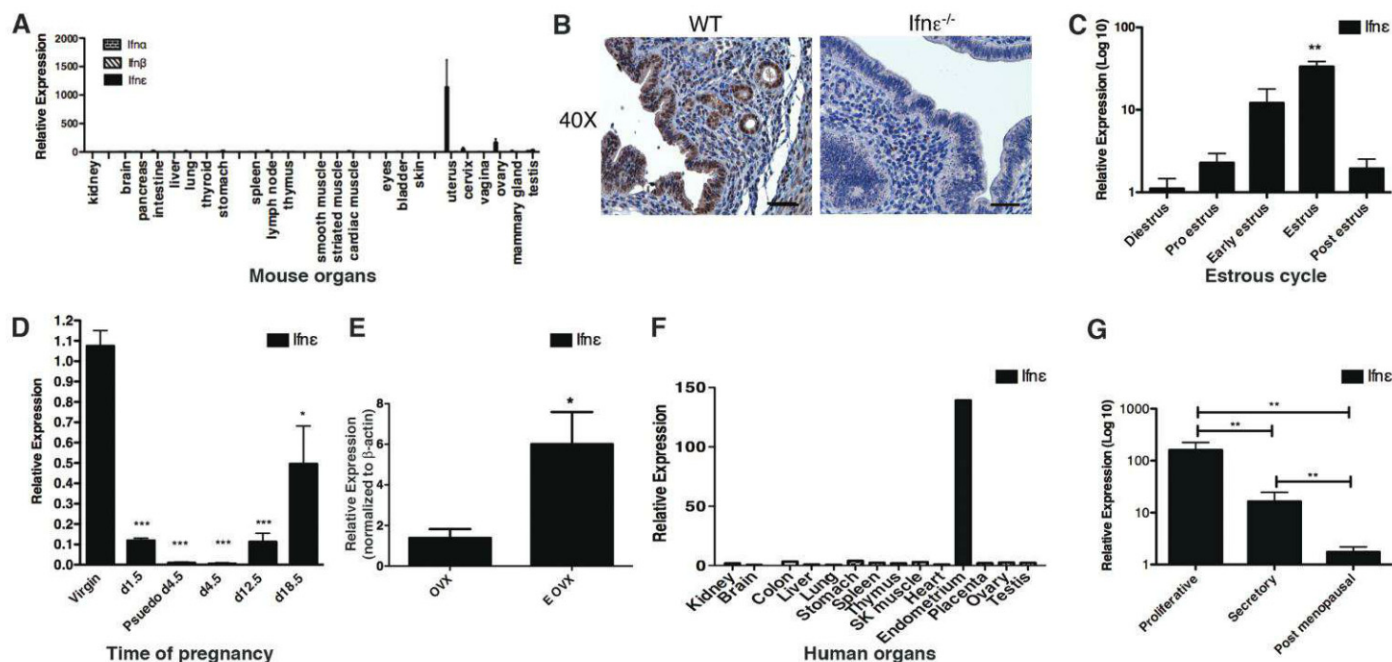


Fig. 2. Interferon- ϵ is expressed in the FRT in both mice and humans. (A) Mouse organs were harvested and *Ifn- ϵ* expression was measured by qRT-PCR, normalized to 18S RNA and presented relative to *Ifn- ϵ* expression in kidney. Data are expressed as the mean \pm SEM (error bars) of at least three individual mice. (B) Representative images showing *Ifn- ϵ* localization in uterine tissue (at estrous stage) of WT and *Ifn- ϵ* ^{-/-} C57BL/6 mice by immunohistochemistry. Scale bars, 50 μ m. These images are representative of at least five individual mice. (C and D) *Ifn- ϵ* expression was measured by qRT-PCR in mouse uterus at different stages of (C) the estrous cycle and (D) pregnancy. Data are expressed as mean \pm SEM of at least three separate experiments. (E) *Ifn- ϵ* expression was determined by qRT-PCR in ovariectomized (OVX) mice and OVX mice treated with estrogen (E OVX). Data are expressed as mean \pm SEM of at least six individual mice and are representative of at least two separate experiments. (F) A cDNA panel of human tissues was examined for *IFN- ϵ* expression by qRT-PCR, and the results were expressed relative to *IFN- ϵ* expression in the kidney. (G) Epithelial cells were isolated from endometrial samples of postmenopausal women or those at different stages of the menstrual cycle, and *IFN- ϵ* expression was measured by qRT-PCR. Values are presented relative to *IFN- ϵ* expression in the human endometrial cell line ECC-1. Data are expressed as mean \pm SEM of six individual patient samples. * P < 0.05; ** P < 0.01; *** P < 0.001 [(A to F) unpaired Student's t test, (G) Mann-Whitney U test].

tomized (OVX) mice and OVX mice treated with estrogen (E OVX). Data are expressed as mean \pm SEM of at least six individual mice and are representative of at least two separate experiments. (F) A cDNA panel of human tissues was examined for *IFN- ϵ* expression by qRT-PCR, and the results were expressed relative to *IFN- ϵ* expression in the kidney. (G) Epithelial cells were isolated from endometrial samples of postmenopausal women or those at different stages of the menstrual cycle, and *IFN- ϵ* expression was measured by qRT-PCR. Values are presented relative to *IFN- ϵ* expression in the human endometrial cell line ECC-1. Data are expressed as mean \pm SEM of six individual patient samples. * P < 0.05; ** P < 0.01; *** P < 0.001 [(A to F) unpaired Student's t test, (G) Mann-Whitney U test].

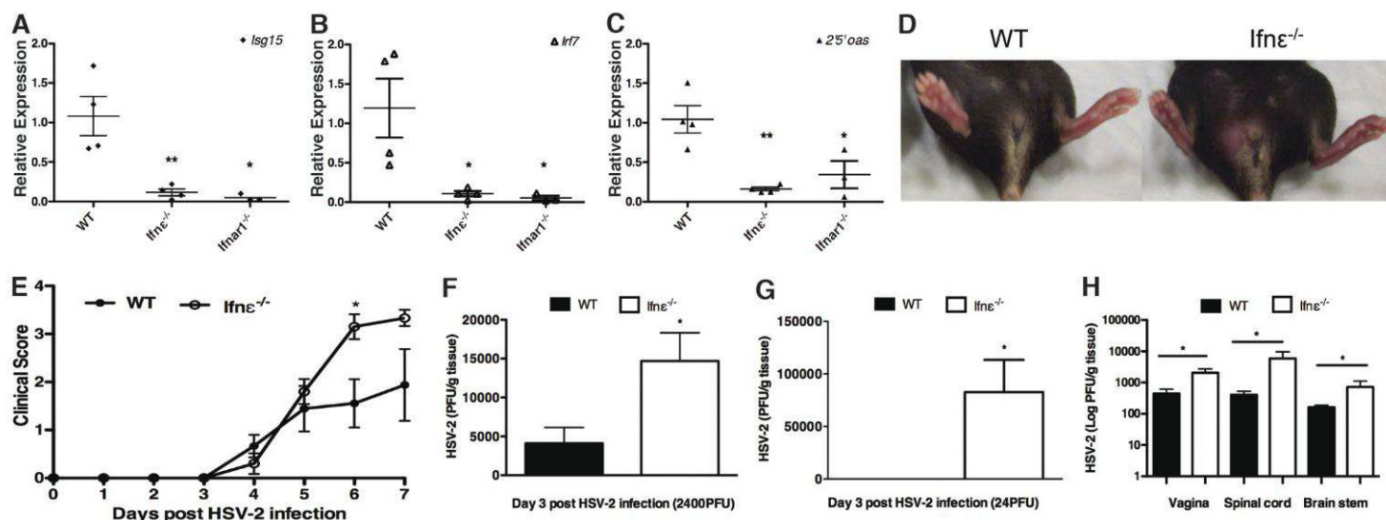


Fig. 3. *Ifn- ϵ* ^{-/-} mice are more susceptible to HSV-2 vaginal infection. (A) *Isg15*, (B) *Irf7*, and (C) *2'5'oas* expression between WT and *Ifn- ϵ* ^{-/-} C57BL/6 mice was determined by qRT-PCR. The values represent means \pm SEM (error bars) of four individual mice. (D to F and H) Mice pretreated with medroxyprogesterone acetate (Depo-Ralovera, Pfizer) at day -5 were infected with HSV-2 (D, E, H) at a level of 2400 or (F) 24 pfu per mouse on day 0. (D) Representative images demonstrating overt genital lesions, redness, and swelling in HSV-2-infected *Ifn- ϵ* ^{-/-} mice at day 7 pi; these qualities are absent in C57BL/6 WT mice. (E) Clinical scores of WT and *Ifn- ϵ* ^{-/-} C57BL/6 mice during the 7-day course of

infection. Data are means \pm SEM of five individual mice and are representative of at least three separate experiments. (F and G) HSV-2 titers (pfu) from vaginal tissue of WT and *Ifn- ϵ* ^{-/-} C57BL/6 mice infected with (F) 2400 and (G) 24 pfu, respectively, at day 3 pi were determined by titration of clarified vaginal tissue samples on Vero cell monolayers by plaque assay. Data are expressed as mean \pm SEM of five individual mice. (H) HSV-2 titers from homogenates of vaginal tissue, spinal cord, and brain stem of infected WT and *Ifn- ϵ* ^{-/-} C57BL/6 mice at day 7 pi were determined as in (F) and (G). Data are expressed as mean \pm SEM of five individual mice. * P < 0.05; ** P < 0.01 (unpaired Student's t test).

endometrium (Fig. 2F). To determine whether human *IFN-ε* was also regulated in different hormonal states, we tested epithelial cells isolated from uterine endometrium from six women in secretory or proliferative stages of the menstrual cycle or after menopause. *IFN-ε* expression was highest in the proliferative phase when estrogen levels were high and was approximately 10-fold lower in the secretory phase when estrogen levels were low and progesterone was high. *IFN-ε* levels were virtually undetectable in samples from postmenopausal women (Fig. 2G) (11). Consistent with the epithelial cell origin of this cytokine, several endometrial cancer-derived cell lines were found to express *IFN-ε* (fig. S1H).

Next, we generated *Ifn-ε*^{−/−} mice to characterize the pathophysiological functions of this gene (fig. S2, A to E, and table S1). No differences were detected in male and female fertility (fig. S3A), or in the reproductive organs from male and female mice (fig. S3B) and immune organs characterized by immunophenotyping (fig. S3, C to H).

The basal levels of *2'5'oas*, *Irf-7*, and *Isg15* were significantly reduced in uteri from *Ifn-ε*^{−/−} mice, similar to the very low levels observed in *Ifnar1*^{−/−} mice (Fig. 3, A to C), indicating that *Ifn-ε* did signal in vivo. IRG levels in other organs were the same between WT and *Ifn-ε*^{−/−} mice (fig. S3I). Furthermore, this difference in IRG levels resulting from constitutive *Ifn-ε* expres-

sion was similar in magnitude to the induction of these IRGs in WT mice that were given *Ifn-α*, *-β*, or *-ε* intravaginally (fig. S4) and to the degree of altered expression observed after *Chlamydia* or HSV-2 infection (see below). These data demonstrate that expression of *IFN-ε* in the female reproductive tract (FRT) is required for maintaining basal levels of IRGs, which play an important role in innate immunity.

To determine whether *Ifn-ε* is important in protecting the FRT from viral infection, we examined the effect of genital HSV-2 infection in *Ifn-ε*^{−/−} mice. After a sublethal dose of a clinical isolate of HSV-2 strain 186 (12), *Ifn-ε*^{−/−} mice had significantly more severe clinical scores of disease [day 6 and 7 postinfection (pi)] with severe epidermal lesions evident compared with WT mice (Fig. 3, D and E). These effects were observed at virus doses of 24 and 2400 plaque-forming units (pfu) per mouse (Fig. 3, F and G) and were consistent with elevated viral titers in infected vaginal tissues of *Ifn-ε*^{−/−} mice at day 3 pi, compared with WT animals. At the low dose of 24 pfu, *Ifn-ε* was protective, as virus was only detectable in the null mice and not in WT animals. In addition, *Ifn-ε*^{−/−} mice had significantly higher viral titers in the spinal cord and brain stem 7 days pi, consistent with either increased replication or retrograde transport of virus (Fig. 3H). Notably, there was no significant change in

the expression of *Ifn-ε* in the first 3 days after viral infection, consistent with our in vitro data showing that this gene is not pathogen induced (fig. S5A). The susceptibility of *Ifn-ε*^{−/−} was less than that of *Ifnar1*^{−/−} mice, which cannot respond to *Ifn-α*, *-β*, or *-ε* (fig. S5B). However, because *Ifn-β* and IRGs were not induced less in *Ifn-ε*^{−/−} mice, the protective effects of *Ifn-ε* in this model of a prevalent sexually transmitted infection (STI) were independent of other type I IFNs (fig. S5, C to F).

We next investigated the role of *Ifn-ε* in a murine model of FRT infection by *Chlamydia*, the most prevalent bacterial STI (13, 14). After a sublethal, intravaginal infection of WT and *Ifn-ε*^{−/−} mice with *C. muridarum* (15), *Ifn-ε*^{−/−} mice displayed more severe clinical signs of disease from 7 until 30 days pi (Fig. 4A). More bacteria were detected in vaginal swabs of *Ifn-ε*^{−/−} mice throughout the course of infection (Fig. 4B). *C. muridarum* recovery from vaginal lavage 3 days pi in WT mice had not increased from day 1 inoculum levels, but there was a 40-fold increase in the levels of bacteria in *Ifn-ε*^{−/−} mice (Fig. 4C). We also observed significantly increased levels of *Chlamydia* at 30 days pi, indicative of increased chlamydial growth in the upper FRT (uterine horns) of *Ifn-ε*^{−/−} mice compared with very low levels in WT mice (Fig. 4D). This finding in particular indicates that *Ifn-ε*^{−/−} mice are

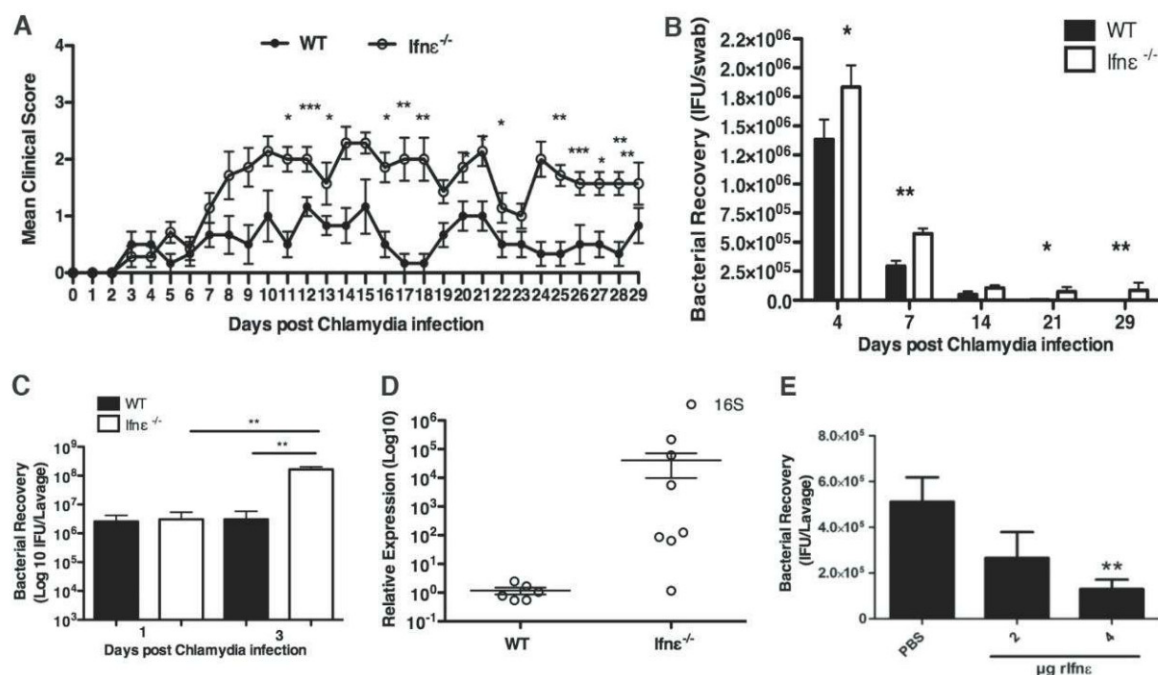


Fig. 4. *Ifn-ε*^{−/−} mice are more susceptible to *Chlamydia muridarum* vaginal infection. (A to D) Mice were pretreated with progesterone at day −7 and infected intravaginally with 5×10^4 inclusion-forming units (IFU) of *C. muridarum*. (A) Clinical scores were recorded daily for 30 days. Data are means \pm SEM (error bars) of at least six individual mice. (B) Bacterial recovery from vaginal swabs of WT and *Ifn-ε*^{−/−} C57BL/6 mice at different time points, as determined by qRT-PCR for bacterial major outer membrane protein. Data are means \pm SEM of at least six individual mice. (C) Bacterial recovery, as measured by qRT-PCR from vaginal lavage at days 1 and 3 pi.

Data are means \pm SEM of at least six individual mice. (D) Bacterial 16S RNA from the uterine horns of WT and *Ifn-ε*^{−/−} C57BL/6 mice at 30 days pi was examined by qRT-PCR. Data are means \pm SEM of at least six individual mice. (E) WT C57BL/6 mice were pretreated with progesterone at day −7 and treated intravaginally with rIfn-ε (2 or 4 μ g) 6 hours before *C. muridarum* infection. Bacterial recovery from the vaginal lavage at day 3 pi was measured by qRT-PCR. PBS, phosphate-buffered saline. Data are means \pm SEM of at least six individual mice. **P* < 0.05; ***P* < 0.01; ****P* < 0.001 (unpaired Student's *t* test).

substantially more susceptible to (and less able to clear) an ascending infection in the FRT than WT mice. Because NK cells have a protective role against this infection (16), we measured their levels at 3 days pi. Notably, both the percentage and total numbers of these cells were decreased in the uteri of *Ifn-ε*^{-/-} mice (fig. S6, A and B). Importantly, there were no changes in *Ifn-ε* RNA expression at the early or late stages of the infection (fig. S6C), consistent with our in vitro data showing that *Ifn-ε* is not regulated by PRR pathways. Furthermore, production of *Ifn-β* and IRGs was higher than the levels in WT mice (fig. S7, A to D), indicating that the protective effects of *Ifn-ε* were not solely due to priming for the production of other type I IFNs. To demonstrate that *Ifn-ε* could directly mediate protection against infection, we observed a dose-dependent reduction in bacteria (Fig. 4E), demonstrating that reconstitution of (progesterone) lowered *Ifn-ε* levels protected against this bacterial infection.

The distinct properties of IFN-ε, compared with other type I IFNs (table S2), make IFN-ε the only one that protects against *Chlamydia*, whereas the others exacerbate disease (17–20). All type I IFNs protect against HSV-2 infection (21, 22), with IFN-ε likely contributing because its constitutive expression by epithelial cells offers immediate efficacy at the site of first contact of mucosal pathogens. Interestingly, the increased susceptibility to FRT infections of women on progestagen-containing contraception (23, 24) may be explained by the lowering of *Ifn-ε* levels (fig. S8A) during progestin pretreatment that is required for all FRT infection models (25, 26). The local effect of

IFN-ε is supported by our observation that IFN-ε makes no difference in a systemic model (fig. S8, B to D). Consistent with the importance of IFN-ε in FRT immunity, IFN-ε is evolutionarily conserved in eutherian mammals, particularly in residues predicted to contact the two receptor components (fig. S9) (27). Because STIs are major global health and socioeconomic problems, the distinctive regulatory and protective properties of IFN-ε may facilitate the development of new strategies for preventing and treating STIs and, perhaps, other diseases.

References and Notes

1. S. Hervas-Stubbs *et al.*, *Clin. Cancer Res.* **17**, 2619 (2011).
2. A. Isaacs, J. Lindenmann, *Proc. R. Soc. London Ser. B Biol. Sci.* **147**, 258 (1957).
3. M. P. Hardy, C. M. Owczarek, L. S. Jermini, M. Ejdebäck, P. J. Hertzog, *Genomics* **84**, 331 (2004).
4. K. Honda, A. Takaoka, T. Taniguchi, *Immunity* **25**, 349 (2006).
5. M. Sato *et al.*, *Immunity* **13**, 539 (2000).
6. N. A. de Weerd, S. A. Samarajiwa, P. J. Hertzog, *J. Biol. Chem.* **282**, 20053 (2007).
7. L. Alexopoulou, A. C. Holt, R. Medzhitov, R. A. Flavell, *Nature* **413**, 732 (2001).
8. S. E. Doyle *et al.*, *J. Immunol.* **170**, 3565 (2003).
9. V. Hornung, E. Latz, *Nat. Rev. Immunol.* **10**, 123 (2010).
10. M. V. Patel, M. Ghosh, J. V. Fahey, C. R. Wira, *PLoS ONE* **7**, e35654 (2012).
11. L. A. Salamonsen, in *The Endometrium*, J. D. Aplin, A. T. Fazleabas, S. R. Glasser, L. C. Giudice, Eds. (Informa Healthcare, London, ed. 2, 2008), pp. 25–45.
12. M. Thapa, D. J. Carr, *J. Virol.* **83**, 9486 (2009).
13. K. W. Beagley, W. M. Huston, P. M. Hansbro, P. Timms, *Crit. Rev. Immunol.* **29**, 275 (2009).
14. World Health Organization (WHO), *Global Prevalence and Incidence of Selected Curable Sexually Transmitted Infections Overview and Estimates* (WHO, Geneva, 2001).
15. K. L. Asquith *et al.*, *PLoS Pathog.* **7**, e1001339 (2011).
16. C. T. Tseng, R. G. Rank, *Infect. Immun.* **66**, 5867 (1998).

17. A. Devitt, P. A. Lund, A. G. Morris, J. H. Pearce, *Infect. Immun.* **64**, 3951 (1996).
18. S. P. Lad, E. Y. Fukuda, J. Li, L. M. de la Maza, E. Li, *J. Immunol.* **174**, 7186 (2005).
19. U. M. Nagarajan, D. M. Ojcius, L. Stahl, R. G. Rank, T. Darville, *J. Immunol.* **175**, 450 (2005).
20. U. M. Nagarajan *et al.*, *Infect. Immun.* **76**, 4642 (2008).
21. B. A. Austin, C. M. James, P. Härle, D. J. Carr, *Biol. Proced. Online* **8**, 55 (2006).
22. C. D. Conrady, W. P. Halford, D. J. Carr, *J. Virol.* **85**, 1625 (2011).
23. J. M. Baeten *et al.*, *Am. J. Obstet. Gynecol.* **185**, 380 (2001).
24. C. C. Wang, J. K. Kreiss, M. Reilly, *J. Acquir. Immune Defic. Syndr.* **21**, 51 (1999).
25. R. P. Morrison, H. D. Caldwell, *Infect. Immun.* **70**, 2741 (2002).
26. M. B. Parr *et al.*, *Lab. Invest.* **70**, 369 (1994).
27. C. Thomas *et al.*, *Cell* **146**, 621 (2011).

Acknowledgments: We thank A. Mansell, R. Ferrero, and L. Salamonsen for their contributions; N. Bourke and S. Forster for helpful discussions and reading of the manuscript; K. Fitzgerald for reagents; and C. Berry for assistance with viral plaque assays. The data presented in this paper are tabulated in the main text and in the supplementary materials. This work was supported by funding from Australian National Health and Medical Research Council (P.J.H., N.E.M., P.M.H., J.R., C.E.G., and B.P.), the Australian Research Council (P.J.H., N.E.M., J.R.), the NIH via grant R01 AI053108 (D.J.C.), and the Victorian Government's Operational Infrastructure Support Program. P.J.H., N.E.M., K.Y.F., H.C., S.A.S., and N.D.W. hold International Patent Application number PCT/AU2011/000715, "Use of interferon epsilon in methods of diagnosis and treatment."

Supplementary Materials

www.sciencemag.org/cgi/content/full/339/6123/1088/DC1
Materials and Methods
Figs. S1 to S9
Tables S1 and S2
References (28–33)

28 November 2012; accepted 8 January 2013
10.1126/science.1233321

Spreading Depression Triggers Headache by Activating Neuronal Pannx1 Channels

Hulya Karatas,^{1,2} Sefik Evren Erdener,^{1,2} Yasemin Gursoy-Ozdemir,^{1,2} Sevdal Lule,¹ Emine Eren-Koçak,^{1,3} Zümri Duygu Sen,^{1,3} Turgay Dalkara^{1,2*}

The initial phase in the development of a migraine is still poorly understood. Here, we describe a previously unknown signaling pathway between stressed neurons and trigeminal afferents during cortical spreading depression (CSD), the putative cause of migraine aura and headache. CSD caused neuronal Pannexin1 (Pannx1) megachannel opening and caspase-1 activation followed by high-mobility group box 1 (HMGB1) release from neurons and nuclear factor κB activation in astrocytes. Suppression of this cascade abolished CSD-induced trigeminovascular activation, dural mast cell degranulation, and headache. CSD-induced neuronal megachannel opening may promote sustained activation of trigeminal afferents via parenchymal inflammatory cascades reaching glia limitans. This pathway may function to alarm an organism with headache when neurons are stressed.

There is agreement that activation of the trigeminocervical complex mediates migraine headache, whereas the brain event that initiates migraine is unclear (1–3). Cortical spreading depression (CSD) thought to cause the migraine aura may activate perivascular trigeminal nerves (4–10) by way of potassium, protons, nitric oxide (NO), arachidonic acid, and adenosine

5'-triphosphate released during CSD (3, 8, 11). However, sufficient concentrations of these mediators may not be sustained in the perivascular space for trigeminal sensitization and hours-lasting headache (10, 12) because of the glia limitans barrier and continuous cerebrospinal fluid (CSF) flow. Trigeminal meningeal nociceptors and central neurons also start firing ~14 and 25 min after CSD in

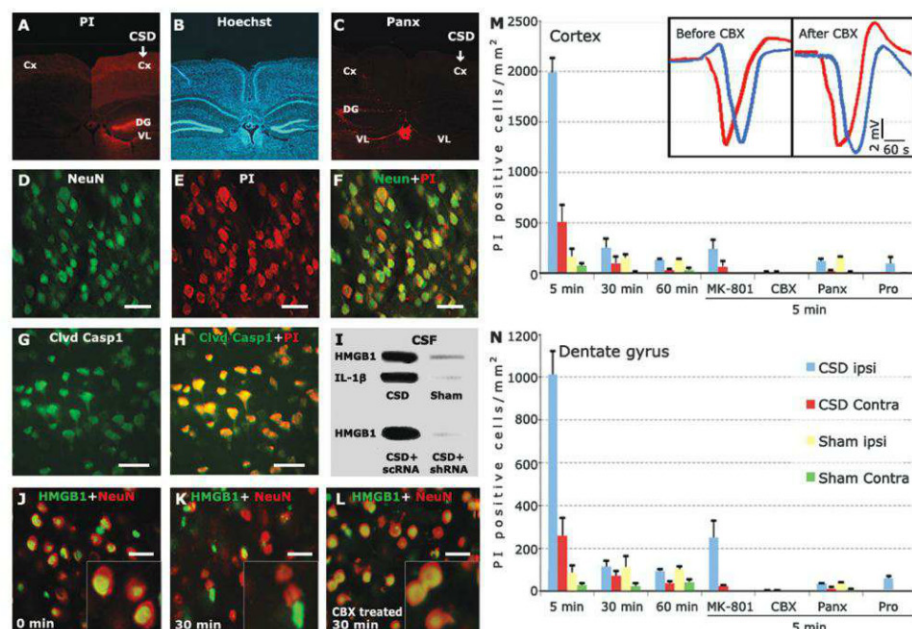
the rat (10, 13). Similarly, there is a 20- to 30-min delay between the end of the aura and the headache (14). Such time lags may be required for transduction of algogenic signals over glia limitans via inflammatory mediators. Intense depolarization and N-methyl-D-aspartate (NMDA) receptor over-activation opens neuronal Pannexin1 (Pannx1) megachannels (15–17). These conditions are present during CSD and suggest that CSD, by activating Pannx1 and downstream inflammasome formation, may trigger inflammation (17, 18). We therefore hypothesize that stress-induced Pannx1 activation may cause headache by releasing pro-inflammatory mediators such as high-mobility group box 1 (HMGB1) from neurons, which initiates a parenchymal inflammatory response, leading to sustained release of inflammatory mediators from glia limitans and, hence, prolonged trigeminal stimulation.

Propidium iodide (PI) is a membrane-impermeable fluorophore used to monitor activity as it passes through megachannels such as

¹Institute of Neurological Sciences and Psychiatry, Hacettepe University, Ankara 06100, Turkey. ²Department of Neurology, Faculty of Medicine, Hacettepe University, Ankara 06100, Turkey. ³Department of Psychiatry, Faculty of Medicine, Hacettepe University, Ankara 06100, Turkey.

*To whom correspondence should be addressed. E-mail: tdalkara@hacettepe.edu.tr

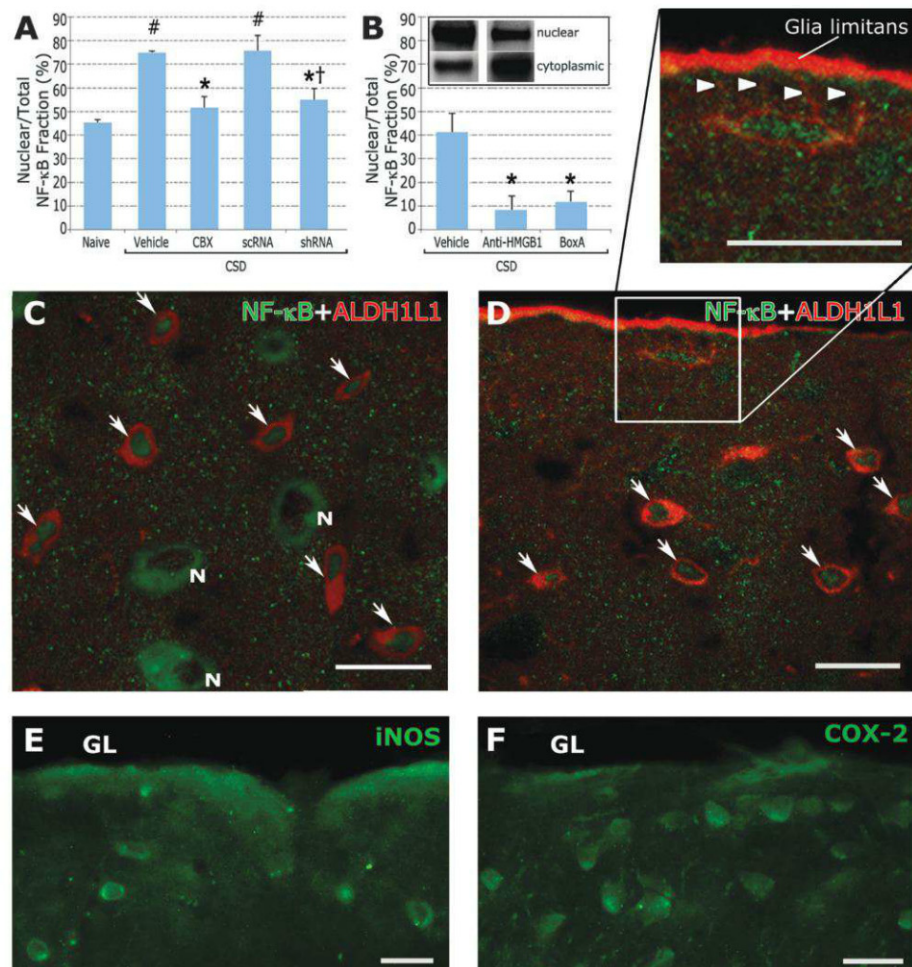
Fig. 1. CSD causes neuronal Panx1 channel opening, caspase-1 activation, and HMGB1 release. A single CSD triggered by pinprick to the intact mouse brain (A) caused PI influx (red fluorescence) to cortical (Cx) and dentate (DG) neurons, (B) identified with Hoechst-33258. PI was injected intracerebroventricularly 2 min before CSD. Non-specific labeling of the ventricular lining (VL) marked successful PI injection (low-magnification images were contrast/brightness-adjusted for better illustration). (C, M, and N) PI-influx was suppressed by Panx1 inhibitors carbenoxolone (CBX), probenecid (Pro), or 10 Panx. (D to F) PI-labeled cells were NeuN-positive neurons. (G and H) PI-positive neurons exhibited cleaved caspase-1 immunoreactivity 5 min after CSD. (I) A robust HMGB1 and IL-1 β release to CSF was detected after KCl-induced CSDs, unlike sham-operated mice. HMGB1-shRNA suppressed HMGB1 release to CSF. (J and K) Neuronal nuclei lost their HMGB1-immunopositivity 30 min after CSD, which (L) was prevented by CBX pre-treatment. Number of PI-positive neurons was maximum 5 min after CSD and disappeared in an hour in ipsi- and contralateral cortex (M) and DG (N) (error bars, SEM, 3 to 6 mice for each time points). PI-labeling was inhibited when CSD generation was suppressed by means of epidural MK-801 application (10 mM adsorbed into a cotton ball) to the pinprick site [(M) and (N)]. Panx1 inhibitors abolished PI-labeling evaluated



5 min after CSD [(M) and (N)]. CBX did not modify CSD generation and propagation (CSDs recorded with 2 electrodes 1 mm apart are shown in inset). Scale bars, 20 μ m.

5 min after CSD [(M) and (N)]. CBX did not modify CSD generation and propagation (CSDs recorded with 2 electrodes 1 mm apart are shown in inset). Scale bars, 20 μ m.

Fig. 2. CSD induces NF- κ B translocation reversed by inhibition of Panx1 channels or HMGB1. (A and B) Western blotting of cytoplasmic and nuclear brain fractions shows that CSD induces translocation of NF- κ B from cytoplasm to nucleus in cortex within 30 min. This is prevented by Panx1 channel inhibition (CBX), by silencing HMGB1 expression, BoxA, and antibody to HMGB1. Columns represent mean \pm SEM from 3 to 4 mice, $P \leq 0.05$ compared with naive (#) and vehicle-treated (*) groups. $P = 0.08$ compared with the scrambled shRNA-treated group (\dagger). Unlike groups in (A), BoxA and antibody to HMGB1 (B) were injected intracortically just before CSD without any prior injections to the brain (19); hence, they exhibited different NF- κ B levels. (C) Thirty min after CSD, astrocytes identified with ALDH1L1 immunoreactivity (red) displayed nuclear NF- κ B-immunoreactivity (green nuclei, arrows), unlike normal cytoplasmic NF- κ B immunostaining seen in neurons (N). (D) NF- κ B translocation was observed all over the cortex, including astrocytes forming (arrowheads in blown-up image) or abutting glia limitans (GL). (E and F) NF- κ B translocation was followed by COX2 and iNOS induction in astrocytes and GL. Scale bars, 20 μ m.



Panx1 (15, 19). In mouse brain in vivo, single or multiple CSDs triggered by pinprick or KCl caused PI influx to cortical and dentate neurons ($95 \pm 3\%$, mean \pm SEM, of PI-labeled cells were NeuN-positive) (Fig. 1). PI uptake was inhibited by Panx1 channel blockers carbenoxolone (CBX) [400 ng intracerebroventricularly (icv)], probenecid (60 μ g icv), 10 Panx (100 μ M intracortical), or Panx1-small interfering RNA (siRNA) (Fig. 1, M and N, and fig. S1) (19). Vehicle alone or nonsilencing siRNA had no effect. CBX and 10 Panx did not affect CSD generation and propagation, suggesting that prevention of PI uptake was not caused by CSD suppression (Fig. 1). No PI uptake was observed in astrocytes (fig. S2A). PI labeling was maximal 5 min after CSD and disappeared in an hour, possibly because of active extrusion of PI from live cells in vivo. PI uptake was not caused by intracerebroventricular injection (19) because it could be inhibited when CSD generation was suppressed by epidural MK-801 application to the pinprick site. During CSD, cells did not take up FITC-dextran-70S, which is also membrane impermeable but too large to pass through mega-

channels, indicating that PI influx was not due to osmotic rupture of the plasma membrane (additional control experiments are available in the supplementary text).

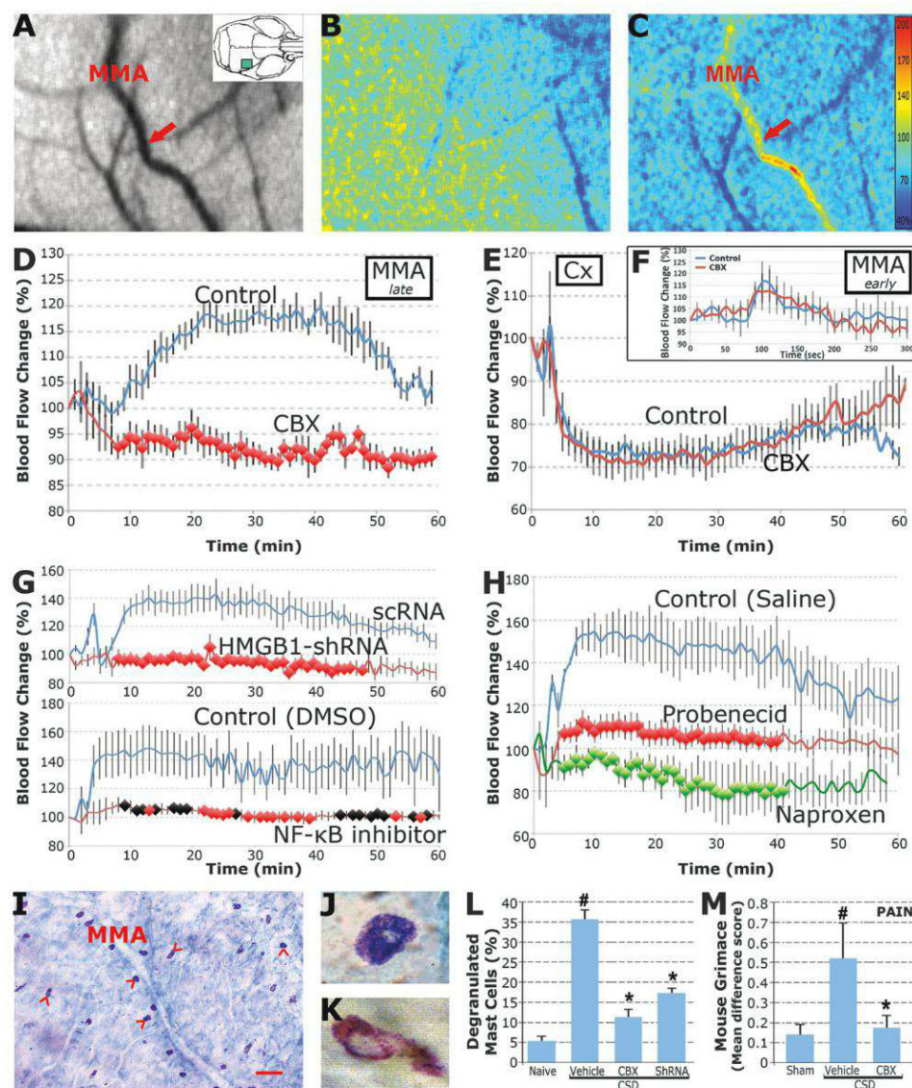
Caspase-1 was activated in $99.2 \pm 0.2\%$ of PI-positive neurons 5 min after CSD (Fig. 1H). Caspase-1 activation initiates inflammation by releasing HMGB1 and interleukin-1 β (IL-1 β) (17, 18, 20). Indeed, CSF collected from lateral ventricles of mice subjected to CSDs for 1 hour showed a 10-fold HMGB1 and 24-fold IL-1 β increase in Western blots (Fig. 1I). HMGB1-short hairpin RNA (shRNA) suppressed HMGB1 release to CSF (19) (Fig. 1I and fig. S3). Double-staining of brain sections illustrated that $88.0 \pm 0.1\%$ and $52 \pm 4\%$ of neurons were HMGB1-positive 5 and 30 min after a single CSD, although all neuronal nuclei were HMGB1-positive without CSD (Fig. 1, J and K). CBX abolished cleaved caspase-1 immunoreactivity and HMGB1 translocation in addition to inhibiting PI-positivity (Fig. 1, L to N).

CSD also induced nuclear factor κ B (NF- κ B) activation; most astrocytes ($82 \pm 6\%$) exhibited

nuclear NF- κ B translocation 30 min after CSD (Fig. 2). CBX inhibited NF- κ B translocation, suggesting that the signal leading to NF- κ B translocation was initiated by the opening of Panx1 channels and release of HMGB1 (Fig. 2A and figs. S2B and S4). Indeed, NF- κ B translocation was also inhibited with neutralizing antibody to HMGB1; BoxA, a fragment of HMGB1 with antagonistic activity; or HMGB1-shRNA (Fig. 2 and fig. S2C) (19). Astrocytes forming glia limitans also showed nuclear NF- κ B translocation followed by cyclooxygenase-2 (COX2) and inducible nitric oxide synthase (iNOS) induction after CSD, which can provide the sustained inflammatory mediator release to subarachnoid space (Fig. 2, C to F).

As reported in the rat (8), CSD induced an early, brief (21 ± 1 s) flow increase followed by a late (peak latency; 21 ± 2 min) but sustained (51 ± 3 min) blood flow elevation in ipsilateral middle meningeal artery (MMA) in mice (Fig. 3). CSD-induced late MMA dilation, which is initiated by activation of the trigeminal nerves around pial vessels (8), was completely inhibited with CBX (Fig. 3D), suggesting that Panx1 channel opening

Fig. 3. Inhibition of Panx1 channels or inflammatory mediators suppresses trigeminovascular activation. (A) Speckle contrast images of the MMA and cortex were captured through thinned skull (inset, green rectangular area) before CSD. Color bar in (C) indicates the relative blood flow change to baseline. (B) The relative blood flow image obtained 2 min after pinprick-induced CSD shows the early cortical oligemia (blue) spreading from anterior to posterior. (C) Twenty-five min after CSD, there is selective flow increase in the MMA (red arrow), whereas the cortex is still hypoperfused. (D and E) The time course of blood flow changes in the ipsilateral MMA and cortex after CSD (vertical bars \pm SEM). Late blood flow elevation in MMA was inhibited with CBX. CBX did not affect cortical blood flow (E) or early and brief MMA flow increase, which (F) can be correctly displayed only with an expanded time scale (19). (G and H) CSD-induced late MMA flow increase was also suppressed by HMGB1-shRNA, NF- κ B inhibitor, probenecid, and naproxen. Diamonds indicate significant difference ($P < 0.05$) as compared with corresponding controls (black diamonds; $P < 0.07$). CBX treatment and HMGB1 silencing also inhibited CSD-induced dural MAST cell degranulation, another manifestation of the trigeminovascular activation. (I) The dura with mast cells concentrated along the course of MMA. Scale bar, 100 μ m. (J and K) Examples of a resting and a degranulated mast cell, respectively. (L) The percentage of mast cells degranulated 30 min after CSD in ipsilateral dura. $P < 0.05$ compared with naive (#) and vehicle-treated (*) groups. (M) CSD-induced pain was assessed by means of mouse grimace scale. Mean difference scores from the baseline show that repeated CSDs induced by a KCl pellet over the dura caused pain-related mimics, which was significantly suppressed by CBX pretreatment. In the sham group, saline was applied over the dura.



and downstream inflammatory cascade play a role in trigeminal activation. The effect of CBX was not due to a direct vascular action or blockade of gap junctions because CSD-induced CBF changes, early MMA dilation, and Ca^{+2} rise in astrocytic syncytium were not altered by CBX (Fig. 3, E and F, and fig. S5) (19). Interrupting this signaling cascade with another Panx1 inhibitor, probenecid or HMGB1-shRNA, or NF- κ B activation inhibitor 4-methyl-N1-(3-phenylpropyl) benzene-1,2-diamine suppressed the late MMA dilation (Fig. 3, G and H). Naproxen (40 mg/kg intraperitoneally), a prostaglandin synthase inhibitor, also suppressed the MMA response. Moreover, CSD-induced dural mast cell degranulation, another manifestation of the trigeminal activation (21, 22), was significantly reduced by CBX and HMGB1-shRNA (Fig. 3, I to L). Last, we assessed the headache-like behavior induced by repeated CSDs (which also induced PI influx and nuclear NF- κ B translocation) (19) with a method based on scoring facial grimace (23). Placement of a KCl-pellet over dura in freely moving mice caused pain-related mimics unlike saline-applied, sham-operated mice. CSD-induced pain was reversed by means of CBX treatment (Fig. 3M).

These data show that CSD opens neuronal Panx1 channels as reported during in vitro ischemia, NMDA over-activation, and aberrant bursting (17). Activation of Panx1 by cellular stressors such as excess potassium or glutamate stimulates the inflammasome complex, subsequent caspase-1 activation, and IL-1 β production (17, 18), suggesting that Panx1 megachannels may play a role as a reporter linking neuronal stress to inflammatory response. Similarly, CSD induced caspase-1 activation and HMGB1 release from neurons whose Panx1 channels were activated.

HMGB1 is a member of the alarmin family, which mediates the communication between injured and surrounding cells (24). HMGB1 is passively released from necrotic cells and actively secreted by cells under distress (25, 26). HMGB1 behaves like a cytokine and promotes inflammation when released (27, 28). Therefore, HMGB1 and IL-1 β released during CSD may take part in initiation of the inflammatory response. Subsequent NF- κ B activation in astrocytes may induce formation of cytokines, prostanoids, and inducible NO synthase-derived NO (as suggested by inhibition of MMA response by naproxen and CSD-induced COX2 and iNOS expression in glia limitans), which may be released to the subarachnoid space via glia limitans and, hence, stimulate trigeminal nerve endings around pial vessels (fig. S6). By promoting sustained headache, HMGB1 may thus serve to alarm the organism that the brain parenchyma has been stressed by CSD or CSD-like events. HMGB1 is most likely not the only mediator playing this role; other cytokines as well as cells (such as microglia) may also take part along the course of inflammatory response (29, 30). In contrast to mediators such as potassium and protons that are transiently released during CSD, activation of the parenchymal in-

flammatory pathways may provide the sustained stimulus required for sensitization of trigeminal nerve endings and lasting pain as suggested by suppression of long-lasting MMA vasodilatation, mast cell degranulation, and importantly, headache-like behavior by interrupting the inflammatory cascade at one of the steps (11).

We propose a previously unknown link between a noxious intrinsic brain event and activation of the trigeminal pain fibers, involving the opening of Panx1 megachannels on stressed neurons, subsequent activation of the inflammatory pathways, and transduction of this signal to the trigeminal nerves around pial vessels (fig. S6).

References and Notes

1. M. A. Moskowitz, *Headache* **48**, 688 (2008).
2. P. J. Goadsby, *Trends Mol. Med.* **13**, 39 (2007).
3. J. Olesen, R. Burstein, M. Ashina, P. Tfelt-Hansen, *Lancet Neurol.* **8**, 679 (2009).
4. M. A. Moskowitz, *Ann. Neurol.* **16**, 157 (1984).
5. M. A. Moskowitz, K. Nozaki, R. P. Kraig, *J. Neurosci.* **13**, 1167 (1993).
6. M. Lauritzen, *Brain* **117**, 199 (1994).
7. T. Dalkara, N. T. Zervas, M. A. Moskowitz, *Neurol. Sci.* **27**, (Suppl. 2), S86 (2006).
8. H. Bolay et al., *Nat. Med.* **8**, 136 (2002).
9. N. Hadjikhani et al., *Proc. Natl. Acad. Sci. U.S.A.* **98**, 4687 (2001).
10. X. Zhang et al., *J. Neurosci.* **30**, 8807 (2010).
11. D. Levy, *Curr. Pain Headache Rep.* **16**, 270 (2012).
12. A. M. Strassman, S. A. Raymond, R. Burstein, *Nature* **384**, 560 (1996).
13. X. Zhang et al., *Ann. Neurol.* **69**, 855 (2011).
14. J. Olesen et al., *Ann. Neurol.* **28**, 791 (1990).
15. R. J. Thompson, N. Zhou, B. A. MacVicar, *Science* **312**, 924 (2006).
16. R. J. Thompson et al., *Science* **322**, 1555 (2008).
17. B. A. MacVicar, R. J. Thompson, *Trends Neurosci.* **33**, 93 (2010).
18. W. R. Silverman et al., *J. Biol. Chem.* **284**, 18143 (2009).
19. Materials and methods are available as supplementary materials on Science Online.
20. M. Lamkanfi et al., *J. Immunol.* **185**, 4385 (2010).
21. S. Markowitz, K. Saito, M. G. Buzzi, M. A. Moskowitz, *Brain Res.* **477**, 157 (1989).
22. D. Levy, R. Burstein, V. Kainz, M. Jakubowski, A. M. Strassman, *Pain* **130**, 166 (2007).
23. D. J. Langford et al., *Nat. Methods* **7**, 447 (2010).
24. D. S. Pisetsky, H. Erlandsson-Harris, U. Andersson, *Arthritis Res. Ther.* **10**, 209 (2008).
25. P. Scaffidi, T. Misteli, M. E. Bianchi, *Nature* **418**, 191 (2002).
26. S. Müller, L. Ronfani, M. E. Bianchi, *J. Intern. Med.* **255**, 332 (2004).
27. G. Faraco et al., *J. Neurochem.* **103**, 590 (2007).
28. M. Pedrazzi et al., *J. Immunol.* **179**, 8525 (2007).
29. P. E. Kunkler, R. E. Hulse, R. P. Kraig, *J. Cereb. Blood Flow Metab.* **24**, 829 (2004).
30. S. Jander, M. Schroeter, O. Peters, O. W. Witte, G. Stoll, *J. Cereb. Blood Flow Metab.* **21**, 218 (2001).

Acknowledgments: We are grateful to M. A. Moskowitz for helpful discussions, K. Kilic and E. Lule for their expert help with the figures, and to A. Can for his help with confocal microscopy. This work was supported by the Turkish Academy of Sciences (T.D.), Hacettepe University Research Fund 08-D07-101-011 (Y.G.-O.), and the Brain Research Association (H.K.).

Supplementary Materials

www.sciencemag.org/cgi/content/full/339/6123/1092/DC1
Materials and Methods
Supplementary Text
Figs. S1 to S5
Table S1
References (31–42)

23 October 2012; accepted 30 January 2013
10.1126/science.1231897

Stress in Puberty Unmasks Latent Neuropathological Consequences of Prenatal Immune Activation in Mice

Sandra Giovanoli,¹ Harald Engler,² Andrea Engler,² Juliet Richetto,^{3,4} Mareike Voget,^{5,6} Roman Willi,⁷ Christine Winter,⁶ Marco A. Riva,^{3,4} Preben B. Mortensen,^{8,9} Manfred Schedlowski,² Urs Meyer^{1*}

Prenatal infection and exposure to traumatizing experiences during peripuberty have each been associated with increased risk for neuropsychiatric disorders. Evidence is lacking for the cumulative impact of such prenatal and postnatal environmental challenges on brain functions and vulnerability to psychiatric disease. Here, we show in a translational mouse model that combined exposure to prenatal immune challenge and peripubertal stress induces synergistic pathological effects on adult behavioral functions and neurochemistry. We further demonstrate that the prenatal insult markedly increases the vulnerability of the pubescent offspring to brain immune changes in response to stress. Our findings reveal interactions between two adverse environmental factors that have individually been associated with neuropsychiatric disease and support theories that mental illnesses with delayed onsets involve multiple environmental hits.

Prenatal maternal infection and postnatal exposure to psychological trauma are two environmental risk factors for developmental psychiatric disorders, including autism, schizophrenia, and bipolar disorder (1–4). In spite of their relatively frequent occurrence (5–7), both factors seem to have rather modest effect sizes

in large populations (4, 8, 9). For example, the global incidence of schizophrenia after influenza pandemics only increases marginally (relative risk ratios of 1 to 2.5) even though 20 to 50% of the general population is typically infected during influenza pandemics (9, 10). It has therefore been proposed that developmental stressors, such as

infection or traumatizing experiences, may unfold their neuropathological impact primarily in genetically predisposed subjects (11). Another feasible scenario is that initial exposure to a prenatal environmental insult, such as infection, can render the offspring more vulnerable to the pathological effects of a second postnatal stimulus, such as stress (12, 13). However, this hypothesis still awaits direct verification. We therefore tested if stress in puberty has the potential to unmask latent psychopathology in neurodevelopmentally vulnerable subjects with prenatal infectious histories.

We compared the consequences of prenatal immune activation with or without additional postnatal stress challenge in mice (fig. S1 and supplementary methods). Prenatal immune activation was induced by the viral mimetic polyriboinosinic-polyribocytidilic acid [poly(I:C)], a synthetic analog of double-stranded RNA that induces a cytokine-associated, viral-like acute-phase response (14). We used a low dose of poly(I:C) [1 mg/kg, administered intravenously on gestation day 9 (GD9)] to mimic physiologically relevant and transient cytokine elevations (fig. S2) (14). Offspring born to poly(I:C)-exposed or control mothers were then left undisturbed or exposed to variable and unpredictable stress during peripubertal development, a maturational period known to be highly sensitive to the disrupting effects of traumatizing events relevant to psychosis-related disease (15, 16). The stress protocol included five distinct stressors: (i) electric foot shock, (ii) restraint stress, (iii) swimming stress, (iv) water deprivation, or (v) repeated home cage changes, applied on alternate days between postnatal days (PNDs) 30 and 40 (fig. S1 and supplementary methods).

We assessed the effects of the double-hit protocol on adult (PND 70 to 100) brain functions using behavioral tests relevant to translational models of neuropsychiatric disease (14) (supplementary methods and tables S1 to S19). Stress exposure increased anxiety-like behavior in the elevated plus maze test independently of the prenatal immunological manipulation (Fig. 1A), which suggests that peripubertal offspring with a prenatal infectious history do not differ from prenatal controls in the development of stress-

induced anxiety-like abnormalities. We further revealed independent effects of immune challenge and stress in the disruption of selective associative learning as measured by the paradigm of latent inhibition (LI): Nonstressed control offspring displayed a robust LI effect in the conditioned active avoidance paradigm (Fig. 1B). This LI effect arising from repeated preexposures to the conditioned stimulus before conditioning was fully abolished in all other groups (Fig. 1B). Prenatal immune activation and peripubertal stress caused synergistic effects in the development of sensorimotor gating deficiency, as assessed by the paradigm of prepulse inhibition (PPI) of the acoustic startle reflex (Fig. 1C), as well as in the precipitation of behavioral hypersensitivity to the psychotomimetic drugs amphetamine (AMPH) (Fig. 1D and fig. S3A) and dizocilpine (MK-801) (Fig. 1E and fig. S3B). Neither immune activation alone nor stress alone affected sensorimotor gating and psychotomimetic drug sensitivity. Abnormalities in these domains became evident only after combined exposure to the two environmental factors.

We further evaluated the postnatal onset of the identified behavioral abnormalities in our environmental double-hit model. With the exception of anxiety-related behavior, none of the other behavioral functions were affected at peripubertal age (PND 41 to 45) (Fig. 2 and fig. S4). Hence, the emergence of multiple behavioral dysfunctions such as LI deficiency, PPI attention, and psychotomimetic drug hypersensitivity in singly or doubly challenged offspring are dependent on postpubertal maturational processes, which, in turn, is consistent with the clinical course of mental illnesses with delayed onsets, including schizophrenia and bipolar disorder (17). We also revealed that a later application of stress in adolescence, at PND 50 to 60, did not elicit the interaction with prenatal immune activation (fig. S5). The findings emphasize that the precise timing of postnatal stress is critical for the interaction with the prenatal immune challenge.

The adult behavioral abnormalities emerging after prenatal immune activation and peripubertal stress exposure are unlikely to be associated with

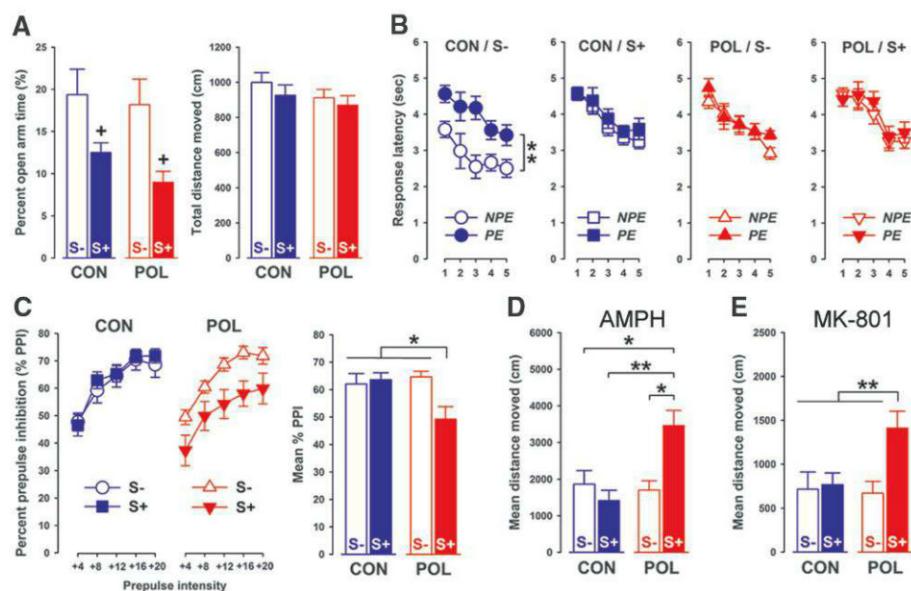


Fig. 1. Prenatal immune activation and peripubertal stress cause independent and synergistic pathological effects on adult behavioral functions. (A) Adult mice subjected to peripubertal stress (S+) display enhanced anxiety-like behavior in the elevated plus maze test (as indexed by the reduced time spent on the open arms) compared with nonstressed (S-) offspring regardless of the prenatal conditions [CON, vehicle control; POL, poly(I:C)]; $*P < 0.05$, main effect of peripubertal stress. $N = 16$ to 19 per group. (B) Response latencies in nonpreexposed (NPE) and CS-preexposed (PE) subjects as a function of successive 10-trial blocks in the LI test with a conditioned active avoidance procedure. The LI effect is present in CON/S- subjects ($**P < 0.01$) but is completely disrupted by prenatal immune activation alone (POL/S-), peripubertal stress alone (CON/S+), or their combination (POL/S+). NPE, $N = 7$ to 9 per group; PE, $N = 7$ to 10 per group. (C) Sensorimotor gating as assessed by PPI of the acoustic startle reflex. (Left) % PPI as a function of increasing prepulse intensities (dB above background of 65 dB); (right) the mean % PPI across all prepulse levels. $*P < 0.05$, reduction of % PPI in POL/S+ animals relative to all other groups. $N = 16$ to 19 per group. (D) The mean distance moved in a standard open-field arena during a 90-min period after administration of AMPH [2.5 mg/kg, intraperitoneally (i.p.)]. $*P < 0.05$ and $**P < 0.01$, increase in AMPH-induced activity displayed by POL/S+. $N = 8$ to 10 per group. (E) The mean distance moved in the open field during a 90-min period after administration of MK-801 (0.15 mg/kg, i.p.). $**P < 0.01$, increase in MK-801-induced activity displayed by POL/S+ compared with all other groups, post hoc group comparisons. $N = 8$ per group. All data are means \pm SEM.

¹Physiology and Behavior Laboratory, Swiss Federal Institute of Technology (ETH) Zurich, 8603 Schwerzenbach, Switzerland.

²Institute of Medical Psychology and Behavioral Immunobiology, University Hospital Essen, University of Duisburg-Essen, 45122 Essen, Germany. ³Center of Neuropharmacology, Department of Pharmacological Sciences, Università degli Studi di Milano, 20133 Milan, Italy. ⁴Center of Excellence on Neurodegenerative Diseases, Department of Pharmacological and Biomolecular Sciences, Università degli Studi di Milano, 20133 Milan, Italy.

⁵International Graduate Program Medical Neurosciences, Charité Universitätsmedizin Berlin, 10117 Berlin, Germany. ⁶Department of Psychiatry, Technical University Dresden, 01062 Dresden, Germany. ⁷Neuroscience Discovery, F. Hoffmann–La Roche Ltd., 4070 Basel, Switzerland. ⁸National Centre for Register-Based Research, Aarhus University, 8000 Aarhus C, Denmark. ⁹Lundbeck Foundation Initiative for Integrative Psychiatric Research, iPSYCH, 8000 Aarhus, Denmark.

*To whom correspondence should be addressed. E-mail: urmeyer@ethz.ch

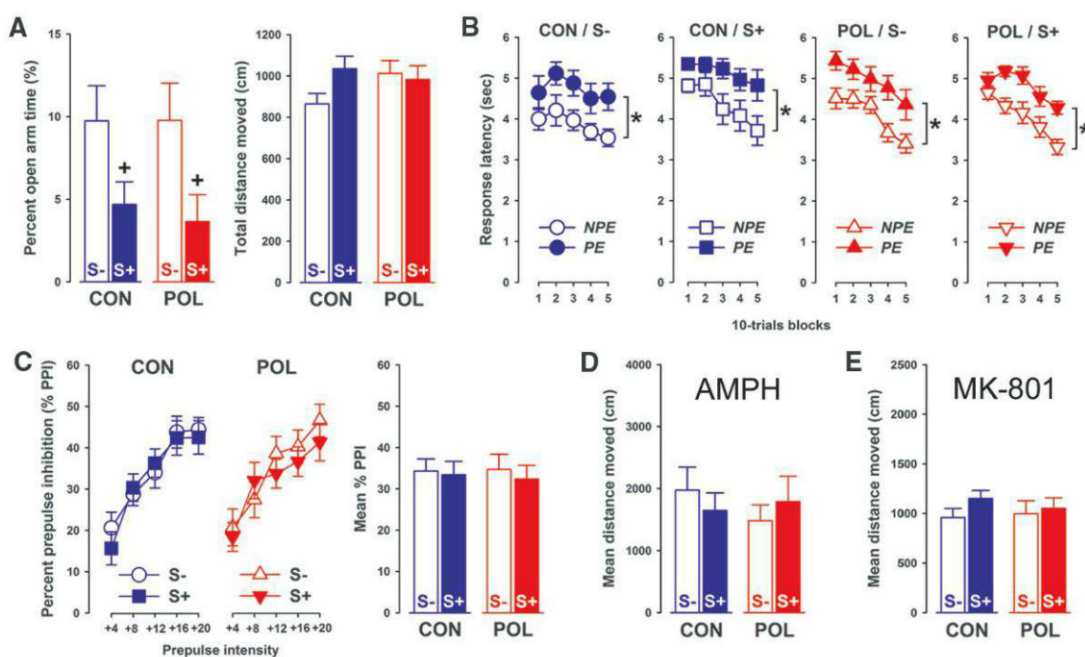
changes in the hypothalamus-pituitary-adrenal (HPA) stress-response system: Neither single nor combined exposure to the environmental adversities affected basal plasma levels of corticosterone (CORT), the main effector hormone of the HPA axis (fig. S6). The developmental stressors also did not affect CORT secretion after acute stress reexposure in adulthood (fig. S6). However, our high-performance liquid chromatography analyses identified brain region-specific neurochemical changes in adult mice exposed to prenatal immune activation and/or peripubertal stress: Prenatal immune activation was sufficient to increase the levels of dopamine (DA) in the

nucleus accumbens (NAc) independently of post-natal stress (Fig. 3A), and stress exposure decreased the content of serotonin (5-HT) in the medial prefrontal cortex (PFC) regardless of the prenatal history (Fig. 3B). It intrigued us that enhanced DA levels in the hippocampus (HPC) were only manifest after combined exposure to prenatal immune challenge and peripubertal stress (Fig. 3A); this highlighted synergistic effects between the two adverse events in the precipitation of adult hippocampal DA imbalances.

Prenatal immune activation (at high intensity) and chronic stress exposure have individually been linked to the development of immune alter-

tations in the brain and periphery (18–20). Here, we elucidated whether initial exposure to prenatal immune challenge could change the offspring's neuroimmunological responses to peripubertal stress. Two brain areas of primary interest were selected, namely, the HPC (including CA1 to CA3 subregions and dentate gyrus) and the PFC (including anterior cingulate, prelimbic, and infralimbic cortices). These brain regions are highly sensitive to chronic stress exposure (21) and show neuroanatomical abnormalities after intense prenatal immune challenge, including CNS immune changes (19). We also included a cortical control region (secondary motor cortex, MC) that is

Fig. 2. Short-term effects of single or combined exposure to prenatal immune activation and peripubertal stress on behavioral functions in pubescence. **(A)** Peripubertal mice subjected to stress in puberty (S+) display enhanced anxiety-like behavior in the elevated plus maze test (as indexed by the reduced time spent on the open arms) compared with nonstressed (S-) offspring regardless of the prenatal conditions; * $P < 0.05$, main effect of peripubertal stress. $N = 13$ to 15 per group. **(B)** Response latencies in NPE and PE subjects as a function of successive 10-trial blocks in the LI test with a conditioned active avoidance procedure. * $P < 0.05$, main effect of CS preexposure (LI) in all groups. NPE, $N = 9$ per group; PE, $N = 9$ to 10 per group. **(C)** Sensorimotor gating as assessed by PPI of the acoustic startle reflex. (Left) % PPI as a function of increasing prepulse intensities (dB above background of 65 dB); (right) the mean % PPI across all prepulse levels. $N = 13$ to 15 per group. **(D)** The mean distance moved in a standard open-field arena during a 90-min period



after administration of AMPH (2.5 mg/kg, i.p.). $N = 12$ to 13 per group. **(E)** The mean distance moved in the open field during a 90-min period after administration of MK-801 (0.15 mg/kg, i.p.). $N = 10$ to 11 per group. All data are means \pm SEM.

after administration of AMPH (2.5 mg/kg, i.p.). $N = 12$ to 13 per group. **(E)** The mean distance moved in the open field during a 90-min period after administration of MK-801 (0.15 mg/kg, i.p.). $N = 10$ to 11 per group. All data are means \pm SEM.

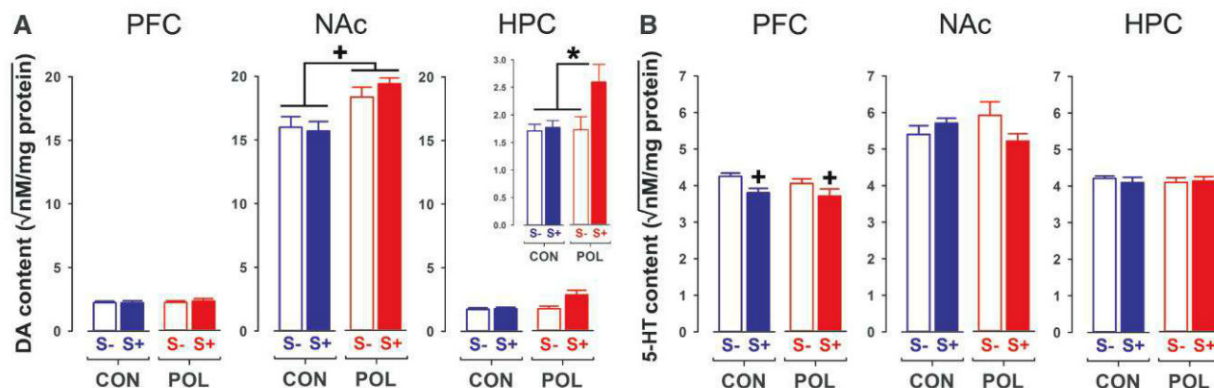


Fig. 3. Neurochemical parameters in adult offspring exposed to single or combined prenatal immune activation and peripubertal stress. **(A)** DA contents (nM/mg protein, square root-transformed) in the medial PFC, NAc, and HPC of adult (PND 70) offspring under the conditions described above. * $P < 0.05$, main effect of prenatal immune activation; * $P < 0.05$,

increase in HPC DA levels in POL/S+ mice relative to all other groups. $N = 8$ to 11 per group. **(B)** 5-HT contents (nM/mg protein, square root-transformed) in the PFC, NAc, and HPC of groups of adult mice. * $P < 0.05$, main effect of stress exposure. $N = 8$ to 11 per group. All data are means \pm SEM.

largely insensitive to neuronal and immunological adaptations after chronic stress.

We first used immunohistochemical techniques to study the activation of microglia, a population of immunocompetent cells in the CNS (22). Unbiased stereological estimations of microglia immunoreactive for the calcium-binding protein Iba1 revealed that peripubertal stress only led to a ~5% increase in total microglia numbers in the HPC at the adult stage (PND 70), without affecting microglia morphology (fig. S7). Neither single nor combined exposure to prenatal immune activation and stress altered the expression of CD68 (fig. S8), a cellular marker typically expressed by activated microglia in the CNS (22). Likewise, the two environmental factors did not change the hippocampal levels of the inflammatory molecules interleukin-1 β (IL-1 β), tumor

necrosis factor- α (TNF- α), and prostaglandin E₂ (PGE₂) in adulthood (fig. S8). Thus, single or combined exposure to prenatal immune activation and peripubertal stress exert only a minimal long-term impact on microglia cells and induce no overt changes in the central and peripheral secretion of prototypical inflammatory factors.

However, we revealed that the prenatal insult markedly increased the offspring's vulnerability to stress-induced neuroimmunological changes at peripubertal age (PND 41): Combined immune activation and stress led to a 2.5- to 3-fold increase in hippocampal (Fig. 4, B to D) and prefrontal (fig. S9, B to D) expression of markers characteristic of activated microglia (CD68 and CD11b) at PND 41. No such changes were found in the MC control region (fig. S10, B and C). The

hippocampal microglia response was further accompanied by the presence of elevated levels of the proinflammatory cytokines IL-1 β and TNF- α (Fig. 4E) but not with plasma changes in inflammatory markers or the stress hormone CORT (fig. S11). The neuroimmunological effects of combined exposure to the two environmental insults thus appear to be localized in stress-sensitive brain areas, such as the HPC and PFC, and are unlikely to be associated with functional changes in the HPA axis. Single or combined exposure to immune activation and stress also did not affect the number or activation status of astrocytes in PND 41 mice (fig. S13), which suggests that the two environmental challenges largely spared astroglial functions at peripubertal age.

We performed additional molecular analyses to explore whether the transient microglia changes

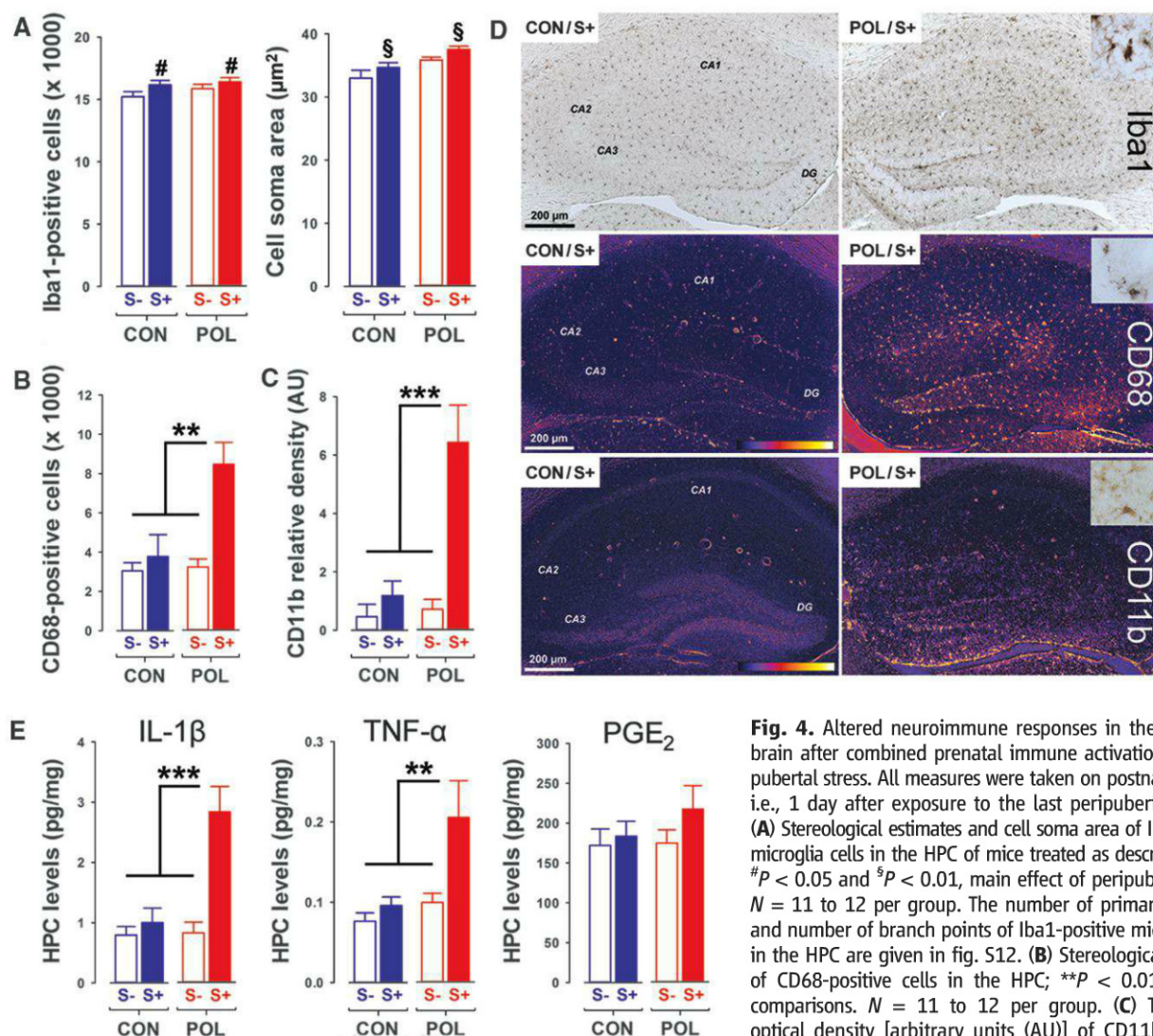


Fig. 4. Altered neuroimmune responses in the pubescent brain after combined prenatal immune activation and peripubertal stress. All measures were taken on postnatal day 41, i.e., 1 day after exposure to the last peripubertal stressor. (A) Stereological estimates and cell soma area of Iba1-positive microglia cells in the HPC of mice treated as described above. #*P* < 0.05 and §*P* < 0.01, main effect of peripubertal stress. *N* = 11 to 12 per group. The number of primary processes and number of branch points of Iba1-positive microglia cells in the HPC are given in fig. S12. (B) Stereological estimates of CD68-positive cells in the HPC; ***P* < 0.01, post hoc comparisons. *N* = 11 to 12 per group. (C) The relative optical density [arbitrary units (AU)] of CD11b immunoreactivity in the HPC; ****P* < 0.001, post hoc comparisons. *N* = 11 to 12 per group. (D) Color-coded coronal brain sections of representative CON/S+ and POL/S+ offspring at the level of the HPC [CA1 to CA3 regions and dentate gyrus (DG) are highlighted] stained with antibodies against Iba1, CD68, or CD11b. Insets are at higher magnification. In color-coded sections (CD68 and CD11b), the strongest staining intensities are yellow; the background is represented in dark purple (color scale bar). (E) Contents of IL-1 β , TNF- α , and PGE₂ in the HPC measured by using particle-based flow cytometry; ***P* < 0.01 and ****P* < 0.001, post hoc comparisons. *N* = 10 to 12 per group. HPC levels of IL-6 and IL-10 protein were below detection limits. All data are means \pm SEM.

in peripuberty would be associated with dysfunctional neuron-microglia inhibitory signaling, which, under nonpathological conditions, aims to restrain microglia from activation (23). Besides other signaling pairs, contact-dependent neuron-microglia inhibitory signaling is governed by CD200-CD200 receptor (CD200R) and CD47-CD172a interactions, in which CD200 and CD47 are primarily expressed by neurons, and CD200R and CD172a by microglia (23). Previous investigations in rats have shown that exposure to severe stress impairs the CD200 expression in the HPC (20). Our real-time polymerase chain reaction analyses of these molecules demonstrated that exposure to an acute stressor was sufficient to severely impair hippocampal and prefrontal expression of CD200, CD200R, and CD47 specifically in prenatally immune-challenged animals (fig. S14). Again, these effects emerged without any group differences in plasma CORT secretion at basal conditions or after stress, which suggested that the observed changes in contact-dependent neuron-microglia inhibitory signaling are unlikely to be attributable to possible alterations in CORT-associated stress responses (fig. S15). However, it remains possible that altered expression of the selected neuron-microglia inhibitory signaling pairs reflects dynamic cellular adaptations, such as neuronal apoptosis and microglia differentiation or proliferation, and therefore, cell-specific expression of these signaling pairs awaits further validation in our double-hit model.

In conclusion, our results show synergistic interactions between two environmental risk factors that have individually been associated with developmental psychopathology. Prenatal adversities (here, in the form of in utero immune challenge) can thus function as a “disease primer” that increases the offspring’s vulnerability to the detrimental neuropathological effects of subsequent stress exposure during peripubertal life. Prenatal

infection and peripubertal stress may thus be important etiological risk factors for long-term mental illness especially upon combined exposure. The concept by which prenatal infection can “prime” the developing organism’s sensitivity to subsequent environmental challenges postnatally is consistent with other models demonstrating synergistic pathological effects between prenatal and postnatal insults, including prenatal exposure to air pollution and chronic high-fat diet consumption in adulthood (24). The transient neuroimmunological changes emerging in peripubertal offspring that are exposed to combined immune activation and stress capture relevant aspects of neuroinflammatory processes. The precise inflammatory signature of these processes needs further elaboration and should be extended to other neuroimmunological aspects, including extension to other members of the cytokine network. Our data here may encourage attempts in this direction because rectifying altered immune responses during sensitive periods of peripubertal brain maturation could offer a valuable strategy to prevent possible neuronal maladaptations and subsequent psychopathology after exposure to multiple environmental adversities.

References and Notes

1. A. S. Brown, *Prog. Neurobiol.* **93**, 23 (2011).
2. C. B. Pedersen, P. B. Mortensen, *Arch. Gen. Psychiatry* **58**, 1039 (2001).
3. M. R. Herbert, *Curr. Opin. Neurol.* **23**, 103 (2010).
4. K. J. Tsuchiya, M. Byrne, P. B. Mortensen, *Bipolar Disord.* **5**, 231 (2003).
5. J. G. Green *et al.*, *Arch. Gen. Psychiatry* **67**, 113 (2010).
6. W. C. Holmes, G. B. Slap, *JAMA* **280**, 1855 (1998).
7. A. S. Brown, P. H. Patterson, *Schizophr. Bull.* **37**, 284 (2011).
8. F. Varese *et al.*, *Schizophr. Bull.* **38**, 661 (2012).
9. J. P. Selten, A. Frissen, G. Lensvelt-Mulders, V. A. Morgan, *Schizophr. Bull.* **36**, 219 (2010).
10. S. A. Mednick, R. A. Machon, M. O. Huttunen, D. Bonett, *Arch. Gen. Psychiatry* **45**, 189 (1988).
11. M. C. Clarke, A. Tanskanen, M. Huttunen, J. C. Whittaker, M. Cannon, *Am. J. Psychiatry* **166**, 1025 (2009).
12. T. A. Bayer, P. Falkai, W. Maier, *J. Psychiatr. Res.* **33**, 543 (1999).
13. T. M. Maynard, L. Sikich, J. A. Lieberman, A. S. LaMantia, *Schizophr. Bull.* **27**, 457 (2001).
14. U. Meyer, J. Feldon, S. H. Fatemi, *Neurosci. Biobehav. Rev.* **33**, 1061 (2009).
15. L. P. Spear, *Dev. Psychopathol.* **21**, 87 (2009).
16. H. L. Fisher *et al.*, *Psychol. Med.* **40**, 1967 (2010).
17. T. Paus, M. Keshavan, J. N. Giedd, *Nat. Rev. Neurosci.* **9**, 947 (2008).
18. E. Y. Hsiao, S. W. McBride, J. Chow, S. K. Mazmanian, P. H. Patterson, *Proc. Natl. Acad. Sci. U.S.A.* **109**, 12776 (2012).
19. U. Meyer, J. Feldon, O. Dammann, *Pediatr. Res.* **69**, 26R (2011).
20. M. G. Frank, M. V. Baratta, D. B. Sprunger, L. R. Watkins, S. F. Maier, *Brain Behav. Immun.* **21**, 47 (2007).
21. T. B. Franklin, B. J. Saab, I. M. Mansuy, *Neuron* **75**, 747 (2012).
22. R. M. Ransohoff, V. H. Perry, *Annu. Rev. Immunol.* **27**, 119 (2009).
23. R. M. Ransohoff, A. E. Cardona, *Nature* **468**, 253 (2010).
24. J. L. Bolton *et al.*, *FASEB J.* **26**, 4743 (2012).

Acknowledgments: We thank L. Weber and T. Wirth for their technical assistance in the immunohistochemical and flow cytometric analyses; U. Stadlbauer and M. Labouesse for assisting behavioral experimentation and animal care; and the laboratory animal technician team, Schwerzenbach, for animal husbandry. We also thank J. Feldon for his past mentoring and W. Langhans for the continuous infrastructural support. This work was supported by the European Union Seventh Framework Programme (FP7/2007–2011) under Grant Agreement no. 259679 awarded to U.M., and by the Lundbeck Foundation, the Stanley Medical Research Institute, and a European Research Council Advanced Grant awarded to P.B.M., and partially by the German Research Foundation (FOR 1581, SCHE 341/19-1; FOR 751, EN 814/1-2). All authors declare that they have no conflicts of interest to disclose. R.W. is employed by F. Hoffmann–La Roche, Ltd.

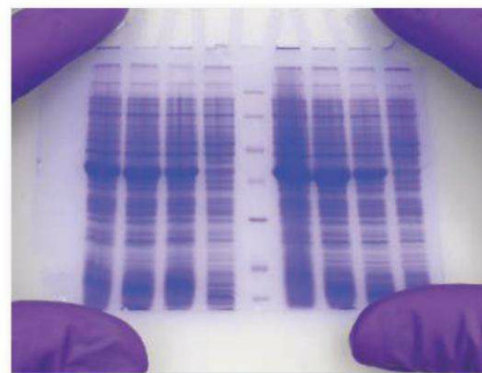
Supplementary Materials

www.sciencemag.org/cgi/content/full/339/6123/1095/DC1
Materials and Methods
Figs. S1 to S16
Tables S1 to S19
References (25–40)

1 August 2012; accepted 16 January 2013
10.1126/science.1228261

Not Your PI's Western Blot

More than three decades after its invention, the Western blot remains a crucial tool for investigators who need to reliably identify specific proteins. A host of recently released products use a variety of approaches to improve the reproducibility, sensitivity, quantifiability, and speed of Western blot experiments. By Anne Harding



While three different people are considered to have developed protein immunoblotting, just one of them—W. Neal Burnette, then working in the lab of Bob Nowinski at the Hutchinson Cancer Center in Seattle—gets the credit for coming up with the name “Western blotting.” The name alludes to Southern blotting (Edwin Southern’s 1975 invention of a technique using gel, nitrocellulose, and blotting paper to identify specific DNA sequences in a complex organism), Northern blotting (a similar strategy invented soon afterwards for identifying RNA), and the West Coast location of the Nowinski lab.

Burnette didn’t get his technique published until 1981; he recalls that reviewers objected “especially” to the name “Western blotting.” Nevertheless, the name stuck, and Western blotting has become one of the most widely used immunochemical techniques.

How It Works

The first step of a Western blot involves using gel electrophoresis to separate proteins by size, which are transferred to a membrane (usually nitrocellulose or polyvinylidene difluoride) by placing the membrane on top of the gel, adding several sheets of filter paper on top of that, and then placing the entire stack in buffer solution, which draws the proteins up to the membrane using capillary action. This is known as wet or tank blotting.

Two additional techniques, dry and semi-dry blotting, are quicker and less messy than traditional wet blotting, but less effective for high molecular weight proteins. In semi-dry blotting, the mem-

brane and gel are placed between layers of buffer-soaked filter papers, which are in turn sandwiched between an anode and a cathode so an electric current helps drive proteins to the membrane. Dry blotting is the fastest method but has the lowest transfer efficiency.

After blotting is complete, the membrane is placed in a dilute protein solution to block nonspecific protein binding. The membrane is then incubated with the primary antibody, washed, and incubated with a secondary antibody labeled with a probe for signal detection.

Detection, which is usually chemiluminescent or fluorescent, is the final step. In chemiluminescent detection, an enzyme-conjugated secondary antibody produces a light-generating reaction with the detection antigen that can be captured on film or with an imaging device. In fluorescent detection, antibody probes are tagged with fluorophores.

The key advantage of fluorescent detection is that it allows for the simultaneous detection of multiple proteins. Its more consistent signal also means it can be more quantitative than chemiluminescent detection.

Companies making devices, software, and consumables for Western blotting are working to make life a little easier for scientists by automating some—or all—of these steps; adding validation checkpoints so that scientists can check on a blot as it develops; and even reinventing the entire process. Scientists are looking for efficiency, robustness, and strategies that will help them avoid wasting sometimes valuable and costly antibodies.

Speeding Up The Immunodetection Process

The blotting, antibody incubations, loading, and wash steps account for 80 percent of the time it takes to do a Western blot, says Michele Hatler, product manager for Western blotting solutions at **EMD Millipore**.

The Temecula, California-based company’s SNAP i.d. 2.0 protein detection system accelerates the process by using a vacuum to drive reagents through the membrane, rather than relying on diffusion alone.

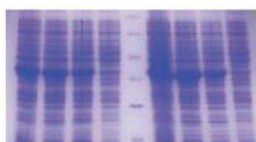
Upcoming Features

Fluorescence Multiplexing—April 12

The Microbiome—May 10

Proteomics: MALDI Imaging—May 31

“Scientists are looking for efficiency, robustness, and strategies that will help them avoid wasting sometimes valuable and costly antibodies.”



This can reduce immunodetection time from four hours to 30 minutes, according to Hatler. “We’re really looking at improving the efficiency of workflow in Western blotting,” she explains. “We’re still following all the traditional steps, we’re just adding a vacuum.”

The 2.0 version, introduced in September 2012, offers several advantages over its predecessor, according to Hatler. It can be used with midi-sized gels (8.5 cm by 13.5 cm) as well as mini-sized gels (7.5 cm by 8.4 cm), while the older version only ran minis.

“It’s very inexpensive and it’s very simple, but it really does improve that efficiency and time,” Hatler says.

Bio-Rad’s Trans-Blot Turbo protein transfer system is a benchtop-size instrument for fast, high-efficiency blotting. Thanks to a new blotting buffer formulation, special filter material, and increased amperage (accommodated by an integrated power supply), the system can complete a blot in as little as three minutes with blot results comparable to tank transfer. Typical semi-dry transfer systems take from 15 to 60 minutes for a complete transfer and often don’t provide robust results for transfer of high molecular-weight proteins.

Adding Checkpoints to Ease Anxiety

The high failure rates that plague Western blots are particularly frustrating when one has to wait days for a result. “It’s a very uncertain technique,” says Ryan Short, marketing manager for Western blotting at Bio-Rad. “When we’ve polled customers we’ve learned that half of customers report a failure rate of at least 25 percent of their Western blots.”

Short adds: “There are very few opportunities to check that the process is going as it’s expected. It’s anxiety producing. We’re introducing the concept of visual checkpoints to add confidence and certainty.”

The company’s Criterion and Mini-PROTEAN Stain-Free precast gels, used with its ChemiDoc MP gel imaging system, allow investigators to quickly see if their proteins were loaded properly onto the gels, and to verify high-quality protein transfer, providing insight in determining if they should move on to the next step in the process or start over. The ChemiDoc MP system is designed for chemiluminescent and multiplex fluorescent blot imaging and can be operated on a PC or Mac with ImageLab software.

These checkpoints are “really useful,” says Aldrin Gomes, an assistant professor at the University of California at Davis who uses the system in his lab. “We can image the stain-free gel without adding an external stain and quickly determine if there’s a problem with the samples run on the gel. We can also image the gel after the transfer of proteins to the membrane and if there’s a problem at either step we can stop the protocol at this point.”

Better Quantitation Through Imaging, Software

While many scientists still use film for Western blot analysis, there is an increasingly wide range of film-free gel documentation imaging systems available that can be used to image and analyze chemiluminescent blots, fluorescent blots, or both. Companies are competing to make these imagers, and the analysis software accompanying them, as user-friendly as possible. Many offer push-button image capture with a benchtop footprint.

Syngene’s PXi, introduced in April 2012, is a compact, one-click system for analyzing both chemiluminescent and fluorescent blots, based on the technology used in the company’s G:BOX imaging system



“We’re introducing the concept of visual checkpoints to add confidence and certainty.”

and fitted with its GeneSys imaging software.

In October 2012, Thermo Fisher Scientific introduced its my-ECL Imager, which uses ultraviolet and visible light transillumination, specialized filters, and charge-coupled device (CCD) camera technology to capture and analyze Western blots as well as protein and nucleic acid gels.

The CCD camera is twice as sensitive as X-ray film, according to the company, with 10 times the dynamic range. There is no need to focus or adjust camera settings, because users simply touch one of the optimized presets on the device’s touchscreen. Users can set custom exposures—and run up to five different exposures simultaneously—or use preset exposures. The imager has a small instrument footprint, making it suitable for benchtop use.

Aplegen’s Omega Lum G gel documentation also features automatic focus and a benchtop footprint, and comes with an integrated tablet computer. UVP’s Chemi-Doc-It TS2 imager, released in January 2012, features an integrated computer and touchscreen that allows users to adjust exposure, aperture, zoom, and focus, and also provides an image sample when users touch the Live Preview button.

LI-COR’s latest version of its infrared imaging system, the Odyssey CLx, has a dynamic range of more than six-log, compared to more than four-log for its previous version. This increased range eliminates saturation when interpreting Western blots, providing a wider linear range over which to quantitate data.

“Not only will researchers not get saturation on their blots, but they can put multiple blots onto the imager and never have to worry about adjusting the blots to different settings,” explains Jeff Harford, senior product marketing manager at the Lincoln, Nebraska company.

Rehana Leak is an assistant professor at Duquesne University in Pittsburgh who uses the LI-COR’s Odyssey CLx in her research on how cells adapt to low levels of stress. “The advantage of the Odyssey [imager] is the 16-bit imager and use of two infrared wavelengths, 700 and 800 nm, to visualize two stains at once,” Leak says. “This means that the phosphorylated and total forms of proteins can be detected simultaneously, for example.” Two protein isoforms can be difficult to distinguish simultaneously by other methods because their masses are so similar.

Leak points out that the Odyssey imager can visualize **continued>**

Featured Participants

Aplegen

www.aplegen.com

Bio-Rad Laboratories

www.bio-rad.com

Duquesne University

www.duq.edu

EMD Millipore

www.emdmillipore.com

LI-COR Biosciences

www.licor.com

Merck & Co

www.merck.com

Protein Simple

www.proteinsimple.com

Stanford University School of Medicine

www.med.stanford.edu

Syngene

www.syngene.com

Thermo Fisher Scientific

www.thermofisher.com

University of California at Davis

www.ucdavis.edu

UVP

www.uvp.com

2¹⁶ shades of infrared signal, compared with the 150 shades of gray visualized on X-ray film. “You’re going from 150 to over 65,000 shades of infrared, so you have much higher resolution with this method,” she adds. “It’s unusually quantitative.”

In December 2012, LI-COR announced a new digital imaging system, the C-DiGit System, which can be used with chemiluminescent blots and will be released some time in 2013. “Just as digital cameras replaced film-based cameras in the last few years, we see the C-DiGit System as a legitimate replacement for film-based chemiluminescence,” says Jon Anderson, a senior scientist at LI-COR. “The technology provides all the sensitivity and image quality that film users are accustomed to, while providing significant improvements in digital image quality.”

Evermore-Intuitive Software

Traditional software for analyzing Western blots requires users to export data from the image to a spreadsheet, where further normalization calculations and analysis are completed manually. BioRad’s Image Lab 4.1 software, released in September 2012, provides built-in, automated normalization to either a housekeeping protein or to a total lane protein.

“It’s one of the best I’ve seen on the market now,” says Gomes, who studies the role of proteasomes and troponins in cardiac and skeletal muscle tissues. “Best of all, it’s free.” Using Image Lab 4.1 is easier than other image analysis software his lab previously used, adds Gomes, and just about anyone can handle it. “It really has enhanced how we quantify the proteins.”

LI-COR has also introduced new imaging software, Image Studio, for use with its Odyssey systems. Users choose a detection channel, and then push a button to acquire an image. The new version of the software allows for analysis in millimeter increments, rather than centimeter increments, and can perform completely automated analysis as well as manual analysis.

Reinventing The Western Blot

Instead of tweaking the traditional Western blot, **ProteinSimple’s** Simple Western has reinvented it, using capillary electrophoresis to fully automate the process. In 2011, the company introduced Simon, an instrument designed to completely replace the Western blot. Simon performs size-based separation, immunoprobings, washing, chemiluminescent detection, and quantitative analysis. Scientists simply load a sample, walk away, and come back later to fully analyzed data. Simon even sends out a tweet to let you know your results are ready.

Next came Sally, in early 2012, which allows users to perform 96 Simple Westerns in one experiment; the latest device is Peggy, introduced in September 2012, which can analyze 96 samples at once and separates proteins by size or charge. The Simple Western overcomes the drawbacks of the manual aspects of the traditional Western, namely lack of reproducibility or quantitative results. In addition, multiplexed detection in a traditional Western has been a challenge. Investigators can now use fluorescence to look at two or three proteins within a sample, and transfer devices that run up to eight mini- or four midi-gels at the same time, but that’s as far as traditional Western blotting can go. Simple Western can multiplex proteins in every capillary, essentially eliminating this limitation of the traditional Western.

For Alice Fan, an instructor in oncology at **Stanford University School of Medicine**, the most exciting thing about the Simple Western technology is its ability to analyze nanoliter-sized samples.

Fan has been banking patient tissue samples for more than a decade, waiting for a tool that will let her analyze the proteomics of tumor cells without using up the entire sample. “I’ve been looking for something for years that will let me be able to do a Western blot with very small amounts of tissue,” she explains.

In addition to helping her to conserve precious banked tissue, Sally has made it feasible for Fan to take several samples from an individual patient over time using fine-needle aspiration, rather than doing a full-fledged biopsy. This, Fan hopes, will let her watch how a patient’s tumor is responding to a drug in real-time. “This really helped my research in terms of how to profile different tumors. It’s a huge leap forward.”

Richard Rustandi, chair of the vaccine biochemistry group at **Merck & Co.**, didn’t have high hopes when he purchased a Simon instrument at the end of 2011. But, he says, he’s been pleasantly surprised. “We liked it so much we actually purchased a second one a few months later.”

According to Rustandi, while Simon is not perfect, it can do true quantitation. And while manual Westerns typically have 35 percent to 45 percent variability, he adds, he and his lab have pegged Simon’s variability at less than 10 percent.

As Western blotting technologies continue to evolve, researchers are finally able to start spending a little—or a lot—less time babysitting their experiments. “Their time is important,” says Peter Fung, the product manager for Simple Western. “And the more efficient you can be with your time, the better research you can do.”

Anne Harding is a freelance science writer based near New York City.

DOI: 10.1126/science.opms.p1300073

TRANSILLUMINATORS

New transilluminators with high-performance blue light LEDs are available for gel documentation purposes. Blue light transilluminators are an interesting alternative to ultraviolet (UV) tables as there is no risk of sample damage during illumination, which is important for processing samples following gel documentation. The transilluminators also benefit users, as there is no risk of UV exposure. Blue light excitation can be used with fluorescent dyes for nucleic acid or for protein stains that have an excitation wavelength around 470 nm. Examples of compatible stains are: SYBR Green, GelGreen™, SYBR Safe, SYBR Gold, and SYPRO Ruby. The instrument's amber lid allows direct viewing of the fluorescent samples, with no need for separate glasses. The new blue light illuminators are available in two versions: the BLstar 9, a handy solution for mini gels, and the BLstar 16, for gels up to size of 16 cm x 20 cm.

Biometra

For info: +49-55-15068-60 | www.biometra.com



MULTIPLEX ANALYSIS

The Image Lab 4.1 software is designed for use with the ChemiDoc MP imaging system. The new software automates multiplex analysis, providing a faster, more accurate alternative for quantifying protein expression levels via Western blotting. Proving that quantitative differences of a target protein are a result of biological differences and not experimental variability (such as unequal protein loading) is critical when conducting Western blotting experiments. Typically, scientists comparing gene expression levels use a housekeeping protein (HKP) as a loading control with the assumption that HKP expression does not change based on treatment type or sample origin. However, total protein normalization has been shown to be more stable than HKP normalization regardless of conditions or sample type and saves time by eliminating the need for multiple probing steps or optimizing a multiplex blot. With Image Lab 4.1 software, researchers can deliver normalized intensities automatically.

Bio-Rad

For info: 800-424-6723 | www.bio-rad.com/imagelabsoftware

PRIMARY ANTIBODY DETECTION

The WestVision Peroxidase Polymer Anti-Rabbit IgG and Peroxidase Polymer Anti-Mouse IgG are designed to detect primary antibodies of mouse or rabbit origin in Western blots. The WestVision conjugates are based on a new method of polymerizing enzymes and attaching these polymers to antibodies that can allow a higher density of enzymes to access a target with lower interference. With a chromogenic substrate, the reagents can provide enough working solution to typically detect 20 to 200 blots (10 cm x 10 cm). With a chemiluminescent substrate, dependent on the dilution employed, 800 to 8,000 blots can be detected.

Vector Laboratories

For info: 800-227-6666 | www.vectorlabs.com

CHEMILUMINESCENT KITS

A new line of chemiluminescent Western blot kits provide the most sensitive detection solutions yet. Forty-five percent of researchers recently surveyed cited a lack of sensitivity and time to results in Western blots as significant challenges. The search for increased sensitivity can amplify background, requiring lengthy optimization to manage signal:noise contrast. SignalLOCK ChemiWestern kits solve these challenges. Each kit is composed of a chemiluminescent substrate, a non-protein blocker, and unique wash solution. All kits offer comprehensive protocols and can be used with both nitrocellulose and PVDF members. Whether using film or an imager, there is an optimized kit that will enable researchers to see more signal with less background in their Western blots.

KPL

For info: 800-638-3167 | www.kpl.com/SignalLOCK

LOW PROTEIN BINDING MICROTUBES

Low protein binding microtubes are now offered in both 0.5 mL and 1.5 mL volumes. These tubes are specially designed to meet the requirements of protein analytics while maximizing protein recovery rates. The microtubes are manufactured from a proprietary polypropylene with low protein binding properties and do not feature any potentially contaminating surface coating like silicone. The low protein binding microtubes feature an attached flat SafeSeal cap with a tooth-like cam that locks over the tube rim, increasing retaining strength and providing a reliable, secure closure. Tubes can be centrifuged to 20,000 x g, and are polymerase chain reaction (PCR) Performance Tested, and therefore certified to be free of human DNA, DNase, RNase, and PCR inhibitors.

Sarstedt

For info: 800-257-5101 | www.sarstedt.com



Science Careers Advertising

For full advertising details, go to ScienceCareers.org and click For Employers, or call one of our representatives.

Tracy Holmes

Worldwide Associate Director
Science Careers
Phone: +44 (0) 1223 326525

THE AMERICAS

E-mail: advertise@sciencecareers.org
Fax: 202-289-6742

Tina Burks

United States/Canada/South America
Phone: 202-326-6577

Marci Gallun

Sales Administrator
Phone: 202-326-6582

Online Job Posting Questions

Phone: 202-312-6375

EUROPE / INDIA / AUSTRALIA / NEW ZEALAND / REST OF WORLD

E-mail: ads@science-int.co.uk
Fax: +44 (0) 1223 326532

Lucy Nelson

Phone: +44 (0)1223 326527

Kelly Grace

Phone: +44 (0) 1223 326528

JAPAN

Yuri Kobayashi

Phone: +81-(0)90-9110-1719
E-mail: ykobayas@aaas.org

CHINA / KOREA / SINGAPORE / TAIWAN / THAILAND

Ruolei Wu

Phone: +86-1367-1015-294
E-mail: rwu@aaas.org

All ads submitted for publication must comply with applicable U.S. and non-U.S. laws. *Science* reserves the right to refuse any advertisement at its sole discretion for any reason, including without limitation for offensive language or inappropriate content, and all advertising is subject to publisher approval. *Science* encourages our readers to alert us to any ads that they feel may be discriminatory or offensive.

Science Careers

From the journal *Science*



ScienceCareers.org



The Leibniz-Institut für Molekulare Pharmakologie (FMP) and the Humboldt-Universität zu Berlin (HU) invite applications for a joint appointment as

Director at the Leibniz-Institut für Molekulare Pharmakologie and Full Professor (W3) of Chemical Biology

The professorship links the leadership of a department and of the research section "Chemical Biology" at the FMP with the representation of this academic subject in research and teaching at the HU. The research section "Chemical Biology" currently comprises protein and peptide chemistry, medicinal chemistry, a screening unit for small molecules including automated microscopy, as well as a state-of-the-art mass spectrometry platform. The successful candidate will function as director in alternation with the present director of the institute according to the constitution of the FMP.

Successful applicants will have a record of outstanding achievements in the field of chemical biology. Preferably, they will apply and develop strategies of organic chemical synthesis to generate novel agents for the detection and manipulation of biological processes in cooperation with the Screening Unit and other research groups at the FMP. The development of optical-chemical methods such as the synthesis of novel caged or switchable probes or fluorescent biomolecules and dyes are also regarded as seminal topics.

The applicant is expected to engage in close collaborations with the FMP research sections "Structural Biology" and "Molecular Physiology and Cell Biology" as well as with research institutes of the HU.

The FMP is funded in equal parts by the federal government and the states (Länder). Its location on the life science campus Berlin-Buch provides for an excellent scientific environment.

Applicants must meet the requirements for a university professor as stipulated in § 100 of the "Berliner Hochschulgesetz". The professor will take part in teaching students at the Institute of Chemistry (with a reduced teaching obligation 2 LVS).

HU and FMP seek to increase the proportion of women in research and teaching, and specifically encourage qualified female researchers to apply. Applications of researchers from abroad are welcome. Preference will be given to disabled persons with equal qualifications. Applicants with migration background are highly welcome.

Applications (including statements regarding both current and future research interests, curriculum vitae, publication list, and the names of three potential reviewers) should be sent by March 31, 2013 to Humboldt-Universität zu Berlin, Dekan der Mathematisch-Naturwissenschaftlichen Fakultät I, Prof. Hecht, code PR/006/13, Unter den Linden 6, 10099 Berlin, Germany. As application materials will not be returned, we ask you to send only copies of all documents.

In order to accelerate the processing of applications, applicants are kindly requested to submit applications in addition electronically. Information regarding electronic submission is accessible at https://www2.physik.hu-berlin.de/ssl/chem_bio/.

For further information, please visit the FMP website www.fmp-berlin.de and the website of HU www.hu-berlin.de



COLUMBIA UNIVERSITY
MEDICAL CENTER

College of Physicians and Surgeons

Vascular Biologist

The Department of Neurology at Columbia University Medical Center, is recruiting for a basic/translational science research faculty (Ph.D. or M.D.) in the area of vascular biology to complement ongoing clinical research in acute stroke, stroke prevention, and stroke recovery. Tenure track Assistant Professor equivalent or higher. Research track record in neuroscience, molecular/cell biology, or neuropathology preferred. Multidepartmental appointments possible.

Qualified candidates should send a letter of interest and curriculum vitae in Word format to:

Randolph Marshall, M.D., M.S.

Elisabeth K. Harris

Professor of Neurology

710 West 168th Street

New York, NY 10032

Marguerite Outlaw, Assistant

212-305-8389

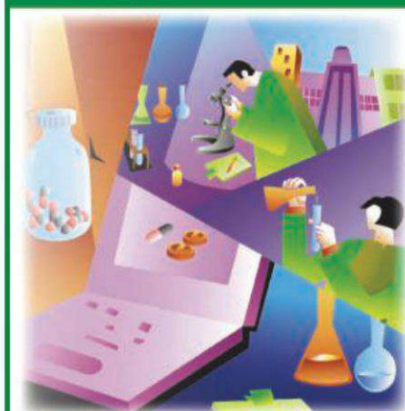
rsm2@columbia.edu

In addition, applicants must apply electronically online at

<https://academicjobs.columbia.edu/applicants/Central?quickFind=57371>

Columbia University is an equal opportunity/affirmative action employer.

CAREER Running TRENDS Your Lab



Download your free copy today at
ScienceCareers.org/booklets

Science Careers

From the journal *Science*



Brought to you by the
AAAS/Science Business Office



Faculty Positions Open

Chemistry

Marine Sciences

Mathematics/Statistics

The Okinawa Institute of Science and Technology Graduate University (<http://www.oist.jp>) invites applications for new faculty positions

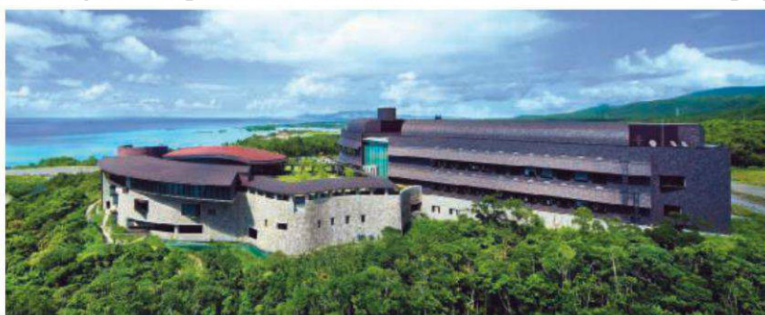
- Two positions in **Chemistry**, including areas related to life sciences and physical sciences
- Two positions in **Marine Science**, including physical oceanography and marine biology
- One position in **Applied Mathematics and Statistics**, including machine learning, data mining, high-throughput measurements, or high-performance computing.

For all positions we seek applicants with strong interdisciplinary interests, and outstanding records of scientific creativity and productivity. Detailed descriptions of all five positions may be accessed at:

<https://groups.oist.jp/facultypositions>

OIST is a new, English-language graduate university offering a world-class research environment and a highly diverse, international research community with faculty, staff and students from over 30 countries. It is located in Okinawa on a beautiful campus overlooking the East China Sea.

OIST Graduate University is an equal opportunity, affirmative action educator and employer and is committed to increasing the diversity of its faculty. We strongly encourage women and minority candidates to apply.



AWARDS

Terumo Life Science Foundation

We welcome your nominations for candidates for the 2nd Terumo Global Science Prize —An academic award for biomaterials researchers—

■ Purpose

In recent years, combined research in the fields of biomaterials and regenerative medicine is accelerating rapidly, and various efforts toward practical application are being made. The fusion of excellence in materials engineering, life science, and the related discipline of systems engineering is essential for this area. This Prize shall be awarded to outstanding researchers who have demonstrated unique, internationally renowned achievements in research, made significant contributions to the field of regenerative medicine particularly through novel biomaterials discovery, and continued to work in the frontline of research. We hope that this Prize will be a great source of encouragement to researchers, resulting in the further evolution of research towards practical application and a brighter future for humankind

■ Details of the Prize

The Terumo Global Science Prize shall be awarded to one outstanding researcher. The awardee will receive a commemorative shield and a gift as the main prize, together with a supplementary monetary prize of 10 million yen.

■ Award ceremony

The award ceremony as well as the commemorative lecture will be held in Tokyo on one Saturday in July, 2014. The recipient of the Terumo Global Science Prize is requested to be present at the ceremony and to give a speech.

■ Application method

An application in the form of a recommendation shall be filed. (No self-recommendation accepted)

Please fill out the application form and submit it to the Secretariat along with all the required documents. The application can be made online or by post. Please refer to the official Web site for more details.

■ Application Deadline

June 30(SUN), 2013

By Post: Must be postmarked on or before the above date

Online: Must be sent at or before 5:00 PM(JST) on the above date

■ The awardee of the 1st Terumo Global Science Prize

Professor Robert Samuel Langer
(Massachusetts Institute of Technology)



NOW ACCEPTING APPLICATIONS

Official
Web Site

<http://www.terumozaidan.or.jp/english>

There's only one GALILEO GALILEI

Born in 1564, Galileo Galilei once contemplated a career in the priesthood. It's perhaps fortunate for science that upon the urging of his father, he instead decided to enroll at the University of Pisa. His career in science began with medicine and from there he subsequently went on to become a philosopher, physicist, mathematician, and astronomer, for which he is perhaps best known. His astronomical observations and subsequent improvements to telescopes built his reputation as a leading scientist of his time, but also led him to probe subject matter counter to prevailing dogma. His expressed views on the Earth's movement around the sun caused him to be declared suspect of heresy, which for some time led to a ban on the reprinting of his works.

Galileo's career changed science for all of us and he was without doubt a leading light in the scientific revolution, which is perhaps why Albert Einstein called him the father of modern science.

Want to challenge the status quo and make the Earth move? At *Science* we are here to help you in your own scientific career with expert career advice, forums, job postings, and more — all for free. For your career in science, there's only one *Science*. Visit ScienceCareers.org today.



For your career in science, there's only one **Science**

AAAS

ScienceCareers.org

Assistant, Associate or Full Professor Positions in Biomedical Sciences

The Division of Biomedical Sciences within the newly-accredited School of Medicine at the University of California Riverside is seeking to hire two new faculty members at the rank of Assistant, Associate or Full Professor. We are looking for accomplished research scientists in a number of specific areas including neoplastic, neurological, vascular, pulmonary and metabolic diseases. Preference will be given to those individuals examining the molecular mechanisms of these diseases who are committed to a collaborative approach to research, and who are expert in their specific disease model.

The successful candidate will be appointed in the Division of Biomedical Sciences, joining a faculty that has directed a successful M.D. program in collaboration with UCLA since the late 1970s. The new School of Medicine at UCR is the sixth University of California Medical School and serves the rapidly growing and dynamic Inland Southern California region by training a much-needed physician workforce and catalyzing innovations in research, education, and health care delivery that improve the health of medically underserved populations. Laboratory and office space will be in a newly-opened School of Medicine research building.

Areas of disease research within the Division include integrative immunology (vaccine development, neuro-immune, endocrine-immune, host-pathogen interactions, allergic inflammation, and the aging immune system), glial-neuronal interactions, neurodevelopmental disorders, cancer biology, neuroendocrinology, and diseases of ion transport. Areas of molecular and cell biology expertise within the department include signal transduction, cell migration and epithelial cell physiology. Particular strengths on the campus include genetics, epigenetics, genomics/bioinformatics, microRNAs, vector biology, bioengineering and nanotechnology, and synthetic and analytical chemistry.

The Division of Biomedical Sciences sponsors an innovative Ph.D. program that integrates the core medical curriculum with biomedical graduate training and research. The successful candidates will be expected to teach in the medical curriculum and actively participate in the Biomedical Sciences Ph.D. program. As such, preference will be given to candidates who are capable of teaching neuro- and/or general pharmacology, pathology, infectious disease (microbiology/virology), physiology (electrophysiology, renal or respiratory) or genetics.

The University of California, Riverside is situated in an historic citrus growing area surrounded by mountain ranges. Riverside is about an hour away from ski slopes, surfing, or hiking in mountain or desert environments, and housing in the area is very affordable. The campus is also located in a prime position to take advantage of the other universities, research institutes, and biotech industries present in Southern California.

Applicants must hold a Ph.D., M.D., Pharm D., or equivalent degree and qualify for a tenure-track/tenured faculty appointment at the University of California. Applications will be reviewed beginning **March 29, 2013** and the positions will remain open until filled. UC Riverside is an Equal Opportunity/Affirmative Action Employer.

To apply, please submit the following items:

- Curriculum vitae
- Statement of research accomplishments and goals and statement of teaching expertise
- In order to facilitate review of your application please choose one of the following categories which best describes your research area and expertise: (a) infectious disease, (b) nervous system, (c) metabolism, (d) vascular biology, (e) endocrinology, (f) cancer, or (g) other and place this in the reference line of your letter of application/subject line of an email (failure to do this will delay the review of your application)
- Names of four individuals who will provide letters of reference

Electronic Submissions are required. Send the items to: **School of Medicine, Division of Biomedical Sciences, University of California, Riverside, CA 92521; BiomedRecruitment@ucr.edu.**



Recruiting Faculty in Biochemistry and Molecular Biology

The Department of Biochemistry and Molecular Biology at the Medical University of South Carolina (MUSC) invites applications for tenure track positions at the Associate and Professor level in all areas of biochemistry and molecular biology. State-of-the-art laboratories, outstanding resources and research support are available. In addition, endowed chair positions are available for exceptional candidates.

Candidates should have a national reputation and a solid record of collaborative and peer-reviewed funded research. We are seeking outstanding scientists who would complement and expand existing research foci and programs at MUSC.

Located on the Atlantic coast in South Carolina, Charleston boasts one of the nation's most historic downtown areas, beaches and year-round outdoor life, as well as international cultural events such as the Spoleto Festival USA.

Interested researchers should send their CV and a summary of future research plans to:

www.jobs.musc.edu/applicants/Central?quickFind=190056

Philip H. Howe, Ph.D.
Professor & Chair
Department of Biochemistry & Molecular Biology
Medical University of South Carolina
173 Ashley Avenue, MSC 509
Charleston, SC 29425
simmonva@musc.edu



Director of Clinical Research

The University of Massachusetts Medical School (UMMS) Center for Clinical and Translational Science (UMCCTS) invites applications for the position of Director of Clinical Research (D-CR). The D-CR will provide cross-system leadership for clinical research across UMMS and its clinical partner, UMass Memorial Medical Center. S/he will work closely with UMCCTS and clinical system leadership to develop and implement processes, systems, educational programs, and other activities necessary to support outstanding clinical and translational research and educational programs.

The ideal candidate is a physician-scientist (MD or MD-PhD) with extensive experience in clinical research and a successful track record in investigator-initiated research. The successful candidate will be hired jointly by UMMS and the UMass Memorial Medical Group and will receive a UMMS faculty appointment at the rank of Associate or Full Professor. It is expected that s/he will continue to be active in clinical work, as well as in funded research in their field while committing to advance clinical research across the entire institution.

UMMS is a highly productive and collaborative research enterprise with first-rate scientific resources and facilities and over \$277M of extramural research funding annually. Support from an NIH/NCATS-funded Clinical and Translational Science Award has driven an expansion of clinical and translational science that capitalizes on UMMS' leading programs in RNA Biology/Therapeutics, Gene Therapy, Monoclonal Antibody/Vaccine Production, and Quantitative Health Sciences to develop novel therapies/approaches for neurodegenerative, cardiovascular, and infectious diseases, as well as cancer and diabetes. The Massachusetts Biologics Laboratory and the Massachusetts Medical Device Development Center serve as additional unique resources that facilitate the translation of discovery into biologics and devices, respectively.

We value the advantages afforded only through a diverse workforce and encourage all to apply.

To apply, please send a cover letter/statement of professional interests, CV, and three letters of reference to: **Nate Hafer, PhD, Director of Operations, UMass Center for Clinical & Translational Science, nathaniel.hafer@umassmed.edu.**



AAAS is here – helping scientists achieve career success.

Every month, over 400,000 students and scientists visit ScienceCareers.org in search of the information, advice, and opportunities they need to take the next step in their careers.

A complete career resource, free to the public, *Science Careers* offers a suite of tools and services developed specifically for scientists. With hundreds of career development articles, webinars and downloadable booklets filled with practical advice, a community forum providing answers to career questions, and thousands of job listings in academia, government, and industry, *Science Careers* has helped countless individuals prepare themselves for successful careers.

As a AAAS member, your dues help AAAS make this service freely available to the scientific community. If you're not a member, join us. Together we can make a difference.

To learn more, visit aaas.org/plusyou/sciencecareers



Icahn School of Medicine at Mount Sinai is one of the world's leading biomedical institutions and internationally acclaimed for excellence in scientific research, clinical care and education. It is among the nation's top twenty medical schools in NIH funding and U.S. News and World Report rankings. The School offers education programs leading to M.D., Ph.D. and master's degrees, and attracts outstanding students to its highly competitive programs and invigorating academic environment.



Icahn
School of
Medicine at
Mount
Sinai

ASSISTANT, ASSOCIATE & FULL PROFESSORSHIPS

The Department of Oncological Sciences is undergoing a major expansion and seeking exceptional candidates (Ph.D., M.D., or M.D.-Ph.D.) of the highest caliber for new faculty positions in laboratory research at all tenure track levels. The collaborative and supportive environment within the Department, Tisch Cancer Institute and School of Medicine provides access to the latest infrastructure for inquiry into genetics, biochemistry, metabolism, computational biology, mouse models, molecular pathology, and drug discovery. It also builds on current institutional expansion in genomics, pathology, metabolism, structural biology, stem cell and developmental biology, and neurobiology. The goal of this broad effort is to create a fruitful and dialectic environment between basic and clinical cancer research.

Successful candidates will augment an intellectually vibrant and growing group of 34 full-time faculty and be expected to develop an independently funded research program or expand their current programs addressing fundamental questions in cancer. We are particularly interested in investigators who plan to bridge a deep knowledge of specific human cancers with cutting-edge technology and analysis. We believe this type of scientific inquiry, which is by definition multidisciplinary, will lead to advances in cancer prevention and therapy.

We offer a highly competitive remunerative package commensurate with the scope of this position, along with an opportunity to join our world class organization. Please submit curriculum vitae, three letters of reference and up to three manuscripts to Dr. Ramon Parsons, M.D., Ph.D., Chairman of the Department of Oncological Sciences, at: oncsci.search@mssm.edu with the subject line Oncological Sciences Faculty Search.

Applications will be considered until all of the positions are filled.

Mount Sinai Medical Center is an equal opportunity/affirmative action employer. We recognize the power and importance of a diverse employee population and strongly encourage applicants with various experiences and backgrounds.

Tenure Track Assistant and Associate Professor Cancer Cell Signaling and Metabolism Positions



The Medical College of Wisconsin (MCW) Cancer Center invites applications for tenure-track positions at the Assistant or Associate Professor level. The successful applicant will be expected to develop a program aligned with major ongoing research efforts in Cancer Cell Signaling and Metabolism. We encourage applications from junior and mid-level investigators with expertise in the following areas relevant to cancer:

Cell Signaling • Redox Mechanisms and Metabolism
Mitochondria and Bioenergetics Epigenetics • Genomic Instability
Chemokines and Inflammatory Mediators

The candidate is expected to establish a vigorous and extramurally funded research program, and participate in collaborative and interdisciplinary projects. Teaching at the graduate level is also expected. Applicants must have a doctoral degree in a relevant area, a minimum of two years of post-doctoral experience, and a strong record of research accomplishments.

Cancer is the top strategic priority at MCW. The Cancer Center is comprised of more than 200 cancer research scientists and physicians at MCW, Froedtert Hospital, Children's Hospital of Wisconsin, Clement Zablocki VA Medical Center, and the BloodCenter of Wisconsin, and has an ambitious plan for growth, including achieving NCI-designation. The MCW Cancer Center occupies 30,000 sq. ft. of space dedicated to cancer-related basic science research on the MCW campus, and an additional 50,000 sq. ft. at the Froedtert Clinical Cancer Center in the MCW medical complex.

Candidates should email a complete curriculum vitae, bibliography, statement of research interests, and names of at least three references to:

Sheri Sasaki (cancer@mcw.edu)
Cancer Cell Signaling & Metabolism Search Committee
Medical College of Wisconsin Cancer Center
8701 Watertown Plank Road, Milwaukee, WI 53226

Deadline for applications is April 1, 2013



Computational Sciences Strategic Team Hire Assistant or Associate Professor

The Institute of Agriculture and Natural Resources (IANR) at the University of Nebraska-Lincoln (UNL) is seeking applicants for a Strategic Team Hire of three tenured or tenure-leading positions each expected to develop a nationally and internationally recognized research program integrating the methodological (e.g., machine learning, Bayesian nonparametrics, risk analysis, and multi-scale modeling) and the field specific (e.g., bioimaging, biomolecular, cellular signaling, remote sensing, and epidemiology) levels of computational biology. The program aims of each successful candidate may include one or more of the following focus areas:

- 1. At the Molecular Level** - Development of statistical theory, algorithms, and software related to the design and analysis of high throughput data (e.g., high density genotypic, transcriptomic, proteomic, metabolomic, and sequence information) with the goal of predicting genetic and metabolic networks.
- 2. At the Organismal Level** - Studies addressing plant and animal genomics, which will include the development of statistical theory, algorithms, and software related to the design and analysis of high throughput data sets with the goal of advancing new methodologies to correlate genetic traits in plant and animal systems with phenotypes (e.g., drought tolerance, enhanced nutritional value, or enhanced economic value of downstream products).
- 3. At the Systems Level** - Studies addressing large empirical datasets from local to regional to continental scale relating to agricultural, environmental and natural resources, which will enable the development of computational approaches and model predictions at each scale -may include the use of Global Circulation Models and the development of statistical theory, algorithms, and software related to the design and analysis of large ecosystem data sets (e.g., water, carbon, methane, and nitrous oxide), with the goal of predicting complex ecosystem networks and climate forecasts.

Each position will have a 70% research, 28% teaching and 2% service appointment, and the tenure home for each of the three positions will be determined based on the expertise of the successful candidate. Potential homes include: Biochemistry, Biological Systems Engineering, Food Science and Technology, Animal Science, Agronomy and Horticulture, Nutrition and Health Science, School of Veterinary Medicine and Biomedical Sciences, Plant Pathology, Statistics, and the School of Natural Resources. Each successful candidate will develop a national recognized research program and contribute to university-wide programs in areas that include biomarkers in disease and stress, quantitative genomics and phenotypes, proteomics, metabolomics, plant and animal genomics, mathematical biology, food safety or ecosystem modeling.

A Ph.D. in Statistics, one of the Natural Sciences, Mathematics, Computational Sciences, Engineering, or a closely related field is required; for the Assistant Professor level two years (or equivalent) of postdoctoral experience is strongly preferred. For the Associate Professor level, an externally supported and nationally recognized research program in the broad area of Computational Biology is required. Preference will be given to candidates that have expertise in the development and implementation of models of large complex systems at the molecular, the organismal, or the systems levels. The successful candidates should have a strong commitment to undergraduate and graduate education and research, excellent communication skills, and the desire and abilities to work cooperatively on multi-disciplinary projects.

To view the details and make application, go to <http://employment.unl.edu>. Search for position number **F_130062**. Click on "Apply to this job." Complete the application and attach a letter of interest, curriculum vitae, and a statement on areas of interest and career goals in computational science (Other Document). Arrange for three letters of reference to be sent to **Joyce Ore** at jore1@unl.edu. Review of applications will begin **April 1, 2013**, and continue until the positions are filled or the search is closed.

The University of Nebraska has an active National Science Foundation ADVANCE gender equity program, and is committed to a pluralistic campus community through Affirmative Action, Equal Opportunity, work-life balance, and dual careers.

**Download
your free copy
today.**

ScienceCareers.org/booklets



From technology specialists to patent attorneys to policy advisers, learn more about the types of careers that scientists can pursue and the skills needed in order to succeed in nonresearch careers.



POSITIONS OPEN

**POSTDOCTORAL POSITIONS in
CRYO-EM**

Two postdoctoral positions are available immediately in the laboratory of **Dr. Joachim Frank**, Department of Biochemistry and Molecular Biophysics, Columbia University, New York.

Applications will be considered from highly motivated individuals with a Ph.D. degree in the Natural Sciences. Preference will be given to applicants with demonstrated expertise in one of the following areas: experimental or computational aspects of cryo-electron microscopy, signal processing, or RNA modeling.

The Frank Lab conducts in-depth research on the mechanism of protein synthesis in bacteria and eukaryotes, using single-particle cryo-EM of in vitro samples, as well as electron tomography of cell sections. Three-dimensional density maps reconstructed are interpreted by flexible fitting, homology modeling of proteins, and ab initio modeling of RNAs. By using classification of heterogeneous samples, multiple states of equilibrating molecular complexes are characterized.

The EM facility in the Frank Lab, situated on the Medical Center campus, has a 300-kV FEI Tecnai Polara microscope equipped with a K2 Gatan 4k × 4k camera, capable of single-electron counting, and a 200-kV FEI Tecnai with a Gatan 4k × 4k CCD camera. Equipment is available for time-resolved cryo-EM using microfluidic nanochips with a minimum of 10 ms reaction time. Additional electron microscopes and supporting facilities such as focused ion-beam milling and high-pressure freezing are available at the New York Structural Biology Center, a nearby Resource Center supported by a consortium of universities that includes Columbia University.

Qualified applicants should send curriculum vitae, including the names of three references, and a statement of career goals to: **Masgan Saidi** (e-mail: ms4597@columbia.edu), Biochemistry and Molecular Biophysics, Columbia University, Black Building 2-221, 650 West 168th Street, New York, NY 10032.

Columbia University is an Affirmative Action/Equal Opportunity Employer.

**Find
your future
here.**



www.ScienceCareers.org

MARKETPLACE

ProMab Biotechnologies, Inc.

**Ascites Production
\$20 - \$30 / Mouse**

UP TO 100,000 MICE / YEAR

1-866-339-0871

www.ProMab.com | info@promab.com

WEBINAR

The Future of High Throughput Assays

From Reporter Genes to qPCR

WEDNESDAY, MARCH 20, 2013

12 noon ET, 9 a.m. PT, 4 p.m. UK, 5 p.m. CET

In vitro high throughput screening in drug discovery has typically been accomplished using reporter gene assays, which offer a versatile, cost-effective, and technically simple way to screen in high throughput, and are amenable to miniaturization. However, these assays are unsuitable for screening primary cells and cannot assess impact on endogenous gene expression. Real-time (quantitative) PCR (qPCR) can overcome these drawbacks and has widespread and proven use in gene expression analysis at both low and medium throughput. Until now, the application of qPCR in high throughput screening (HTS) has been limited by an often laborious multistep process to generate suitable template, and high reagent cost due to large reaction volumes. Recent advances in streamlining the qPCR workflow, liquid handling, and instrumentation have enabled scientists to generate sensitive and cost-effective high throughput qPCR data in drug discovery processes.

During the webinar the expert panel will:

- Discuss the pros and cons of qPCR vs. traditional reporter gene assays in HTS
- Describe the advances in technology that have enabled the application of qPCR in HTS
- Outline the necessary steps required for fully automated implementation of qPCR technology in HTS
- Answer your questions live during the broadcast.

SPEAKERS



Andrea Weston, Ph.D.
Bristol-Myers Squibb
Wallingford, CT



Patrick Faloon, Ph.D.
Broad Institute of MIT
and Harvard
Cambridge, MA



Daniel G. Sipes
Genomics Institute
of the Novartis Research
Foundation
San Diego, CA

Webinar sponsored by



Brought to you by the
Science/AAAS Custom
Publishing Office



Illuminate Cancer Biology

The complexity of cancer systems biology requires innovative tools for interrogating the signaling pathways responsible for oncological transformation.

Promega's integrated tools for reporter gene analysis assure biologically relevant results in cancer research.

FuGENE® HD

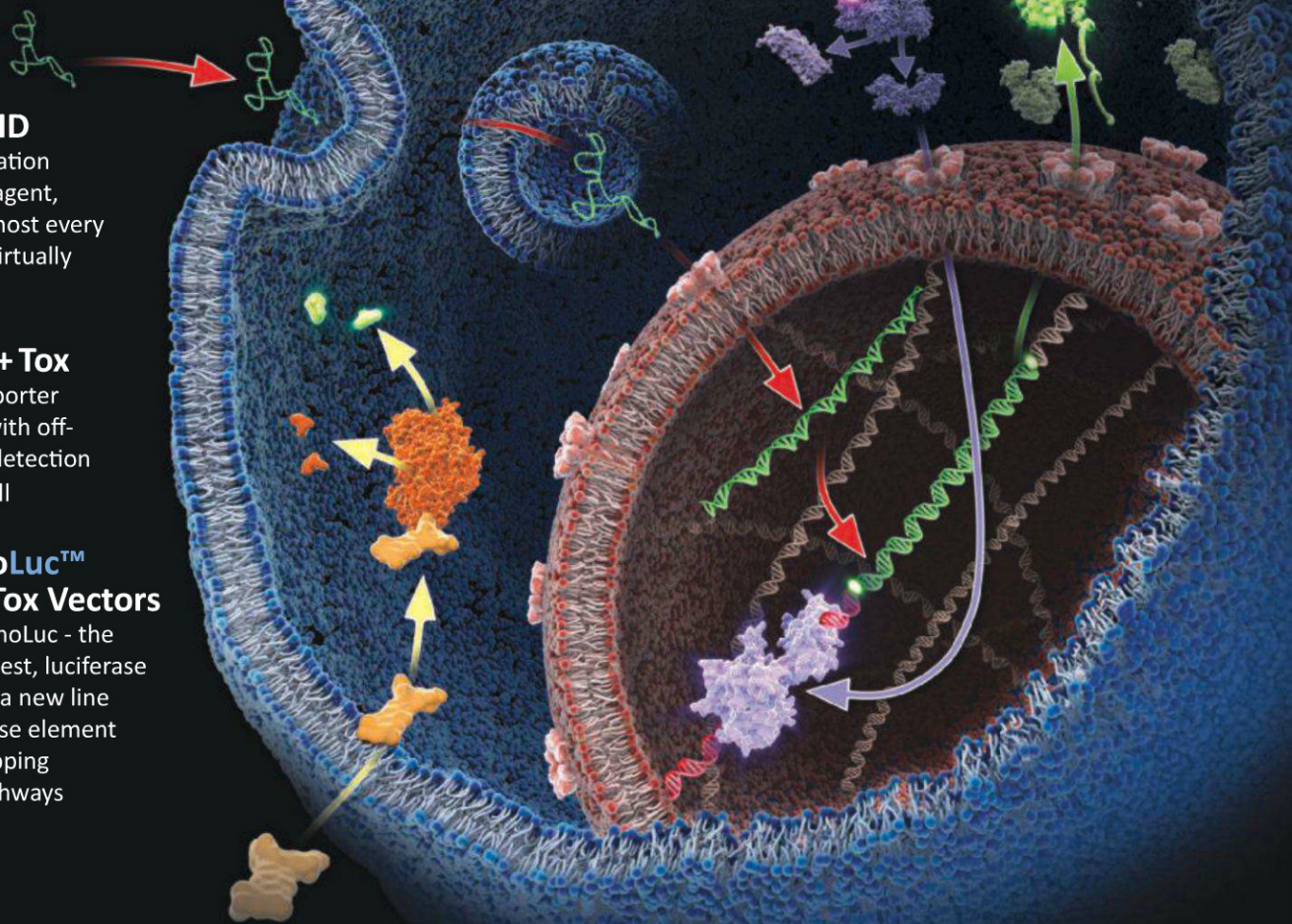
The next generation
transfection reagent,
effective on almost every
cell type with virtually
no cell toxicity

ONE-Glo™ + Tox

Multiplexed reporter gene analysis with off-target toxicity detection in the same well

New! NanoLuc™ and pGL4 Tox Vectors

Introducing NanoLuc - the brightest, smallest, luciferase available - plus a new line of pGL4 response element vectors for mapping oncological pathways



Promega

To get a **FREE** sample of any one of these reagents, visit:
www.promega.com/pathwaybiology